Synthesis, Characterization, and Mode I Fracture Toughness of Aligned Carbon Nanotube Polymer Matrix Nanocomposites

by

Dale L. Lidston

B.Eng., Mechanical Engineering
University of Pretoria (2011)

Submitted to the Department of Aeronautics and Astronautics
in partial fulfillment of the requirements for the degree of

Master of Science in Aeronautics and Astronautics

at the

MASSACHUSETTS INSTITUTE OF TECHNOLOGY

June 2017

Signature redacted

Author . . . .
Department of Aeronautics and Astronautics
May 25, 2017

Certified by . . . . Signature redacted
Brian L. Wardle
Professor of Aeronautics and Astronautics
Thesis Supervisor

Accepted by . . . . Signature redacted
Youssef M. Marzouk
Associate Professor of Aeronautics and Astronautics
Chair, Graduate Program Committee

Synthesis, Characterization, and Mode I Fracture Toughness of Aligned Carbon Nanotube Polymer Matrix Nanocomposites

by

Dale L. Lidston

Submitted to the Department of Aeronautics and Astronautics
on May 25, 2017, in partial fulfillment of the
requirements for the degree of
Master of Science in Aeronautics and Astronautics

Abstract

In an effort to fully understand the contribution of carbon nanotubes (CNTs) to strength and toughness enhancement in hierarchical nanoengineered composites, particularly steady state Mode I fracture toughness, RTM6 and EPON 862/W epoxy based vertically-aligned carbon nanotube (A-CNT) polymer nanocomposites (A-PNCs) are manufactured. These A-PNCs can be tested to isolate structure-property relationships between the polymer matrix and the A-CNTs without the presence of the micro-scale fibers. Additionally, A-CNT volume fraction can be varied via a densification process to realize 1-30% volume fraction (vf.%) A-PNCs. An investigation of the Mode I initiation fracture toughness via single edge notch beam (SENB) testing of A-PNCs with 1-5 vf.% uniaxially densified A-CNT forests finds that RTM6 baseline and A-PNC samples have a $K_{Ic,i}$ of ~ 1 MPa·m$^{1/2}$, with the exception of 1 vf.% having 1.33 ± 0.09 MPa·m$^{1/2}$, which needs to be further explored due to process-structure questions of specimen quality. No statistically significant change is observed in EPON 862/W A-PNCs at 1-5 vf.% over baseline specimens having a $K_{Ic,i}$ of 1.49 ± 0.06 MPa·m$^{1/2}$, indicating that A-CNTs do not offer any toughening at initiation in this system. Scanning electron microscopy of the fracture surface for both A-PNC systems reveals that $< 10\%$ of the A-CNTs available are engaged during crack bridging, *i.e.*, in a 5 vf.% A-PNC specimen, at most 0.5 vf.% of the A-CNTs are engaged during fracture, and pull-out from the matrix is less than 1 μm. Thus, the pullout and debonding toughening contribution offered by the A-CNTs is expected and measured to be negligible. It is possible that these A-CNTs may offer steady-state toughening, however, results are not achieved due to limitations in specimen size and geometry. While changes in Mode I initiation toughness are not observed, significant changes in properties from both quasi-static and dynamic nanoindentation testing are observed. The A-CNT alignment confers a non-isotropic mechanical response when quasi-statically tested with A-CNTs parallel or perpendicular to the indentation load. An $\sim 270\%$ modulus increase over baseline for the 30 vf.% EPON 862/W A-PNC parallel configuration and a $\sim 140\%$ increase in the perpendicular configuration, are observed and dynamic nanoindentation supports this finding with, *e.g.*, a storage modulus increase of $\sim$ 200% in the parallel orientation. RTM6 A-PNCs show less of an increase in indentation modulus ($\sim$ 33% in 10 vf.% specimens in the parallel direction) over baseline when compared to those of EPON 862/W, likely due to the relatively stiff RTM6 (modulus is $\sim$ 1.5× larger than EPON 862/W) and therefore there is a relatively smaller A-CNT stiffness contribution. Looking forward, the A-CNTs used in this work are noted to be unmodified/as-grown, and the A-CNT fracture results highlight the need for modifying the A-CNTs towards increased A-CNT strength (defect density reduction), and/or reducing the strength of the CNT-polymer interface, to increase A-CNT toughness contribution further.

Thesis Supervisor: Brian L. Wardle
Title: Professor of Aeronautics and Astronautics

Acknowledgements

Personal Acknowledgements

This thesis marks the end of a very significant chapter in my life: having been a part of the living, breathing, rapidly developing, boundary stretching organism that is MIT, my 3 year journey has brought about profound personal growth not only in my academic career, but as a well rounded individual. I will forever cherish my time here and, who knows, MIT might see me again.

First and foremost, I would like to thank my advisor, Professor Brian Wardle, without whom this adventure would not have been possible. The office door (or email) to Prof. Wardle was always open whenever I had a question about my research or writing, and I appreciate that he consistently allowed this project to be my own, but steered me in the right the direction whenever he thought I needed it. And, Carpe Noctem!

My sincere thanks goes to Sunny, who provided me with an opportunity to start my research journey in 2010 as her undergraduate intern on my study-abroad program at MIT; her passion for pushing the boundaries of science has been a continuous source of inspiration.

I thank my fellow labmates for the stimulating discussions, the sleepless nights we spent working together before deadlines, and for all the fun (and lab cleanups) we have had in the last three years. Estelle, thank you for the hours you spent at the TEM and SEM with me, and for being a constant supporter in my work. Luiz, the witty banter kept time in the lab fun and helped pass time during tedious CNT growth runs. Itai, your wise council and patience through my challenges/inadequacies with writing and Matlab will not be forgotten. Jeonyoon, Rich, Doug, and Akira thank you for sharing my workload at the most stressful times. To all my great UROPs, Christian, Roberto, Christine, Elisheva, and Alex, your contributions to this work have been priceless! Most notably, Sofi, thank you for sticking with me on this long journey of ups and downs, and for all the late nights spent in front of the SEM! To Mariam, Mike and Jeremy, your assistance with the polymer cure study is greatly appreciated (we clocked a lot of hours on the DSC together). To Jeff and Yulin, thank you for being my partners in crime, I mean... collaboration. Your insights, enthusiasm, and dedication to understanding the science behind the data kept me motivated and dedicated to our work even when nothing made sense!

To the Institute of Soldier Nanotechnologies (ISN), Nano-Engineered Composite aerospace STructures (NECST) Consortium, Mr and Mrs Hardy, and Mr and Mrs Vos, my heartfelt thanks for making this all possible!

To my friends, thank you for keeping me sane. Specifically, Diana, with memorable extramural activities like post-holing Frankenstein Cliff, building snow thrones on icy lakes and "driving" around New England in Rattling Rosie/Lurching Lucy/Galloping Gurty seeking new adventures.

Finally, I must express my very profound gratitude to my parents, Michelle and Derek, for providing me with unfailing support, love, laughs and continuous encouragement throughout my years of study. And to my husband, thesis-editor, matlab-graph-maker, personal-chef, canoe fishing partner and fellow adventurer: Jeremy, my life would not be the same without you, in spite of the mock ultimatums and deadlines during the process of researching and writing this thesis. This accomplishment would not have been possible without you (editing 200 references is true love!). Thank you, with all my heart.

This thesis is dedicated to my grandmother, Dawn, and sister, Kelly. While they will never grasp what it is about, they are always keen to know how it is proceeding. Thank you for all your encouragement!

Professional Acknowledgements

This work was supported by:

- Airbus, Embraer, Lockheed Martin, Saab AB, Hexcel, Saertex, TohoTenax, and ANSYS through MIT's Nano-Engineered Composite aerospace STructures (NECST) Consortium.
- The U. S. Army Research Laboratory and the U. S. Army Research Office through the Institute for Soldier Nanotechnologies, under contract number W911NF-13-D-0001.
- The U.S. Army Research Office under contract W911NF-07-D-0004.

This work was performed in part at:

- The Center for Nanoscale Systems (CNS), a member of the National Nanotechnology Infrastructure Network (NNIN), which is supported by the National Science Foundation under NSF award no. ECS-0335765. CNS is part of Harvard University.
- MIT's Microsystems Technology Laboratories, and made use of the MIT MRSEC Shared Experimental Facilities supported by the National Science Foundation under award number DMR-0819762.
- MIT MRSEC Shared Experimental Facilities supported by the National Science Foundation under award number DMR-0819762.

Contents

List of Figures

List of Tables

Chapter 1

Introduction

By the turn of the century, advancements in composite materials and their manufacture, allowed the commercial aerospace industry to significantly increase their use of these materials. These developments were driven mainly by the defense sector due to the demands for light-weight aerospace materials for extensive utilization in military aircraft. A timeline is known for commercial aircraft (with a focus on Airbus and Boeing) and is shown in Figure 1-1 to highlight the exponential rate of composite utilization. In October 1958, the Boeing 707 was launched with a mere 2 weight % (wt.%) of the structure made of fiberglass. By April 1983, Airbus followed suit by including 5 wt.% composite material in the A310 and went on incorporate 10 wt.% in the A340 by March 1993. Over a decade later in October 2007, Airbus launched the world's largest passenger airliner, the A380, with 25 wt.% composite materials. The next biggest milestone occurred in October 2011, where Boeing became the first airliner to launch a commercial aircraft with composite wings and fuselage, the Boeing 787, with a total of 50 wt.% (80% by volume), just over 50 years from the first incorporation of composites in commercial aircraft. This feat was matched in January 2015, with the Airbus A350 XWB having a fuselage and wing structures made primarily (53 wt.%) of carbon fibre reinforced polymer (CFRP), including its upper and lower covers – the single largest aviation parts made from carbon fiber, measuring 32 metres long by six metres wide[1–3].

Composite materials, especially CFRPs (illustration of structure in Figure 1-2), are comparatively lightweight, insensitive to corrosion, can be manufactured into large complex

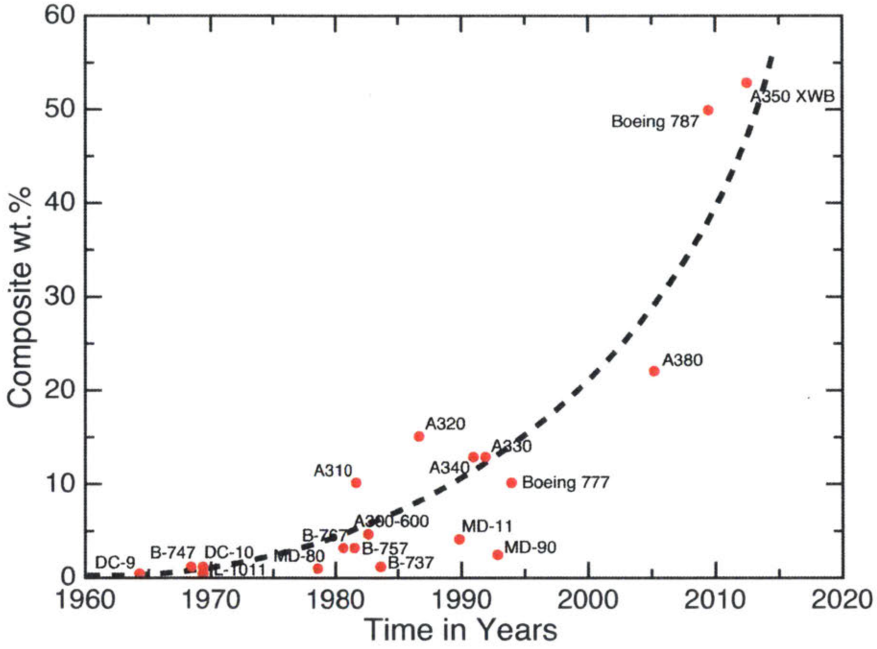

Figure 1-1: Reported historical composite wt.% of various aircraft models showing the rapid increase of composite employment to date. It is noted that an inflection will occur as 100 wt.% is approached where significant multifunctional improvements to composites will be required for minor increases in wt.% contributions (adapted from original[4]).

parts, and lend to overall reduction in maintenance costs through increased service intervals owing to increased durability. A life cycle assessment of aircraft panels made from CFRP and aluminum plates was performed to determine emissions savings of CFRPs over the life of the component[6]. Despite being more energy intensive to manufacture and dispose of, CFRP leads to a significant decrease in the overall environmental impact due to the reduced fuel consumption. The break-even flight distance above which CFRPs show a net reduction of environmental damage compared to the aluminum plate was 70,000 km[6].

CFRPs, however, still have a number of shortcomings such as limitations in electrical and thermal conductivity, poor recyclablity, costliness of manufacturing making them significantly more expensive than aluminum alloys, and poor impact damage resistance concomitant with damage being difficult to assess[6,7]. Thus, even on the "nearly-all-composite" aircraft, metals are still found on the engine pylons to offer fire protection, on the leading edges for bird strikes, and in highly loaded joints such as between the undercarriage

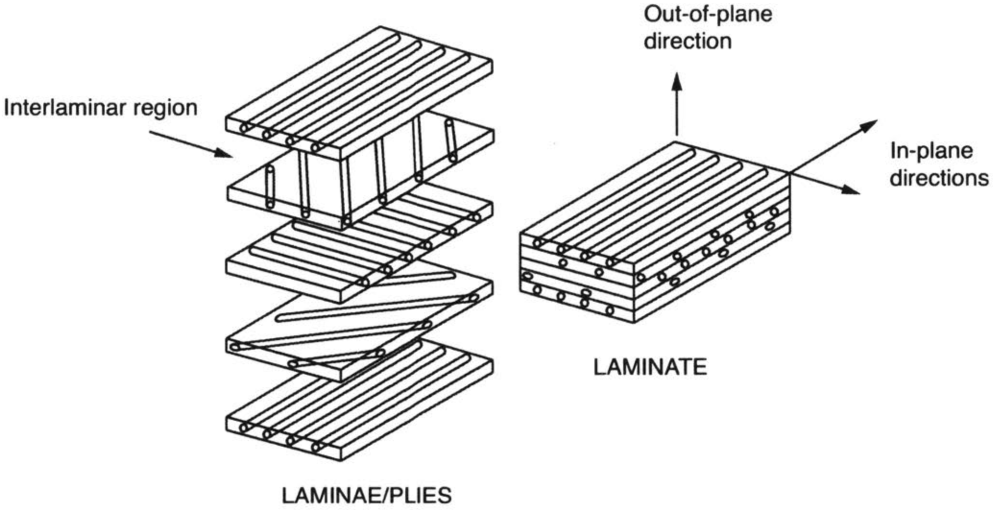

Figure 1-2: Laminated composite terminology, indicating interlaminar region, in-plane directions that are dominated by fiber properties, and out-of-plane (through-thickness) direction that is dominated by matrix properties (reproduced[5]).

and composite structures[2,8,9]. To improve composites further, key capabilities are required through the development of next-generation multifunctional structural materials exhibiting properties such as high heat resistance, increased electrical conductivity, damage sensing capabilities and radiation shielding, while remaining lightweight with significantly increased damage tolerance[10].

The incorporation of carbon nanotubes (CNTs), and other nanoparticles, into composite layups to create hierarchical materials shows promise in realizing these desired multifunctionalities. The idea of using fillers as a reinforcing agent is nothing new: straw has been used to reinforce mud bricks since about 4000 BC[11]. The combination of properties of the nanofiller with that of the matrix material can introduce multifunctionalities without the deterioration of other important physical properties. Researchers can take advantage of conductive and high aspect ratio nanofillers (i.e. CNTs) to produce conductive plastics with low percolation thresholds[12]. In another area, thermal resistivity of defective CNTs can be exploited for Joule heating[13]. However, probably the most promising area involves the mechanical enhancement of laminated composites and polymers using reinforcing fillers.

1.1 Carbon Nanotubes (CNTs) and Their Polymer Nanocomposites (PNCs) in Novel Hierarchical Material Architectures

Some (macroscopic) materials have a complex microstructure that is itself made up of nanoscale components, with the interaction of components of each level playing a major role in determining bulk material properties. These characteristic length-scales can range from the nm-scale, such as in the several atomic diameter wide CNTs, to the μm-scale, e.g. in carbon fibers that are similar in width to a human hair, and up to meter-scale, such as the plates that comprise an aircraft's wing. Understanding the structural contribution of each level of the hierarchy, can steer research towards the synthesis of new materials with bulk physical properties that are tailored to specific applications. Hierarchical materials are widely observed in nature where high mechanical performance is obtained from fairly weak constituents by using a range of length-scales, e.g. in wood, bone, and marine animals such as siliceous sponges and mollusk (nacre)[14–16].

A man-made example is the introduction of nanomaterials into conventional fiber reinforced polymer composites, creating a hierarchical structure composed of macroscopic epoxy, microscale reinforcing fibers, and nanoscopic components[17–20]. The main driver for this is the reinforcement of the weak interlaminar region that is created between laminae in layered fiber reinforced plastics[19,21,22]. These regions consist only of comparably low strength and toughness polymer matrix which limits performance and manifests as delamination and matrix cracking in shear and out-of-plane loading conditions[23]. By using nanoscale structures, improvements in this region can be realized by matrix property modification, and increased load transfer capabilities can be realized.

Of the numerous nanofiller options available, CNTs are one of the best choices with superior and tailorable mechanical, thermal, and electrical properties, providing not only mechanical reinforcement, but elements of multifunctionality[13,25,26]; Figure 1-3 highlights the attractive strength-to-weight and stiffness-to-weight ratios when compared to other en-

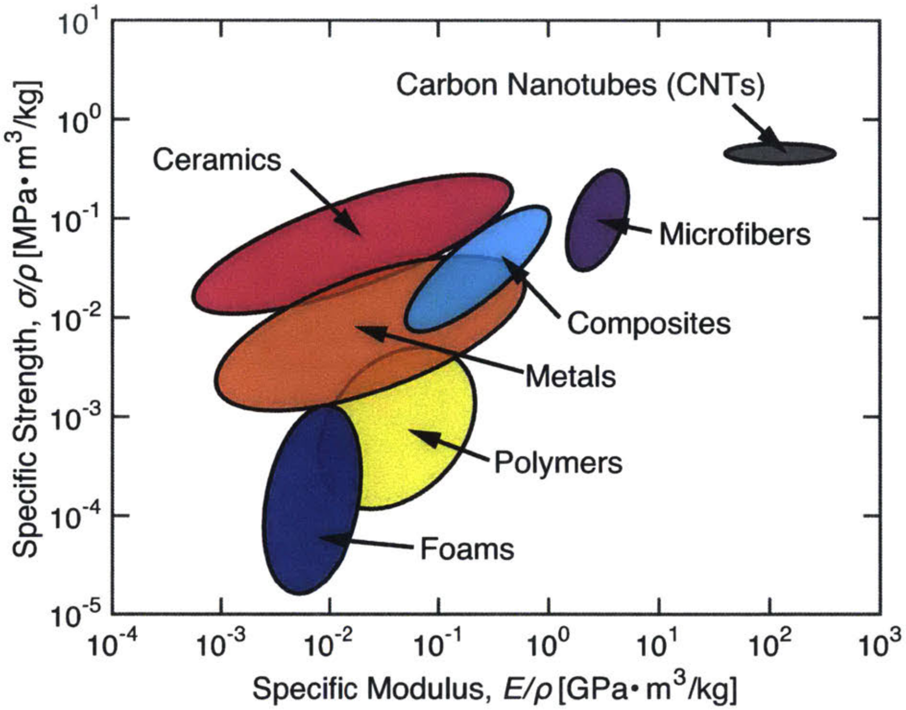

Figure 1-3: Ashby plot of specific strength and stiffness of CNTs and composites relative to other engineering materials (reproduced[5,24]), showing superior strength-to-weight and stiffness-to-weight ratios making them attractive as a nanofiller.

gineering materials, demonstrating the potential of CNTs as nanoscale reinforcement in composites. However, while CNTs exhibit exceptional material properties, these properties span large ranges (resulting from synthesis variations) and depend on number of walls, diameter, chirality, defect density, and other stochastic morphological characteristics such as waviness and CNT-CNT interactions[27–29]. Coupled with this, their tubular geometry has been manipulated through controlling CNT orientation during manufacturing to create non-isotropic material response[30,31]. These varied CNT properties and orientations transfer into the hierarchical construction, and can manifest a wide range of results in the literature.

Before laminate level improvements in properties can be consistently achieved and the full potential of CNTs realized, more needs to be understood about how CNTs affect local material properties. Also, by aligning CNTs such that the long axis is perpendicular to propagating interlaminar cracks, the Mode I fracture toughness response can potentially be increased by mechanisms such as bridging toughening[19,32,33].

1.2 Thesis Outline

This thesis thoroughly details the background, processing parameters, characterization, test methods, Mode I initiation fracture toughness (steady state could not be achieved), and other mechanical properties of aligned carbon nanotube polymer nanocomposites (A-PNCs).

Chapter 2 provides an overview of current composite material reinforcement strategies using nanomaterials, and highlights shortcomings in delineating contributions of the nanoparticles from the final composite properties. Motivations are provided for the work herein, specifically understanding how aligned carbon nanotubes affect the local mechanical and material properties of the laminate through the use of polymer nanocomposites (PNC).

Chapter 3 clarifies the thesis objectives and provides the scope of this work, laid out as follows: identifying the limits of aligned carbon nanotube (A-CNT) production, which directly impacts the manufacturability of test samples, and suitably testing and characterizing resulting materials not only to determine the mechanical reinforcement effects, but also to create a platform for future work.

Chapter 4 begins the exploration of the aforementioned A-CNT manufacturing limits to select A-PNC sample preparation techniques and test method selection. Morphological characterization is performed to map how parametric changes in growth conditions affect the as-grown A-CNTs, and how this affects process-structure(-property) relations of A-PNC test specimens.

Chapter 5 uses findings from Chapter 4, and builds on previous work, to develop test sample manufacturing methods to carry out this work, with the aim of developing generalized techniques for use in complementary and future work. A procedure to evaluate the quality of the A-PNC test specimen preparation technique as well as individual specimens is described. These evaluations allowed the development of procedures to minimize porosity and the ability to select non-porous regions for testing.

Chapter 6 details test methods and findings that are used to evaluate the performance of A-CNTs as Mode I initiation fracture toughness reinforcing agents in structural epoxy. The effects of A-CNT structure and sample processing on fracture behavior is presented. This data sets the basis of recommendations for future work in tailoring A-CNT interactions with epoxy polymers.

Chapter 7 focuses on supplementary mechanical behavior testing such as dynamic nanoindentation (nanoDMA), and nanoindentation for stiffness, storage and loss modulus. Such specimens can be used to explore nano-scale interaction effects and these properties are used to support findings regarding the multifunctional nature of CNT incorporation into composite laminates.

Chapter 8 summarizes the important findings of this thesis and discusses what conclusions can be drawn. Future research direction is suggested based on current limitations, such as specimen processing and configuration, A-CNT morphology and surface characteristics, and test methods employed.

Chapter 2

Background and Prior Work

CNTs were identified more than two decades ago as a nanomaterial that can revolutionize the way traditional materials behave through the careful use of process-structure-property relations to create high performance multifunctional materials. The majority of the CNTs produced today are utilized in bulk applications such as rechargeable batteries, automotive parts, sporting goods, and in more recent years, thin-film electronics, super-capacitors, actuators and coatings. Advances in CNT synthesis and manufacturing techniques, coupled with the continuous demands to push the operational envelope of modern aerospace structures, has driven research of organized CNT architectures into advanced hierarchical composite materials. The next section contains an overview of the current state-of-the-art advanced fiber reinforced composite materials, including the integration of various CNT morphologies, and the resulting influence on physical properties. Of particular interest is the effect on Mode I initiation and steady state fracture toughness and this is discussed in subsequent sections. The remainder of the chapter discusses the use of morphology-controlled nanocomposites as representative volume elements to study the isolated effects of the CNTs within the polymer phase of these laminated composites.

The purpose of this chapter is to provide the necessary information to create a foundation on which the work in this thesis is built. Additional background will be provided in subsequent chapters as needed.

2.1 CNTs in Advanced Composites

The main driver behind modifying composite laminates is to address load bearing function in the out-of-plane direction - delamination and matrix cracking between laminae are the primary failure modes[34,35]. Historically, attempts to increase load bearing in the out-of-plane direction have been either detrimental to load bearing in the in-plane direction, or have decreased other functional requirements[36]. However, through the use of nanomaterials, specifically CNTs, the load bearing function can be independently increased while simultaneously adding multifunctional non-structural properties, such as deicing and damage sensing etc.[37,38] Although structural weight is not a function, it is an extremely important factor in the creation of multifunctional lightweight aerospace materials. And, using nanomaterials to create multifunctionality, contributes to global composite behavior with insignificant weight gain.

This section broadly introduces nanoparticles as out-of-plane reinforcement agents for hierarchical composites with a refined focus on CNTs. Of the numerous structural and non-structural property improvements that CNTs impart, Mode I initiation and steady state fracture toughness is central to this thesis, and hence background on the influence of CNTs on Mode I fracture toughness of laminate composites is included. Due to the multiple length scales present in hierarchical composites, the contribution of CNTs cannot be clearly elucidated and thus polymer nanocomposites are created as approximations of the CNT-polymer interaction. The manufacture of PNCs and their resulting Mode I fracture toughness is discussed with a summary of attributable reinforcement mechanisms seen in literature.

2.1.1 Nanoparticles as Composite Reinforcement

Nanoparticles have been used in polymeric materials, and laminated composites, to enhance a number of structural and non-structural properties. They are attractive due to their relatively large surface area to volume ratio (e.g., a CNT has 1000× the surface-to-volume ratio of a carbon microfiber of equivalent length), meaning that only relatively small amounts of nanoparticles are needed to influence the properties of the surrounding polymer. While the reinforcement aspects are of key interest in this thesis, a number of potential property improvements are important to note: structural properties such as strength, stiffness, fracture toughness, and non-structural functions, including electrical and/or thermal conductivity, sensing and actuation, energy harvesting/storage, self-healing capability, electromagnetic interference shielding[39], barrier properties, resistance to flammability, and membrane properties[40]. Using nanomaterials harnesses the "nano-effect," which is the enhancement of material properties as the dimensions decrease to the nanoscale[40,41]; this is because the critical flaw size becomes larger than the dimensions of the nanomaterial. To clarify, nanoscale is where the dimensions of a particle are in the 1-100 nm range - in the case of a fiber, the smallest dimension, diameter, is considered for that range.

A popular nanomaterial is the CNT, which gained prominence following an article by Iijima in 1991[42]. CNTs have a diameter in the nanoscale range, and are described as seamless cylinders of graphene, which can have either single or multiple walls, respectively termed single-walled carbon nanotubes (SWNT) and multi-walled carbon nanotubes (MWNT), see Figure 2-1 for illustration. The concentric walls of MWNTs are held together with relatively weak van der Waals forces which makes property prediction challenging. A perfect CNT contains carbon atoms all bonded in a hexagonal lattice (except at the ends where they may be capped or uncapped). Quantum mechanics calculations predict a pristine SWNT to have an elastic modulus (E) of $\sim$1 TPa with a tensile strength on the order of 100 GPa[43–45]. Experimental testing has shown that these values are attainable with a mean modulus of $\sim$955 GPa being measured in arc-discharge-grown MWNTs and a nominal failure stress of $\sim$100 GPa using CNTs with irradiation-induced cross-links[46]. However, the majority of the CNTs produced contain defects where other polygons are introduced into the hexagonal structure[47,48]. It is these defects[49], as well as other physical characteristics such as chirality and diameter, that determine the mechanical properties of each CNT. Due to handling difficulties, measuring the actual mechanical properties for CNTs is challenging[11]. This, coupled with variations in CNT structure due to specimen pedigree, results in a very wide range of measured modulus and strength values of 0.27-1.3 TPa and 33-110 GPa, respectively, depending on manufacturing and testing conditions[50–52]. It is noted that these properties are also exhibited by 2D graphene and nanographite, however dispersion and handling difficulties, limit their use to relatively low levels of graphene loading, and challenges still remain in obtaining good mechanical properties for high volume fractions of reinforcement[53].

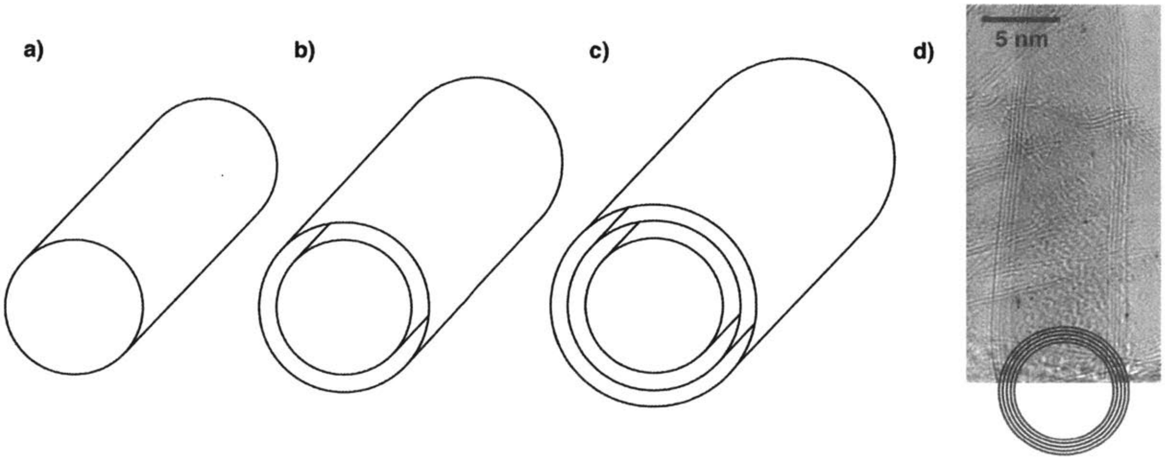

Figure 2-1: Illustration of structural model for a) single walled b) double walled c) triple walled and d) multiwalled CNTs. Each cylinder represents a coaxial closed layer of carbon hexagons (adapted from Iijima[42]).

Regardless of the range of properties, attempting to exploit the tensile strength and elastic modulus of CNTs has been the driving force behind their integration into polymers and laminates; incorporation of CNTs can increase stiffness, strength and toughness without compromising other mechanical properties[54]. Various morphologies of CNTs have been included, for example (see Figure 2-2 for illustration): (I) CNT powder can be mixed with polymers or resins prior to infusion into the fiber reinforcement, (II) CNTs can be sandwiched between plies of the laminate, one example being called "nanostitch" or, (III) CNTs can be grown radially from the fibers creating "fuzzy fibers"[5,55].

To highlight some examples of the use of nanomaterials in composite materials: following case I, Manjunatha et al.[56] observe a 2-3× increase in tensile fatigue life with the addition of 10 wt.% sol–gel-formed nanosilica to the epoxy matrix of a glass fabric-reinforced epoxy composite. Garcia et al.[32] joined prepreg composite interfaces with aligned nanotubes (case II) in a process called "nanostitch" that focuses on improving interlaminar strength and toughness through the use of the aligned CNT forests. As shown in Figure 2-2, vertically aligned CNT forests bridge and strengthen this interlaminar region. More specifically, the

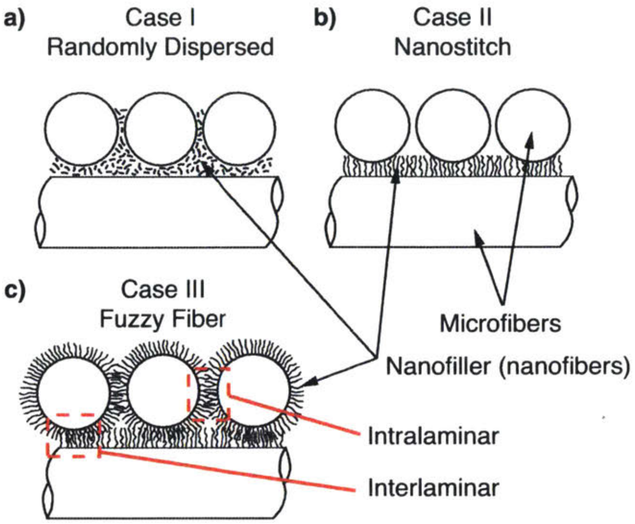

Figure 2-2: Representations of composite interlaminar and intralaminar reinforcement using CNTs in the a) random dispersion (case I), b) nanostitch (case II) and c) fuzzy-fiber (case III) approach. Nanostitch involves sandwiching an A-CNT forest between plies while fuzzy-fibers result from growing A-CNTs radially from the microfiber used in the fiber reinforced plastic.

CNT modified interfaces increased the Mode I interlaminar fracture toughness of aerospace grade carbon fiber/epoxy laminates by 1.5–2.5× and the corresponding Mode II by 3×. Case III involves the growth of CNTs on the surfaces of micron-sized fibers - the "fuzzy-fiber"[57–60]. In this process CNTs are grown on the surface of macroscale cloth or weaves comprised of micron-diameter fibers such as glass, alumina, and carbon fiber using chemical vapor deposition (CVD). The fabric is stacked and then infiltrated with a polymer (usually epoxy resin) to form a 3D composite. The fuzzy-fibers can provide both interlaminar and intralaminar reinforcement, like case I, (Figure 2-2) through an increase in the interfacial shear strength[61] and local reinforcement of the matrix[18]. When comparing fuzzy-fiber to baseline composites, significant improvements in the Mode I and Mode II fracture toughness, flexural modulus, flexural strength, coefficient of thermal expansion, thermal conductivity and electrical conductivity have been reported[39].

However, the degree of enhancement is dependent on the CNT type, aspect ratio, dispersion and orientation, as well as the interface between the CNTs and the polymer matrix. Of these parameters, the issue of dispersion is critical to reinforcement efficacy as aggregation is found to diminish properties in composites. When considering techniques for integrating A-CNTs into composites, case I where CNT powder can be mixed with polymers or resins prior to the infusion into the fiber reinforcement, is especially met with dispersion challenges. Loose CNTs tend to assemble in bundles, which when added to a polymer, do not disperse due to the high surface energy of the CNTs. During loading, individual nanotubes that are not bonded to the matrix slip within the bundle, affecting the elastic properties. The "nano-effect" is also affected by agglomeration because of the reduction in aspect ratio (length/diameter) of the reinforcing material (i.e. the effective diameter increases). Similarly, other nanomaterials, such as nanoclays and graphite, require exfoliation to allow all surfaces to come into contact with the polymer.

Dispersion techniques for case I fit into two main categories: mechanical dispersion methods and chemical modification of the nanoparticle surface. Mechanical techniques include shear mixing, sonication (bath or probe), calendering and ball mixing. Shear mixing is commonly utilized and is effective in dispersing spherical nanoparticles, however, volume fraction is limited due to the increase in viscosity. For large aspect ratio nanoparticles, shear mixing, and other direct mechanical or high energy input methods, such as sonication, cause undesirable breakage into smaller lengths, called scission[62–64], which is considered to be a major disadvantage due to the reduction of aspect ratio. Chemical methods, namely functionalization, aim to change the nanoparticle interaction with the polymer leading to enhanced dispersion. Depending on the method employed, a drawback of these methods, specifically when using concentrated acids, is that they can be aggressive, leading to the formation of structural defects that deteriorate the nanoparticle properties. Non-covalent physical treatments such as surfactants or intermediate polymer coatings do not tend to damage the nanoparticle structure and lower the nanoparticle surface tension, preventing them from agglomerating[65].

Other attempts to control agglomeration of nanoparticles in composite laminates include spraying and rolling (this is similar to case II). While a uniform layer of nanoparticles can be achieved, in the case of CNTs, alignment in a direction perpendicular to typical crack propagation cannot be controlled. Rather, by utilizing nanostitch or "fuzzy-fiber" techniques, growth morphologies allow control over dispersion and orientation.

Laminate property tailoring is not only affected by nanoparticle dispersion and orientation, it is dependent on the individual properties of the constituents as well as the complex interaction between them. Nanoparticles can have a marked affect on their surrounding polymer. PNCs are used to create a material that harnesses the properties of both the nanoparticle and the polymer, and to study the effect that the nanoparticles have on the morphology of the polymer.

2.1.2 Polymer Interactions with CNTs in PNCs

While composite materials can be manufactured from a wide variety of polymers, the unique operating conditions in aerospace applications requires the use of polymers that can withstand high temperatures, exhibit environmental stability, as well as possess high strength and toughness that can promote lightweight construction[66,67]. Mangalgiri[67] suggests that the most popular polymers are thermoset epoxies that have been optimized to perform in required operational envelopes; these account for 80% of aerospace applications. Other common thermoset matrices are phenolics, polyesters and polyimides. Another route is to consider high temperature thermoplastics such as polyphenylene sulphide (PPS) or poly-ether-ether-ketone (PEEK) however, material processing limits utilization as melting temperature is $\sim$ 300-400°C.

With the utilization A-CNTs as reinforcement agents in the above mentioned composite configurations, the potential CNT-polymer interactions must be understood to establish the mechanistic role it plays in the mechanical reinforcement process. It is well-recognized that crystallization rate and degree of crystallinity can be influenced by confined spaces[40], such as the interstices between CNTs arranged in an array. Additionally, a number of studies suggest that polymer interactions with the CNT interface result in an inter-phase region where the polymer morphology and properties are different from the bulk. Some studies have shown that polymer chains can wrap around the CNT[68] while others have shown crystalline polymer growth nucleating from defects in the nanotubes[69–71]. During pullout experiments, numerous groups have observed polymer coatings on the nanotubes which demonstrates high interfacial bonding as well as higher shear strength properties of the polymer layer[72–74].

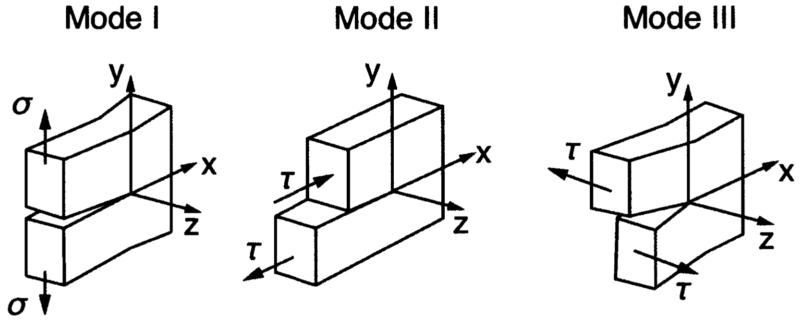

Figure 2-3: Three modes of crack loading: Mode I or crack opening mode, Mode II or sliding mode, and Mode III or tearing mode (reproduced[76]).

These experiments, however, are focused on thermoplastic polymers, and the inter-phase response is very polymer specific. The curing and physical behavior of the highly utilized aerospace epoxy is likewise not disturbed by the presence of aligned CNTs[75]. Hence, any potential improvements in mechanical properties will stem from the physical interaction between CNT and the epoxy. Due to the brittle nature of the epoxy matrix utilized in composite laminates, an increase in resistance to crack propagation is desirable to limit delamination and matrix cracking, as discussed in the following section.

2.2 Mode I Fracture Toughness

A cracked component can be subjected to, predominantly, three modes of deformation as seen in Figure 2-3, namely:

- Mode I takes places when a crack is subjected to pure bending in the same plane as the crack, or pure tensile loading perpendicular to the crack plane; both methods induce a tensile stress normal to the plane of the crack. Mode I is termed the "opening mode" where the crack face opens without any sliding.
- Mode II or "sliding mode" results from shear stresses acting parallel to the crack plane (but perpendicular to the crack front) causing crack faces to slide without any opening.
- Mode III is similar to Mode II however shear stress act parallel to both the crack plane and crack front causing a "tearing mode."

Fracture toughness is the resistance to crack growth. Given the laminated nature of typical composites, delamination is a common failure mode that results from Mode I loading of the polymer-rich interlaminar region. Polymer reinforcements in this weak region, using CNTs, are the focus of this work and this section discusses the literature for Mode I fracture toughness of both reinforced advanced composites and polymer nanocomposites.

Fiber toughening during fracture is attributed to two main mechanisms, namely: debonding at the matrix/fiber interface with an associated toughness (energy) contribution of G_d, and friction that results from the debonded fiber pulling out from the matrix with a contribution of G_p[77]. G_p is typically much larger than G_d and these are calculated as follows:

$$G_d = \frac{v_f l G_{int}}{r} \tag{2.1}$$

$$G_p = \frac{v_f l^2 \tau_f}{3r} \tag{2.2}$$

Where v_f is volume fraction of the fiber, l is the pull-out length, r is the fiber radius, G_{int} is the interface toughness, and τ_f is the shear stress due to friction during pull-out. From Equation 2.1 and Equation 2.2, it can be seen that both toughening mechanisms are a function of fiber geometry and volume fraction. Thus, to increase contributions from these mechanisms, radius should be small, pull-out length should be long and volume fraction should be large. Nanofibers, especially CNT, are a obvious choice due to their large aspect ratio hence their incorporation into hierarchical composites is warranted. However, it has been shown that toughening by A-CNTs through pull-out is often strength limited which reduces pull-out[22]. Note that these relations are derived for typical macroscale columnar fibers and are typically assumed valid for nanofibers. These equations do not, however, account for morphological features such as waviness. Accurate modelling of these features is beyond the scope of this work, and the above equations are presented as a basis for a high-level discussion of findings in this thesis.

During fracture, there are two main areas of interest: crack initiation and steady state propagation. The toughness G (or strain energy release rate) during these regions is of key interest, and is typically determined by[78]:

$$G = \left(\frac{\sigma^2 \pi}{E}\right) a \tag{2.3}$$

Where σ is the applied stress, E is the Young's modulus and a is the crack length. Notice from Equation 2.3 that G increases linearly with a for a constant applied stress. Initiation of the crack will occur when applied stress increases to a critical point where the material can no longer resist crack growth at a flaw of size a_o, and the strain energy at this critical initiation point is denoted as $G_{Ic,i}$ where "I" represents Mode I crack opening. For ideal brittle materials (such as epoxies), after the crack initiates, the material offers no resistance to crack growth, R, thus the steady state toughness remains constant and equal to the initiation toughness due to the creation of the new surfaces during crack growth with no additional toughening, i.e., R is independent of crack length for brittle materials, and this is shown in Figure 2-4a. While crack length increases, R remains constant and G increases linearly based on the applied load.

In ductile materials, however, resistance to crack growth can increase from initiation during crack growth due to dynamic toughening mechanisms. In metals and polymers, crack tip plasticity is an example of a toughening mechanism. In fiber based systems, G_p and G_d are both toughening mechanisms that add to crack growth resistance. These resistance mechanisms all increase from initiation until a steady state is reached. With only marginal increases in resistance, it is possible for the resistance curve to remain below that of the (linear) G curve for the constant applied load, as can be seen in Figure 2-4b, where the crack will propagate in an unstable manner, similar to brittle fracture.

In instances where significant resistance is offered as in Figure 2-4c, the R-curve is such that the resistance increases beyond G which will lead to crack arrest. To continue propagating the crack, an increased applied stress ($> \sigma_1$) in necessary such that G becomes greater than R once again. Multiple arrest points can occur, and with each arrest, the load applied must be increased to continue propagating the crack until the point where resistance reaches a steady state below G at (σ_4) and the crack propagates without arrest. The strain energy release rate at this steady state point is denoted G_{ss}.

2.2.1 Mode I Fracture Toughness of CNT Reinforced Advanced Composites

Mode I fracture toughness in composite laminates can be tested using double cantilever beam (DCB) specimens according to ASTM D5582[79]. In these specimens, Mode I propagates cracks along the polymer-rich interface between plies, and significant a increase in steady state toughness of up to 100% is demonstrated in literature (Table 2.1) by adding CNT reinforcement to that interface[19,33,80–83].

Table 2.1: Mode I steady state fracture toughness results as presented in the literature for CNT reinforcement of fiber reinforced plastics showing a large range of reported increases, up to 100%. Different fiber systems as well as various reinforcement techniques are presented, whilst all employ double cantilever beam specimens.

Fiber System	Matrix	CNT Loading	Reinforcement	% Change
Glass fibers[80]	Polyester	1 wt.% CNTs	Randomly dispersed	100%
Carbon fibers[81]	Epoxy	0.1-1 wt.%	Randomly dispersed	60%
Carbon fibers[82]	Epoxy	0.5 wt.%	Randomly dispersed	80%
SiC fibers[33]	Epoxy	MWCNTs	"Fuzzy fiber"	60%
Alumina fibers[19]	Epoxy	MWCNTs	"Fuzzy fiber"	76%
E-glass[83]	Resin blend	0.1 wt.%	Randomly dispersed	0%

Owing to a wide range of functionalization treatments, polymers, polymer additives and assorted pedigree CNTs utilized, there is no consensus about which reinforcement approach is most effective, see Table 2.1 for details. Also, most studies that disperse CNTs into the polymer matrix prior to infusion do not report the final CNT orientation, however, it is most likely random, or parallel to microfibers due to flow field alignment during infusion. Additionally, caution should be applied in the interpretation of some of these results as the incorporation of CNTs can increase the thickness of the interlaminar region to which toughness is very sensitive. Although a thicker interlaminar region will enhance Mode I steady state toughness, it will degrade performance in the in-plane directions as the fiber volume fraction decreases.

Thus, to elucidate the contribution of the CNTs to Mode I steady state (and initiation) fracture toughness of the laminate, the polymer-CNT interaction must be decoupled. A representative element in the form of a polymer nanocomposite can be constructed and tested in Mode I likely to achieve this.

2.2.2 Mode I Fracture Toughness of Epoxy PNCs

Linear elastic fracture mechanics enables the measurement of intrinsic Mode I fracture toughness. Researchers typically utilize either single edge-notch beam (SENB) or compact tension (CT) specimen configurations as described by ASTM D5045[84] for initiation toughness testing, however other configurations are also available such as double cantilever beams and circumferentially notched bar samples[78], see Figure 2-5. Mode I steady state toughness testing is typically performed using the DCB configuration, however this can be achieved using CT or SENB specimens.

Independent of the specimen geometry described in Figure 2-5, information can be gained about the initiation of cracks in epoxy nanocomposites. Using the peak load gathered from the load-displacement curve, the initiation critical stress intensity factor ($K_{Ic,i}$) is then calculated. With the calculated $K_{Ic,i}$ and the elastic modulus E, the critical energy release rate ($G_{Ic,i}$) can be calculated, assuming isotropy, from:

$$G_{Ic,i} = \frac{K_{Ic,i}^2(1-\nu^2)}{E} \tag{2.4}$$

$G_{Ic,i}$ can also be determined by numerically integrating the load-displacement curve to the point of the $K_{Ic,i}$ peak load, providing the energy of the net generated fracture surface during initiation. Assuming representative Young's Modulus and Poisson ratio, ν, both methods will correspond well.

For the common SENB and CT specimens, if the samples fracture in a brittle manner (stress-strain curve remains linear until fracture), $K_{Ic,i}$ is calculated, by:

$$K_{Ic,i} = \frac{P}{Bw^{1/2}} \cdot f\left(\frac{a}{w}\right) \tag{2.5}$$

For SENB specimens, $f(\frac{a}{w})$ is given by:

$$f\left(\frac{a}{w}\right) = 6 \times \left(\frac{a}{w}\right)^{1/2} \times \frac{\left[1.99 - \frac{a}{w}\left(1 - \frac{a}{w}\right)\left(2.15 - 3.93\frac{a}{w} + 2.7\left(\frac{a}{w}\right)^2\right)\right]}{\left(1 + 2\frac{a}{w}\right)\left(1 - \frac{a}{w}\right)^{3/2}} \tag{2.6}$$

Similarly, for CT specimens, $f(\frac{a}{w})$ is given by:

$$f\left(\frac{a}{w}\right) = \frac{\left(2 + \frac{a}{w}\right)\left(0.886 + 4.64\left(\frac{a}{w}\right) - 13.32\left(\frac{a}{w}\right)^2 + 14.72\left(\frac{a}{w}\right)^3 - 5.6\left(\frac{a}{w}\right)^4\right)}{\left(1 - \frac{a}{w}\right)^{3/2}} \tag{2.7}$$

With this, contradictory reports have been found in literature regarding the effects of both CNT morphology and material processing on the Mode I initiation fracture toughness, $K_{Ic,i}$, of polymer nanocomposites. Using CT-specimens, Gojny et al.[85], report an increased $K_{Ic,i}$, independent of nanoparticle filler type as shown in Figure 2-6a. The samples were manufactured by dispersing carbon black or carbon nanotubes with various functionalization treatments, into an epoxy using the calendering technique. The epoxy matrix was a modified bis-phenol-A-based epoxy resin (MGS L135i) together with an amine-curing agent H137i. The epoxy averaged $K_{Ic,i} = 0.65$ MPa·m$^{1/2}$ with an increase range of 10-25% depending on filler, with a maximum loading of 1 wt.%. Figure 2-6b displays tensile test curves, where the neat epoxy samples exhibit polymer ductility, indicating that these samples do not fail in a completely brittle manner which is unusual for an epoxy, likely resulting from the epoxy modification.

Also, using a calendering technique for CNT dispersion, Thostenson and Chou[86] added several different weight fractions, up to 5 wt.%, to a bisphenol-f epichlorohydrin epoxy resin system (EPON 862/Epikure W). Figure 2-7 reveals test data obtained from the SENB specimens that were tested and show, firstly, that initiation fracture toughness is increased with the addition of CNTs, secondly, maximum reinforcement occurs at $\sim$ 0.2 wt.% loading and decreases thereafter, and finally, their processing methods have a direct impact on $K_{Ic,i}$. The authors discuss that a higher calendering gap width presents with an increase in $K_{Ic,i}$

indicating that agglomerated CNTs are likely the cause by providing a larger inclusion size to interact with the crack front. Information about post shear-mixing CNT length, as a function of calendaring gap width and weight %, is not provided nor are conclusions drawn regarding the decrease in $K_{Ic,i}$ with increasing CNT loading.

In a popular article by Zhou et al.[87], the authors use a high-intensity ultrasonic liquid processor to create an EPON 862/Epikure W epoxy system and MWCNT mixture. A reported increase is seen in flexural modulus of up to 11.7% as CNT loading increases up to 0.4 wt.%[87], as presented in Figure 2-8. Likewise flexural strength is enhanced by up to 28.3% with 0.3 wt.% CNTs, however, the positive trend reverses at 0.4 wt.% to which the authors attribute either non-uniform dispersion or voids. Additionally, initiation fracture toughness testing was performed using SENB specimens where $K_{Ic,i}$ is said to increase up to 0.3 wt.% CNTs, beyond which a decrease is observed, see Figure 2-9. Fractography shows an increase in surface roughness with higher CNT content, and although not discussed, it is seen that CNT pullout is $< 1\ \mu$m. It must also be noted that Zhou et al.[87] and Thostenson and Chou[86] used the same epoxy resin/cure agent system, however, there is a 3× difference between their reported $K_{Ic,i}$ values for neat, cured, epoxy baseline specimens. Additionally, given the reported increase in flexural modulus, the authors do not comment on how this contributes to the increased $K_{Ic,i}$.

Few studies have dealt with higher weight percent of nanofiller, likely due to the challenges of dispersion as results typically decrease below that of control specimens. For example, Gryshchuk et al.[88] report a 14% decrease in $K_{Ic,i}$ from the non-reinforced baseline when attempting to go beyond 1 wt.% with CNTs in vinylester. A similar trend is observed by Ayatollahi et al.[89] who observe a peak $K_{Ic,i}$ at 0.5 wt.% in their 0-1 wt.% CNT loading range.

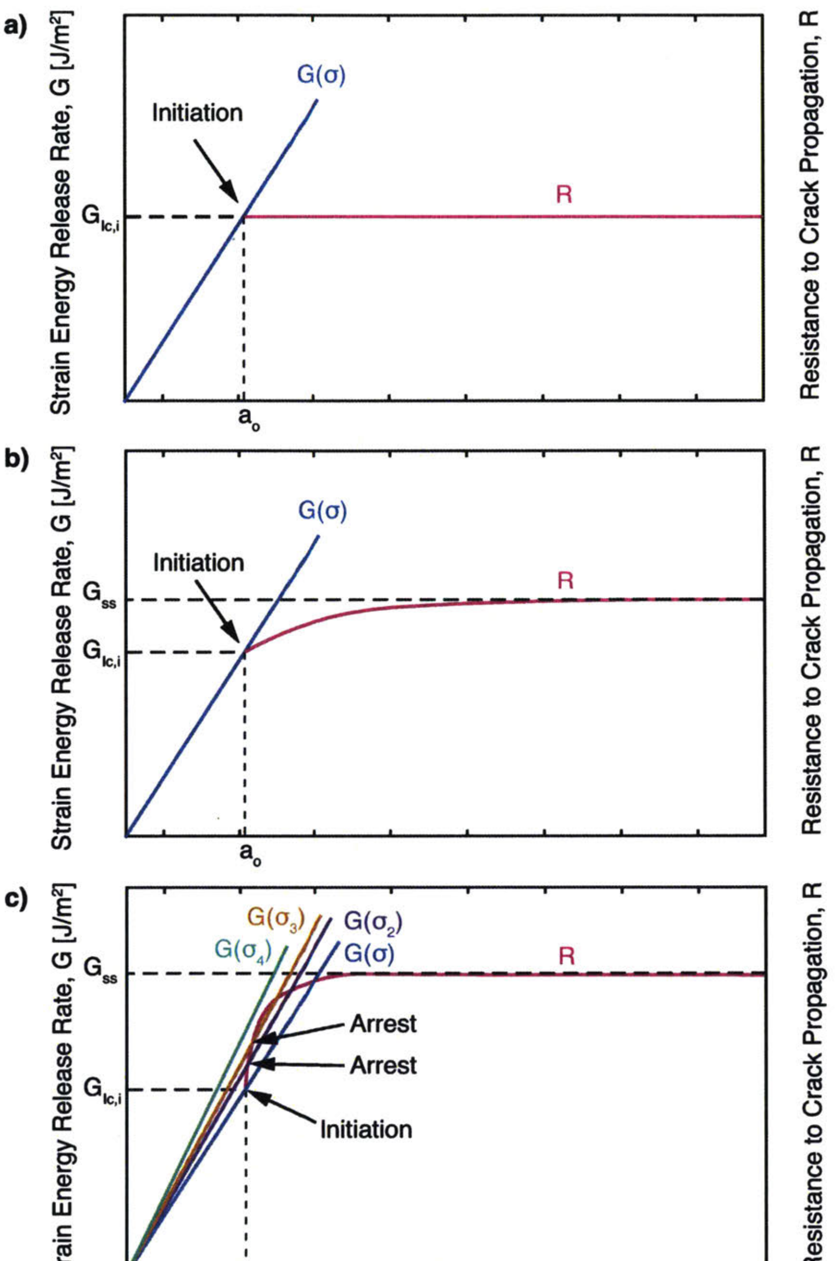

Figure 2-4: Illustration showing the interaction between the resistance to crack arrest, R and the strain energy release rate, G, for an ideal uniaxially-driven Mode I crack. The R-curve for a) brittle materials or b) ductile materials with marginal resistance to crack growth both fall below the G-curve and thus cracks are not arrested. However if c) resistance to crack growth is sufficient such that R increases beyond G, the crack will be arrested (adapted from original[78])

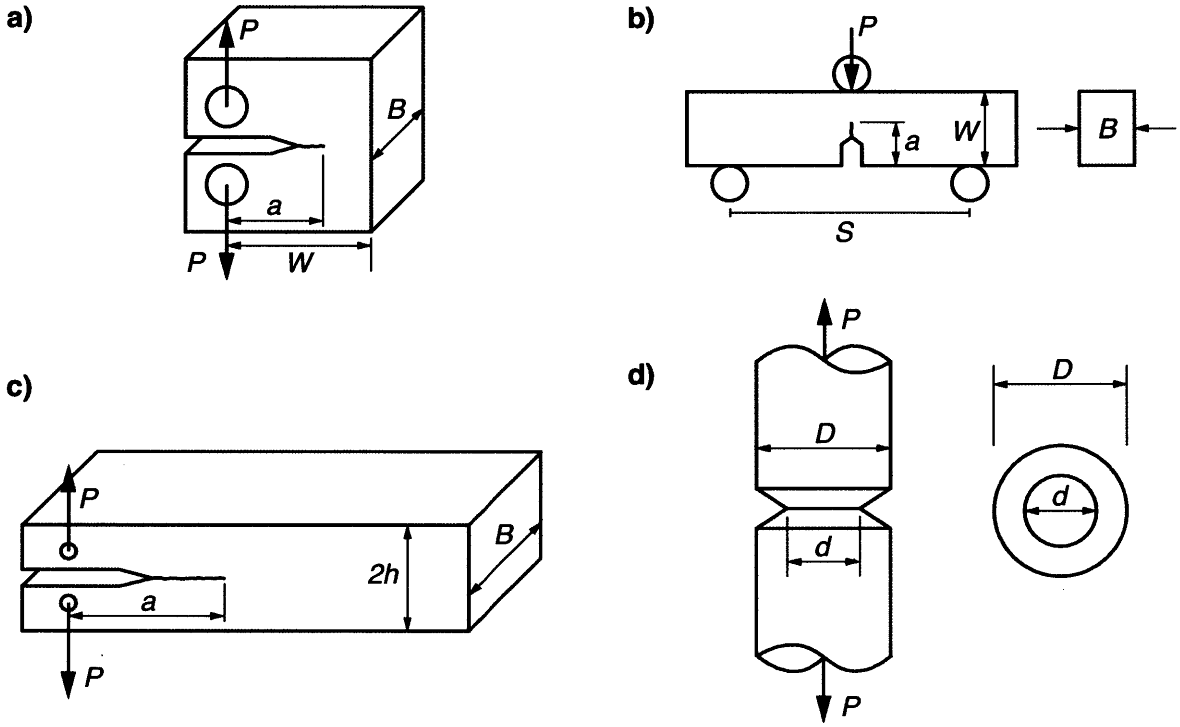

Figure 2-5: Mode I fracture toughness testing specimen solutions as determined from linear elastic fracture mechanics. (a) Compact tension specimen configuration for tensile test fixtures, (b) single edge notch beam configuration for three-point bend test fixtures, (c) double cantilever beam specimen (can have plane stress or plane strain solutions) and the less commonly used (d) circumferentially notched bar sample[78]. Compact tension and single edge notch beam specimens are both designed with a plane strain assumption (reproduced[78,84]), and are primarily used for initiation toughness determination while the DCB configuration is used for steady state toughness tests (typically).

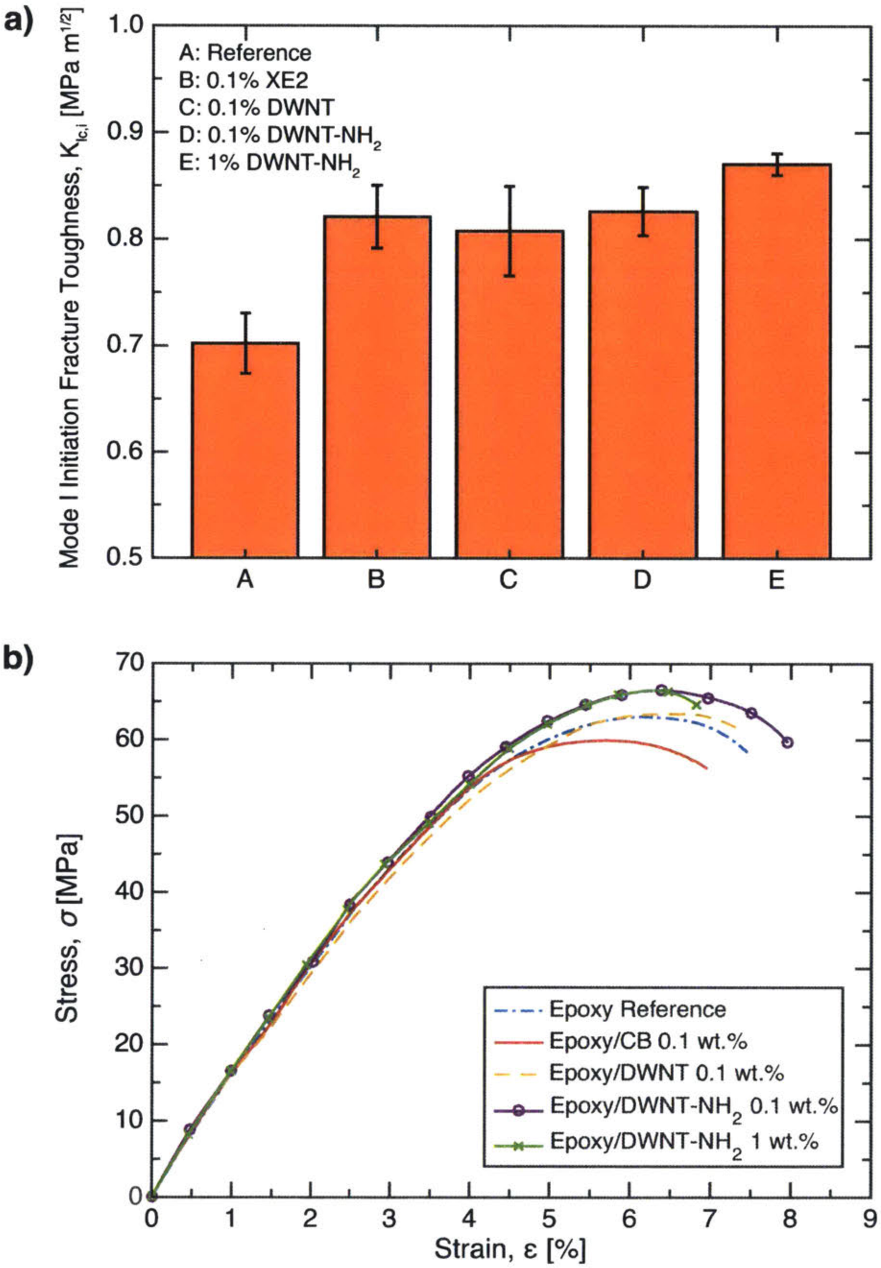

Figure 2-6: Test data reported by Gojny et al.[85] for (a) $K_{Ic,i}$ showing a general 10-25% increase by all nano-scale reinforcements utilized and, (b) tensile test stress-strain curves of the tested nanoparticle reinforced composites showing increase in elastic modulus (reproduced[85]). Aside: note epoxy ductility.

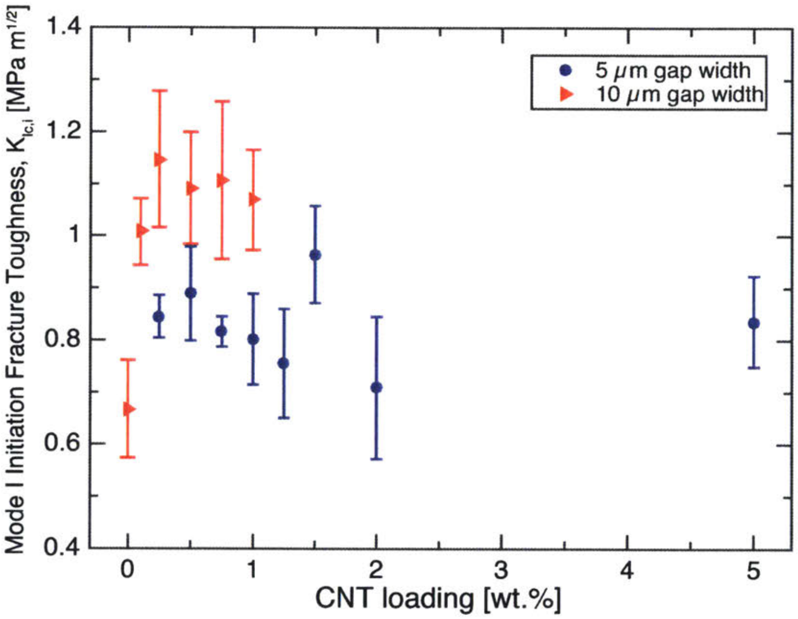

Figure 2-7: Test data reported by Thostenson and Chou[86] shows that calendering conditions affect $K_{Ic,i}$ initiation fracture toughness: increased gap width translates to larger agglomerates (larger inclusion size) that interact with the crack front. CNT reinforcement concentration maximizes $K_{Ic,i}$ at ~ 0.2 wt.%, beyond which increasing loading decreases $K_{Ic,i}$ (reproduced[86]).

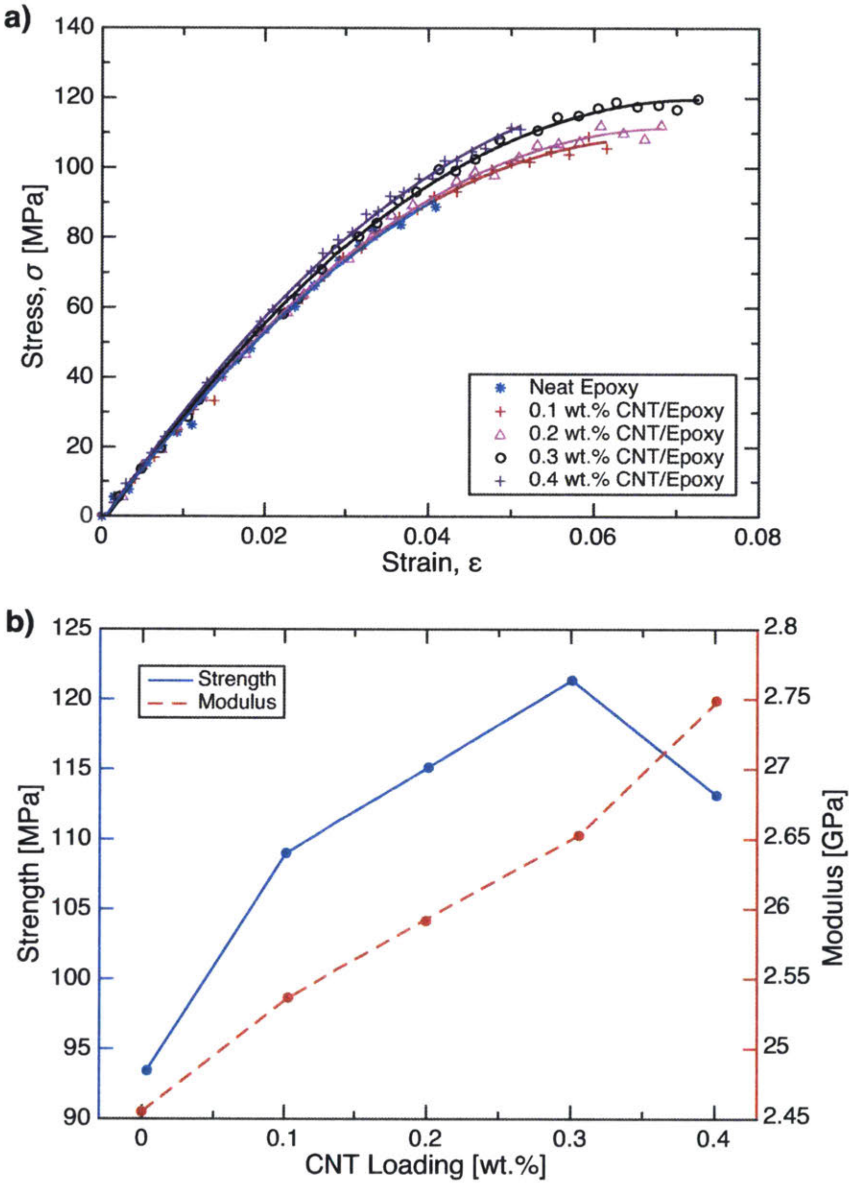

Figure 2-8: CNT loaded flexural specimens are tested by Zhou et al.[87] to yield (a) stress strain curve from which (b) flexural strength and modulus can be determined. Increasing CNT content increase flexural modulus, however flexural strength reaches a maximum at 0.3 wt.% attributed to agglomeration or voids (reproduced[87]).

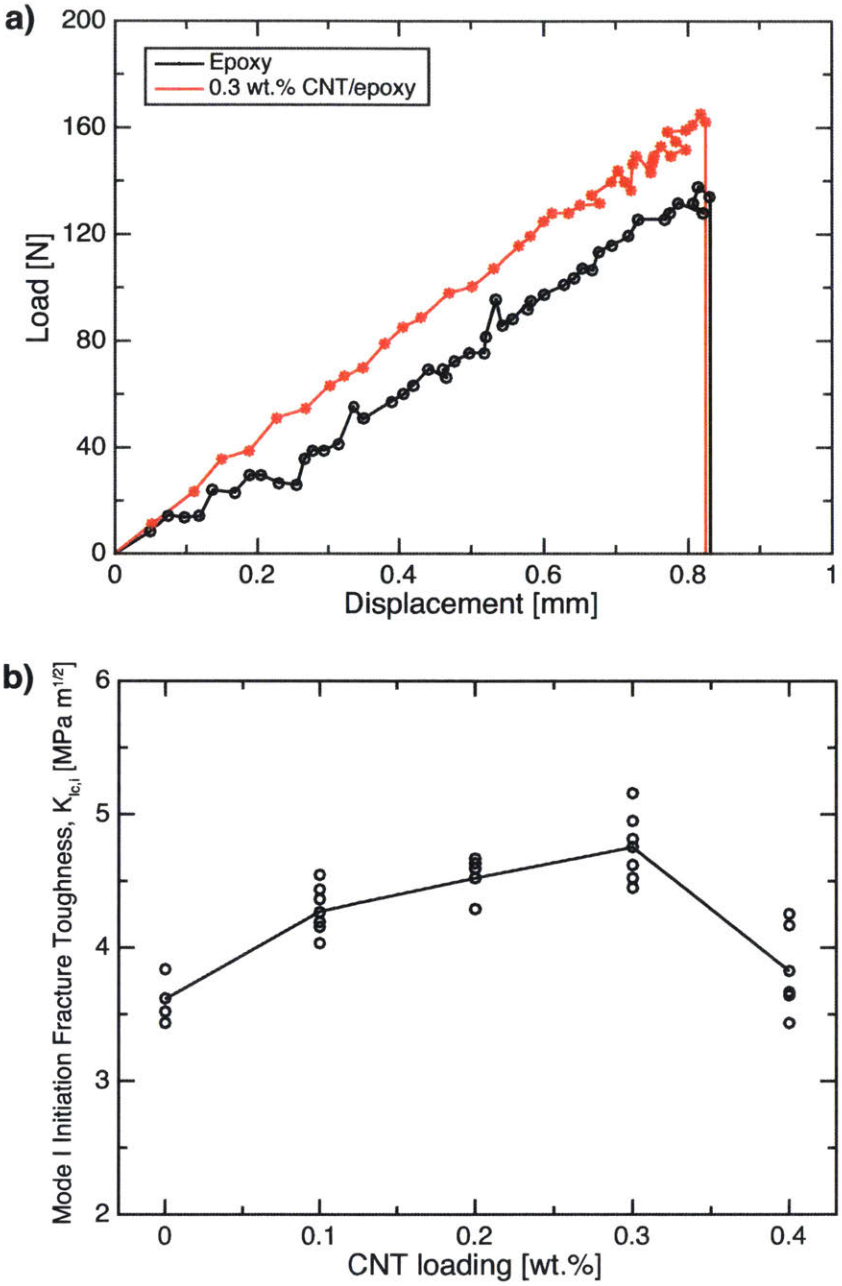

Figure 2-9: Using the same epoxy system as Thostenson and Chou[86], Zhou et al.[87] present (a) load displacement curves and (b) corresponding $K_{Ic,i}$ initiation fracture toughness results: increasing CNT content increases initiation toughness up to 0.3 wt.% beyond which $K_{Ic,i}$ decreases as claimed by the authors. Note that statistical significance is not reported (reproduced[87]).

Numerous groups have attempted to change the interface between the CNTs and the polymer by using various functionalization techniques. Most of these techniques are, however, only applicable to bulk CNTs. For example, Sun et al.[90] oxidized SWNTs with concentrated sulfuric and nitric acid, and then functionalized them prior to incorporation into an EPON 862/Epikure W epoxy. Manufactured $K_{Ic,i}$ test samples were as follows: neat epoxy, epoxy/pristine CNTs, epoxy/functionalized CNTs, epoxy/functionalizing chemical, with $K_{Ic,i}$ results of 0.56 ± 0.03, 0.58 ± 0.04, 0.66 ± 0.04, 0.75 ± 0.03 MPa·m$^{1/2}$ respectively. An 18% increase in $K_{Ic,i}$ is seen when using functionalized SWNTs, however the increase in initiation toughness is due to the functionalization treatment inadvertently altering the epoxy to increase tensile strength and ductility as is shown in the last sample group.

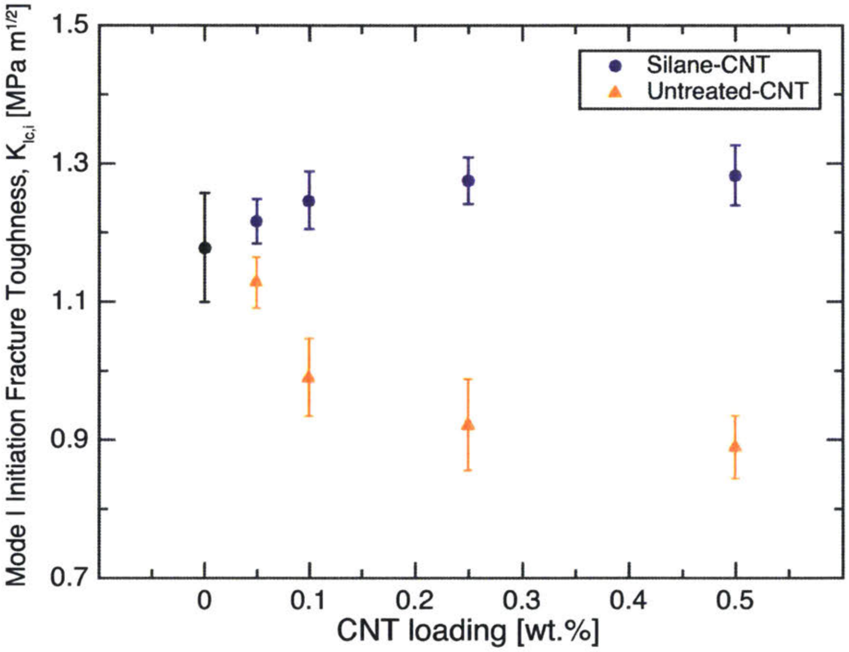

Figure 2-10: Fracture toughness, $K_{Ic,i}$ of nanocomposites with untreated, and silane treated CNTs of various loadings as tested by Ma et al.[91]. Increasing untreated CNT content yields decreasing $K_{Ic,i}$ values, attributed to agglomeration. The authors indicate that silane treated CNTs of increasing wt.%, increase $K_{Ic,i}$ by increasing interfacial adhesion (reproduced[91]). Note, original graphic reported $K_{Ic,i}$ in MPa·mm$^{1/2}$.

Ma et al.[91] used both pristine and silane functionalized CNTs dispersed in epoxy to manufacture compact tension specimens of 0.05, 0.1, 0.25 and 0.5 wt.%. $K_{Ic,i}$ decreased from baseline by 2.5%, 15%, 23% and 24%, respectively, by addition of untreated MWCNTs which is attributed to agglomeration, and increased 2.5%, 6%, 9% and 10% by addition of functionalized MWCNTs, respectively, when comparing means. However, data for the functionalized CNTs is not statistically significant as can be seen in Figure 2-10.

Lachman and Wagner[92] used compact tension specimens to assess the relationship between the CNT-epoxy interface and the overall mechanical properties by using a variety of CNT (pristine, carboxylated and aminated) and carbon species, and all specimens used 0.34 wt.% carbon reinforcement. $K_{Ic,i}$ was speculated to increase with enhanced interfacial adhesion which is altered by various functionalization treatments, Figure 2-11, which is opposite to what is observed in traditional fiber based systems where, as a rule of thumb, increased interfacial adhesion increases strength but also decreased interfacial adhesion increases toughness.

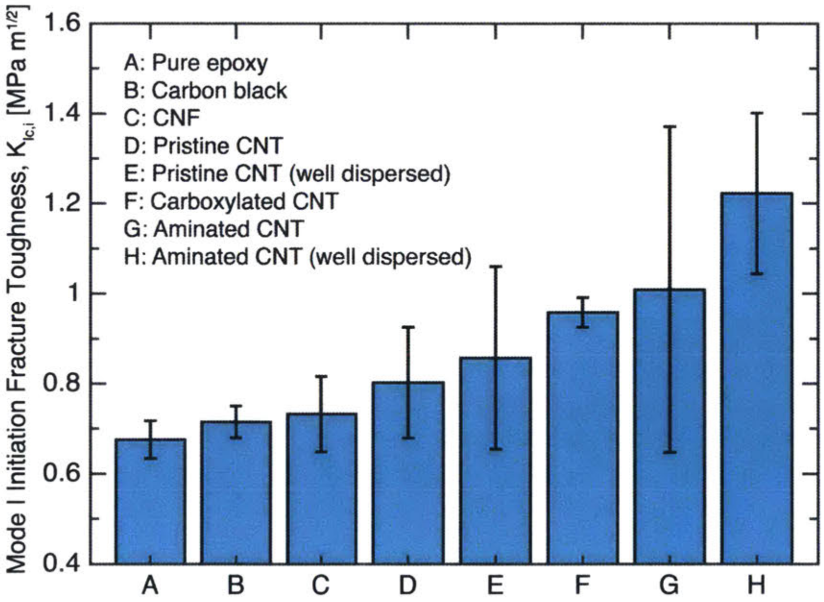

Figure 2-11: Fracture toughness, $K_{Ic,i}$ of pure epoxy, and of nano-composites based on various forms of carbon material as presented by Lachman and Wagner (reproduced[92]).

Literature is dominated by studies of randomly dispersed CNTs, and understanding the fracture toughness (mainly initiation) thereof. However, given the concept of fuzzy-fiber and nanostitched fiber reinforced plastics where CNT reinforcement is aligned, investigations regarding the fracture toughness of PNCs with aligned CNTs is expected. The method employed for alignment of the CNTs within the polymer will be based on the selected dispersion technique. The following subsection highlights methods employed in literature for controlling CNT alignment.

Manufacturing Methods of A-PNCs

Aligned carbon nanotube polymer nanocomposites have been manufactured using various methods, and the primary ones are highlighted below:

1. Randomly dispersing CNTs in the liquid polymer and controlling the alignment through the use of magnetic or electric fields.
2. Mechanically forcing the CNTs to align with a particular axis.
3. Infusing polymer into already aligned CNT structures.

Thostenson and Chou[93], controlled alignment by extruding a polymer melt containing CNTs through a rectangular die to manufacture highly aligned polymer films, an example of method 2. Other mechanical methods have been to mechanically stretch a polymer/CNT film at an elevated temperature[94], and shearing a liquid polymer/CNT mixture between flat substrates under pressure[95].

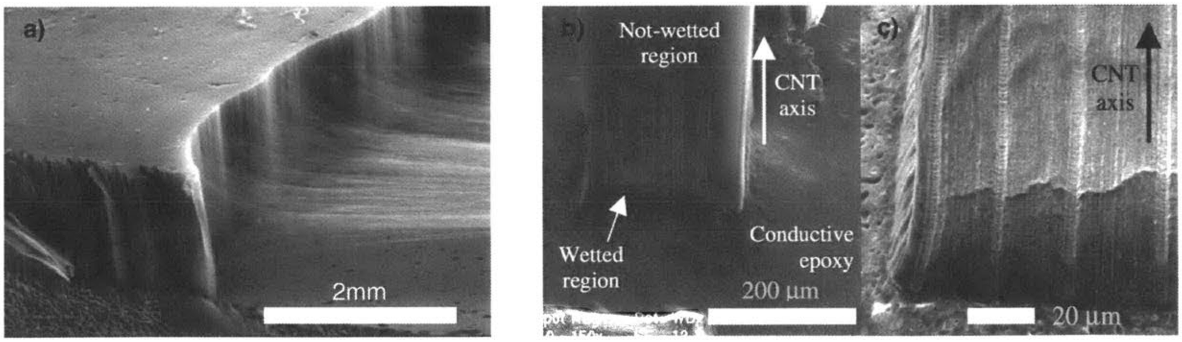

Figure 2-12: Examples of CNT alignment methods. (a) Drawing CNTs into a sheet as is done by Cheng[96] and Ogasawara[97] and (b) (with (c) enlarged) using the CNT morphology for capillary driven wetting as shown by Garcia et al.[98]

Following method 3, Cheng et al.[96], manufactured aligned carbon nanotube structures by stacking drawn CNT sheets, Figure 2-12a; a process similar to that used for yarns where CNT loading of 8.13 wt.% was achieved. Epoxy resin was infused into the stack using vacuum infusion methods. Similarly, using the same drawing method as Cheng et al.[96], other researchers[97] have manufactured PNC films using a hot melt method to infuse uncured epoxy films into the drawn CNT sheets. Aligned CNT sheets have also been manufactured by collecting nanotubes aligned by flowing argon gas in a laser ablation reactor. Lee et al.[99] re-oriented and densified CNT forests by knocking them down by rolling a teflon rod over the surface. Alternately, aligned CNT forests can be infused in their as-grown state. Garcia et al.[98] wetted as-grown forests with polymer by taking advantage of the capillary network created by an A-CNT forest, Figure 2-12b,c. Moreover, the packing density of the A-CNT forests can be tailored through mechanical densification as is done by Cebeci et al.[75], and others[100,101], to create A-PNCs containing up to 20 vf.% A-CNTs.

By aligning CNTs in the polymer matrix, a non-isotropic composite is created[100]. The CNTs can be aligned normal to the crack surface, encouraging the mechanisms underpinning increases in fracture toughness.

Mode I Fracture Toughness of A-PNCs

Literature on Mode I fracture toughness of A-PNCs is limited, and likely due to challenges in specimen manufacture. Most of the A-PNC fracture toughness literature focuses of Mode I initiation toughness with little work focusing on steady state fracture toughness.

Wu et al.[102], functionalize fully graphetized (at 2800°C) carbon nanofibers (CNF) with Fe_3O_4 nanoparticles to enable magnetic alignment of the CNFs after dispersion in a marine epoxy system (West System 105/206). ISO 25217 was followed for testing where the CNF/epoxy mixture creates a 1 mm thick adhesive joint between two composite substrates that constitute the bending arms of DCB specimens, as depicted in Figure 2-12a. While steady state toughness is not reported, the Mode I initiation fracture energy $G_{Ic,i}$ is reported showing that aligned CNFs provide more toughening than those randomly orientated, examples of which are shown in Figure 2-13b,c. It must be noted that provided load-displacement curve, with multiple load drops due to crack arrest, should produce an R-curve similar to that seen in Figure 2-4c.

Ladani et al.[103] have a similar approach to Wu et al. however, surfactant-dispersed,

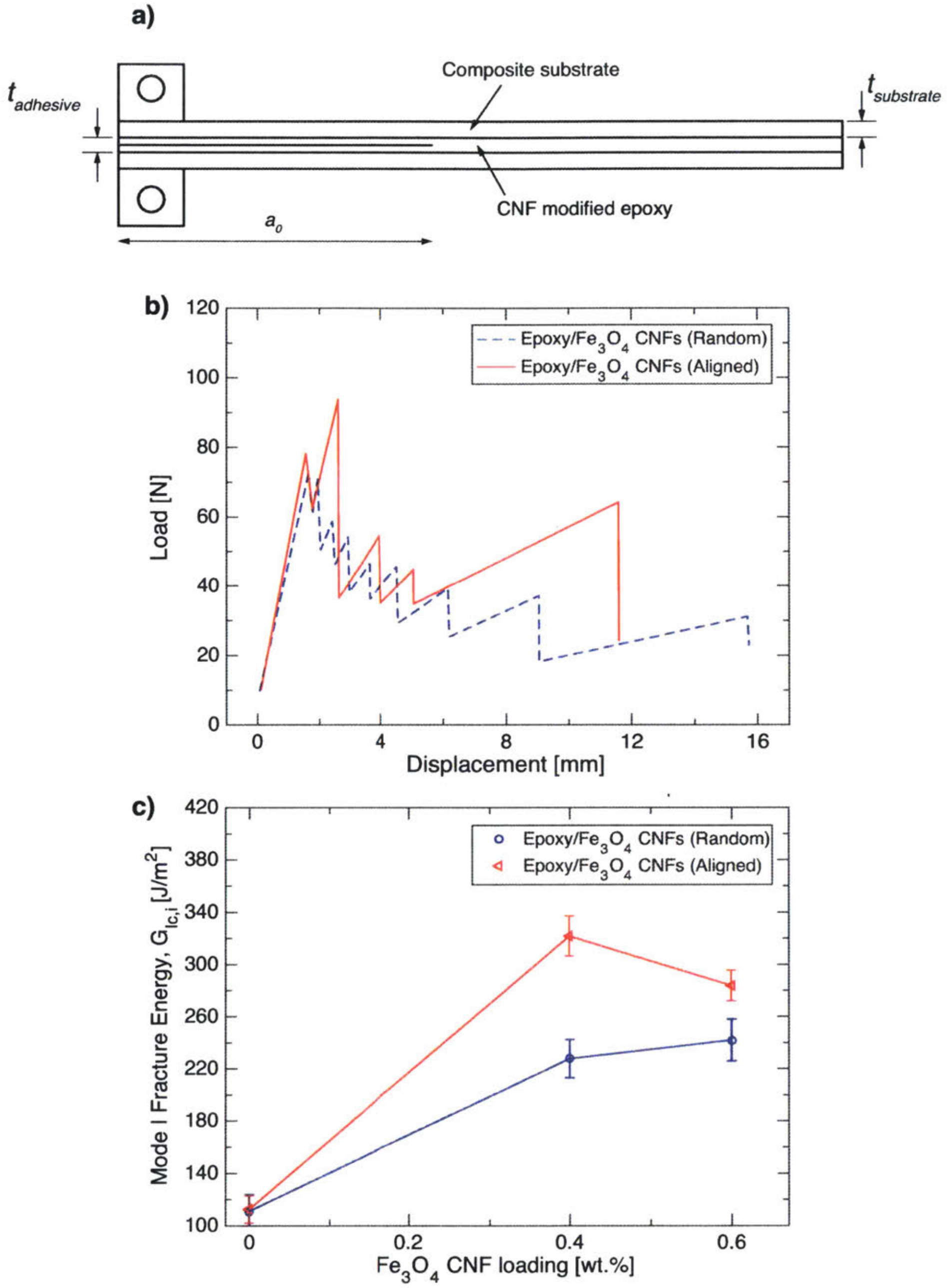

Figure 2-13: Testing done by Wu et al.[102] uses (a) double cantilever beam specimens with a PNC adhesive layer in which dispersed Fe_3O_4 functionalized CNFs have been aligned by magnetism resulting (adapted[102]). Following ISO 25217, (b) representative load versus displacement curves of the epoxy nanocomposites with 0.6 wt% of randomly-oriented or aligned CNFs are obtained from which, (c) the Mode I fracture energy, G_{Ic}, of the epoxy nanocomposites are determined (reproduced[102]).

untreated CNFs are aligned with the use of an alternating current electric field. During the cure of the marine epoxy system (West System 105/206), CNFs align with the electric field to increase fracture toughness during DCB testing of the adhesive layer. The average Mode I fracture energy, G_{Ic}, of the unmodified epoxy layer was found to be 134 J/m^2. Through the addition of CNFs, both aligned and randomly dispersed, G_{Ic} is increased to $\sim$ 2300 J/m^2 and $\sim$ 2200 J/m^2, respectively, at the maximum CNF loading of 1.6 wt.%. The authors observe that the main toughening mechanisms leading to the increase in G_{Ic} fracture energy with the addition of CNFs to the epoxy system were (a) pull-out of CNFs from the epoxy, (b) void growth of the epoxy initiating from holes in the epoxy caused by pull-out and debonding, and (c) CNF rupture. Aligning the CNFs perpendicular to the crack path led to a higher G_{Ic} when compared to those randomly aligned.

Another group, Khan et al., used DC electric fields to align MWNTs during composite curing as it has been shown that AC electric fields cause coarsening of CNT bundles (a form of agglomeration) as voltage is increased to drive alignment. Ultra-violet/ozone (UV/O_3) treated MWNTs are dispersed in an epoxy system and aligned. Compact tension testing is performed with both aligned and randomly orientated CNTs with a peak increase in $K_{Ic,i}$ occurring at 0.3 wt.% which corresponds to the peak observed in elastic modulus.

In A-PNC work done by Wicks[5], reinforced aerospace grade structural epoxy, as well as the aforementioned marine epoxy systems with $\sim$ 1 volume fraction.% (vf.%) A-CNT forests, is tested using SENB specimens. No increase in $K_{Ic,i}$ is observed in either epoxy system when tested using SENB specimens. Fractography reveals CNT pullout lengths of $\sim$ 2 μm, suggesting that pullout toughening is strength limited due to high CNT/epoxy interfacial strength.

2.2.3 Reinforcement Mechanisms

Based on literature, the use of nanoreinforcements in polymers has produced some improvements in mechanical properties of the composites due to various mechanisms[104], namely:

- CNT pull-out from the matrix (frictional sliding),
- Sword-in-sheath sliding,

- Crack deflection, and
- "Stick-slip" (fatigue based).

Pull-out is typically seen in Mode I fracture where the CNTs bridge the crack until they either completely pull out or break/fail away from the crack plane[11,105]. The interfacial sliding leads to friction which increases fracture toughness to resist crack propagation in the matrix and restrains the crack from opening. This interfacial sliding depends on the adhesion between the outer wall of the CNT and the matrix, or can occur after any decohesion.

Similarly, sword-in-sheath pull-out occurs in MWNTs when the frictional sliding occurs between fractured inner walls and the polymer bonded outer walls of the MWNT; particularly prevalent with high CNT/matrix interfacial bonding. These mechanisms increase the Mode I fracture toughness of hierarchical composite laminates or can cause crack deflection. Additionally, these mechanisms are believed to suppress matrix cracking and reduce delamination growth rates, which increases fatigue life.

Similar to pull-out, "stick-slip" is a term coined to describe the process of frictional sliding motion between the nanoparticle and the polymer that acts as an energy dissipation mechanism. Zhou et al.[106] developed a model for the frictional sliding mechanism between CNTs and the polymer matrix, and Koratkar et al.[107] show a >1000% increases in the loss modulus of polycarbonate (PC) reinforced with 2 wt.% oxidized single-walled CNTs, without significant reductions in the storage modulus.

2.3 Summary and Conclusions

The potential for mechanical reinforcement of laminated composites with CNT nanofiller is evident through the increase in Mode I initiation and steady state fracture toughness results presented in literature. However, caution should be applied in the interpretation of these results as the potential exists for increasing the thickness of the interlaminar region with the addition of CNTs. A thicker interlaminar region will enhance Mode I toughness, but will degrade performance in the in-plane directions. Additionally, in "fuzzy fiber" laminates, the swelling of plies leads to a morphological change in the interlaminar region which likely leads to an increase in Mode I fracture toughness (both initiation and steady state).

To accurately understand the role of CNTs in these hierarchical materials, isolating the nanofiller-polymer interaction can be performed using PNCs. Literature shows CNTs are very promising for polymer reinforcement, but they have to be incorporated in such a way that prevents their aggregation and optimizes their orientation for maximum toughening. The toughening response is also highly dependent on matrix type and CNT morphology. The following key focus areas have been highlighted as having room for improvement:

- Techniques to control dispersion and alignment of CNTs in PNCs do not typically preserve CNT properties. Additionally, even with extreme energy input, complete homogeneous dispersion is not likely, resulting in the formation of agglomerates which act as stress concentration sites within the composite during loading.
- A wide range of results exist between researchers using the same polymer system and CNT loading, suggesting that manufacturing quality Mode I fracture toughness specimens is critical.
- No reliable indication of post-manufacture specimen void content is presented in literature.
- CNT content is limited to $\sim$ 1 wt.% due to dispersion challenges at higher nanofiller loading.
- Discussion relating the observed reinforcement mechanisms to results obtained, i.e. pullout length, is slight.

With this, the ideal PNC likely contains a high loading of CNTs that are aligned and well dispersed in the surrounding matrix in such a manner that preserves CNT aspect ratio and material properties. To improve on previous research, assessment tools for PNC quality in terms of voids will be implemented to reveal true mechanisms by which CNTs influence matrix toughness.

Chapter 3

Objectives and General Approach

The use of A-CNTs in hierarchical materials for aerospace applications is beginning to gain traction and the role that A-CNTs play must be understood for next-generation composites. This chapter details an approach to decouple the nanoscale and macroscale material response by focusing only on the polymer-CNT interaction and excluding the relatively large reinforcing fibers. This approach includes sample design and manufacturing, characterization, and testing methods.

3.1 Objectives

The objectives of this thesis are to gain insight into the role A-CNTs play in the observed increase in Mode I initiation and steady state fracture toughness of fuzzy-fiber and other reinforced composites through their direct interaction with aerospace grade or similar structural epoxies, using PNCs to isolate the regions of interest from the hierarchical composite as a whole. Due to the requirement of a developing crack for the activation of A-CNT pull-out mechanisms, toughening will likely only be seen under steady state conditions, provided the resistance to crack growth is greater than the strain energy release rate, as described in Figure 2-4c. If the R falls beneath $G(\sigma)$, it is likely that unstable crack growth will result (Figure 2-4b), limiting data collection to initiation toughness toughness only. Additionally, a platform for future testing of A-CNT functionalization or coating treatments for further tailoring of these composite materials must be developed.

3.2 General Approach

When incorporating CNTs into laminates for the main purpose of increasing toughness, it is critical to consider the potential presence of alternate toughening mechanisms that may arise due to the additional constituent. In nanostitch, for example, incorporation of A-CNT forests can lead to an increase in the interlaminar polymer region that allows increased plastic yielding to develop during crack propagation, thus adding toughening via a compliant interlayer. While toughness has increased, it is unclear to what it should be attributed. Similarly, when grafting CNTs onto microfiber surfaces (fuzzy-fibers), changes to laminate initiation and steady state toughness can occur due to damage to the microscale fibers, and changes to microfiber packing (Figure 3-1) through decreased compressibility attributed to fiber tows swelling as a result of impregnation with CNTs[5].

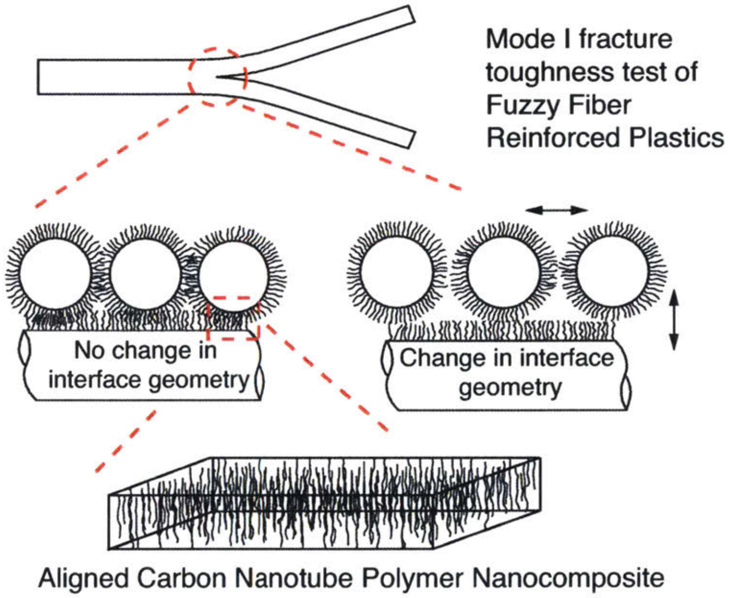

Figure 3-1: A polymer nanocomposite is a representative volume element of the inter- and intra-laminar region of CNT reinforced composite laminate used to isolate the nanotube/polymer interactions. This representative volume element is applicable to both nanostitch and fuzzy-fiber reinforced interfaces. In the case of fuzzy-fiber changes in interface geometry are caused by tow swelling.

By creating representative volume elements in the form of PNCs (Figure 3-1), the interlaminar region can be decoupled from the composite and the nanotube/polymer interaction can be studied without the added complexity of the microfibers. The CNT alignment created in the case of fuzzy-fibers can be approximated by vertically aligned CNTs, which can be grown as a forest and infused with a polymer, and would similarly represent nanostitch.

This thesis will use PNCs to examine the effect A-CNTs have on the surrounding epoxy matrix, to be achieved through the detailed plan outlined in the sections to follow. The strategies to be employed and their limitations are highlighted here and detailed in subsequent chapters.

3.2.1 Dimensional Limitations of Aligned Carbon Nanotube (A-CNTs) Polymer Nanocomposites (A-PNCs)

The limiting factor in testing of A-PNCs is the resulting size of the test specimen, which is consequently limited by the dimensions of the A-CNT reinforcement. The A-CNT forest size is determined by manufacturing capabilities and substrate size. The first step is to determine the bounds of A-CNT growth capabilities in order to establish maximum test specimen size. This study requires quantification and analysis of A-CNT morphology, using experimental techniques to ensure that parametric changes in growth process yield predictable and consistent A-CNT conformation. Following determination of A-CNT growth limitations, establishment of appropriate sample dimensions will result in suitable selection of test method and specimen configuration.

3.2.2 A-PNC Manufacturing Procedures

Bearing in mind that future work may employ a variety of polymer systems or A-CNT morphologies, a generic A-PNC manufacturing method is required with a specific focus on polymer accessibility to the A-CNT forest and containment of A-CNT forests of various volume fractions. This is especially necessary, where spacing between adjacent nanotubes approaches the characteristic polymer chain length causing expansion of high density arrays on chain arrangement and cross-linking during curing. Manufacturing techniques must be developed such that A-PNC test specimens are consistent and reproducible. It must also be understood how the variations in A-CNTs affect the manufacturing method to incorporate flexibility for changes in morphology. Coupled with the development of a suitable manufacturing process is the establishment of quality control protocols to reinforce the validity of test data, a methodology to correctly evaluate sample outliers and detect artifacts such as toughening due to voids.

For this thesis, A-PNC manufacture is limited to selected structural epoxies and CVD as-grown A-CNT forests. Self-densification of A-CNT forests during polymer infiltration, beyond mechanical densification, is not considered, and longitudinal entanglement/bundling of individual A-CNTs with neighbours is assumed negligible.

3.2.3 Test Sample Manufacturing Methods

Based on A-PNC specimen size limitations, their integration into test scale sample is required such that an accurate representation of the A-PNC is achieved i.e., propagating a crack through the A-PNC region of a global test specimen. Appropriate location of seams, well bonded interfaces and notch placement are a few examples of areas to be addressed in this body of work. Dimensional extension of A-PNCs with bulk polymer will be limited to utilization of the same polymer as that used for A-PNC manufacture.

3.2.4 Selective Mechanical Property Determination for A-PNCs

The main focus of this thesis is the determination of both initiation and steady state fracture toughness of for A-PNC systems as a function of A-CNT packing density, i.e. changing volume fraction through mechanical densification techniques. However, the A-PNC elastic modulus as well as storage and loss moduli, as a function of A-CNT v_f and orientation, is supplementary. This can be compared to previously reported data for A-PNCs using nanoindentation[75] and tensile tests[100]. This application of A-PNC architectures beyond Mode I fracture toughness will extend the body of work of A-PNC multifunctional properties.

3.2.5 Approaches for Assessing A-CNT Toughness Contribution

Finally, several important A-PNC level fracture toughness topics set near-term directions for future research, such as interface or strength tailoring of as-grown A-CNT forests. Forming a basis for comparative studies and an experimental platform from which to direct efforts is required. Future work can be found in Chapter 8.

3.3 Limitations

The general approach outlined above is limited by the following items. Chapter 8, however, includes suggestions for future work where these scope exclusions are addressed.

- CNT morphological optimization is rangebound by growth time only.
- A-CNT volume fraction is increased from the as-grown state through mechanical densification methods only, tuning of CNT forest density through CVD conditions is excluded from this scope.
- Functionalizations for interfacial shear strength optimization are considered future work.
- Interfacial shear strength testing is not performed, and high level calculations for CNT pull-out from the matrix are performed using experimental data from literature.
- Fracture toughness testing is limited to Mode I.
- While both Mode I initiation and steady state fracture toughness are sought, it is likely that only initiation toughness will be determined as A-PNC specimen manufacture will be a limiting factor in the crack ligament length that can be achieved. A longer crack ligament length is typically required for toughening mechanisms to develop to a steady state value that can arrest the crack.
- A thermoset aerospace grade structural epoxy and a commonly utilized experimental thermoset structural epoxy are included only. Other polymers, as well as modifiers, are not employed, however the developed fabrication and testing methods are considered extendable in many cases to support future work with other polymer systems.
- While other nanofillers, such as graphene and nanographite are gaining momentum

as a reinforcement agent[53,108,109], this work focuses only on understanding toughening provided by aligned carbon nanotubes as a subset of hierarchical composites.

A-PNC Mode I initiation and steady state (provided stable cracks can be propagated) fracture toughness will be explored in detail to isolate the epoxy-CNT interactions as a component of the toughness enhancement observed at the laminate level. To accomplish these objectives, the contributing fields of knowledge have been outlined above, including determining limits of A-CNT growth, morphology characterization, manufacturing of aligned CNT polymer nanocomposites, and Mode I fracture toughness testing. The following chapter explores A-CNT manufacturing limits and details morphological characterization to map how parametric changes in growth conditions affect the as-grown A-CNTs.

Chapter 4

Aligned Carbon Nanotube Architectures: Morphology and Growth Envelope

As the first step in meeting the objective of this thesis, the limitations of the chosen A-CNT forest characteristics must be established as an input to the structure-property relations of the manufactured A-PNCs. This chapter begins by establishing the upper bound of A-CNT forest height, and characterizes the resulting morphology of both the upper bound and mid-range forest heights. Following this, for the process of A-PNC manufacture (Chapter 5), A-CNT forest removal from the growth substrate is required and thus, various treatments are studied herein to modify the post-growth A-CNT forest adhesion to the substrate. Finally, densification techniques for A-PNC volume fraction tailoring are detailed.

4.1 Vertically Aligned CNT Synthesis and Characterization

Numerous methods for the synthesis of CNTs exist, with the most common being chemical vapor deposition (CVD), carbon-arc discharge, or laser ablation[54,110]. As previously mentioned in Chapter 2, CNT material and morphological properties are strongly dependent on the manufacturing method. In this work, vertically aligned carbon nanotube forests are manufactured using CVD[99,111–113]. Previously, 10 mm × 10 mm catalyst-coated Si wafers had been used to grow ∼ 1 mm tall A-CNT forests for the manufacture of A-PNCs[5,75,98,100,101]. However, an important consideration for fracture toughness testing is to ensure that the crack remains in the required test region. Previous work, with ∼ 1 mm tall A-CNTs, has shown that the crack can propagate from the A-PNC to the interface between the A-PNC and the surrounding epoxy. An example of this observation is shown in Figure 4-1. Moving the interface further away from the crack region would mitigate this, and can be achieved by growing taller A-CNT forests.

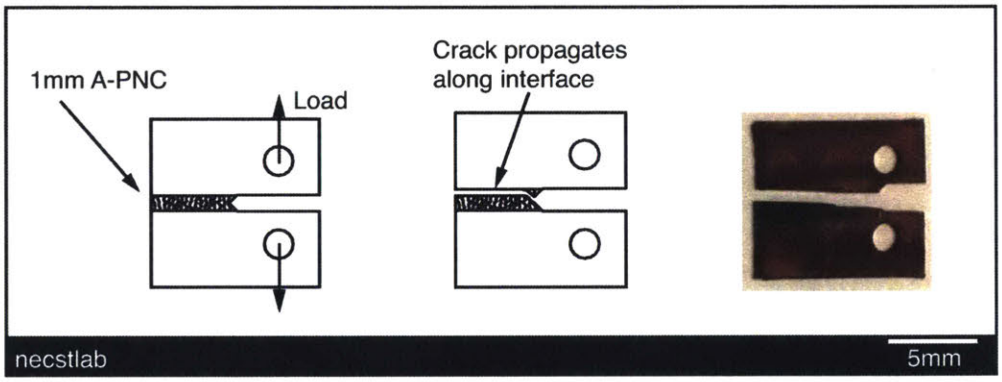

Figure 4-1: When using ∼ 1 mm tall A-CNT forests for A-PNC manufacture, cracks are periodically seen to migrate out of the A-PNC region to the interface between the A-PNC and the bulk epoxy, as is shown in this compact tension specimen.

Coupled with this, the creation of higher volume fraction A-PNCs requires the uniaxial or biaxial densification of the A-CNT forest[101]. When starting out with a 10 mm × 10 mm planar dimension, the final dimensions of a 10 vf.% forest are ∼ 1 mm × 10 mm using uniaxial densification, or ∼ 3.2 mm × ∼ 3.2 mm with biaxial densification, limiting sample size and bulk test specimen manufacture. By increasing the wafer area, larger A-CNT forests can be densified to higher volume fractions while maintaining dimensions suitable to manufacture specimens.

Experimental Procedure for A-CNT Growth and Characterization

A-CNTs are grown on (1 0 0) silicon wafers, covered by a 500 nm thick, thermally grown, oxide layer onto which a 10 nm alumina (Al_2O_3) diffusion barrier and a 1 nm thick iron (Fe) catalyst film is deposited by an electron beam deposition system[114]. Jacobs[111] provides a detailed account of the growth system employed. In brief, the process starts by flushing the furnace with helium to remove all oxygen, followed by heating the furnace to 740°C. The catalyst film is reduced in a mixture of hydrogen (H_2) and helium (He) for 5 mins during the temperature ramp. Once the growth temperature is reached, an ethylene gas mixture ($C_2H_4/He/H_2/H_2O$) is introduced into the system that is controlled by mass flow controllers (MFCs). Growth time (t) is varied to achieve A-CNT forest height (H).

Changing growth time necessitates re-characterization of the A-CNT forest for comparison to the traditionally utilized $\sim$ 1 mm tall forests. Parameters include height, waviness, inner and outer diameter, number of walls, and inferred quality. This is done by:

- Optical microscopy for measurement of the A-CNT forest height.
- Scanning electron microscopy (SEM) on Zeiss Merlin High-resolution SEM at 1 kV using the InLens detector.
- Raman spectroscopy, performed using a 514 nm laser with a 100× objective lens giving an $\sim$ 1 μm spot size.
- Thermogravimetric analyses (TGA), carried out on a Discovery TGA TGA1-0075 controlled by a DSC/TGA DCC1-00177 data station. Approximately 5 mg of as-grown A-CNT forest sample is heated in an open platinum pan in excess air from room temperature to 900°C at a rate of 10°C/min.
- Transmission electron microscopy (TEM). TEM samples are prepared by ultrasonication of forest cuttings in isopropyl alcohol for 5 mins followed by dropcasting onto a copper TEM grid. It must be noted that sonication of A-CNTs in solution for TEM dropcasting is observed to be less appropriate owing to the introduction of nanotube defects and fractures as a result of the sonication process; this process of scission is described elsewhere[62–64]. Additionally, dispersion is noted to be a function of growth time, i.e., small bundles persist for low growth times. Previously, the focused ion beam

(FIB) technique for CNT lamella preparation was attempted, see Figure 4-2a, however no walls were observed during TEM as is seen in Figure 4-2b. This is either due to the presence of gallium ions, or that the ion bombardment gives rise to defects or in the extreme case, nanotube amorphization[48,115,116].

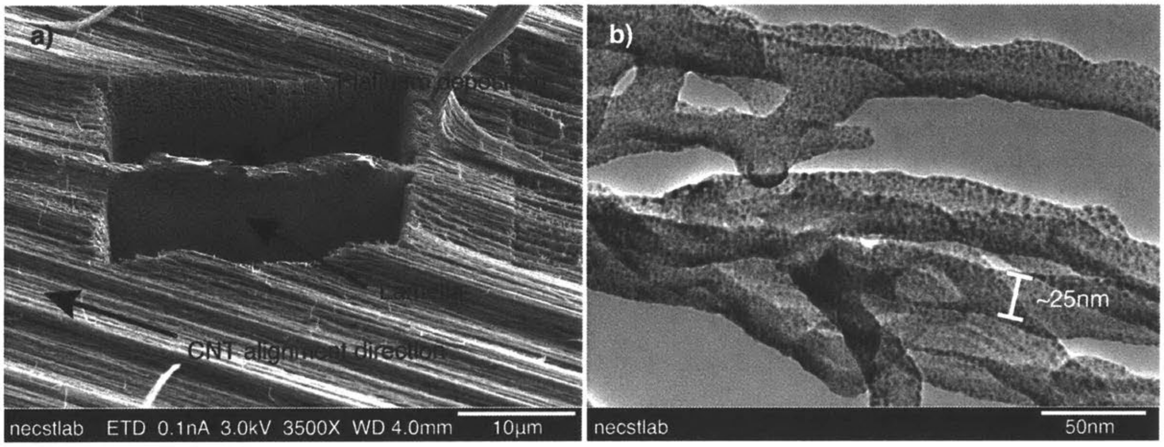

Figure 4-2: The focused ion beam method for TEM sample preparation by creation of a) a lamella yields b) samples that exhibit no walls when imaged.

Results and Discussion of A-CNT Morphological Characterization

Through extensive collaborative work in tailoring growth conditions[111,117], the A-CNT forest height can be grown beyond the previously used ~ 1 mm to >5 mm, see Figure 4-3a,b. Additionally, Figure 4-3c shows an A-CNT forest grown on a 20 × 100 mm substrate, increasing the initial area and allowing for densification to higher volume fractions.

To fully map the growth height limits, A-CNT forests are grown with growth times ranging from 9 min to 80 min, with the addition of an extreme point a 180 min. Post growth, the A-CNT forest heights are measured, using an optical microscope, and are presented as a function of growth time in Figure 4-4.

As has been reported by several other groups, it is observed that a sudden termination in growth height follows an almost constant growth rate[118–123]. The full growth process is explained by Figure 4-5. The tangled upper crust is developed during the process of self-organization where the entanglement occurs because not all catalyst nanoparticles be-

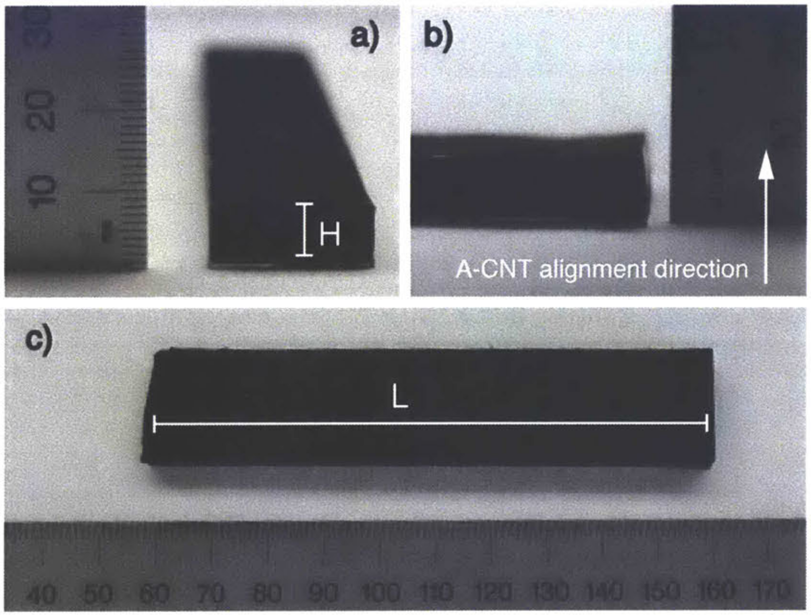

Figure 4-3: Greater than 5 mm tall A-CNT forest is grown on a 20 mm × 100 mm Si wafer: a,b) show that height is > 5 mm on the leading edge and c) shows coverage of the Si wafer. Note that the leading edge is marginally taller (~ 1 mm) than the trailing edge, likely due to depletion of the carbon feedstock concentration as gases flow through the CVD tube furnace.

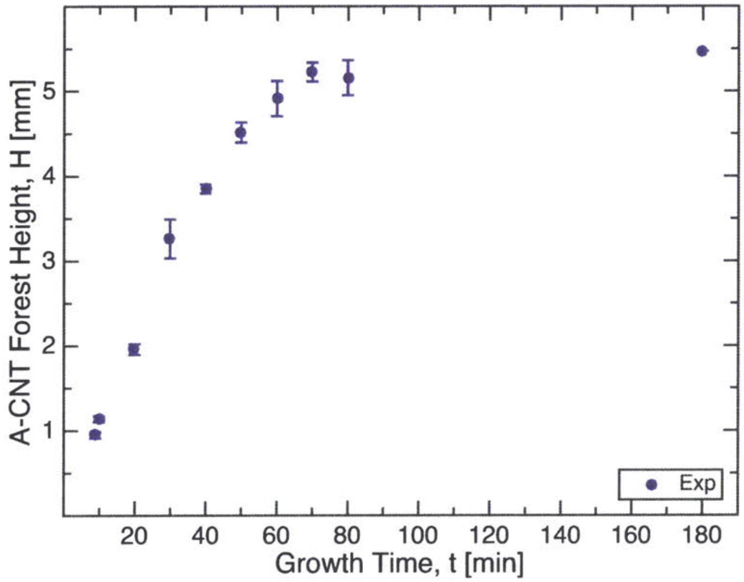

Figure 4-4: A-CNT forest height (H) as a function of growth time (t) showing a linear increase in height with increasing growth time with no further statistically significant increase occurs beyond ~ 50 mins owing to the abrupt termination phase of the growth process. These measurements are taken from three forests, at three locations on each.

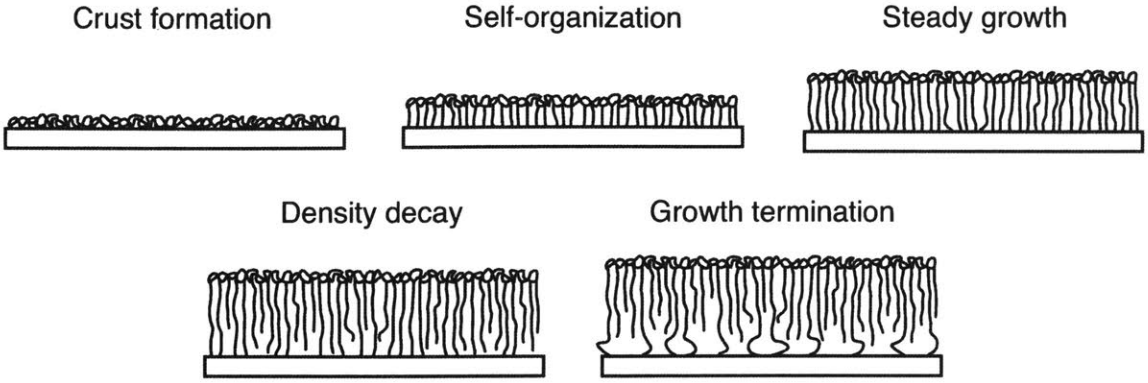

Figure 4-5: Sequential stages of A-CNT growth beginning with the formation of the upper crust, followed by self-organization, steady growth, density decay, and finally termination. Adapted from Bedewy et al.[118].

gin growth simultaneously, thus the initial CNTs have more room to grow, so they grow randomly. When all sites are active, the CNTs can only grow vertically due to steric hindrance: becoming a vertically aligned forest with an aligned morphology that dominates the majority of the forest height. During longer growths, individual CNTs begin to terminate leading to a decay of number density as growth progresses. The A-CNT number density continues to decrease to a point which is too low to support the forest structure, and further growth is prevented, explaining the ceiling reached in Figure 4-4. There are several studies dedicated to growth limiting factors that cause individual A-CNT termination such as local reaction rates at the catalyst surface, Ostwald ripening, and surface poisoning by pyrolysis byproducts[118,122,124–128]. Once the individual A-CNTs begin terminating, a loss of structural arrangement in the A-CNT forest prevents a further height increase[119,129,130].

Scanning Electron Microscopy

SEM images are captured at the top, middle and bottom of the forest as indicated in Figure 4-6a. The complete evolution of the growth process is represented in the $\sim$ 5 mm A-CNT forest. The tangled upper crust is seen in (Figure 4-7a,b), and transitions into the steady growth region with aligned morphology for most of the forest height (Figure 4-7c,d). Nearer the wafer, density decay is observed (Figure 4-7e) where individual A-CNTs begin terminating, followed by an $\sim$ 500 μm abrupt self-termination region (Figure 4-7f) where the forest

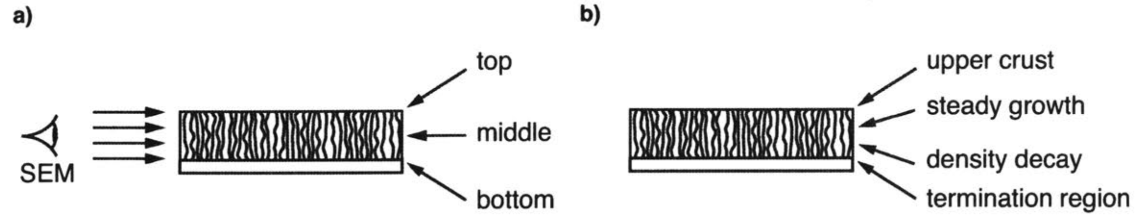

Figure 4-6: Spatial variation of CNT crystallinity and morphology can be observed by staggering points along the height of the A-CNT forest, and this is shown for a) SEM imaging and b) Raman spectroscopy.

terminates, collectively.

Similarly, a $\sim$ 2 mm tall A-CNT forest is imaged at the top and middle of the A-CNT forest as seen in Figure 4-8. When comparing SEM images of the top region in the $\sim$ 5 mm A-CNT forest to that of the $\sim$ 2 mm forests, the A-CNTs appear to have a scaly outer surface, as observed in Figure 4-7a. This is due to the accumulation of carbonaceous impurities (likely both amorphous and graphitic) during the growth process[131]. This is more prominent at the top of the $\sim$ 5 mm A-CNT forest because of the longer exposure time in the base-growth conditions, and a schematic of this is offered in Figure 4-9. This phenomenon is most noticeable in the 180 min A-CNT forest where vertical growth is terminated at $\sim$ 50 mins, but radial accumulation of impurities continues, as shown in Figure 4-10. When considering A-PNC manufacture and the requirement to prevent cracks jumping to the interface of test samples as seen for the 1 mm A-CNT forests, a $\sim$ 2 mm tall A-CNT forests would not shift the A-PNC/bulk polymer interface as far as would be achieved with the $\sim$ 5 mm tall A-CNTs forests, however, the $\sim$ 2 mm tall A-CNTs forests will likely have a more constant number density over the height (limited individual CNT termination) and have a reduced accumulation of carbonaceous impurities. Thus, a more uniform morphology along the height is expected with a $\sim$ 2 mm tall A-CNT forest.

In general, carbonaceous impurities are difficult to discriminate quantitatively from the A-CNTs. Infrared spectroscopy has been reported as a plausible method, however it is

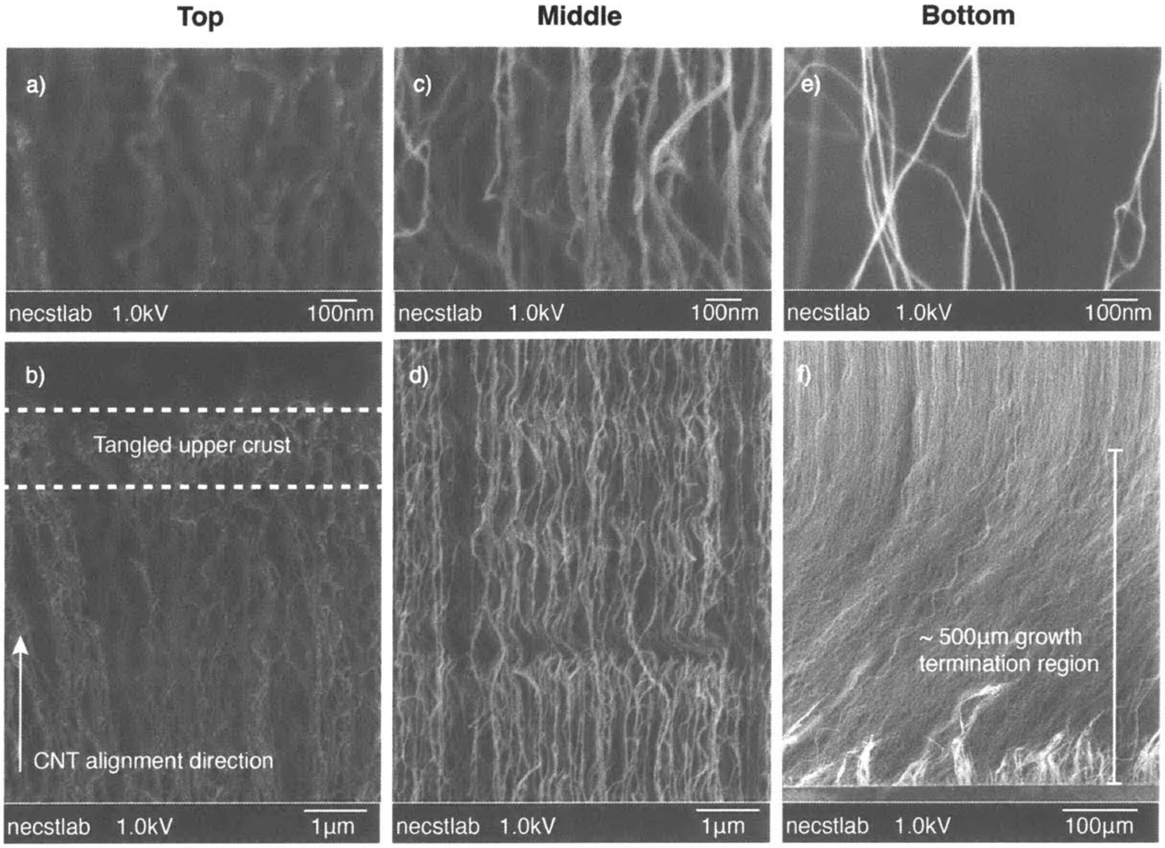

Figure 4-7: SEM images of the ~ 5 mm A-CNT forest at various locations over the height showing in detail, morphology of a) the top of the forest where b) the tangled upper crust is observed, c) the middle of the forest which exhibits an d) aligned and dense morphology, and e) the bottom of the forest where density decay is seen and f) self-termination occurs approaching the wafer.

limited by the ability to disperse A-CNTs in potassium bromide for the creation of a test pellet[132]. Raman spectroscopy, however, can be used to verify a hypothesis of carbon impurity accumulation, as well as understanding many aspects of sp^2 carbons such as disorder in sp^2 hybridized carbon systems, and diameter of nanotubes[133]. Unfortunately, Raman has a very small penetration depth, limiting characterization to the surface region of the assessed sample[134], thus multiple measurements are required for a representation of the whole sample.

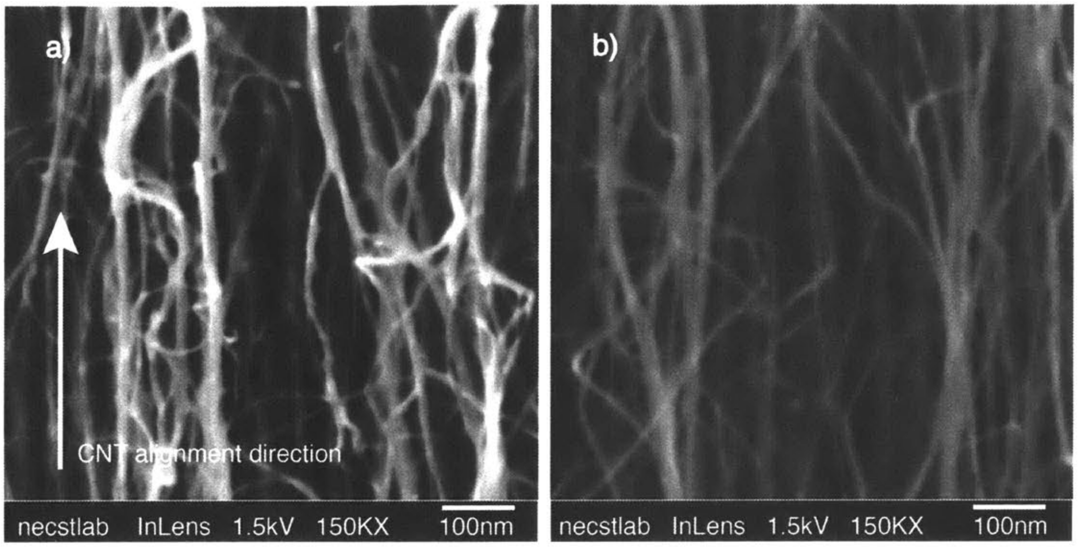

Figure 4-8: SEM of ~ 2 mm CNTs showing minimal carbonaceous impurities at the a) top crust or b) middle of the A-CNT forest. Shorter forests have less exposure to carbonaceous impurities due to a reduced growth time.

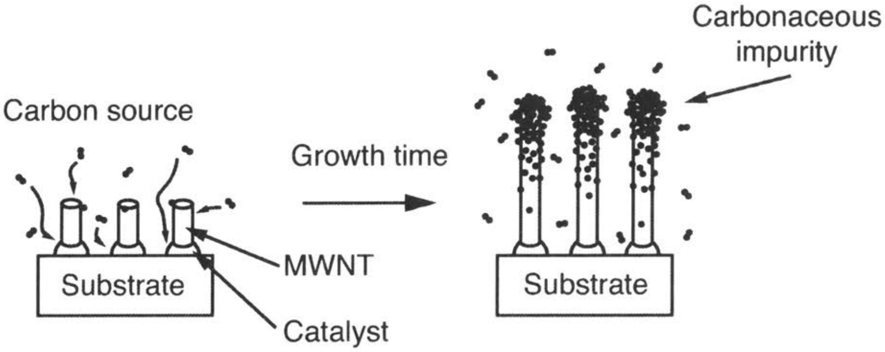

Figure 4-9: Schematic showing the evolution of carbon impurities on the A-CNT forest. A thicker layer is anticipated on the top due to the longest exposure duration in this base growth system.

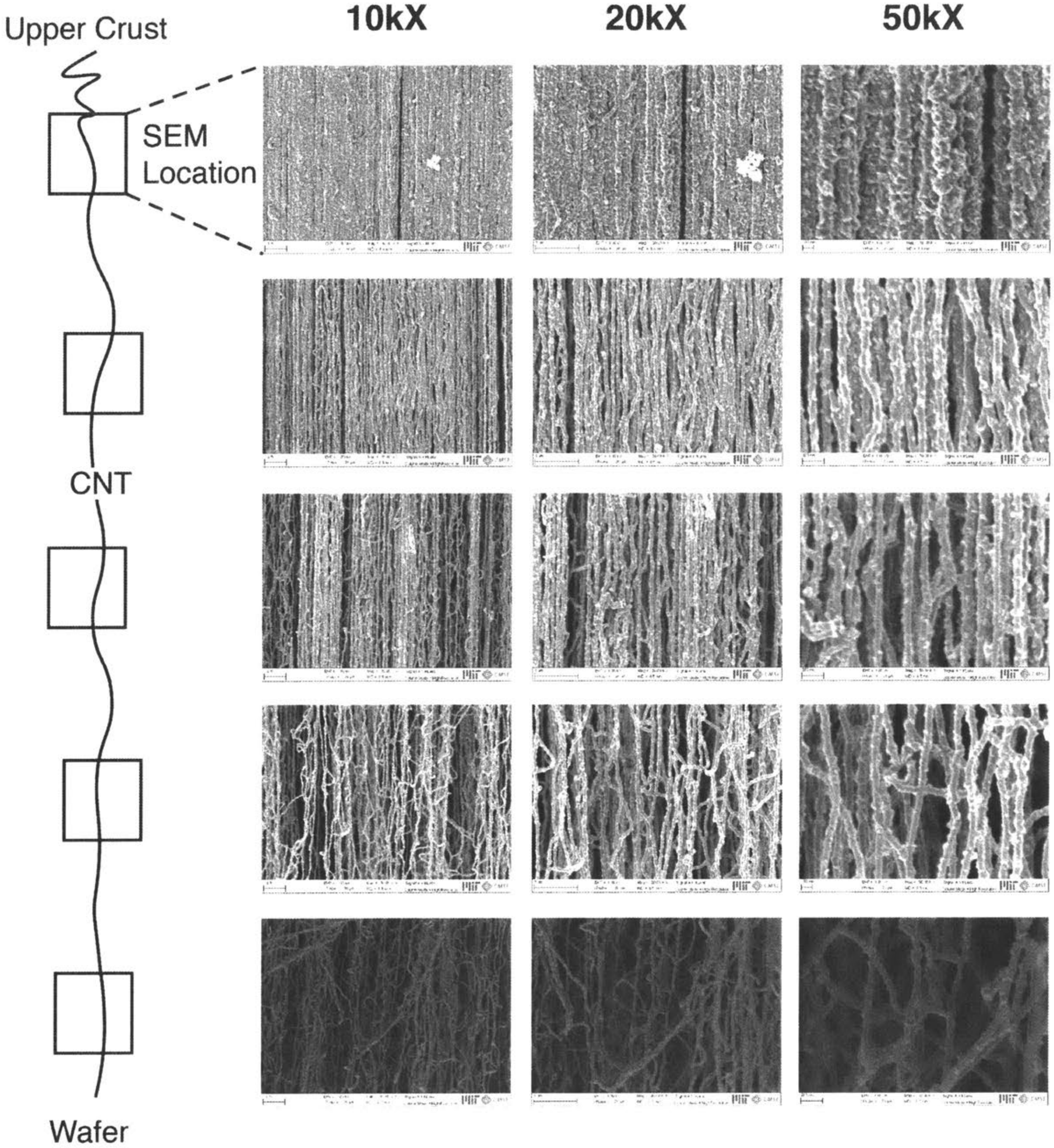

Figure 4-10: SEM images over the height of a ~ 5 mm forest grown for 3 hr (note CNT growth terminates at 50 mins) taken at 5 locations along the forest height showing the accumulation of carbonaceous impurities. Significant accumulation at the top of the A-CNT forest is such that interstitial space is almost nonexistent.

Raman Spectroscopy

Figure 4-11 provides a general profile of a Raman spectrum for a representative CVD grown multiwall A-CNT forest. There are dominant features from which CNT quality can be estimated such as the tangential mode (G-band), disorder induced D-band, radial breathing modes (RBM not shown) and G' or 2D-band (attributed to the overtone of the D-band). RBM Raman features, associated with atomic vibration of the C atoms in the radial direction, are not typically observed in MWNTs because of the large number of walls yielding weak intensities[135], however in SWNTs the RBM features are useful in characterizing A-CNT diameter and chirality.

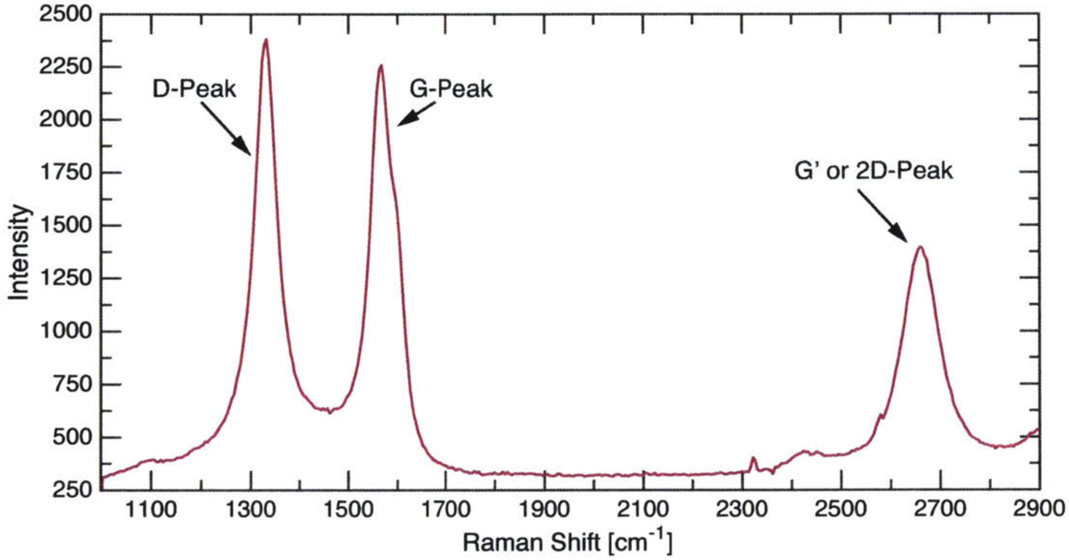

Figure 4-11: Raman spectra of typical CVD grown A-CNT forest, sampled at the top of the A-CNT forest. Common features of CNTs are observed such as the D-Peak at ~1350 cm^{-1}, G-Peak at ~1580 cm^{-1} and 2D-Peak at ~2680 cm^{-1}. Using these peaks, the quality of the A-CNTs can be inferred.

The tangential modes or G-band occur around 1580 cm^{-1}, with a shoulder at ~1600 cm^{-1}, which are assigned to the in-plane vibration of the C-C bond, and are representative of the graphitic nature of the CNTs. In smaller diameter CNTs, the G-peak can be observed as multiple peaks, often lumped together as G^+ and G^-, which assists in differentiating between CNTs and graphite. In the larger diameter MWNTs, the G-band is smeared, making it more difficult to differentiate between the MWNTs and graphite[135]. It must be noted that Raman spectra show some dependence on the wavelength of the incident radiation. This work does not explore the peak evolution as a function of wavelength, but draws conclusions based on the 514 nm laser.

The disorder induced D-band is typically observed at ~1350 cm^{-1}, but occurs in a 1300-1400 cm^{-1} range, and may be attributed to lattice defects in the sp^2 carbon material[136]. A large D-peak, when compared with the G-peak, is typically indicative of a high defect density or the presence of amorphous carbon - a gradual increase in the graphitic (G-band) to disorder band (D-band) intensity ratio, presented as I_D/I_G[137], would be attributed to an increase in the impurity deposit. The Raman spectrum also exhibits a band at ~2680 cm^{-1} which is commonly referred to as G′, but more accurately termed the 2D-band, as it is the second order of the D-band resulting from a double resonance process. A decrease in 2D-band intensity corresponds to an increase in diameter and/or wall thickness of the CNT[138].

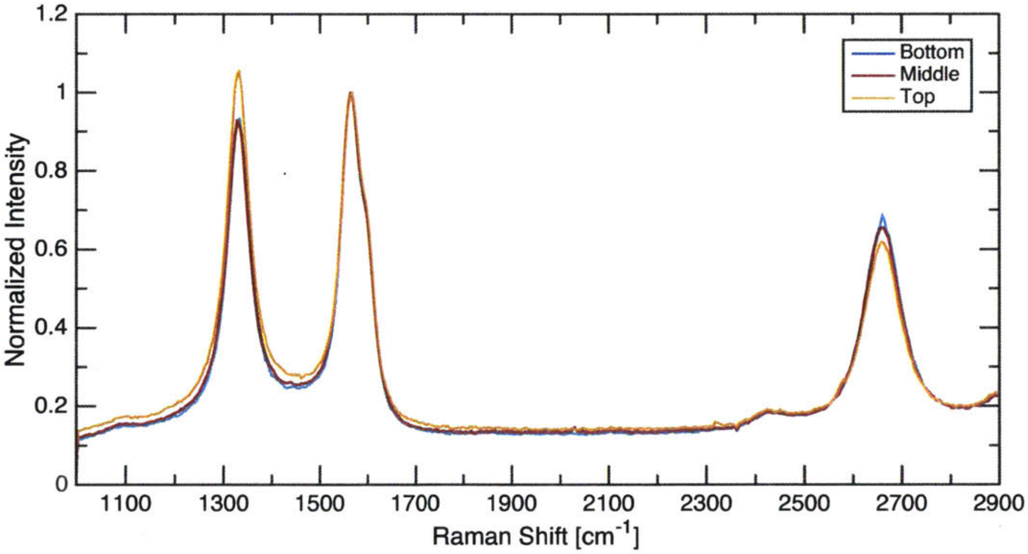

Figure 4-12: Raman spectra collected along the side of a ~ 2 mm A-CNT forest at top, middle and bottom locations. The increased D-peak from the top location suggests lower purity when compared to the bottom of the forest. Similarly, this lower purity translates into a lower observed 2D-peak where CNT diameter is larger due to carbon impurity accumulation.

Raman data are collected from the bare, as-grown ~ 2 mm A-CNT forests at the top (crust side), middle, and bottom (wafer side), as shown in Figure 4-6b. Results are normalized according to the G-peak for comparative purposes and shown in Figure 4-12. Considering the D peak, the spectra from the bottom of the forest has a visibly smaller full width half maximum (FWHM) which is associated with higher purity and less defects. The 2D-peaks at ~ 2700 cm^{-1} indicate that the bottom of the forest (having the highest 2D-peak peak) has the smallest wall thickness meaning that there is less accumulation of carbon impurities, corresponding to the highest purity. The spectra for the middle and the top of the forest are very similar, however the 2D-peak for the top of the forest is less than that of the middle of the forest indicating a slightly larger wall thickness. This is consistent with SEM images where carbonaceous deposits are seen more readily at the top of the forest due to the longer exposure to the growth environment. Additionally, notice at ~ 1500 cm^{-1} that the top of the forest has a higher intensity in this region when compared to the bottom of the forest, and is due to an amorphous carbon peak being present in this range[139]. This further indicates that carbon impurity deposition is occurring at the top of the forest but not at the bottom to as great an extent. Raman results for the ~ 5 mm A-CNT forests are shown in Figure 4-13 and exhibit the same trend as that seen in the ~ 2 mm A-CNT forests. Again, I_D/I_G decreases when moving from the top of the forest to the bottom suggesting the larger amounts of disordered carbon at the top of the forest, consistent with SEM observations.

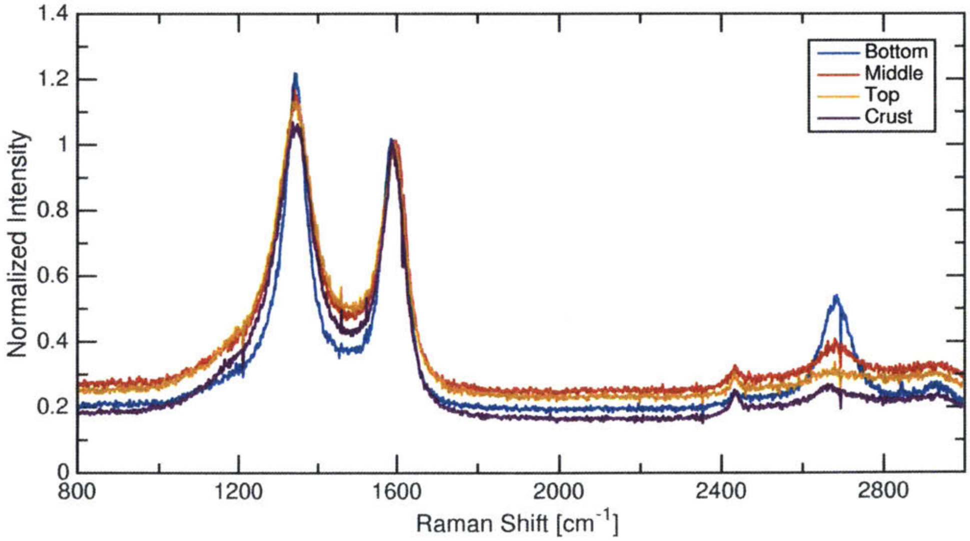

Figure 4-13: Raman spectra collected along the side of a ~ 5 mm A-CNT forest at crust, ~ 1 mm down from the top (top), middle and bottom locations. The same trend is noted for the 5 mm forest as for the ~ 2 mm forest.

Thermogravimetric Analysis

The hypothesis that thicker layers of amorphous and turbostratic carbon impurities form towards the upper crust, could be further assessed by TGA. Different carbon species combust at different temperatures in air, and performing TGA on samples of different growth time will elucidate the particular species present on the CNT surface. Because the walls in CNTs are formed by sp^2 bonds[140], the oxidation temperature is higher than that of amorphous carbon which is $\sim$ 420°C. The common combustion temperature of CNTs is also dependent on the degree of graphitization. Graphite combusts at $\sim$ 645°C while MWNTs have a range from 550-700°C[141]. Given the TGA profiles, results strongly indicate that the carbon impurities are dominated by graphitic rather than amorphous species, consistent with the literature[131,141,142].

A TGA sweep presented in Figure 4-14 shows results for forests grown for 20 mins, 50 mins and 3 hrs. There is negligible weight decrease at temperatures below 500°C, followed by the full combustion of the A-CNT forest in the range of 600-700°C with no apparent residue above 750°C. For a given sample, the TGA indicates what percentage of the sample mass is represented by various carbon species. While the presence of amorphous carbon is likely limited, the presence of somewhat ordered carbon impurities are present in varying degrees. The composition of a mm-scale forest will primarily be sp^2 A-CNT walls while the $\sim$ 5 mm forest will have a large percentage of non-amorphous carbon impurities contributing to the mass. The carbon impurities on the 3 hr forest, however, are likely to be non-graphitizing carbon (a network of sp^2 platelets) due to increased anneal times, and the A-CNTs themselves will have experienced a thermal anneal process. The combined result of this would be that the $\sim$ 5 mm forest would be the least combustion resistant while the 3 hr forest would be the most combustion resistant, as is observed in Figure 4-14. As an aside, the lack of combustion residue above 750°C indicates that catalyst particles and other non-carbonaceous impurities are not present in the A-CNT forests.

To increase the purity of the A-CNT forest, the non-graphitic carbon materials can be burned out in air at a temperature of $\sim$ 500°C, however, the removal of the graphitic impurities is currently impossible without damage to the CNT itself. Based on this, further

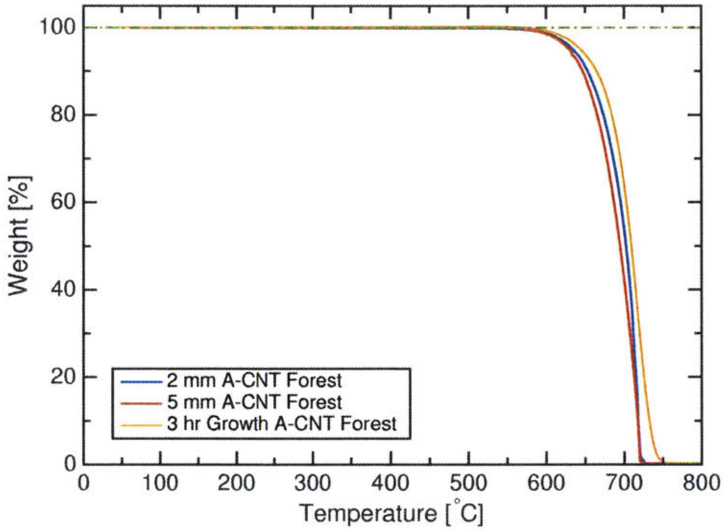

Figure 4-14: TGA data collected for the 20 min (~ 2 mm), 50 min (~ 5 mm) and 3 hr forest (~ 5 mm), no significant difference in profiles is observed indicating that carbonaceous impurities on the 5 mm forest are graphitic in nature. Negligible amounts of both amorphous carbon and catalytic impurities are detected.

processing of the A-CNT forests cannot be performed to create morphological consistency over the forest height, thus forest heights must be selected such that an agreeable balance is achieved between forest height and carbon impurity accumulation.

Transmission Electron Spectroscopy

A far more direct way of visualizing nanocomposite morphology is via TEM. Given that the TEM spot size only reveals a very small region of the CNT, it is critical to take images at different magnifications and from different locations to establish an accurate representation of the morphology. TEM is not performed as a function of height; comparison is however drawn between the ~ 1 mm tall forest that has been historically utilized, and the current ~ 5 mm tall A-CNT forest.

Figure 4-15 compares TEM images of the ~ 1 mm and ~ 5 mm tall A-CNT forests to show the growth extremes. For a 9 min growth (~ 1 mm), TEM images show A-CNTs generally free from carbon impurities. By contrast, for a growth time of 50 mins (~ 5 mm),

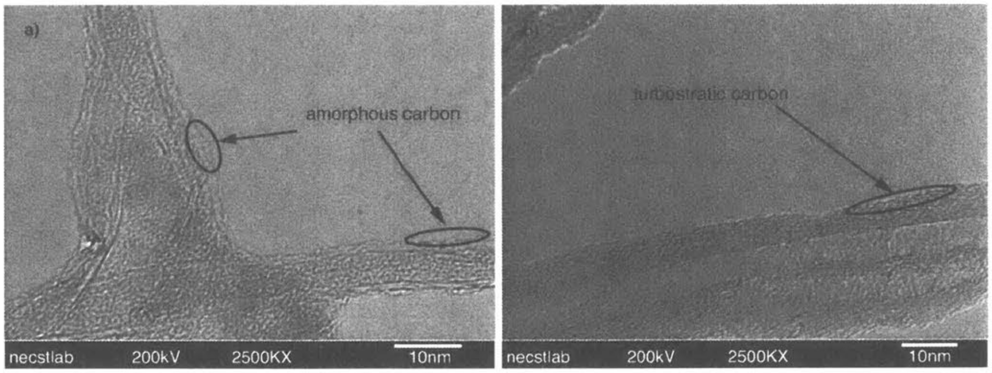

Figure 4-15: TEM images of a) $\sim$ 1 mm tall and b) $\sim$ 5 mm A-CNT forest. The $\sim$ 1 mm A-CNT forest shows small amounts of amorphous carbon on the surface of the CNTs while the $\sim$ 5 mm CNTs are coated with a layer of turbostratic carbon. Sample preparation of these TEM specimens are not limited to a specific location in the A-CNT forest.

the CNTs have layers of additional carbon deposits. The stratified nature of the additional deposits suggest a level of graphitization. Figure 4-16 presents three representative TEM images of a $\sim$ 2 mm A-CNT forest, also showing limited amounts of accumulated impurities. Note that sample preparation of these TEM specimens are not limited to a specific location in the A-CNT forest.

Additional Morphological Characterizations

Based on the gradient nature of carbon impurity deposition and density decay, the evolution of additional characterizations such as diameter, spacing and waviness[13,27,143,144] are considered as a function of height. These parameters are determined by capturing SEM images every 1 mm along the forest height, beginning at the upper crust. Various forest heights are analyzed thus a $\sim$ 5mm forest will be analyzed in 6 locations, a $\sim$ 4mm forest will be analyzed in 5 locations, and so on. Along each latitudinal location, three images are captured and analyzed to ensure spatial variation is captured. To measure the diameter of the A-CNTs at each location, SEM images at 100 kX magnification are uploaded to ImageJ and measurements are taken using the line tool. These measurements are compared to those captured by TEM for process validation. To measure the spacing between A-CNTs at each location, the images are processed using the ImageJ threshold tool, which covers any brightness below 50%, revealing CNTs on a plane of focus as can be seen in Figure 4-17. These

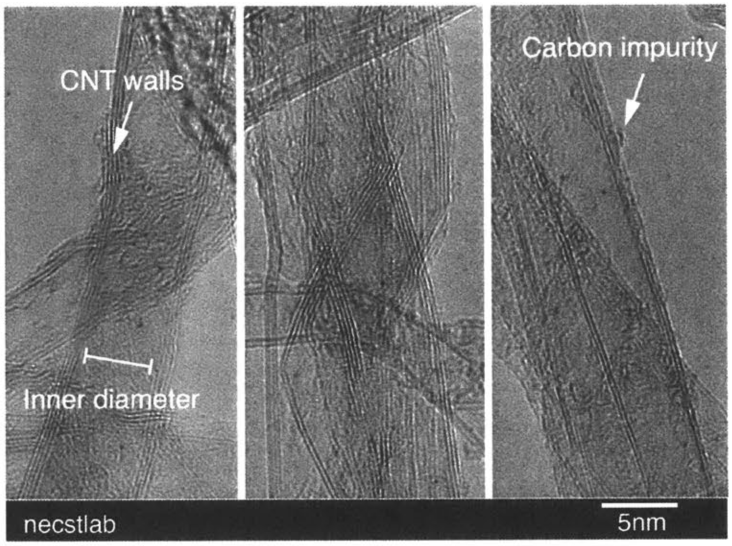

Figure 4-16: TEM of $\sim$ 2 mm tall A-CNT forest showing 3-5 walls and an inner diameter of $\sim$ 5 nm. Observe trace amounts of carbon impurities present on the surface of the outer CNT wall. Three separate images are provided captured at different locations on the TEM grid. It is uncertain as to which location within the forest these A-CNT originate.

A-CNTs, with previously determined diameters, are counted and the combined diameters are subtracted from the width of the image. The average spacing is determined by dividing the remaining space by the number of expected interstices. The reported spacing is thus outer wall to outer wall spacing, or inter-CNT distance. To measure the waviness of the A-CNTs at each location, SEM images at 20 kX magnification are uploaded to Microsoft PowerPoint where a sine wave (calculated and graphed in Microsoft Excel) is superimposed to the A-CNTs, an example of this is shown in Figure 4-18. The height and width of each fitted sine wave is measured, from which amplitude and wavelength can be calculated. A total of 15 sine waves are used at each latitude for the determination of waviness.

The results for diameter, spacing and waviness are shown in Table 4.1, Table 4.2 and Table 4.3, respectively. Note that the same forest is used for determination of all three measurements. The forest heights associated with each growth time are as follows: 80 min - $\sim$ 5 mm, 50 min - $\sim$ 5 mm, 40 min - $\sim$ 4 mm, 30 min - $\sim$ 3 mm, 20 min - $\sim$ 2 mm, and 90 min - $\sim$ 1 mm. While this method is less accurate than TEM for diameter measurement (Table 4.1), it reiterates the observation that carbon impurities increase the diameter at the top of the forest more readily than the bottom. For a $\sim$ 5 mm forest, grown for 50 mins, the

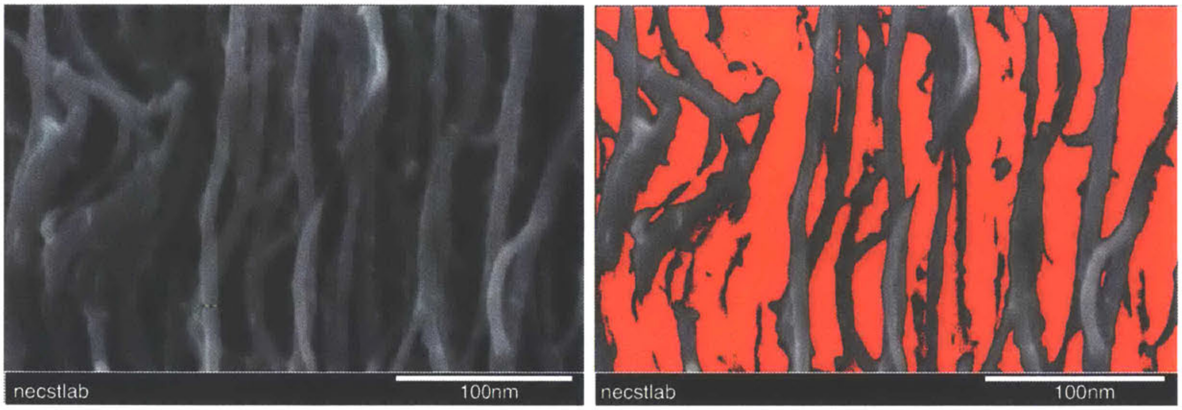

Figure 4-17: SEM image where a 50% brightness filter is applied in ImageJ to isolate A-CNTs in the same plane for determination of spacing.

Figure 4-18: A-CNT waviness is characterized by fitting a sine wave to individual CNTs.

diameter is $\sim$ 30 nm while at the bottom of the forest it is $\sim$ 14 nm. This can be compared to the $\sim$ 2 mm forest (grown for 20 min) where the diameter at the top is measured to be $\sim$ 20 nm while the bottom is $\sim$ 14 nm. It is expected that the bottom of the 9, 20, 30, 40 and 50 min forests all have a similar diameter as this location has limited carbon impurity accumulation, however this is not seen and is likely due to measurement inaccuracy, as well as accurate latitude determination when navigating in the SEM environment. Such inaccuracies are equally applicable to both spacing and waviness determination, with spacing error being increased due to the dependence on locational diameter. Nevertheless, is can be seen from

Table 4.1: A-CNT diameter as measured from 100 kX SEM images using the line tool in ImageJ. A-CNT diameter decreases from top to root. Data is collected from 3 images along the latitude of each location with 5 data points collected per image. All data is in nanometers.

Location	80 min	50 min	40 min	30 min	20 min	9 min
Top	37.2±5.3	29.1±2.6	32.1±2.2	29.9±2.3	19.8±1.8	13.9±1.0
Top - 1 mm	34.1±5.1	26.1±3.5	28.8±2.3	21.7±2.6	18.8±2.1	11.5±0.6
Top - 2 mm	30.5±3.9	24.0±2.6	23.6±2.7	20.7±2.7	14.4±1.4	
Top - 3 mm	26.6±2.2	22.8±1.9	18.7±2.1	19.6±2.7		
Top - 4 mm	24.7±1.9	21.1±1.9	17.4±1.7			
Top - 5 mm	21.7±3.9	13.6±1.6				

Table 4.2: A-CNT spacing as measured from 100 kX SEM images, using an ImageJ 50% brightness filter to isolate A-CNTs in one plane. Data is collected from 3 images along the latitude of each location. All data is in nanometers.

Location	80 min	50 min	40 min	30 min	20 min	9 min
Top	15.7±4.1	19.9±3.1	16.3±4.5	14.1±6.6	18.3±6.6	24.7±7.5
Top - 1 mm	21.4±3.5	23.1±3.3	13.6±4.1	21.7±5.7	19.4±5.0	36.9±7.7
Top - 2 mm	23.3±3.0	24.3±6.9	22.9±5.2	33.8±3.9	29.9±4.8	
Top - 3 mm	26.3±4.1	25.6±4.3	27.7±7.5	44.1±4.0		
Top - 4 mm	55.9±3.9	43.8±4.0	57.4±6.4			
Top - 5 mm	59.6±3.6	46.7±3.5				

Table 4.2 that spacing increases when moving from the upper crust to the roots of the A-CNT forest. This is expected due to both number density decay from individual CNT termination, as well as the diameter gradient. For the $\sim$ 1 mm forest (grown for 9 min) where density decay and impurity accumulation is minimal, inter-CNT (outer wall to outer wall) spacing in the steady growth region are $\sim$ 40 nm. From Table 4.3, there is no statistically significant difference in waviness over the forest height.

In line with the general approach outlined thus far, the growth limit of the A-CNT forest is established to be $\sim$ 5 mm. The extended growth time results in a non-negligible amount of graphitic carbon impurities on the $\sim$ 5 mm A-CNT forest that is difficult to discriminate

Table 4.3: Waviness as measured by fitting sine curves to A-CNTs captured in 20 kX SEM images. Data is collected from 3 images along the latitude of each location with 5 sine waves fitted per image. All data is in nanometers.

Location	80 min	50 min	40 min	30 min	20 min	9 min
Top	0.14±0.03	0.16±0.03	0.12±0.03	0.16±0.04	0.12±0.02	0.13±0.02
Top - 1 mm	0.11±0.01	0.13±0.02	0.10±0.02	0.13±0.04	0.16±0.04	0.16±0.03
Top - 2 mm	0.13±0.03	0.11±0.01	0.13±0.05	0.13±0.04	0.12±0.03	
Top - 3 mm	0.16±0.01	0.13±0.02	0.10±0.02	0.15±0.05		
Top - 4 mm	0.14±0.02	0.12±0.04	0.08±0.01			
Top - 5 mm	0.10±0.03	0.09±0.02				

and remove. Given the establishment of the effects of the growth process on the A-CNT structure, A-PNC properties determined during testing can be interpreted in light of the A-CNT process-structure relationship. A $\sim$ 5 mm forest is expected to produced a different A-PNC than the $\sim$ 2 mm, however as previously mentioned, the $\sim$ 5 mm forest will move an interface between pure polymer and the A-PNC further away from the precrack when test specimens are manufactured. Again, an agreeable balance is required between the A-CNT morphology and the distance of the interface from the intended crack path.

Continuing onto the manufacturing procedure for A-PNCs, the removal of the A-CNT forest from the substrate is required, a process herein referred to as "delamination". The ability to remove the A-CNT forest as a function of growth time is studied to ensure manufacturability, and the effect of post-growth treatments on delamination is explored.

4.2 Delamination and Cementation

There are numerous potential applications for which CNTs and their adhesion to or delamination from the growth substrate will be desirable based on the specific application. Examples of adhesion required applications are CNT-based microfluidic elements[145], field-effect transistors, field emission displays, atomic force microscopy probes and CNT microelectrodes[146]. Poor adhesion of the CNTs to the substrate in these devices poses a reliability concern as CNTs could detach during operation yielding the device inoperable. Numerous techniques have been explored to increase adhesion such as adding a layer between the substrate and catalyst layers (e.g., titanium or nickel[147]) or by attaching the CNTs to the substrate using amorphous carbon deposition as seen in AFM applications[148]. Should post-growth treatments of the A-CNT forest be desired, adhesion to the substrate would be advantageous for maintaining morphology as well as ease of handling. On the other hand, there are applications that require the transfer of CNTs from the substrate, driving the need for low adhesion and easy delamination. PNC manufacturing is one such example that requires easy delamination of the CNT forest from the substrate.

Some adhesion testing is qualitative: the substrate and attached CNTs, are sonicated in a buffer solution, or inserted into an agar gel and dragged back and forth several times[146], followed by SEM imaging to observe the difference between various adhesion treatments. While these methods are very subjective, quantitative mechanical testing is not standardized and each technique has limitations. Shearing the forest off of the substrate using scotch tape[149,150] or other variations of shear tests[151] have been used in literature, and are depicted in Figure 4-19. With tape based shear tests, it is unknown if all the CNTs are making contact with the tape, and a large amount of friction can be generated if the shear surfaces are not parallel, or the CNTs are not a uniform height. Other methods have been suggested such as nanoscratch where a Berkovich tip is used to scratch the substrate from a region without CNTs to a region with CNTs[152]. This technique is limited to short forests and does not account for spatial variation by only considering a region at the edge of the specimen. More so, it does not account for CNTs that do not debond, but influence lateral force through the dense tangled network or are pushed aside by the wedge-like geometry of the nanoindenter tip.

There are numerous test standards available for peel tests such as ASTM B905[153] and ASTM D3359[154], however most require carefully controlled peel angles, provide qualitative pass/fail data, use scoring/scribing surface preparation techniques or require test specimens that are unsuitable given the CNT forest geometry and substrate, this includes T-type peel tests[155], see Figure 4-19.

Direct tensile testing methods have been developed for measuring adhesion of organic

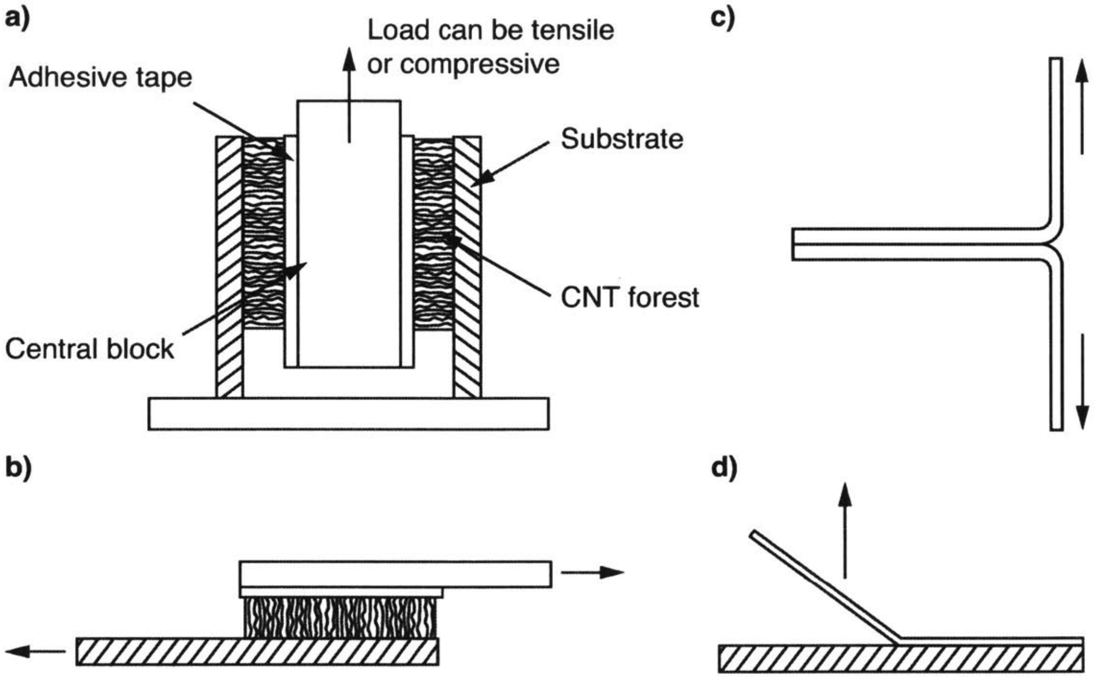

Figure 4-19: Examples of various mechanical testing methods used to establish adhesion of a coating (or A-CNT forest) to a substrate including: a) double shear test (adapted from Zhang et. al[151]) b) lap shear test c) T-type peel tests and d) tape peel tests.

coatings to plastic substrates in ASTM D5179[156]. It involves mounting an aluminum stud to the coating and then testing it in a tensile mechanical tester to determine the force required to debond the coating from the substrate. Given the growth morphology of the CNT forest, an adaptation of this test standard is most suitable to determine the adhesion of the vertically aligned CNTs to the substrate.

Important considerations when performing these tests to determine adhesion strength are:

- The total area of the adhesive surface cannot be used to calculate strength as this will underestimate the actual strength required to detatch individual CNTs from the substrate - the total cross sectional area of the CNTs (also considering local root density) must be used.
- CNTs can debond at the substrate interface or break at a defective location along the length; the former measurement providing the force required for delamination and the

latter providing the ultimate tensile strength of the remaining CNTs attached to the wafer.

- CNT diameter changes as a function of the growth period due to the accumulation of carbon impurities.
- CNT number density at the substrate interface decreases with an increase in growth time noting abrupt termination or debonding.

Experimental Procedure for Cementation/Delamination

This study is divided into two sections:

1. A-CNT growth time is varied to determine the changes in adhesion to the substrate. With an increase in growth time we expect the forest height to increase until the point of self termination beyond which the nanotubes will remain within a carbon rich environment. It is anticipated that a longer growth time, beyond termination, will increase adhesion to the substrate due to accumulation of carbon impurities, or diffusion and other reactions at the CNT-catalyst-substrate interfaces.
2. A standard growth time of 20 mins is selected with resulting ~2 mm forest heights, and the post growth treatment is varied. This is limited to varying anneal times in the presence of helium or helium/water at the standard growth temperature of 740°C. Thus, growth is terminated by discontinuing hydrogen and ethylene gas flow while introducing helium to ensure an inert environment is maintained during the temperature anneal. In the cases were water is introduced during the anneal stage, helium is used as a carrier. The test conditions are: as-grown, 6 mins anneal with 250 sccm hydrogen gas (with helium carrier), 20 mins anneal, 40 mins anneal, and a 20 min anneal followed by a 20 min anneal with 5 sccm water (5 sccm helium bubbled through water). The water and hydrogen treatment both act to remove amorphous carbon from the catalyst nanoparticle.

A-CNTs are grown on 10 mm × 10 mm Si wafers using the standard growth recipe with modifications as indicated above. A minimum of four samples are grown for each data point. Aluminum SEM stubs are used as the mounting surfaces. Flat surfaces are machined into the cylindrical post to allow for sufficient clamping in the mechanical tester. The faces of the stub are sanded with 80-grit sandpaper ensuring that the surface is adequately roughened. The SEM stubs are then cleaned thoroughly with acetone and then rinsed sequentially in acetone, isopropanol, methanol, and DI water to remove any debris and oils, to allow for good adhesion. They are dried in an oven at 120°C for 1 hr. MG Chemicals two-part silver epoxy is used as the adhesive for two reasons:

1. Using a conductive epoxy allows imaging the forest using an SEM after the test - this replaces the requirement for conductive tape or gold sputtering.
2. A high viscosity epoxy is required to prevent wicking of the epoxy into the forest, potentially adhering to the substrate.

The silver epoxy is mixed with a 1:1 ratio using a wooden stir stick until well blended. A thin layer is applied to the SEM stub ensuring the surface is completely coated - excessive amounts of epoxy is avoided as it could create spillover and contaminate the forest. The Si wafer is positioned on top of the silver epoxy and a gentle downward force is applied to the corners, care being taken not to disturb the CNT forest. The epoxy is allowed to cure for >4 hrs at room temperature. The SEM stub is inserted in the lower grip of the mechanical tester. A clean, bare SEM stub is inserted into the upper grip and a 0.5 mm thick layer of silver epoxy is applied directly to the face of this SEM stub. The epoxy layer is thick enough to account for any possible variation in the forest height but does not interact with any region of the A-CNT/substrate interface when applied. The upper grip is lowered down until the epoxy coated stub makes contact with the top of the forest with a load of 0.1 N. The load will return to zero as the epoxy repositions itself in the stub/CNT interface and the upper grip is again lowered until 0.1 N is applied. This process in repeated until the epoxy begins to bulge around the edges, suggesting that the stub/CNT interface is completely filled with epoxy. The epoxy is allowed to cure while mounted in the mechanical tester. The final assembly can be seen in Figure 4-20.

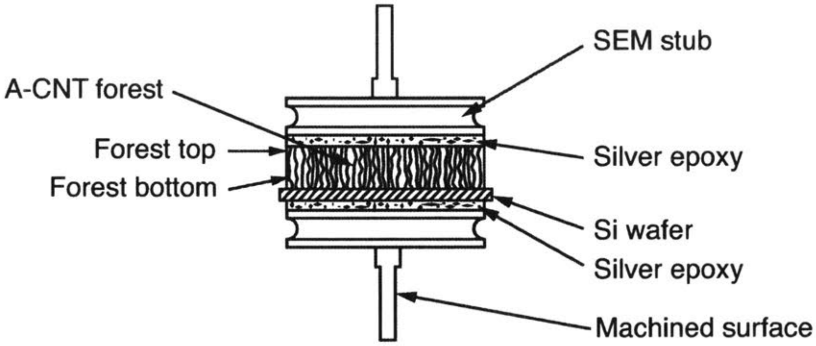

Figure 4-20: Test setup for tensile testing of the A-CNT forest to determine adhesion to the substrate. The A-CNT forest (still attached to the substrate) is carefully adhered to two aluminum SEM stubs with silver epoxy prior to tensile testing.

The samples are tested on a Zwick Roell mechanical tester with a 500 N load cell. The samples are loaded at 50 mm/min, and load and stroke are recorded. Following testing, numerous characterizations are performed, see Figure 4-21:

- The detached Si wafer is imaged using optical microscope to provide a broad view of the surface (Figure 4-21a).
- TEM samples are prepared from the roots of the CNT forest (Figure 4-21b) to observe the number of walls, outer diameter, inner diameter and any other carbon families that may be present on the CNTs at the growth points.
- Raman spectroscopy is performed on the bottom of the forest to assess the quality of the as-grown CNT forests at the growth points.
- SEM is to be performed as future work.

Results and Discussion of Delamination Study

For the first part of this study, we track adhesion of the forest to the wafer with increasing growth time. However, as noted previously, the forest height also increases with growth time as can be seen in Figure 4-22 (note that the forest height was measured specifically for this study as a precaution as a transition in wafer manufacturing method occurred where growth of the oxide layer was transferred from in-house to supplier). An average growth rate is found to be ~ 100 μm per minute before termination occurs at 50 mins. Beyond 50 mins,

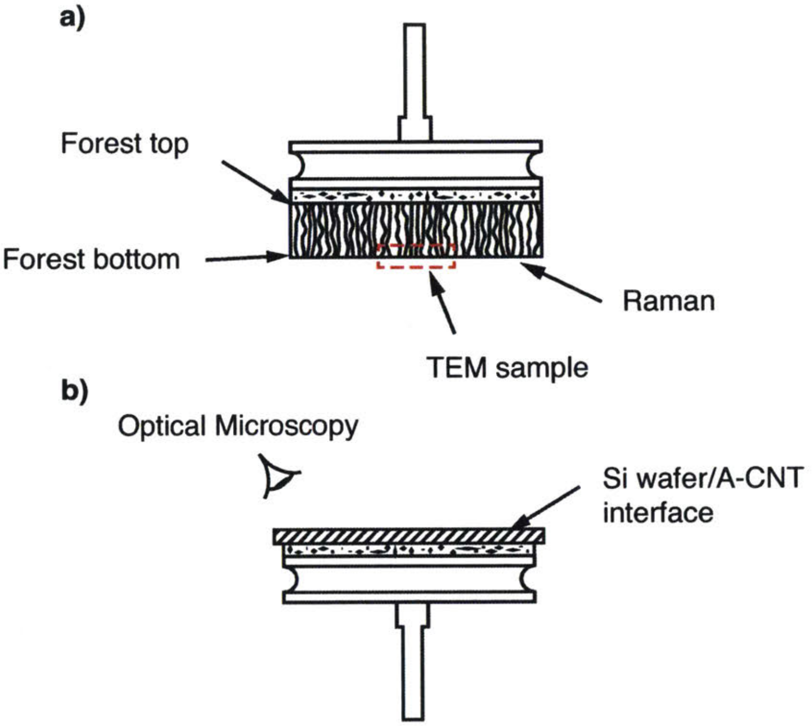

Figure 4-21: Locations for a) imaging/sampling locations on the underside of the detached A-CNT forest for Raman spectroscopy and TEM, and b) imaging the Si wafer/A-CNT interface using optical microscopy.

the forest height no longer increases with increasing growth time while the forest remains in a gaseous carbon rich environment, as already discussed in Subsection 4.1. It is noted that a similar growth profile results from use with the new wafers.

The adhesion force required to remove these forests from the substrate is shown in Figure 4-23, where F_a decreases from ~ 5 N to ~ 1 N between 9 mins and 40 mins growth time. Growth times greater than 40 mins exhibit an order of magnitude increase in the removal force.

The optical microscopy images of these Si wafers presented in Figure 4-24 support this adhesion force finding. There are no observable CNTs attached to the wafer after forest detachment, up to 40 mins growth time. After 40 mins growth time, CNT residue, seen as black patches, is observed on the wafer after removal of the forest. This indicates that by 50 mins, the forests have terminated, as previously described in Figure 4-5. At this stage, it is likely that the large adhesion force is created by breaking of the remaining A-CNTs in

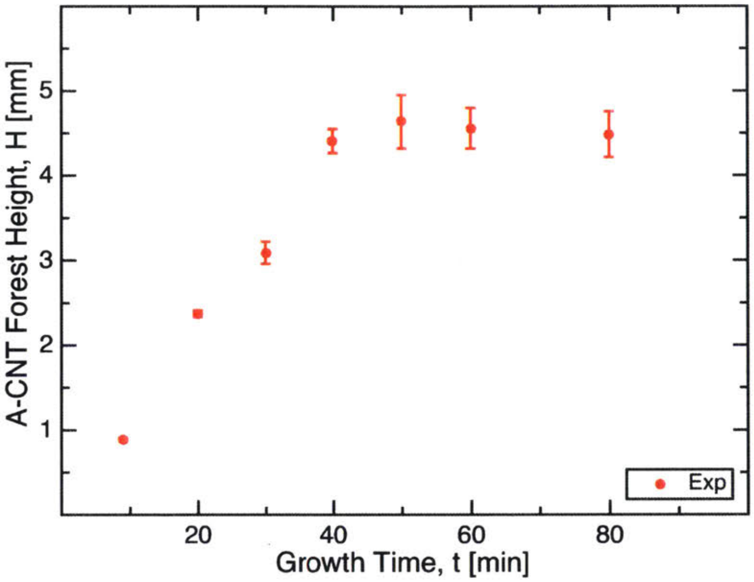

Figure 4-22: A-CNT forest height as a function growth time showing an increase in forest height up to ~ 50 mins where beyond this, no increase seen due to abrupt termination in growth of the A-CNT forest. One measurement is taken at the center of each sample, with 4-8 samples per growth time.

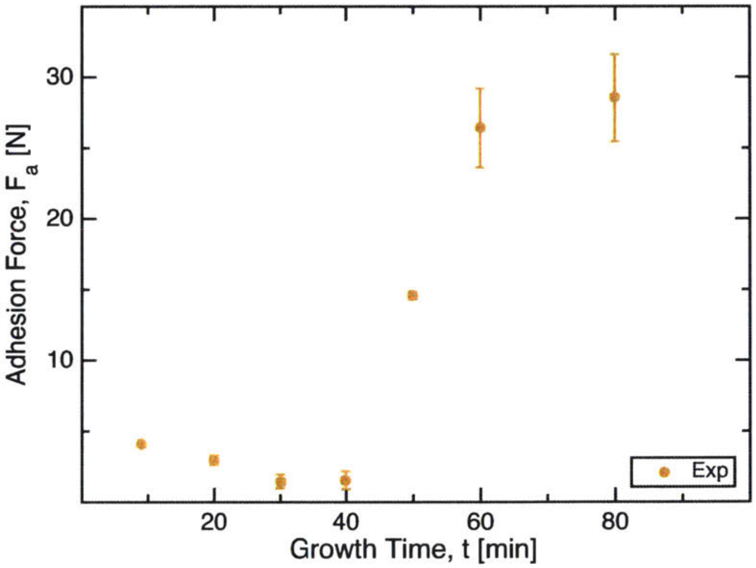

Figure 4-23: Force required to remove the A-CNT forest from the wafer. A decrease in adhesion force (F_a) is seen up to 40 min, beyond which F_a increases by an order of magnitude due to cementing of the A-CNT forest to the wafer.

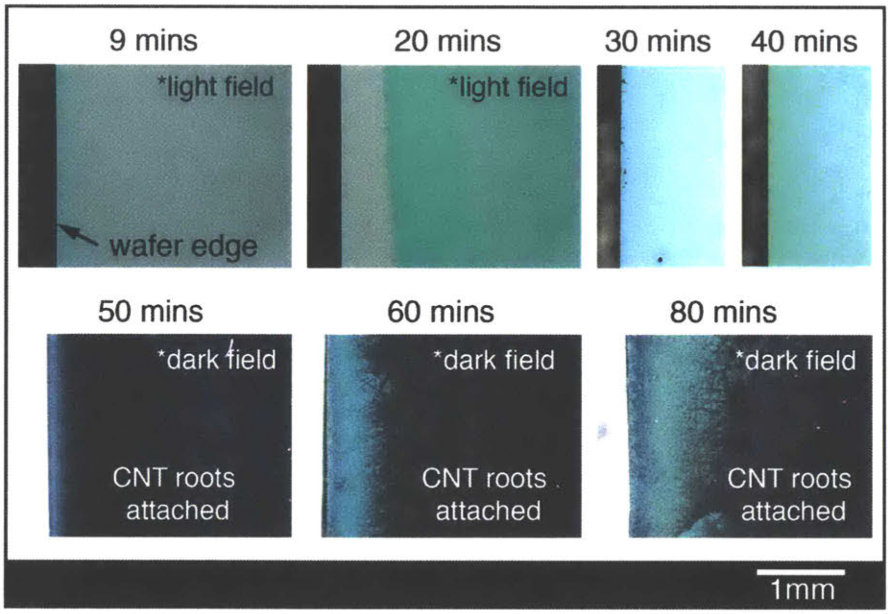

Figure 4-24: Optical microscope images of the wafer, post A-CNT removal, showing clean wafers (green) up to 40 min growth time, beyond which A-CNT residue is observed on the wafer (black), indicating that roots of the A-CNTs are remaining adhered during the forest removal process.

the forest that are still attached to the wafer (not separation from the wafer but breaking), or there is perhaps another cementation/adhesion mechanism at play.

Consider only the results for $\leq$ 40 mins growth time (linear increase in forest height), the decrease in adhesion force may be explained, again, by the sequential stages of A-CNT growth, as depicted in Figure 4-5. During the steady growth phase, almost all of the CNTs are in contact with the wafer interface via the catalyst. As growth progresses, individual CNTs terminate and the number density starts to decay. With less CNTs in contact with the substrate, i.e., less points of contact, the force required to remove the forest will decrease.

Now, consider the region of $\geq$ 50 mins, where the forest no longer increases in height: CNT forest residue is seen on the wafer during optical microscopy, and a marked increase in adhesion force is observed. This is the region where the forest self terminates and a post termination regime begins where carbonaceous impurities further accumulate on the A-CNT forest.

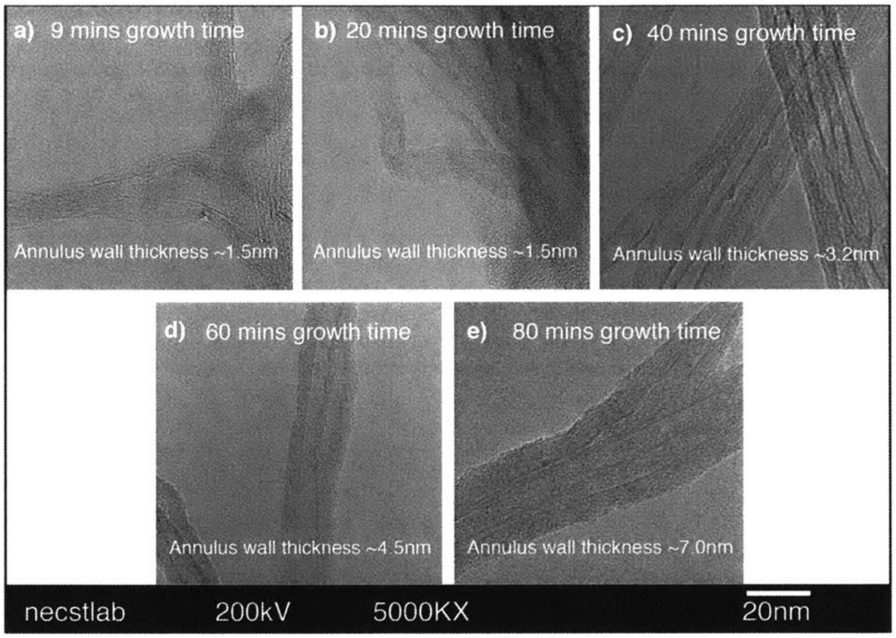

Figure 4-25: TEM micrographs of the bottom of the forest, after delamination, showing increasing total annulus thickness by progressively increasing growth time from a) 9 mins to e) 80 mins.

TEM is performed on the A-CNT forest with sampling done as described in Figure 4-21b. TEM micrographs are presented in Figure 4-25, and data are reported using the naming convention outlined in Figure 4-26. The A-CNTs that are in the steady growth phase, i.e., $\leq$ 40 mins, have a total annulus thickness of $\sim$ 1.2 nm with 3-5 walls, an inner diameter of $\sim$ 6 nm and an outer diameter of $\sim$ 8 nm. From 50 mins onwards, with increasing growth time, we observe in Figure 4-27, an increase in the outer diameter of the A-CNTs. The inner diameter remains constant (Figure 4-28a) at $\sim$ 6 nm, thus the total annulus thickness increases as a function of time, see Figure 4-28b.

As previously mentioned, the number density of the A-CNT forest decays as growth progresses due to individual CNT termination. When the number density becomes too low to support the forest, there is an abrupt halt in vertical forest growth. The CNTs that did not self-terminate when the forest terminated would still be in contact with an active catalyst particle and would still be exposed to gaseous carbon. Thus, carbon is still deposited on the catalyst into which it diffuses and reorganizes, possibly cementing the CNT to the catalyst, and the catalyst to the substrate. Coupled with this, amorphous carbon is

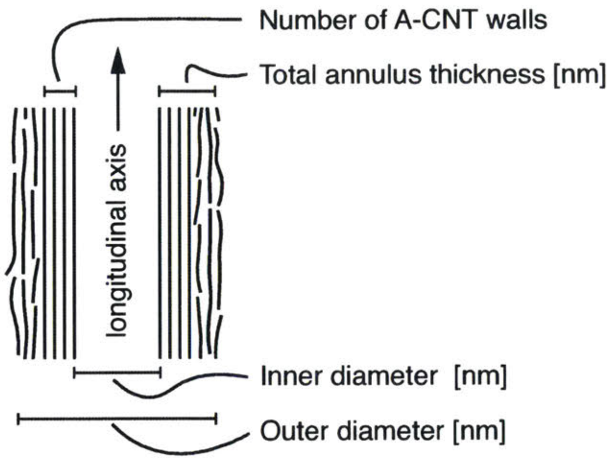

Figure 4-26: Naming convention for reporting TEM data of the A-CNTs. Note that the carbon impurities are included in the measurement of outer diameter.

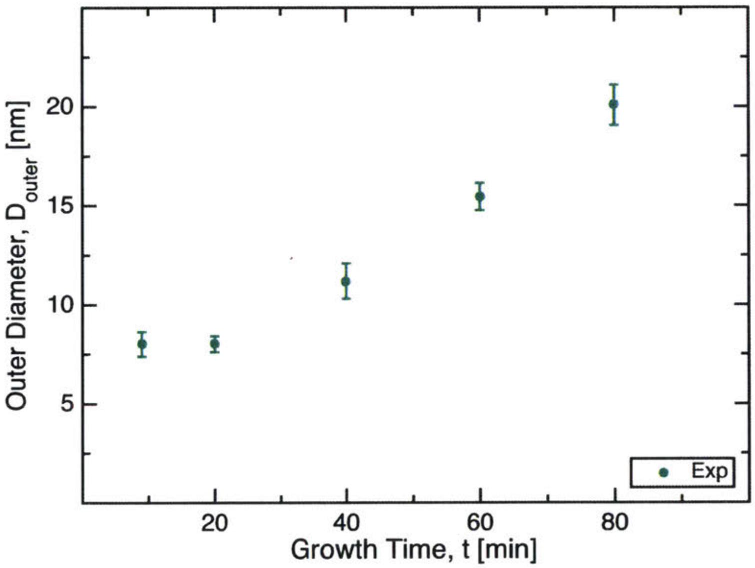

Figure 4-27: A-CNT outer diameter at the bottom of the forests as a function of growth time, as measured by TEM. Carbon impurities cause an increase in the A-CNT outer diameter at growth termination starting at ~ 50 mins.

continuously deposited onto the outer walls of all the A-CNTs, regardless of location. As previously mentioned, the top of the forest would have a thicker layer of carbon deposit than the roots due to the difference in exposure time. An actively growing root would have almost no amorphous carbon present at the catalyst-CNT growth zone. An inactive root would, however, begin to accumulate carbon on the surface in this region, causing an increase

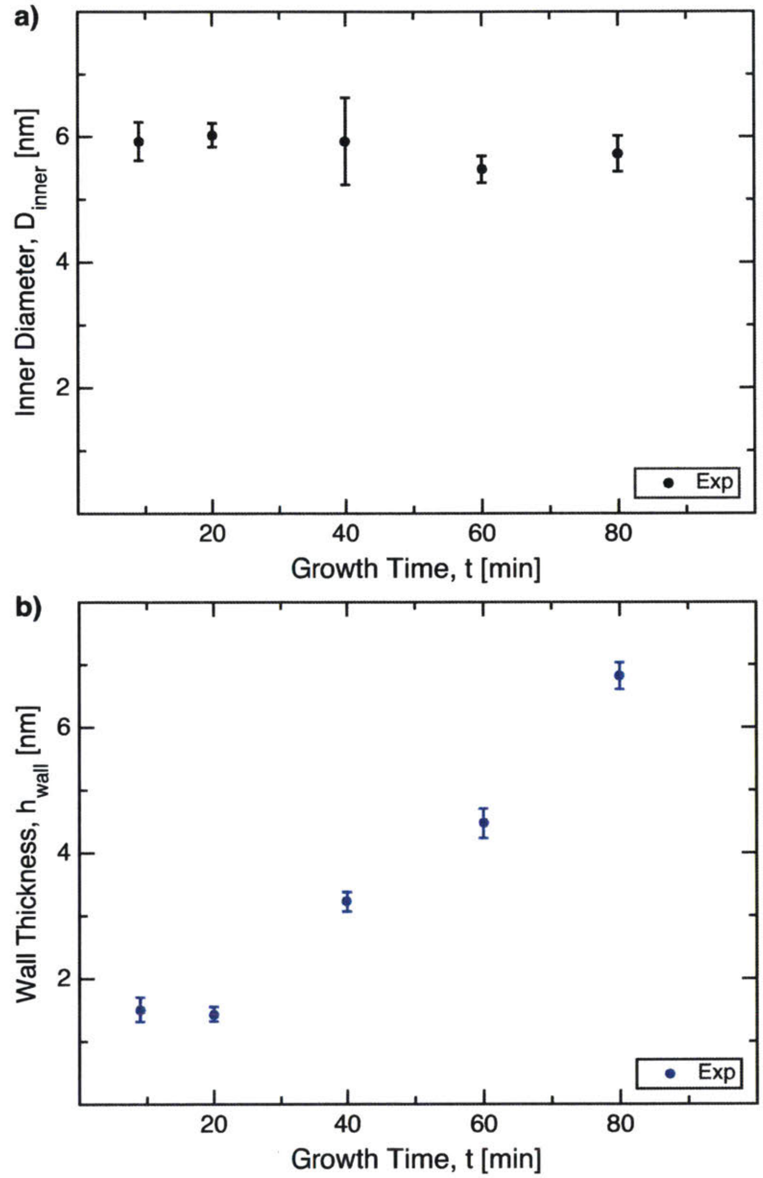

Figure 4-28: CNT wall characteristics from TEM micrographs, a) A-CNT inner diameter and b) total annulus (wall) thickness are reported for the bottom of the forest as a function of growth time. Inner diameter remains unchanged with growth time. The resulting difference between inner and outer diameter provides the trend for annulus thickness.

in the total annulus thickness. TEM shows that the increase in annulus thickness is not, however, an increasing layer of amorphous carbon, but what appears to be increasing number of "walls" as shown in Figure 4-25.

While the extra "walls" appear to be A-CNT walls, it can be discerned, with difficulty,

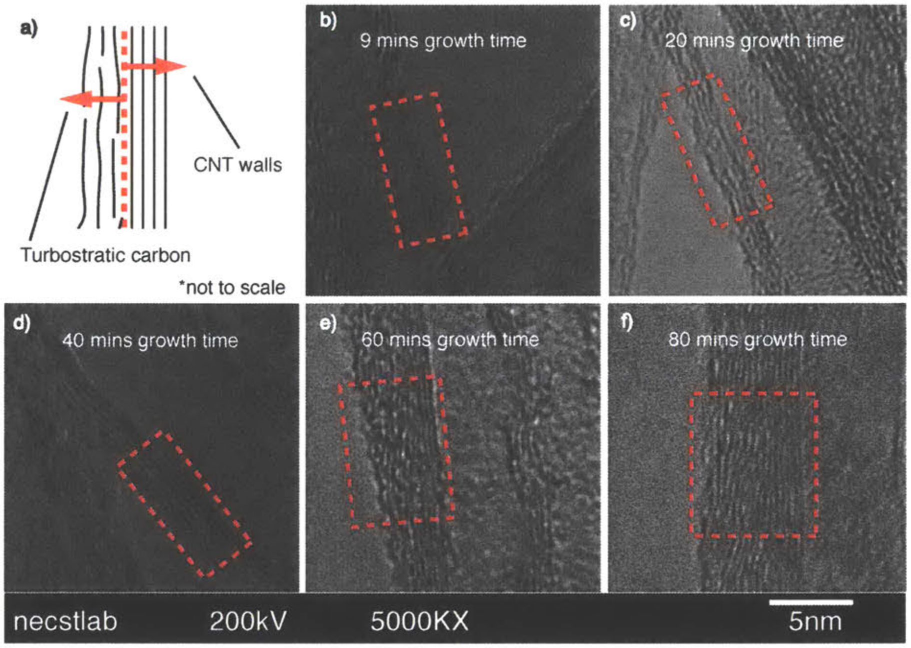

Figure 4-29: TEM images of the A-CNT walls as a function of growth time: a) illustration of the key observation in b)-f) is offered: with increasing growth time, the number of disordered layers surrounding the A-CNT walls increases.

that these layers are more disordered when compared to the original A-CNT walls and layer-to-layer spacing is > 0.34 nm, Figure 4-29. Thus, while the A-CNTs remain in the CVD furnace at temperature, gaseous carbon is being deposited on the walls and graphitizing, using the A-CNT walls as a template. The turbostratic layers appear more ordered closest to the original A-CNT walls and more disordered towards the surface. The A-CNTs still have 4-6 original walls and additional graphitic "walls", increasing in number as growth time increases. This essentially becomes a chemical vapor infiltration (CVI) process using amorphous carbon.

There are two main I_D/I_G regions observed in the Raman results presented in Figure 4-30. As previously discussed, I_D/I_G is higher in regions of low purity when compared to less defective regions. Additionally in this system, this should correspond to a decreased 2D-peak shown as decreased I_{2D}/I_G due to an increasing diameter/wall thickness due to impurity accumulation. A statistically significant difference is seen between samples grown for 40 mins or less, and those grown for 50 mins or more. While growth continues, the root

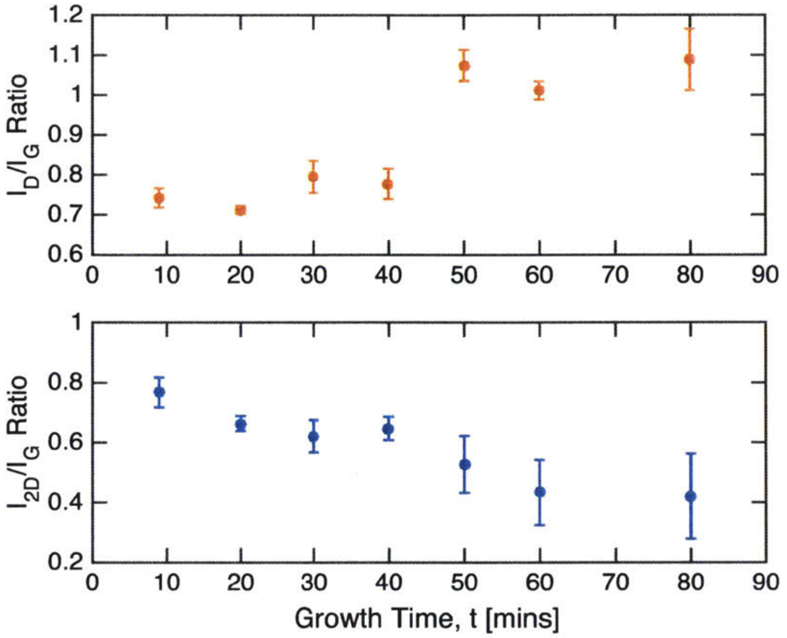

Figure 4-30: Key Raman intensity ratios support the finding that A-CNT purity decrease significantly at the bottom of the forest for ≥ 50 mins growth time, where carbon impurities accumulate on the roots of the terminated forest.

purity is high, however following termination, impurities begin to accumulate thus increasing defects. Within the growth region (0-40 mins) the slight increase in I_D/I_G can be attributed to the individual A-CNTs that terminate and begin collecting carbon impurities.

In parallel to establishing the effect of growth time on F_a, the effect of common post-growth treatments on A-CNT adhesion to the substrate is studied and compared to untreated specimens. As previously mentioned, a standard growth time of 20 mins is selected with resulting $\sim$ 2 mm forest heights. The post-growth treatments are limited to varying thermal anneal times in the presence of helium, thermal anneal with helium/hydrogen, or thermal anneal with helium/water at the standard growth temperature of 740°C.

The F_a adhesion results are shown in Figure 4-31. The 6 min hydrogen anneal, where 250 sccm hydrogen is carried with helium, offers no statistically significant change in F_a over the standard water assisted growth process (indicated by 0 min anneal). In both the case of the 0 min anneal and the 6 min hydrogen, the wafer is optically clean and free from black A-CNT residue following delamination of the A-CNT forest as shown in

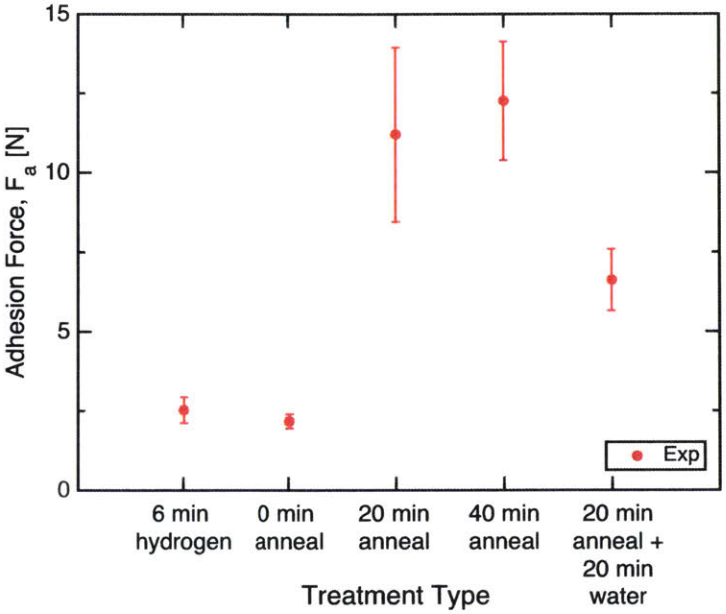

Figure 4-31: Force required to remove the A-CNT forest from the wafer as a function of different post-growth treatments. Successful cementation occurs by performing a temperature anneal after completion of growth. The lowest force required to remove the A-CNT forest from the wafer occurs in the as-grown case (0 min anneal).

Figure 4-32a,b. Increasing thermal anneal time only (helium carrier, no water) to 20 mins and 40 min after growth, leads to cementation of the forest to the wafer, as can be seen by the increased F_a in Figure 4-31. This also results in A-CNT residue remaining on the wafer (black region) as shown in Figure 4-32c,d, with a longer anneal time leading to increased adhesion. Additionally, there is no statistical difference between F_a for the 20 min and 40 min anneal. A likely explanation for this is that amorphous carbon present at the reaction site graphitizes around the nanoparticle and the CNT root, effectively cementing the growth site to the root. The Raman intensity ratios I_D/I_G for this work, as presented in Figure 4-33, support this hypothesis through the increase in the D-peak relative to the G-peak in the case of the 20 and 40 min thermal anneal times. A D-peak increase occurs due to defects being introduced into sp^2 carbon structures. Thus, if amorphous carbon is graphitizing, this would form defective sp^2 carbon impurities and increase the I_D/I_G. Again, this process appears to be complete after the 20 min anneal time, as no change is observed for the 40 min anneal time. The final treatment consists of performing a 20 min thermal anneal followed

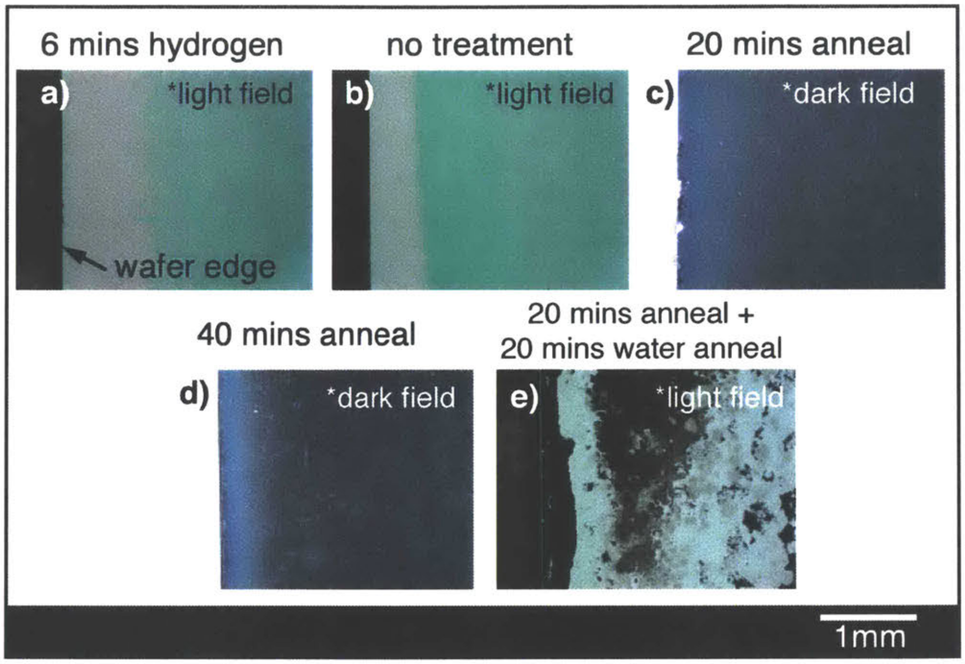

Figure 4-32: Optical microscope images of the wafer, post A-CNT removal, showing adhesion of the A-CNT roots to the wafer with temperature anneal treatments. This is observed as black A-CNT residue on the wafer (green when no A-CNTs are present).

by a 20 min anneal with water/helium. This treatment would first cement that A-CNT forest to the Si wafer (similarly to the 20 min thermal anneal described above with $F_a = \sim 12$ N), followed by the 20 min water treatment which reduces the final F_a by a statistically significant amount to ~ 12 N. This is a $\sim 40\%$ when compared to the 20 or 40 min anneal times. The optical microscope image of this wafer is presented in Figure 4-32, where reduced A-CNT residue is observed. The Raman spectra for the underside of this A-CNT forest present not change when compared to that of the 20 and 40 min thermal anneal times. This indicates that no structural change is occurring during the additional 20 min anneal with water. The exact mechanism for the reduced F_a is unknown and future work is required.

Given the necessity to remove the A-CNT forest from the wafer for the purpose of A-PNC manufacture, it is clear from the first part of the delamination study that utilization of a forest grown for longer than 40 mins will require additional force to remove the A-CNT forest from the wafer, with the likelihood of mechanical damage occurring in the

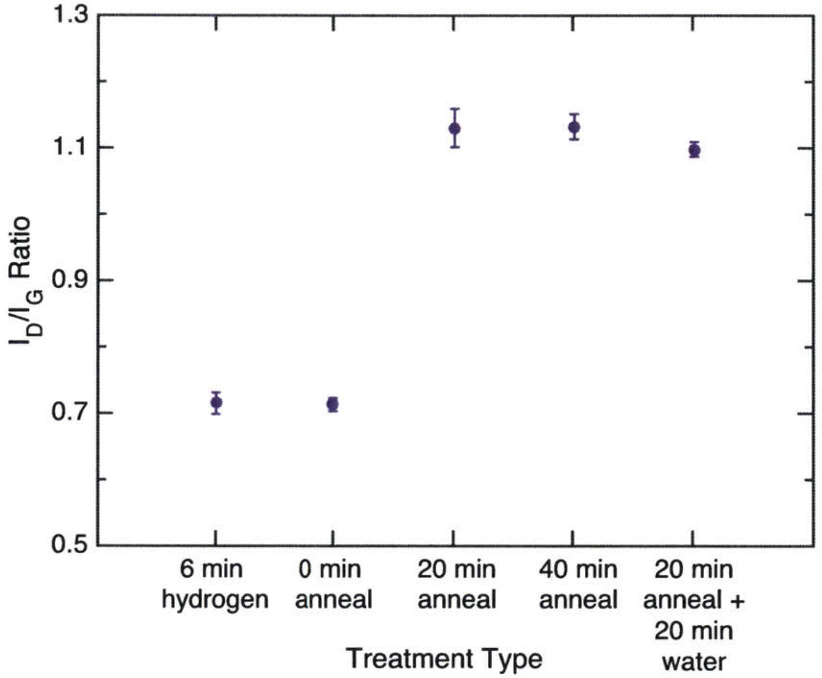

Figure 4-33: Raman data, captured under the A-CNT forest after delamination, for various post-growth treatments.

process. However, it is shown that forest height does not increase significantly beyond 50 mins, thus the full forest height range can be feasibly delaminated for A-PNC use. Part 2 (cementation) of this adhesion study is not required for this thesis, however future work in A-CNT functionalization for A-PNC manufacture will likely require A-CNTs to be attached to the wafer for post-growth treatments.

4.3 Densification of A-CNT Forests

A-CNTs in their as-grown state occupy $\sim$ 1 vf.% of the forest, on average. With such low volume fractions, mechanical, electrical or thermal enhancements the CNTs will be mitigated due to the low volume contribution. By selectively varying the CNT volume fraction, the contribution of the CNT properties to the composite can be tailored. As previously discussed, high loading of randomly orientated, well dispersed CNTs in polymers is typically challenging due to their tendency to agglomerate[157]. Therefore, to increase the CNT loading, post-

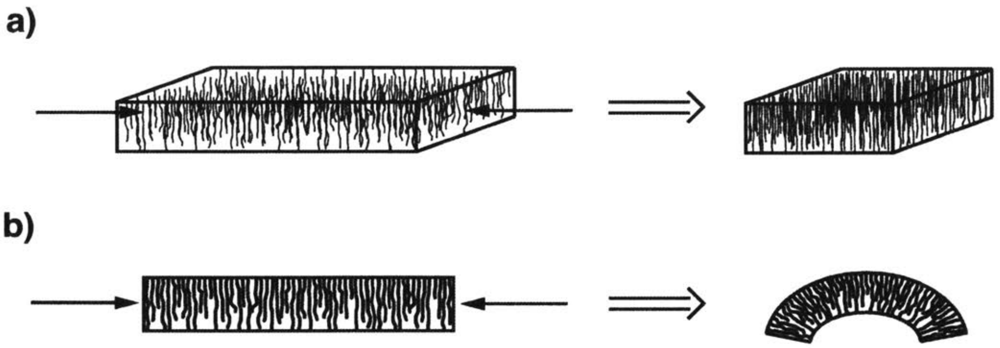

Figure 4-34: Illustration of densification of a 5 mm A-CNT forest showing a) the ideal case and b) observation. The buckling of the 5 mm forest occurs due to the carbon impurities and number density decay creating a stiffness gradient over the forest height.

processing techniques of CNT forests have been developed to align CNTs to take advantage of capillarity-induced wetting. One approach is through shearing, rolling or knocking-down the forest as is done by Lee et. al[99]. Additionally, these methods that utilize CNT alignment for polymer infiltration, lead to unique directional PNC architectures.

Changing the volume fraction of the forest (while maintaining CNT structural morphology) through the growth process alone is fundamentally limited by the standard CVD catalyst preparation methods[158]. Furthermore, changing catalyst parameters offers only small modification to forest density while oftentimes changing parameters such as CNT diameter and number of walls. Thus, alternate alignment-maintaining methods of densification are performed on as-grown forests. Numerous groups have developed densification techniques suitable to their applications in order to maximize the benefit of adding/utilizing A-CNTs. In this work, free standing forests are compressed using a mechanical densification instrument to desired volume fractions[75].

As discussed in Section 4.1, there is a non-negligible amount of carbonaceous impurities on the top of the ~ 5 mm, and number density decay occurs during the growth process: the result is an A-CNT forest that is stiffer at the top. During densification, the axial load applied to the 5 mm forest causes buckling and fragmentation. This concept is shown in Figure 4-34 where the ideal densification is compared to observations.

Experimental Procedure for A-CNT Densification

Both uniaxial and biaxial densification techniques can be employed based on sample requirements. In this work, biaxial densification is performed on 1.1-1.2 mm tall A-CNT forests with an initial area of 10 mm × 10 mm. Biaxial densification is performed up to $\sim$ 30 vf.% (final aerial dimensions of 1.8 mm × 1.8 mm). In uniaxial densification, 2 mm tall A-CNT forests are utilized, and up to $\sim$ 10 vf.% is achieved. 2 mm tall A-CNT forests also exhibit a marginal stiffness gradient across the height which leads to a plate-type buckling (similar to that shown in Figure 4-34b) condition during uniaxial densification to high volume fractions. This is managed by two approaches:

- "Sandwiching" two 1.2 mm forests root-side together such that a symmetric stiffness gradient is created about the midplane. A slight vertical pressure is applied to the 2.4 mm stack to create a final height of 2 mm. This is termed a butt-jointed forest.
- Restraining the forest through the thickness by compressing the 2 mm height to 1.4 mm during densification, disallowing motion in the out-of-plane direction.

The as-grown A-CNT forest is released from the substrate using a razor blade to gently apply a force on the side of the forest thereby detaching the forest. The released forest is placed in a small device that allows mechanical compression in two orthogonal directions in the biaxial densification case, and in one direction in the uniaxial case. After densification, the morphology the A-CNT forests are imaged to observe changes in morphology as a result of the densification process. SEM images are captured on surfaces that have been cleaved with a razor blade as the external edges are typically damaged by the device during the densification process.

1 mm Tall A-CNT Forest Biaxial Densification

Representative images of the densified 1 mm A-CNT forest are compared to an undensified A-CNT forest in Figure 4-35. Notice that the interstices between the A-CNT forest become smaller with increasing volume fraction to the point where in the 30 vf.% specimen, almost no space is seen between A-CNTs as they are densely packed[75,159]. Additionally, the A-CNT

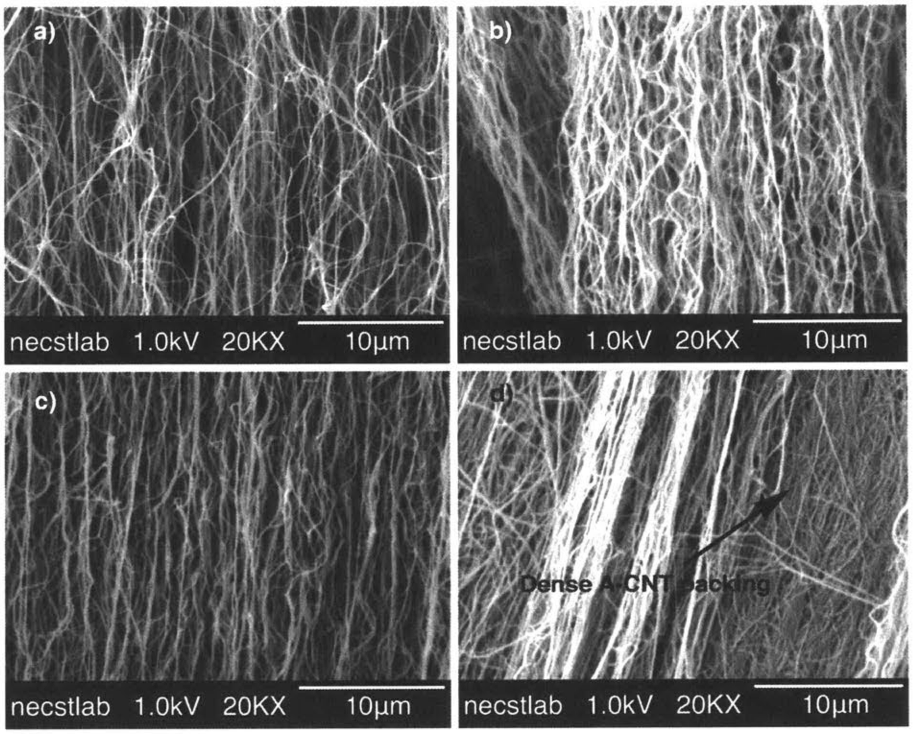

Figure 4-35: SEM images of biaxially densified 1 mm tall A-CNT forests of a) 1 vf.% (undensified), b) 5 vf.%, c) 10 vf.% and d) 30 vf.%. Images are captured at the middle of the A-CNT forest.

waviness decreases with increasing volume fraction[27,160]. SEM imaging is done on internal cut faces away from damage created by a razor.

2 mm Tall Vertically Restrained A-CNT Forest Uniaxial Densification

Restraining the single 1 mm tall forest in the vertical direction allows for uniaxial densification up to $\sim$ 8 vf.% without plate-type out-of-plane buckling. SEM imaging of the outside of the densified forest shows buckling of A-CNTs where a high spot "pillar" is observed on the top of the forest, see Figure 4-36. Internal observations of A-CNT buckling are difficult, as the razor causes damage to the A-CNTs, and cleavage is more challenging in the densified form. Additionally note that in some instances, increased waviness is observed as in Figure 4-36b. The buckled regions are typically limited to the top of the forest, likely due to the increased impurity build-up. At the bottom of the forest, shown in Figure 4-37, a $\sim$ 100 μm compressed zone results from the vertical restraints. This is a region where impurity accumulation is lower, especially at the roots where a $\sim$ 10 μm crushed zone is observed.

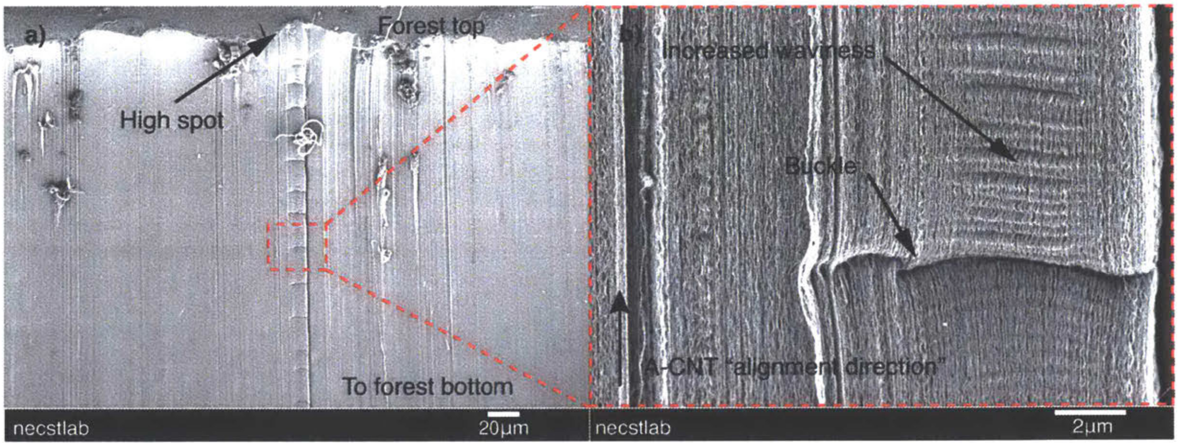

Figure 4-36: SEM imaging of the a) top of the 2 mm vertically restrained forest shows buckling of high spots with additional regions of b) increased waviness.

2 mm Tall Butt-jointed A-CNT Forest Uniaxial Densification

An optical microscope image of the external face of a 5 vf.% butt-jointed forest is shown in Figure 4-38. The interface between the two forests can be seen interpenetrating at the macroscopic level. However, as shown at the microscopic level in Figure 4-39a, a definite interface is observed. In a similar manner to the 2 mm tall vertically restrained A-CNT case, a compression zone and crushed zone develops at the bottom of each forest where A-CNTs are no longer aligned in the vertical direction and in some instances become horizontal. However, densification of higher volume fractions can be achieved using this method; up to 15 vf.% has been achieved uniaxially.

For all forests, a degree of vertical pressure is applied to the densification process. For the 1 mm forests this results from using $\sim$ 1.05-1.1 mm A-CNT forests, however no significant vertical morphological changes such as vertical buckling or compression zones are observed. The 1 mm forest has a less significant stiffness gradient over the height when compared with the 2 mm forest and thus plate-type buckling is easier to control with the slight vertical pressure. For a 2 mm single forest without vertical compression, buckling begins when

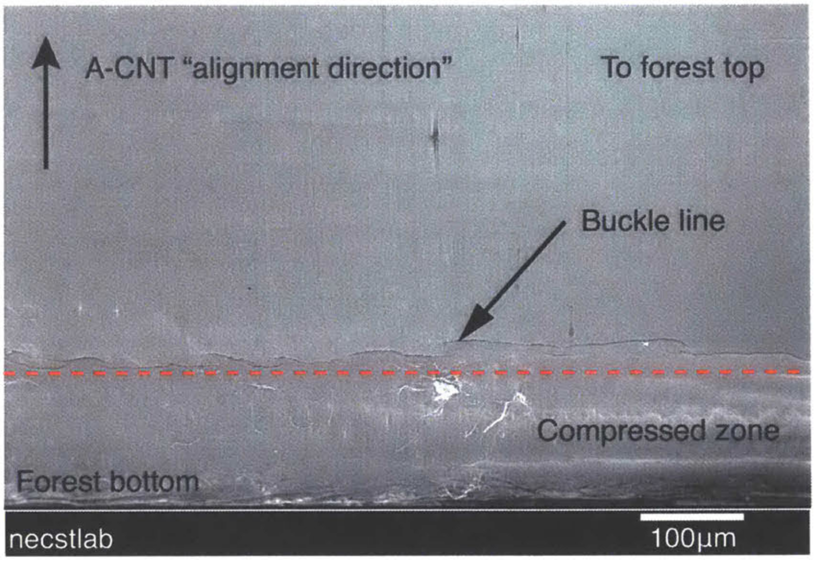

Figure 4-37: A $\sim$ 100 μm compression zone is noted at the bottom of an A-CNT forest that has been restrained in the vertical direction to reduce out-of-plane plate-type buckling. Additionally, crushing over $\sim$ 15 μm can be seen at the roots.

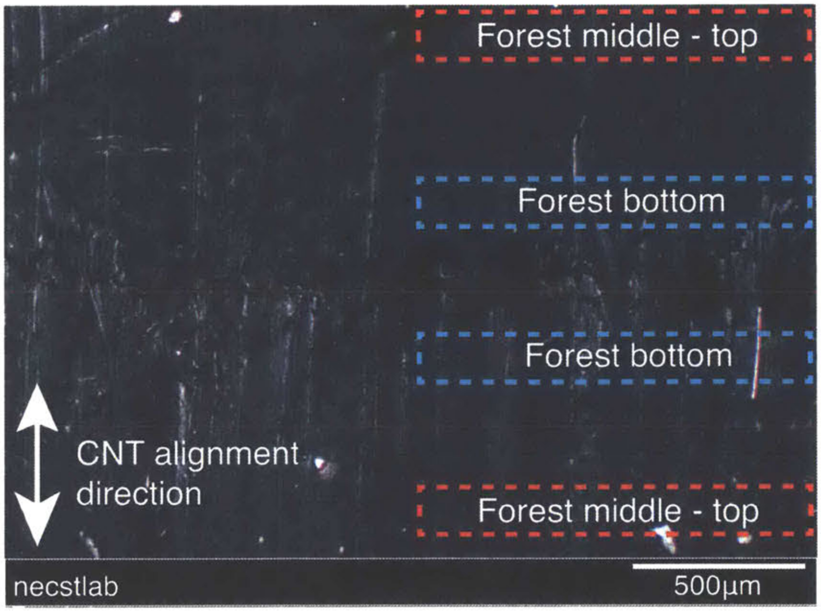

Figure 4-38: Optical microscope image of a butt-jointed A-CNT forest showing the jointed interface and orientation of the individual forests.

the length, L, exceeds 40 mm for densification down to 10 mm. This can be mitigated by further restraining the A-CNT forest in the vertical direction to prevent out-of-plane

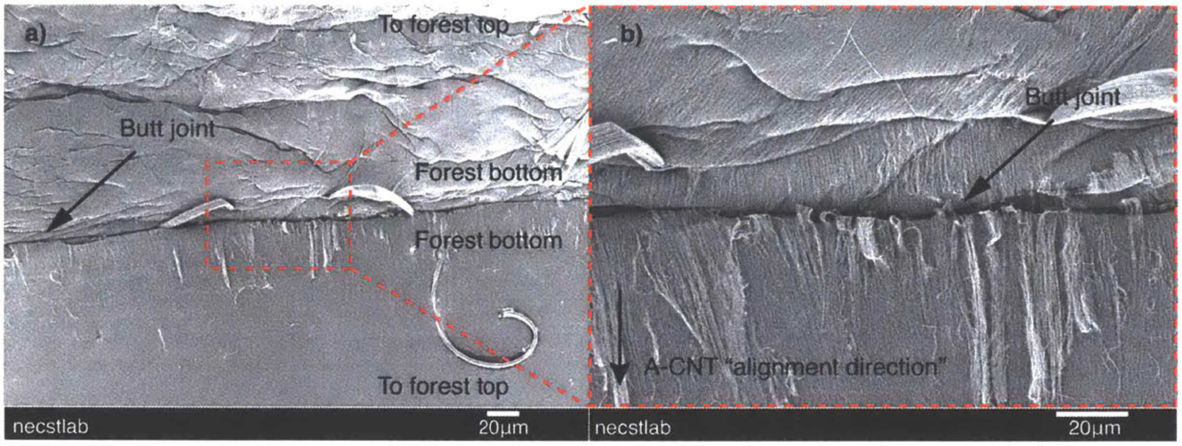

Figure 4-39: SEM images of the a) butt-jointed forest interface showing b) A-CNT forest crushing on the microscopic scale resulting in loss of vertical alignment.

buckling. Alternately, a symmetric sandwich can be created by aligning the forests together bottom-to-bottom/ root-to-root prior to densification. A vertical restraint is still required due to the marginal spatial gradient that occurs in the 2 mm forest due to carbonaceous deposits as well as individual A-CNT termination. A densification method can be selected based on sample manufacturing or volume fraction requirements.

4.4 Conclusions

The purpose of this chapter was to support the first step in the general approach to achieving the objectives of this thesis. The relationship between increasing growth time and A-CNT morphology was established, and it can be shown that increasing amounts of carbon impurities are deposited on the A-CNT forest with the thickest layer occurring at the forest crust, and decreasing towards the CNT root. The A-CNT forest height reaches a maximum at $\sim$ 5 mm at 50 mins beyond which carbon impurities continue to accumulate and result in CNT bulking at the top as well as cementation of the forest to the wafer. For A-CNT forest heights such that growth has not terminated, easy removal from the wafer is achievable without excessive force for the purpose of manufacturing A-PNCs.

The increased adhesion force, F_a of the A-CNT forest to the wafer for growth times beyond termination or due to a thermal anneal process, can likely be decreased as is shown in a preliminary post-treatment study where a water anneal is performed on a cemented forest. Future work is required to quantitatively describe this phenomenon and tailor the cementation/delamination response for a wide range of applications.

Finally, densification techniques for A-PNC volume fraction tailoring are detailed, but are limited to $\sim$ 1 mm and $\sim$ 2 mm A-CNT forests as the stiffness gradient occurring over the height of the $\sim$ 5 mm forest (due to carbon impurity deposits and number density decay) results in destructive buckling of the A-CNT forest. These densified forests can be utilized to increase the A-CNT loading in A-PNCs with the intention of increasing the crack bridging mechanism during Mode I fracture.

Chapter 5

Manufacturing of Aligned Polymer Nanocomposites

Approximately 80% of polymer matrices used in the aerospace industry are epoxies because their tailorability allows for a wide variety of properties and morphologies[67]. This chapter describes the two epoxies used in this work and details a manufacturing procedure for various volume fraction A-PNC specimens to be used for Mode I initiation fracture toughness testing. A polymer cure study is performed to reduce degree of cure variation in specimens and select an appropriate the cure cycle. Following finalization of the polymer cure cycle, details regarding A-CNT forest infiltration are provided, including methods to assess A-PNC void content and specimen validity for $K_{Ic,i}$ determination.

5.1 Polymer Matrices and Cure Cycle Selection

For this work, two epoxies are selected with different properties and applications:

1. Hexel HexFlow RTM6: an aerospace epoxy commonly used in resin transfer molding or vacuum infusion for structural applications. RTM6 has historically been utilized for fuzzy-fiber and previous PNC work.
2. Hexion EPON 862 with Epikure Cure Agent W (EPON 862/W): a structural polymer selected for low room temperature viscosity and long gelation time allowing for ease

of handling. EPON 862/W, an epoxy resin commonly utilized in molecular dynamics (MD) and many academic research studies, has been identified for complimentary work.

EPON 862 is a Diglycidyl Ether of Bisphenol F manufactured from epichlorohydrin and Bisphenol-F giving a low viscosity epoxy resin. Manufacturer specifications (excluding curing agent) are detailed in Table 5.1 and viscosity as a function of temperature is presented in Figure 5-1[161]. EPON 862 resin can be cured with Epikure Curing Agent W, diethyltoluene diamine. This combination cures at high temperature and has a fully cured T_g of ~ 150°C[162].

Table 5.1: EPON Resin 862 (excluding curing agent) specifications as provided by the manufacturer[161].

Property	Value	Units
Viscosity at 25°C	25 – 45	P
Weight per Epoxide	165 – 173	g/eq
Density at 25°C	1174	kg/m^3

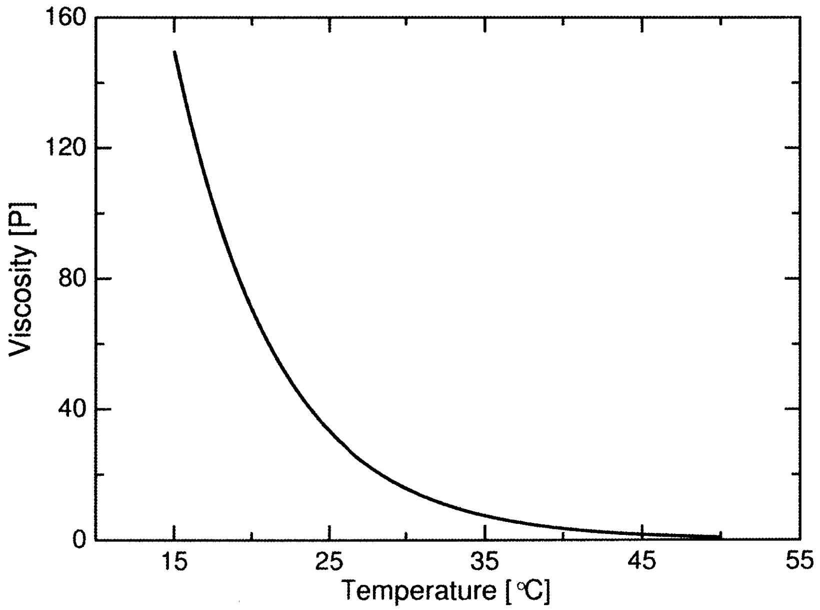

Figure 5-1: Viscosity of EPON 862 as a function of time during a temperature ramp at 1 hour at typical processing temperatures of 80 and 120°C (reproduced[161]).

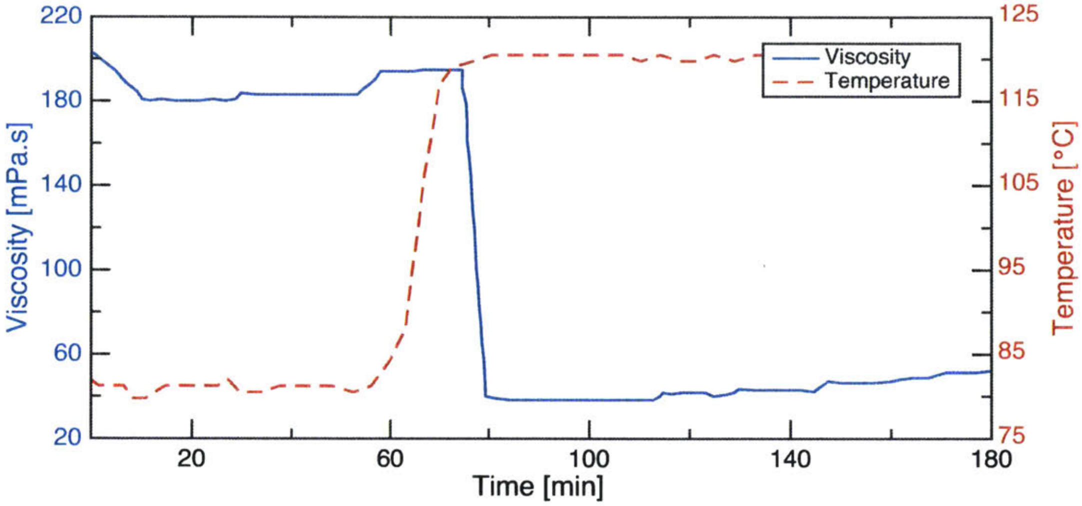

Figure 5-2: Viscosity of RTM6 as a function of time during a temperature ramp at 1 hour at typical processing temperatures (80 and 120°C) (reproduced[163]).

Table 5.2: Cure cycles used by O'Brien et al.[162] for manufacturing EPON 862/W specimens - numbers given are time in minutes spent at each temperature[162].

	Hold Temperatures (°C)								
Cycle	75	100	110	125	150	177	50	177	Degree of cure [%]
1	600	60	–	60	60	120	1	480	100
2	600	60	60	–	–	–	1	–	90
3	600	30	–	–	–	–	1	–	79

HexFlow RTM6 is an advanced two component (Part A: 100, Part B: 68.1 mix ratio by weight) engineering resin system that is used in the aerospace industry for resin transfer molding. Aerospace epoxies, often from a resin of tetraglycidyl 4,4'-diaminodiphenylmethane (TGDDM) with diaminodiphenylsulfone (DDS), are highly cross-linked and designed to operate at high temperatures[5]. Hexel recommends a cure cycle for RTM6 as 120 min at 180°C with no post-cure and dry DMA shows a fully cured T_g of ~ 200°C[163].

EPON 862/W Cure Study

RTM6 is supplied with a manufacturer prescribed cure cycle. For EPON 862/W, however, literature presents numerous combinations of times and temperatures for curing once the resin mixture is degassed appropriately:

- The manufacturer's recommended cure cycle is 1 hour at 121°C and 2.5 hours at 177°C as reported by O'Brien et. al[162].
- Theodore et al. suggest that the sample be cured at 121°C for 4 hours[164,165].
- Komuves et al. use a cure cycle that consists of 77°C for 2 hours and then an additional 2 hours at 177°C[166].
- O'Brien et al. provide a complicated cure cycle that was determined by trial and error and is shown in Table5.2.

A number of research studies suggest disparate cure cycles,[167–169] and this discrepancy will form the basis of this subsection as it is undesirable to have partially cured samples. Additionally, spatial variation within the sample should be avoided. The objective of the polymer cure study is to characterize the spatial trend associated with the degree of cure (DoC) throughout the resin specimens, and to determine a suitable cure cycle.

Experimental Procedure for Cure Study

In order to meet the objective of characterizing a spatial trend associated with DoC, several samples are prepared by a two-part mixing procedure using a manufacturer specified ratio of 100:26.4 EPON 862 to Epikure Curing Agent W by weight. After mixing and thoroughly degassing, the resin is then cast in a preheated mold and cured in a plate-heated oven at different combinations of time (t) and temperature (T).

The next step is to create a sample replicated 2^2 full factorial design with center points. Low, high and center point levels for time and temperature are selected based on literature[162,164–166] and are shown in Table 5.3. Thus, tested combinations are Low Temperature - Low Time, Low Temperature - High Time, High Temperature - Low Time and High Temperature - High Time with the center point at 149°C for 5 hours.

Coupons are then drilled from each sample at five different locations and analyzed using Differential Scanning Calorimetry (DSC) for an output of normalized heat flow. A representation of the five locations from which coupons were drawn is shown in Figure 5-3. Based

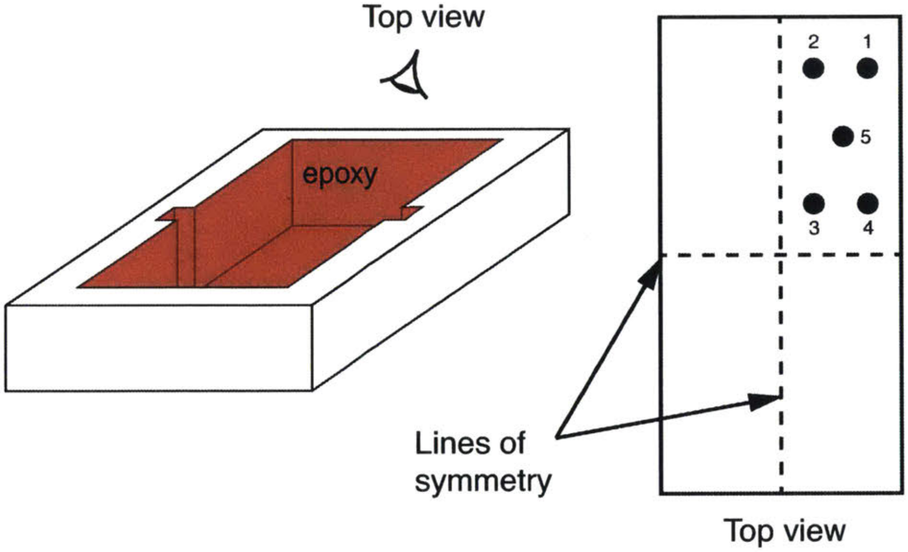

Figure 5-3: Drilling locations in each epoxy sample; top right quadrant is assumed to representative of the spatially symmetric sample.

Table 5.3: Low, high and center point values for time and temperature set points as single temperature cure cycles.

	Factor	Low Value	High Value	Center Point
t	Time (hours)	4	6	5
T	Temperature (°C)	121	177	149

on symmetry, an assumption is made that the top-right quadrant of each bulk sample is representative of the sample's top surface.

After performing a DSC run on the five individual coupons from each sample, a plot of normalized heat flow as a function of temperature is generated from the output. A representative plot of the low-temperature-low-time cycle cycle is shown in Figure 5-4. For each DSC run, the coupon is subjected to two heating/cooling cycles and a difference in heat flow is observed between first-pass and second-pass DSC temperature sweeps as a result of residual curing during the first-pass. Using Numerical Integration techniques, the area between curves (grey region in Figure 5-4) is integrated with respect to temperature to establish the difference in enthalpy. This measure is indicative of residual cure, whereby the net heat flow is inverse to the DoC. Thus, a sample with a high enthalpy between the first and second heating cycles has a lower DoC, and vice versa.

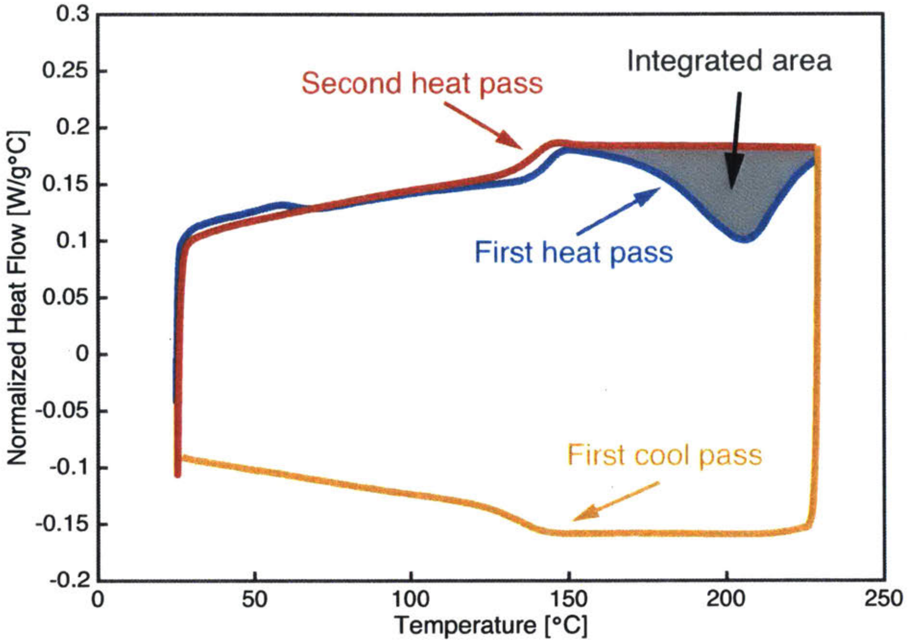

Figure 5-4: Differential scanning calorimetry (DSC) results for a representative low temperature low-time EPON 862/W polymer sample showing a heat-cool-heat-cool cycle at a rate of 5°C per minute. The difference between the first and second pass cycles, shown in grey, is indicative of the degree of cure. The higher the difference in enthalpy between the first and second pass, the lower the degree of cure.

Results and Discussion of EPON 862/W Cure Study

As detailed above, the experiments are designed to test for the influence on the difference in enthalpy between pass one and two of the DSC cycles of two factors: time and temperature. For an initial analysis with respect to time and temperature, a graph depicting the trend of enthalpy is generated (Figure 5-5). Each data point on the graph is an average of the measured values of ten coupons for each of the five primary conditions.

As expected, an increase in cure time results in a lower enthalpy difference between the first and second pass DSC traces. The higher temperature also results in a lower enthalpy at both levels of time. Figure 5-5 (summarized in Table 5.4) depicts a difference in the rate at which the enthalpy decreases as a function of temperature with time, suggesting there is likely an interaction between temperature and time with respect to enthalpy. The normalized heat flow decreases over twice as quickly at high temperature as at low temperature. The

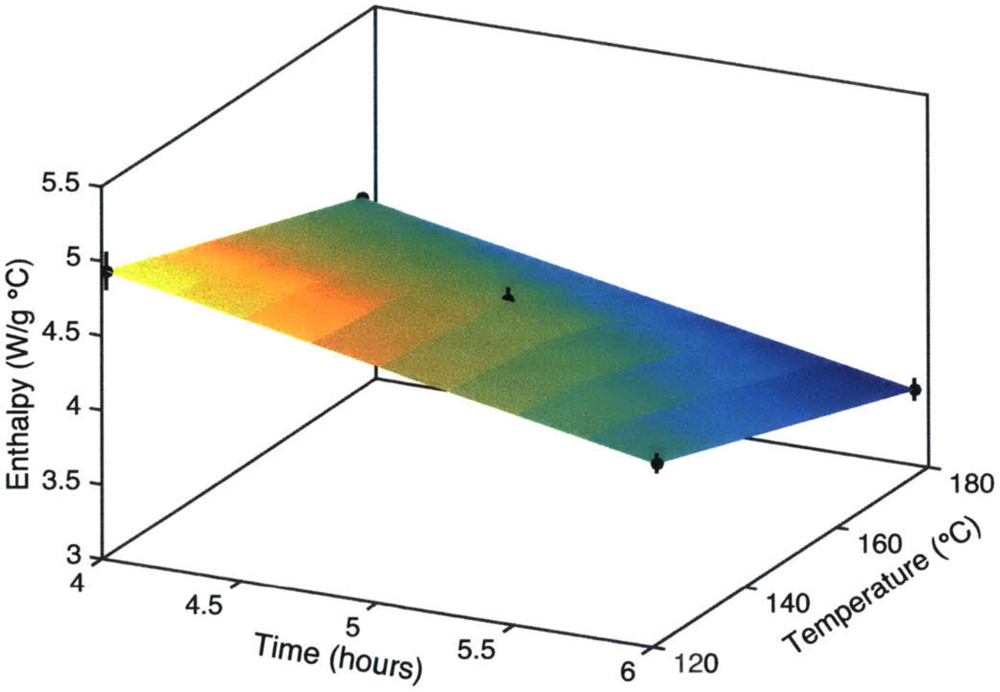

Figure 5-5: Response surface of EPON 862/W enthalpy at each combination from the 2^2 test with center points showing that both increased cure time and temperature result in a lower enthalpy difference between the first and second DSC passes.

Table 5.4: Normalized heat flow (in units of W/g°C) as a function of time (t) and temperature (T) for EPON 862/W. The high (t_H and T_H), center point (t_C and T_C) and low (t_L and T_L) of t and T can be found in Table 5.3. Minimizing normalized heat flow leads to maximized DoC.

	T_L	T_C	T_H
t_L	4.91 ± 0.12		4.28 ± 0.03
t_C		4.44 ± 0.08	
t_H	4.22 ± 0.07		3.58 ± 0.08

longer cured samples have lower enthalpy differences at each level of curing temperature and the enthalpy generally decreases as function of increasing temperature. However, unlike above with respect to time, the decrease of enthalpy at the shorter cure time decreases only minimally as function of increasing temperature; the enthalpy decreases almost three and a half times as much at the longer cure time as a function of temperature than at the shorter cure time. This difference also suggests there is an interaction between time and temperature with respect to enthalypy (Table 5.4).

Additionally, to reduce the error between test samples when performing mechanical testing, it is preferable to have samples with minimum spatial variation. While a minimum enthalpy is desired, it is equally important that samples have a minimum variation spatially for reproducibility and repeatability. Coupled with this, being able to manufacture samples from a large polymer block, provides a large set of data, however, if there is large curing variation in the sample, such a large sample would not be appropriate or if used, the conclusions would be clouded by the spatial variation in cure. By characterizing the spatial variation within the bulk sample, it enables being more 'selective' in the areas used for manufacturing test specimens, if necessary. Reducing the curing variation in the test specimens will reduce the error and allow for statistically significant conclusions about the inclusion of A-CNTs and the effect on the fracture toughness (or other properties) of the material PNC. Spatial uniformity is an issue throughout numerous manufacturing processes and being able to characterize the variation is key to determining the overall quality of the samples and drawing meaningful conclusions from experimentation.

Guo[170] presents a Multiple Response Surface (MRS) modeling technique originally aimed at the semiconductor industry and motivated by the 'within-a-batch' variation as it contributes significantly to total variation, but is generally very difficult to model. Guo claims that the MRS technique presents a number of advantages over a more general Single Response Surface (SRS) approach whereby it requires fewer data points, can rapidly adapt to process disturbances and the models are relatively immune to the presence of noise[170].

Following the methodology described in Guo and using the entire experimental data set, a first order response surface (enthalpy difference dependent on temperature and time) was fitted to each measurement site on the bulk sample. Based on the average and variance function, a coefficient of variation contour plot is generated and shown in Figure 5-6. With reference to Figure 5-6, it is clear that the SENB bulk sample will be of higher uniformity (i.e. lowest coefficient of variance) at high time (> 6 hrs) and moderate-high temperature (149°C) for the EPON studied here.

It is noted however, that the optimal point is at the boundary of the experimental range.

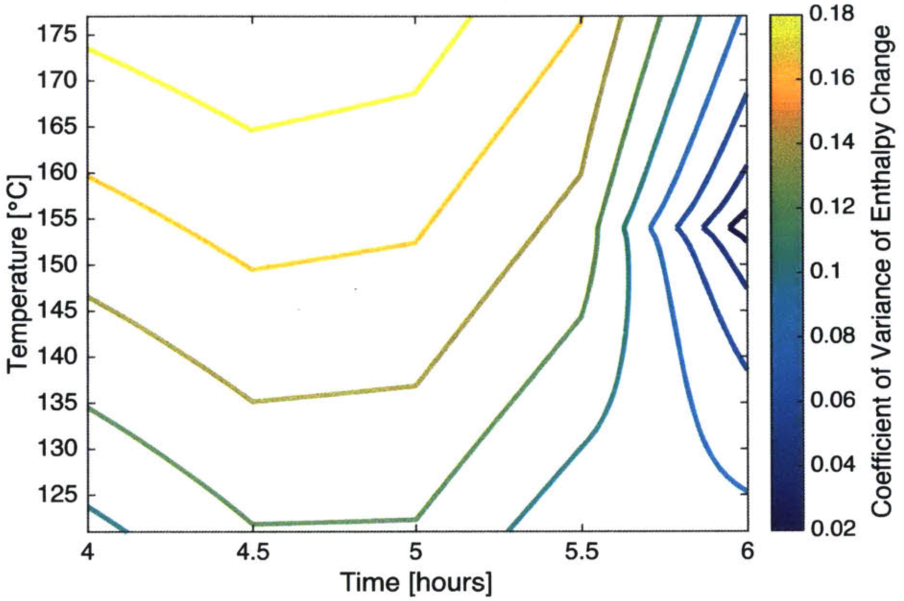

Figure 5-6: Coefficient of variance of enthalpy change for EPON 862/W contour plot shows high variation within the sample for low cure time with high temperature (yellow). Further reduction in spatial variation can be achieved by moving beyond a 6 hr cure at medium to high temperature.

However, as will be described in the following section, the manufacturing process is such that the PNC sample experiences two cure cycles in SENB sample preparation, hence undergoing a total of 12 hours at 149°C such that selective utilization of specific sample areas is unnecessary. Additionally, RTM6 cure cycle and resulting spatial variation is not studied as the manufacturer supplied cure cycle is consistently utilized in literature.

Using the viscosity profiles of the two epoxy systems, as well as the established/manufacturer supplied cure cycles, generic manufacturing methods are created for A-PNC as well as Mode I toughness specimens.

5.2 A-PNC Sample Manufacturing

This section presents the manufacturing methods developed for A-CNT forest infiltration with polymer to create A-PNCs, and detailing the incorporation of A-PNCs into full size specimens for fracture toughness testing.

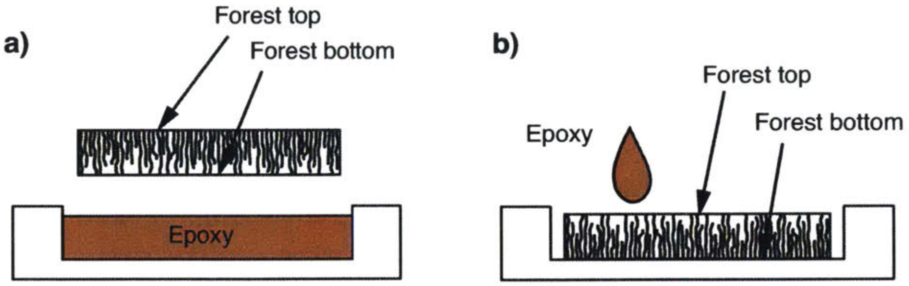

Figure 5-7: A-PNC polymer infiltration is done by either a) lowering the A-CNT forest roots-first into a pool of warmed epoxy, or b) placing the A-CNT forest crust side down in the mold and then carefully filling the mold with warmed epoxy.

Polymer Infiltration into A-CNT Forests

Thostenson[50] identified dispersion and CNT alignment to be some of the primary processing factors that influence mechanical properties of hybrid composites. One of the key challenges associated with the manufacture of polymer nanocomposites is CNT dispersion because CNTs tend to agglomerate, causing stress concentrations and preventing complete adherence to the matrix[50]. As previously discussed in Chapter 2, numerous methods have been utilized to achieve CNT dispersion with varying levels of success. Of the mechanical techniques, shear mixing and sonication are a popular choice by research groups, however efficacy deteriorates beyond ~ 3 % CNT volume fraction, and CNT alignment is not able to be well controlled[171].

1 vf.% and aligned CNTs are achieved during CVD growth, thus by infiltrating polymer into these forests, both alignment and dispersion can be maintained in the final A-PNC. Additionally, the morphology of the A-CNT forest, drives capillarity-assisted wetting[171]. Others have used dissolved polymer in solvents to wet the A-CNT forest, however, extensive contraction due to capillarity effects is observed[59,172–174]. This being said, the epoxies utilized in this work have relatively low-viscosity, either at room temperature for EPON 862/W or elevated temperatures (both RTM6 and EPON 862/W), such that solvent dissolution is not necessary. For RTM6 epoxy samples, polymer infiltration occurs at 90°C, and for EPON 862/W, at 70°C. The RTM6 epoxy is cured following the recommended procedure received from the manufacturer[163] for 1 hour at 180°C (half of the full cure cycle), while EPON 862/W is cured at 149°C for 6 hours.

Regardless of polymer type, one of the common ways to apply polymer matrices to CVD grown A-CNT forests is by pouring/dripping the solution onto the top of the CNTs. However, without removal of the upper crust, capillarity is limited leading to incomplete infiltration. The following two techniques (Figure 5-7) can be utilized as an alternative:

1. Heated liquid polymer is placed in the intended cure mold, creating a reservoir. The A-CNT forest is removed from the substrate (by the process of delamination) and lowered roots-first into the epoxy pool.
2. The A-CNT forest is delaminated from the substrate and placed crust-side-down in the mold such that the CNT roots are facing upwards. The heated liquid polymer is carefully poured onto the forest until the mold is filled.

This work employs both methods, depending on the forest morphology utilized. Method 1 is not suitable for densified forests as, during the infiltration process, the forest attempts to expand (to approximately its original dimensions). As a result of the mold restraining lateral motion, the forest expands and bends out of the mold. To prevent this, the forest is inserted into the mold and then capped with an aluminum mesh sheet, as shown in Figure 5-9. For this, method 2 is more suitable as the open forest bottom is exposed to the incoming polymer. Method 1 is suitable for as-grown forests with $\sim$ 1 vf%. The delaminated forest is gently placed on the epoxy pool and gradually becomes submerged into the polymer as infiltration occurs ($\sim$ 15 mins). With taller forests (i.e., $\sim$ 5 mm tall), in which individual A-CNTs have terminated growth, the inter CNT spacing is wider at the roots of the forest. During infiltration using method 1, capillary forces cause the forest to bend during infiltration. However, this is temporary and once infusion is complete, capillary forces cease and the forest relaxes as shown in Figure 5-8. CNTs preserve their alignment during polymer infiltration into the forest, however, for $\sim$ 1 vf% forests, a small overall decrease in area occurs (from capillary collapse) of the low density forest regions (most noticeable at the roots) into higher density regions leaving resin rich pockets. The local densification during capillary infusion of low density forests is discussed in Chapter 6.

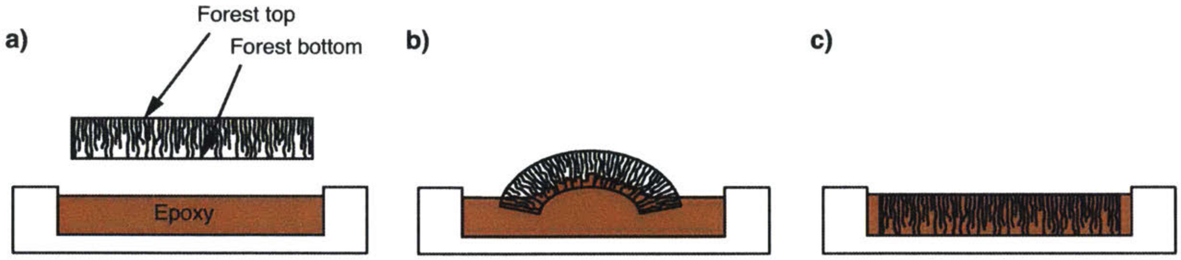

Figure 5-8: Illustration depicting how a tall A-CNT forest, a) when lowered roots-first into a pool of warmed epoxy, b) curls due to capillary action. When infiltration is complete, the forest c) relaxes into a flat configuration.

Test Specimen Manufacture

The manufacturing procedure for SENB and CT specimens (Figure 5-10) are shown in Figure 5-11 and Figure 5-12, respectively. Generically, the A-PNC specimen is roughened with 160-grit sandpaper and thoroughly washed with acetone and isoproponal. The A-PNC, with epoxy locating tabs, is inserted into a mold designed according to the specimen configuration required. Epoxy resin is added to surround the A-PNC and placed in a vacuum oven for degassing to remove trapped bubbles on the surface of the A-PNC. Degassing is performed at 90°C for RTM6 and 70°C for EPON 862/W and 300 mbar (absolute) pressure for 30 mins. The temperature is incrementally increased by 10°C every 15 mins to reduce viscosity, further assisting degassing. Additionally, a clean glass rod can be used to gently "sweep" bubbles from the surface of the A-PNC and mold walls. These bubbles then move to the epoxy free surface. Specimens are then cured: RTM6 is cured for 2 hours at 180°C and EPON 862/W is cured at 149°C for 6 hours. The cure time for the RTM6 is increased to 2 hours for this cure cycle due to the large volume of polymer used and the unidirectional application of heat in the plate-heated vacuum oven. Thus, the epoxy in the A-PNC effectively undergoes curing twice; A-PNC DSC thermographs for both EPON 862/W and RTM6 are supplied in Chapter 7.

The resulting slab is machined using an endmill to remove the locating tabs and ensure a cuboid is achieved prior to segmenting into individual samples. The difference in manufacturing procedure between the SENB and CT specimens diverges at the final machining stage of sample preparation.

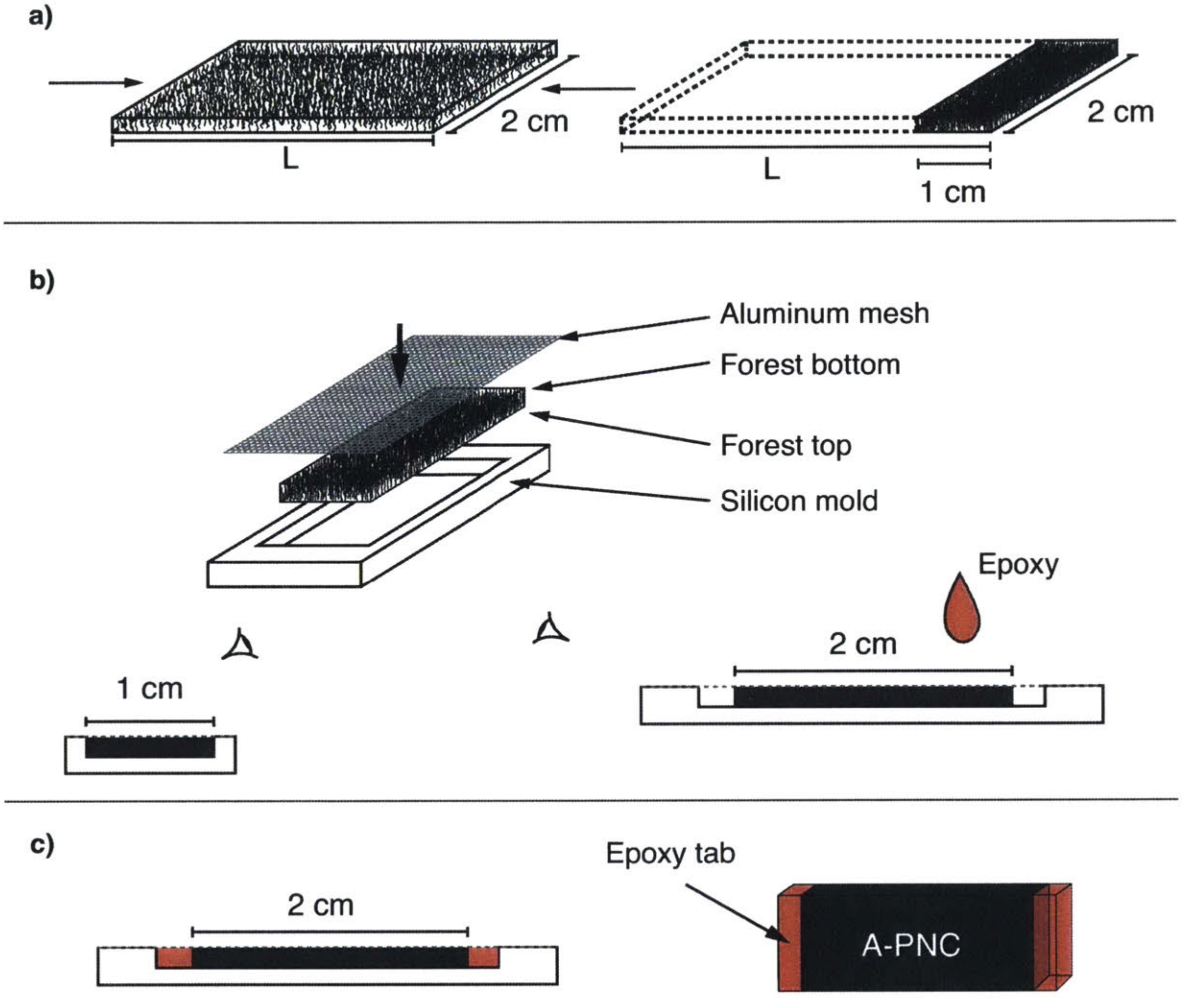

Figure 5-9: A-PNC manufacturing is done by a) densifying the A-CNT forest (uniaxial illustrated), and b) inserting it into a mold that restrains expansion in the densification direction. Depending on the densification amount, the mold can be capped with a metal mesh prior to curing. The result is a c) tabbed A-PNC specimen.

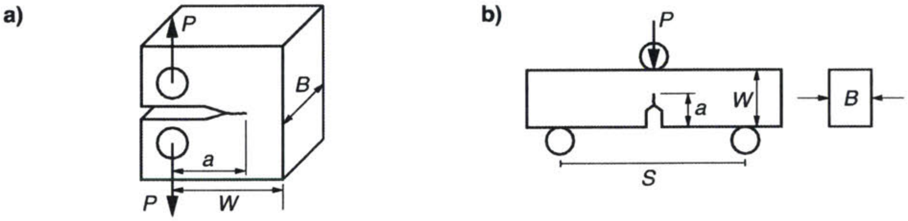

Figure 5-10: Specimen configurations from Chapter 2 reproduced for convenience. a) CT and b) SENB require an a/w ratio of between 0.3-0.5.

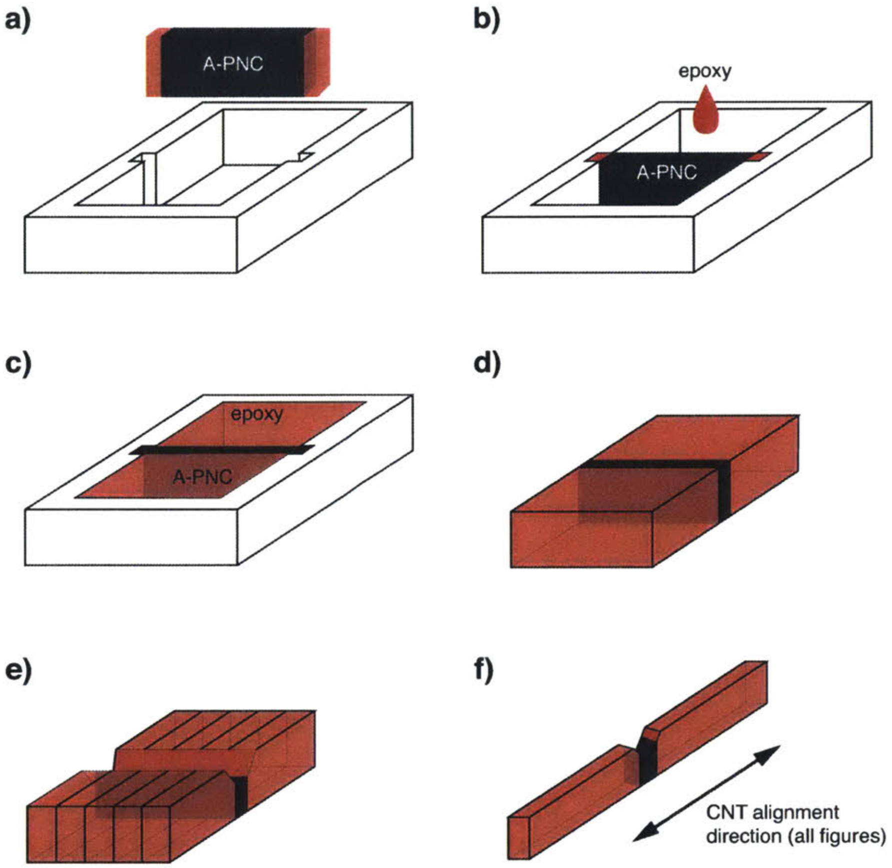

Figure 5-11: SENB specimens manufactured by a) inserting the A-PNC into a silicone mold, b) surrounding with epoxy and c) curing following established cure cycle. d) Initial machining is performed followed by e) v-notching using an end-mill at 45° and finally f) slicing using a diamond grit bandsaw.

For SENB specimens, the edge-notch is machined using a 6-fluted square-end endmill tilted at 45°: the result is illustrated in Figure 5-11e. The endmill is replaced every 20 samples to keep the notch tip sharp. Following notching, the bulk block is sliced (Figure 5-11f) using a diamond grit bandsaw blade with a material loss of 1 mm width kerf factored in for dimensional accuracy of the final specimens. Four or five specimens can be machined from the bulk block depending on the alignment accuracy of the A-CNT forest in the mold during A-PNC manufacture.

The final cuboid for the CT specimen is illustrated in Figure 5-12d. Holes are drilled using a diamond coated, 1/8 in diameter, spiral flute drill bit (purchased from McMaster-

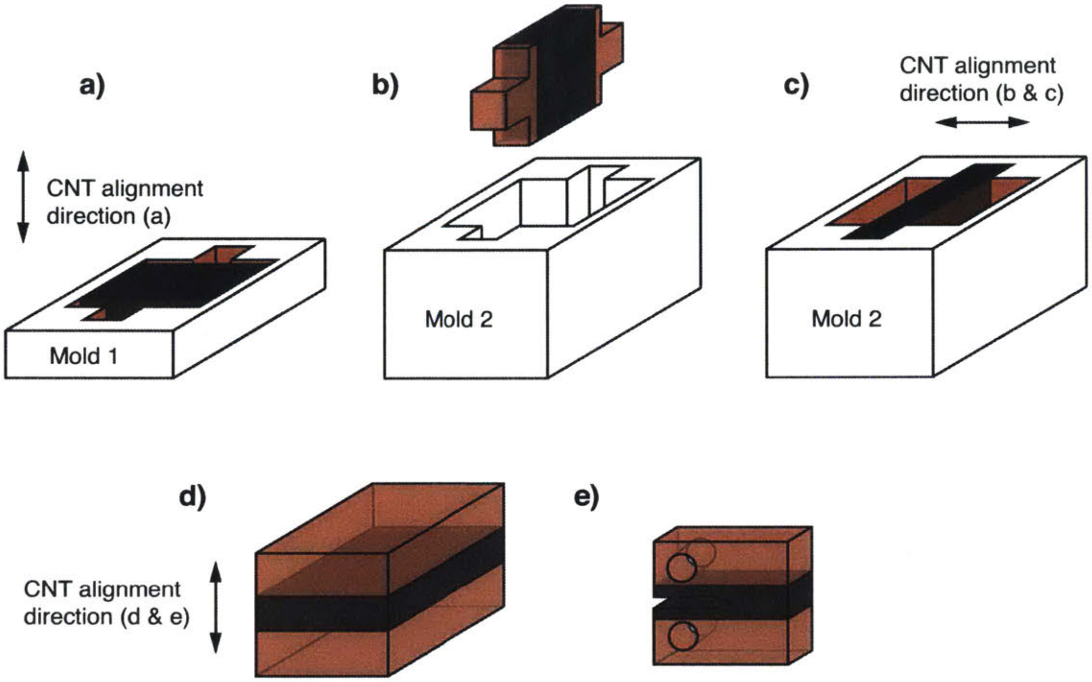

Figure 5-12: Compact tension specimens are created by manufacturing a) A-PNCs and b) inserting them into a larger mold to be c) surrounded by polymer and cured. A d) bulk block is obtained from which e) compact tension specimens can be machined.

Carr, product number: 3162A16) in the bulk material to ensure locational consistency of the tension bearing holes between samples. The notch is inserted using a diamond grit bandsaw blade moving at 2.5 ms^{-1} (Macro-Mark, product number: 8220m) prior to slicing the bulk block into individual specimens, Figure 5-12e.

Following ASTM D5045[84], the machined notch is to be sharpened by tapping or sliding a razor-blade in the existing notch tip such that a natural crack is initiated: the crack must be sufficiently sharp to ensure that a minimum value of toughness is obtained[84]. A natural crack, in the ideal case, will then only require energy to create the new fracture surfaces, thus no energy is contributed to crack initiation, and this is an intrinsic material property. However, a large number of samples were destroyed by tapping the razor-blade due to the brittle nature for the epoxy, and thus sliding of the razor blade is preferred. This, however, still results in sample loss. Owing to $\sim$ 50% of the samples being destroyed while trying to introduce a natural crack, the dependence of $K_{Ic,i}$ on the notch-root radius is examined to determine the necessity of sharpening.

5.3 Crack Radius Effect on Initiation Toughness

In metals, it is known that the notch root radius must be much smaller than the half-value of the critical crack-tip opening displacement in order to obtain an accurate value for $K_{Ic,i}$ and this is typically achieved by fatigue[175]. However, fracture in brittle materials, such as epoxy, is typically propagated catastrophically from cracks. A major challenge for reliability of $K_{Ic,i}$ determination, in brittle materials, is the introduction of a "natural crack." Specifically, practical problems include:

- Attempting to introduce a sharp natural crack is difficult to control, often leading to specimen fracture during crack sharpening due to unstable crack propagation, or alternately, a precrack geometry outside the tolerances required by the test standard, i.e., the value of a/w exceeds the 0.3-0.5 required range.
- When a natural precrack is achieved, determination of the precrack length is uncertain as it cannot be easily discerned on the fracture surface, or accurately measured using optical microscopy prior to testing. For future work, microcomputed tomography will be a helpful tool in assessing the precrack prior to testing.
- Different razor sharpening techniques lead to different $K_{Ic,i}$ values. Pressing, tapping or sawing are typical in creating a sharpened precrack. Pressing a new razor blade into a specimen has been found to produce a higher $K_{Ic,i}$ due to compressive residual stress at the crack tip, while razor-sawn precracks have lower fracture toughness values[175].
- Pure epoxy specimens cannot be easily precracked using fatigue because of unstable crack growth[175].

Given the difficulties with introducing a natural crack, a major factor leading to inaccurate $K_{Ic,i}$ determination (overestimation) is the dependence of notch-root radius[176]. According to Nishida et. al[176], there is no general consensus on what the lower limit for the notch-root radius should be for reliable $K_{Ic,i}$ in epoxies, as it is dependent on micro-structural morphology.

Procedure to Assess Notch Radius Contribution to Mode I Initiation Toughness in EPON 862/W

CT specimens are manufactured as described in Figure 5-12, and a notch was introduced at the center of the tensile surface using on of two methods:

- a diamond grit bandsaw blade with a slot width of ~ 1 mm.
- a 45° diamond endmill with tip radius of ~ 150 μm.

Specimens were cut 20 mm × 8 mm ($W \times B$) with a/w averaging 0.4 (ASTM D5045[84] requires 0.3-0.5 range). A sub-set of specimens were carefully and slowly sharpened by sliding a razor blade in the first notch. Thus the sample combinations for precracks are:

- a diamond grit bandsaw blade only.
- a diamond grit bandsaw blade with additional razor sharpening by sawing.
- a 45° diamond endmill only.
- a 45° diamond endmill with additional razor sharpening by sawing.

Figure 5-13 shows the representative notch geometries and the microscope measured tip diameters. Samples are tested according to ASTM D5045[84] using a Zwick mechanical tester with a cross-head speed of 1 mm/min. $K_{Ic,i}$ is calculated according to Equation 2.5 and 2.7.

Results, and Discussion of Notch Radius Effects on $K_{Ic,i}$

Figure 5-14 shows the dependence of $K_{Ic,i}$ on the root-notch geometry in compact tension specimens. The natural crack sample shown in Figure 5-13e has the lowest $K_{Ic,i}$ at ~ 1.25 MPa·m$^{1/2}$ and increases to ~ 1.35 MPa·m$^{1/2}$ for razor sharpened cracks that did not form a natural crack, irrespective of first notch method. Increasing the notch radius, by changing manufacturing technique, further increases $K_{Ic,i}$ to ~ 1.9 and ~ 3.9 MPa·m$^{1/2}$ from crack radii of 150 and 500 μm, respectively. These are obviously not true values since most brittle epoxies usually have $K_{Ic,i}$ values ~ 1 MPa·m$^{1/2}$[175]. No value with fatigue precracking was obtained owing to unsuccessful attempts in producing test specimens, and razor blade pressing was not performed.

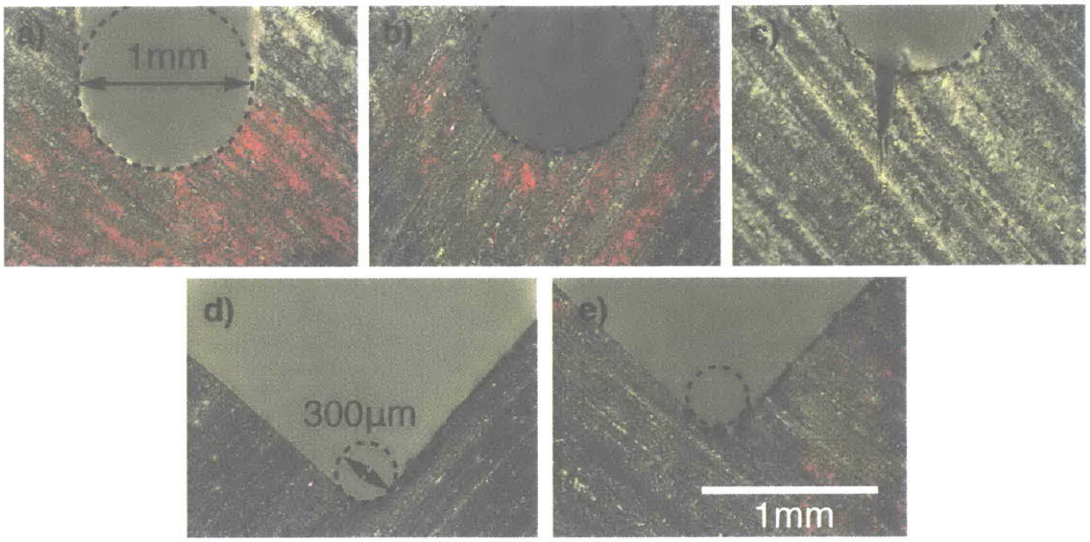

Figure 5-13: Crack starter manufacturing methods: a) using a diamond grit bandsaw blade only, b) razor sharpening a bandsaw blade notch by sawing, c) razor sharpening (sawing) a bandsaw notch to the extent that a natural crack initiates, d) machining a v-notch with an end-mill and e) crack sharpening an end-milled v-notch in EPON 862/W baseline samples.

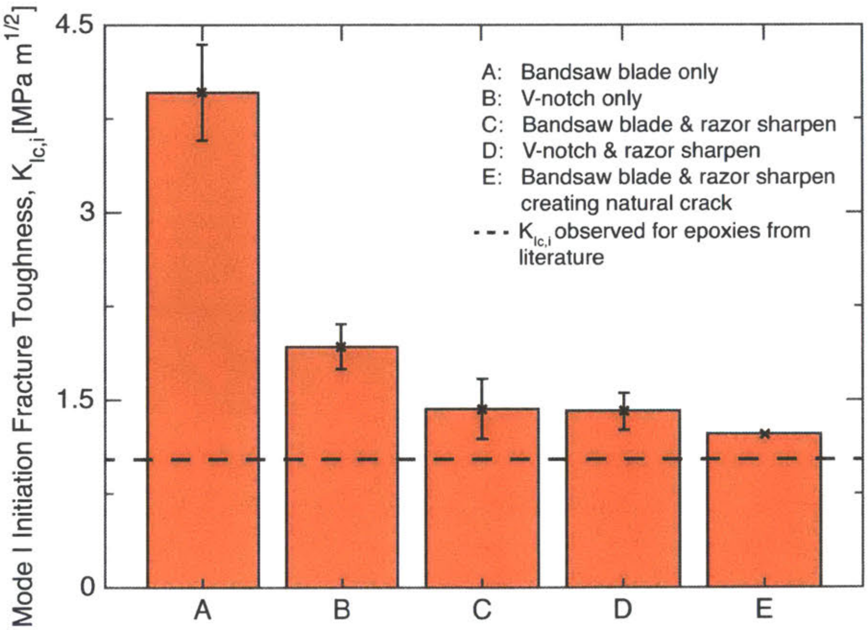

Figure 5-14: Results of various crack sharpening techniques show that a larger crack starter radius yields a larger $K_{Ic,i}$ initiation toughness for EPON 862/W samples. Note that only one specimen is achieved for case E.

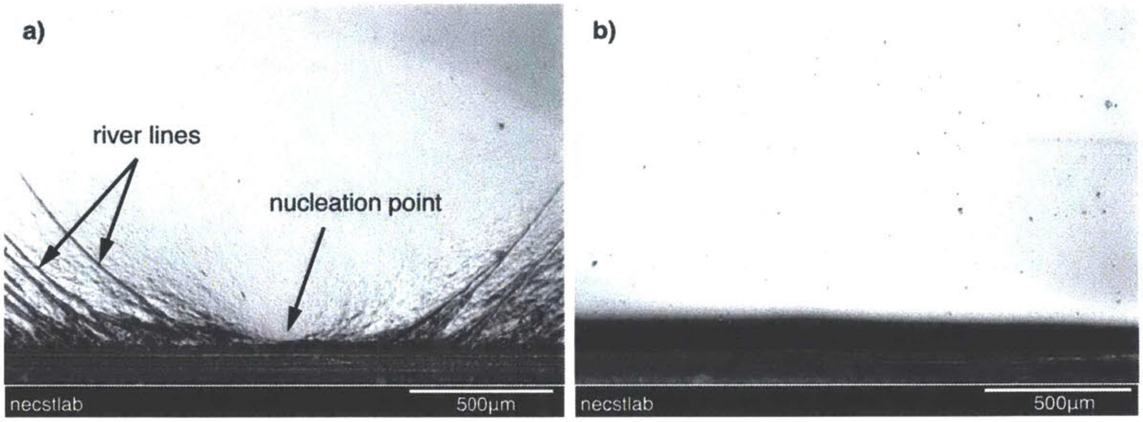

Figure 5-15: Optical microscope images of EPON 862/W pure epoxy fracture surfaces show that a) an endmill-only precrack produces a fracture surface with lines scattering from the precrack front, while on the contrary, b) a razor sharpened precrack is smooth and mirror-like.

The post-fracture surface of the pure epoxy specimens precracked with the endmill show river lines from the precrack front as shown in Figure 5-15. On the other-hand, the razor-sawing method produces the smooth fracture surface as expected from brittle fracture. This indicates that much more energy was dissipated during crack growth of the large notch-root radii specimens, consistent with an increased $K_{Ic,i}$.

From literature studied and results presented thus far in this thesis, the following manufacturing techniques and observations are adopted:

1. Razor blade sawing or tapping is the most appropriate method to produce the precrack.
2. There is a $\sim$ 5-10% overestimation of $K_{Ic,i}$ when a natural crack is not initiated during tapping.
3. Care must be taken to avoid pressing the razor-blade into the material as a large amount of plastic deformation and residual stress is introduced around the crack tip resulting in high $K_{Ic,i}$ values[175].

While variation in baseline $K_{Ic,i}$ specimens is due to crack sharpening difficulties, the varying response from A-PNC based fracture specimens beyond initiation, i.e., large variation in total fracture strain energy (see Figure 5-16 for illustration of energy calculation) is likely a function of the internal structure of the nanocomposite material, and voids are suspected.

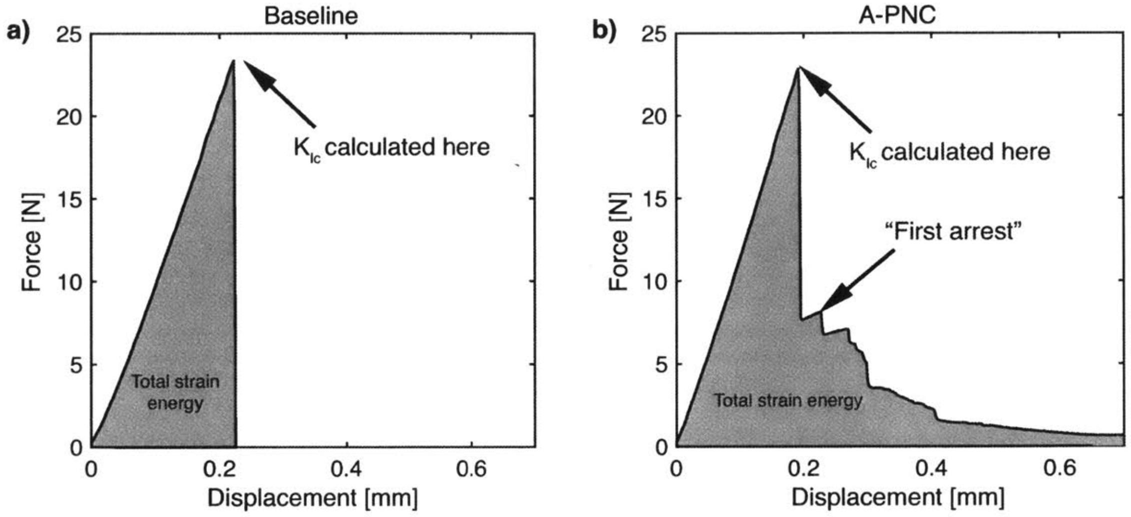

Figure 5-16: Calculation of total strain energy performed by integrating the area under the force-displacement curve of SENB specimens, with notional data. The a) baseline specimen has a total strain energy less than the total strain energy of the b) A-PNC specimen that exhibits tortuous crack growth and arrest. Note that $K_{Ic,i}$ initiation toughness is calculated at the same load point for both specimens.

5.4 Microcomputed Tomography Manufacturing Quality Control

X-ray microcomputed tomography (microCT or μCT) is frequently used for composites to characterize sample porosity, fiber breakage, fiber (or particle) distribution, fiber/matrix decohesion, matrix cracks, and the spatial scale of internal features such as fiber diameter, fiber distribution, bulk density etc[177]. The advantage of μCT is that it is nondestructive and a 3D image can be acquired of the (opaque) sample with microscopic resolution. Despite the advantages, μCT has not frequently been exploited for the description of void space in PNC fracture samples. The shape, size and distribution of voids can be used to assess efficacy of the manufacturing procedure[178]. Additionally, given the influence of voids on fracture behavior, this work employs μCT as a quality control tool for both sample and result validity post fracture.

Description of Test Setup

A Nikon Metrology (X-Tek) HMXST225 MicroCT system equipped with X-ray gun in reflection target mode (minimum 3 µm focal spot size) at Harvard University's Center for Nanoscale Science (CNS) is used in this work. For all these polymer-based samples, a molybdenum X-ray target is used. Unless otherwise noted, data are collected at 80 kV and 70μA. Specimens are mounted on the precision manipulator such that the volume of interest is maximized, i.e., the magnification and transverse translations are such that only the PNC region is captured. For μCT reconstruction, the reflection X-ray images are acquired from 200 rotation views over 180° of rotation (0.9° rotation step).

Results and Discussion of μCT A-PNC Characterization

Already fractured preliminary RTM6 A-PNC SENB specimens, manufactured according to Figure 5-11 with at 90°C infusion temperature and cured according to manufacturer specifications, are imaged to establish whether the observed crack tortuousity (see Figure 5-16b) is the result of crack deflection by the A-CNTs or identify the presence of another mechanism. Figure 5-17 reveals that no voids are detected in the 1 vf.% A-PNC specimen while large voids (darker regions) are present in the 11 vf.% uniaxially densified A-PNC specimen. The large voids are located within the A-CNT forest and the crack is seen to deflect towards the nearest void before passing through the void and continuing along the boundary of the A-PNC region of the SENB specimen. The intersection of the crack with the voids is likely the result of the tortuous crack path and the increased total strain energy observed in these specimens. Additionally, void content increases with increasing A-CNT volume fraction indicating that the decrease in inter-CNT spacing results in a decrease in polymer infiltration distance into the forest even with capillary assisted wetting. While only RTM6 is shown in Figure 5-17, similar results are seen for EPON 862/W epoxy that is degassed at room temperature for 6 hrs and then infiltrated into the forest at 70°C.

Based on the limited epoxy infiltration at the higher A-CNT volume fraction, two main avenues (or a combination of both) are explored:

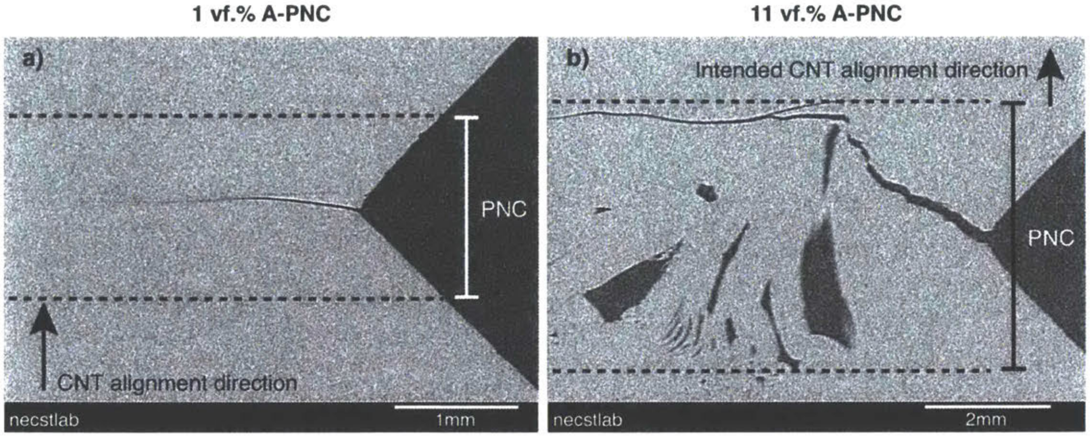

Figure 5-17: In preliminary RTM6 SENB specimens, a brittle crack response is seen in a) 1 vf.% A-PNCs with the absence of voids, however, in b) uniaxially densified 11 vf.% the crack tortuousity observed externally does not result from crack deflection by CNTs as a toughening mechanism, but rather due to the presence of voids.

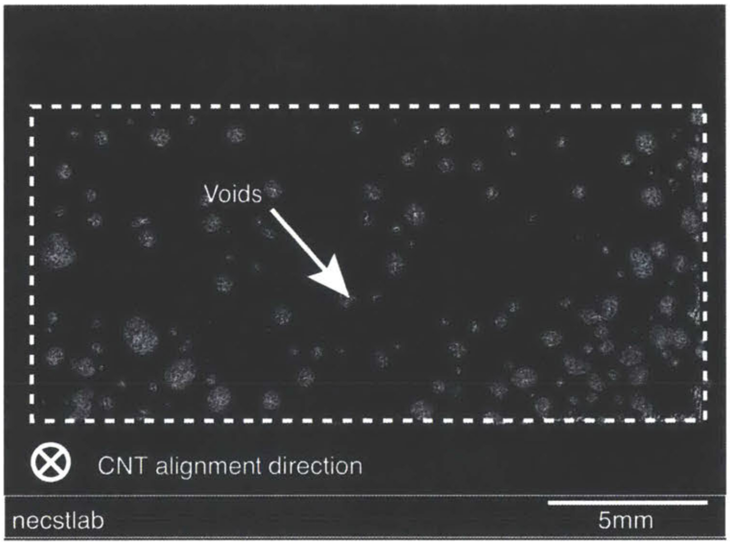

Figure 5-18: Large voids result in a 1 vf.% A-PNC as a result of degassing at 300 mbar during curing.

1. Decreasing polymer viscosity to promote capillarity driven wetting, and increase infiltration length.
2. Increase the vacuum during degassing to increase the pressure differential between trapped voids and the free surface of the epoxy, thereby increasing degas efficacy.

Viscosity modification in this work is limited to solvent dissolution[31] and temperature control, as mechanical property alterations can result with the use of viscosity modifiers. Vacuum adjustments must be performed such as to not go below the vapor pressure of the individual constituents present in the resin, resulting in evaporation (primarily solvents present in resin) causing bubbles. Figure 5-18 shows an example of a sample that was held under vacuum during cure where the vapor pressure was reached during gelation resulting in trapped bubbles.

Solvent Dilution Method

Acetone[179] (20 wt.%) is used to decrease the viscosity of mixed EPON 862/W prior to infusion into the forest. Two-forest butt-jointed samples are infused and degassed overnight at ambient to remove trapped bubbles and to evaporate solvent. An elevated temperature is not used as this accelerates the gelation time of the EPON 862/W. Following degassing, samples are cured at atmospheric pressure for 6 hrs at 149°C. The resulting A-PNCs with various A-CNT volume fractions (uniaxially densified) are assessed using μCT and results are seen in Figure 5-19.

While being completely surrounded by polymer, feather-like lenticular voids are observed in the A-CNT forests. At the butt-joint where the low number density regions of the forest occur, full infiltration occurs. The pocket is narrower at the top of the A-CNT forest where CNT diameter is larger and packing density is higher. Towards the bottom of the forest, the void is wider - this is where A-CNT packing density is lowest and higher interstitial spacing is recorded.

The void shape on the top view is a function of the degree of uniaxial densification. In the as-grown 1 vf.% A-CNT forest, voids have no directional-preferential shape. In the densified A-CNT forest, voids take on a directional-preferential shape where the long axis is perpendicular to the densification direction. The highest tested volume fraction 7 vf.% has finer voids than of the 5 or 1 vf.% uniaxially densified A-CNT forests. It must be noted that this solvent dilution study was performed using butt-jointed forests and EPON 862/W. The observed response may be strictly limited to this configuration as these tests were not repeated on single forests or using RTM6 resin. Given the increased void content present in

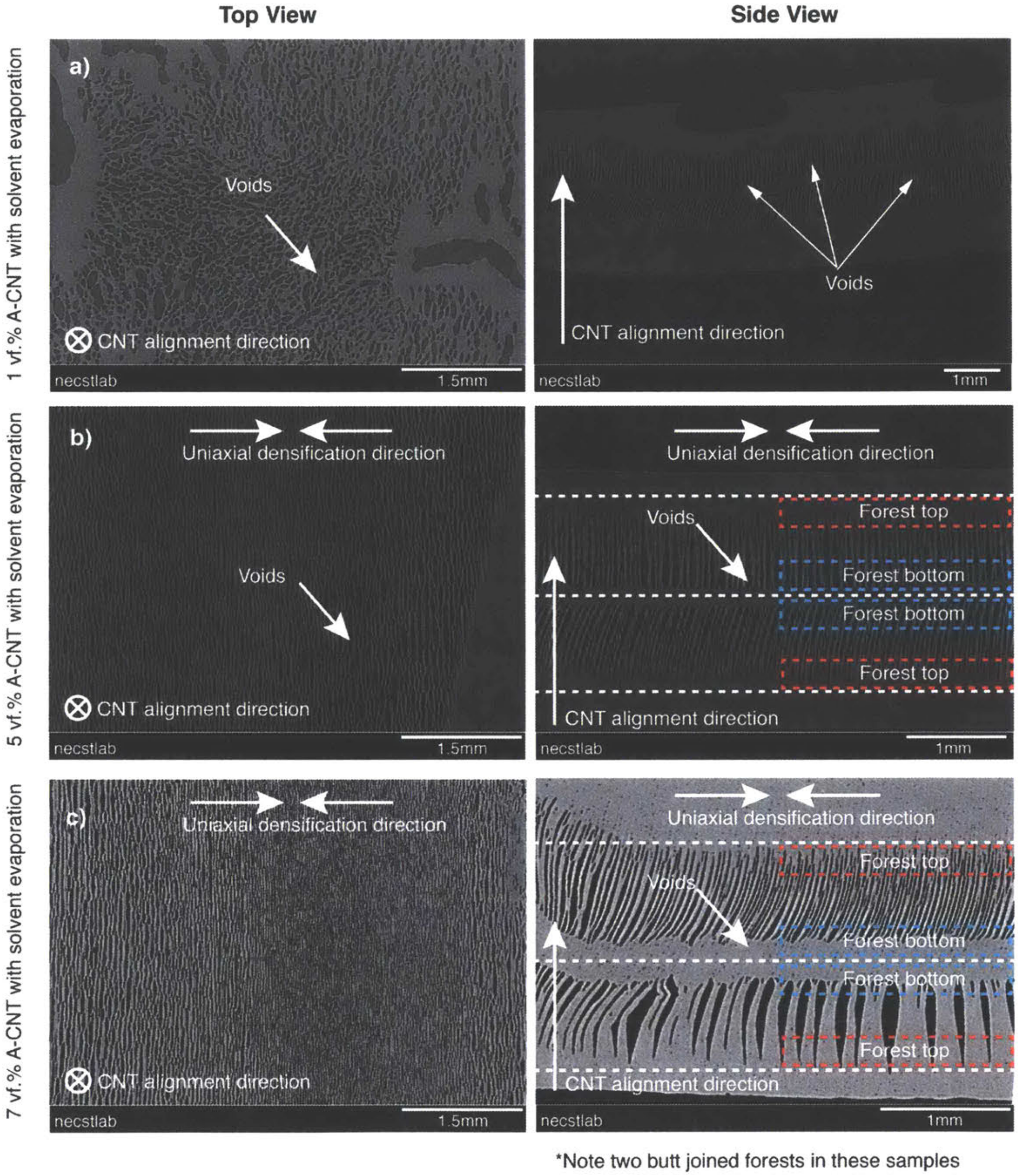

Figure 5-19: Solvent dilution of EPON 862/W in an attempt to reduce polymer viscosity produces striated void formation in butt-jointed samples. a) 1 vf.% A-PNC shows random void structure from the top view and feather-like voids from the side view. The b) 5 vf.% and c) 7 vf.% specimens show a similar feather-like void structure from the side however, the voids in the top view form corresponding to densification direction.

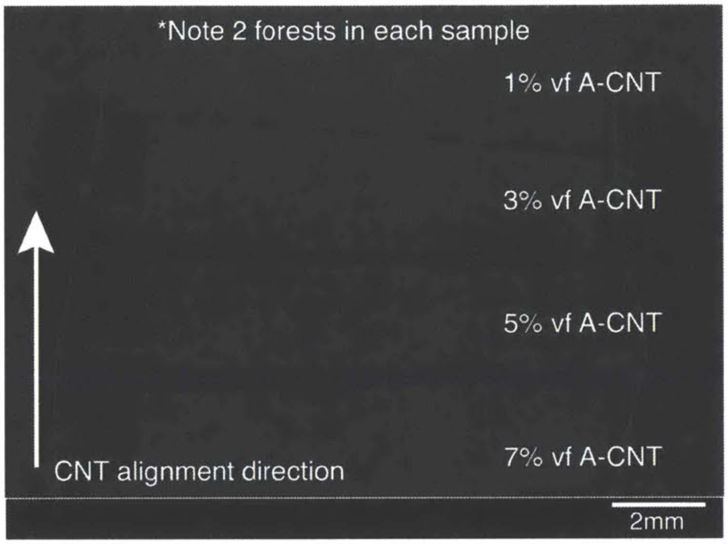

Figure 5-20: MicroCT image of EPON 862/W without degassing for a variety of volume fraction A-CNTs. Viscosity reduction by heating facilitates increased infiltration lengths, however voids are still seen in higher volume fraction specimens.

the A-CNT forests when using solvents for viscosity modification, the temperature-viscosity-void process-structure relationship is investigated next.

Infusion Results of Vacuum Degas Method

The EPON 862/W and RTM6 epoxy resin viscosity can be decreased thermally, shown in Figure 5-1 and Figure 5-2, respectively. An increase in temperature alone is insufficient to yield void-free samples as air is trapped in the A-CNT forest during infusion, this is shown in Figure 5-20 for EPON 862/W. Vacuum assisted heating is thus required to remove trapped air from the A-CNT forest, and the combination of temperature, pressure and hold times are varied such that increased infiltration is obtained.

The procedure was developed based on trial and error and the following key findings resulted in the current procedure:

1. Infusion of epoxy at room temperature cannot be achieved with RTM6, and local separation of the CNTs is exacerbated with room temperature EPON 862/W. Thus, infusion must be performed at moderate temperatures. The manufacturer suggested infusion temperature of 80°C for RTM6[163] is adjusted to 90°C to account for the

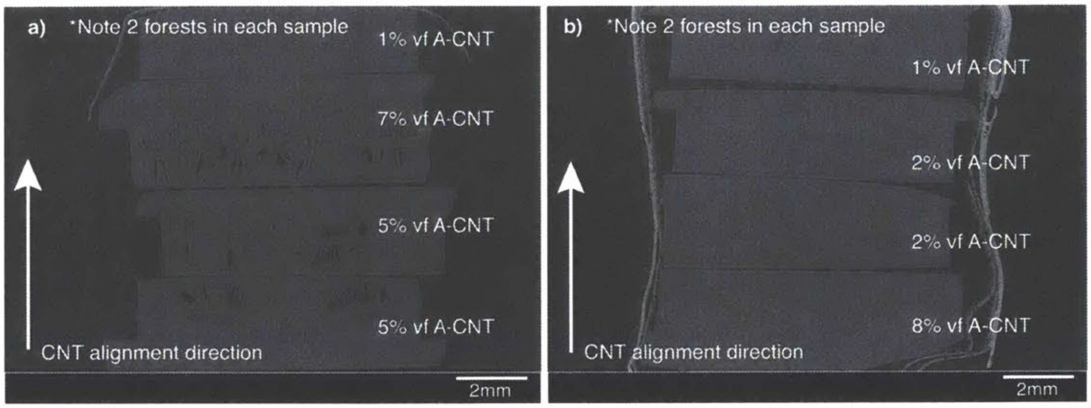

Figure 5-21: Comparison of a) RTM6 and b) EPON 862/W A-PNC butt-jointed samples after temperature, vacuum, and time variation. Due to the short gelation time of RTM6, voids still remain after degassing, whereas EPON 862/W appear void free at this resolution due to the extended gelation time allowing extensive degassing and infiltration.

mold not being heated to 120°C before adding the polymer as is suggested by the manufacturer[163]. EPON 862/W is infused at 70°C.

2. High temperature degassing results in a quick gelation time, running the risk of trapping expanded air bubbles within the forest. Thus degassing begins at infusion temperature.
3. Vacuum pressures below 300 mbar can be used, however this must be incrementally increased if temperature is increased to prevent solvent evaporation (and bubbles).

Degassing is performed after infusion for 30 mins at 300 mbar at the infusion temperature. The temperature is increased by 10°C every 15 mins to further reduce viscosity while vacuum is kept constant. RTM6 is only heated to 120°C and EPON 862/W only heated to 110°C before vacuum is returned to atmospheric pressure and the cure cycle initiated. Samples from this method yield void free specimens in RTM6 up to 5 vf.% and void free samples are achieved in EPON 862/W up to 7 vf.%; see Figure 5-21.

5.5 Conclusions

In conclusion, manufacturing procedures have been designed and developed for Mode I initiation fracture toughness testing of A-PNC samples. While RTM6 and EPON 862/W are selected polymers, the A-PNC manufacturing method is generic and is likely applicable for a wide range of moderate to low viscosity polymers. Infusion procedures can be adjusted to facilitate efficient infiltration through the use of X-ray microcomputed tomography to characterize the internal geometry in the A-PNC specimens. This can be used to assess the efficacy of the manufacturing processes employed for high quality void-free specimens.

Chapter 6

Mode I Fracture Toughness of Aligned Carbon Nanotube Epoxy Polymer Nanocomposites

Thermoset polymers such as epoxies have been widely used for engineering components, and particularly as a matrix for fiber-reinforced composites due to superior mechanical properties when compared to thermoplastic polymers. However, since they are usually brittle and vulnerable to rapid crack propagation, tougheners including filler materials such as CNTs are added to increase fracture toughness. With reference to Figure 2-4, for cracks to be arrested, the resistance to crack growth needs to develop such that it supersedes the strain energy release rate caused by the applied load, σ, at initiation. Contributions to increased crack resistance can come from the CNTs. As discussed in Chapter 2, (nano)fibers can increase toughness by two main mechanisms, namely: (nano)fiber debonding with associated toughness, G_d, and pull-out, contributing G_p. These parameters are only activated when the crack begins propagating and the toughening contribution is calculated by[77,180]:

$$dG_{CNT} = \frac{da}{a}(G_d + G_p) = \frac{da}{a}\left(\frac{v_f l G_{int}}{r} + \frac{v_f l^2 \tau_f}{3r}\right) \tag{6.1}$$

Where r is the fiber radius, G_{int} is the interface toughness, τ_f is the shear stress due to friction during pull-out, da is the change in crack length, a is the total crack extension from the initiation point, and l, the CNT pull-out length, becomes a function of where the (nano)fiber is within the crack tip, as defined in Figure 6-1. The instantaneous pull-out length l_{inst} can be found through[77,180]:

$$l_{inst} = 2a\tan\left(\frac{\phi}{2}\right) \tag{6.2}$$

Where ϕ is the crack tip opening angle. At the crack tip, the pull-out length is zero, and as the crack front propagates, pull-out increases incrementally in the crack wake until a critical point l_c is reached where the (nano)fiber breaks, or fully pulls out, and no longer contributes to toughening.

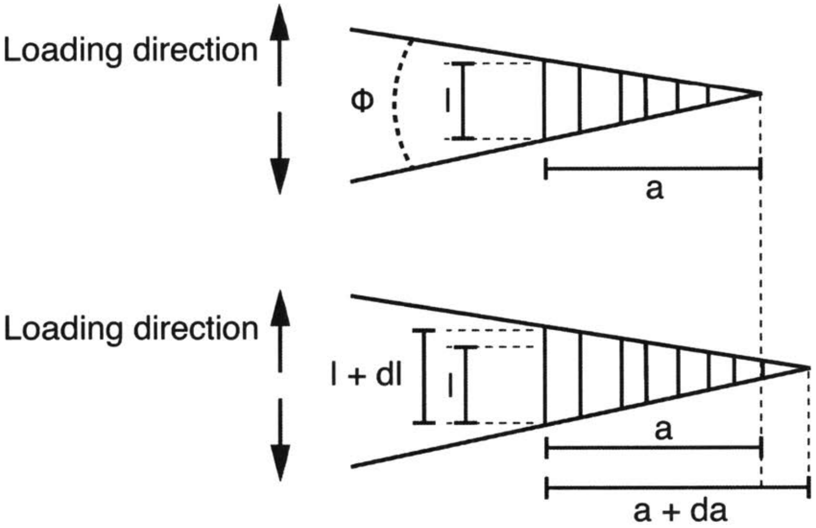

Figure 6-1: Illustration defining nomenclature utilized for debonding and pull-out toughening contribution from A-CNTs.

The total strain energy contribution from CNTs can be found by integrating Equation 6.1, and determined by:

$$\Delta G_{CNT} = 2\tan\left(\frac{\phi}{2}\right)\frac{v_f}{r}\left(G_{int}\cdot a + 2\tan\left(\frac{\phi}{2}\right)\frac{\tau_f a^2}{6}\right) \tag{6.3}$$

This ΔG_{CNT} gets added to the flat R-curve expected from the brittle matrix to provide an R-curve for the PNC system, denoted here as R_{PNC}. See Figure 2-4 for different situations of lack of crack arrest and unstable crack growth. For crack arrest events, the crack propagation path can be easily observed and the R_{PNC}-curve can be determined. In the unstable case, if the crack propagation can be captured, the R_{PNC}-curve can likewise be determined. If the progression of the crack front cannot be captured, the R_{PNC}-curve and steady state G_{ss} cannot be determined. However, the initiation toughness can still be established in unstable crack propagation, but is not expected to increase unless the A-CNTs contribute significantly to strength, as initiation toughness is oftentimes associated with strength rather than toughness, as a natural crack has not yet formed.

In this chapter, Mode I fracture toughness testing of RTM6 and EPON 862/W thermoset epoxies reinforced with as-grown A-CNT forests is presented. Typically, for steady state toughness testing at the laminate level, DCB test configurations are utilized. Attempts made to manufacture DCB A-PNC samples were met with challenges, namely: introducing a sharp crack into the specimen is difficult, or cracks immediately jumped to the interface between the bending arms and the A-PNC. Additionally, DCB tests are limited to 1 vf.% samples due to required specimen dimensions, unless A-CNT forests are tiled together to create a complete specimen, however, a joint is present where cracks are likely to jump to the interface. For these reasons, SENB and CT configurations are utilized.

6.1 Mode I Fracture Toughness Experimental Procedure

Mode I fracture toughness is conducted using CT and SENB specimens, the preparation of which was detailed in Chapter 5. Baseline (control epoxy) specimens are similarly produced using the same two step cure procedure, with the middle section of the specimens being twice cured. Prior to testing, the notch tip is imaged using an optical microscope to ensure a sharp crack tip is present, and the crack ligament (w less a, see Figure 2-5) is measured. Due to the developmental nature of the test procedure, only some individual specimens are scanned using μCT prior to testing, allowing observation of the crack tip and internal specimen geometry. However, post-test μCT scans of the specimens are performed to assess validity of the obtained results; when voids are suspected, the μCT procedure was detailed in Chapter 5. Additionally, in order to investigate any toughening mechanisms present, the fracture surfaces are imaged using SEM after testing.

Specimens are tested at room temperature using a screw-driven Zwick mechanical tester using a 10 kN load cell and constant displacement rate of 10 mm/min to prevent viscoelastic behavior, as suggested by ASTM D5045[84]. The initial crack length is measured by optical microscopy prior to testing and verified after fracture by taking measurements from the specimen fracture surfaces. SENB specimens are tested in a three-point-bend rig that has a 3 mm diameter loading nose and stationary roller configuration. CT tests are performed using a clevis designed according to ASTM D5045[84]. Digital image correlation (DIC) equipment (a PointGrey GRAS-50S5M-C camera sensor with a Tamron SP 180 mm F3.5 Di 1:1 macro lens is used, with images acquired using the Correlated Solution's Vic-Snap software[111]) is used to capture crack growth with an image captured every 1 ms, the fastest achievable rate with the current setup. Specimens are spray-painted white to provide contrast between the A-PNC region and the propagating crack.

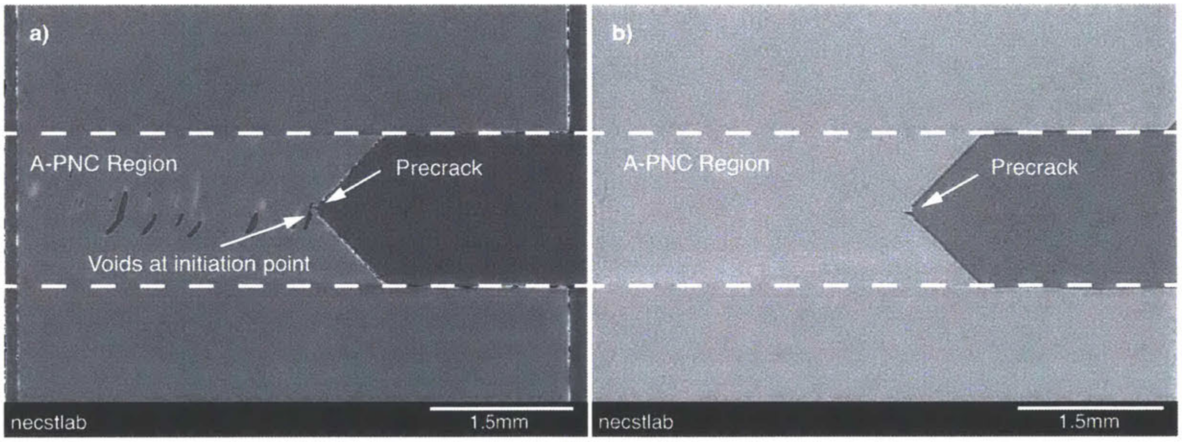

Figure 6-2: Representative μCT images illustrating the benefit of evaluating specimens prior to fracture testing. In an example of a) a poor quality 5 vf.% EPON 862/W specimen, voids are observed through-out the A-PNC region as well as intersecting the precrack, that can result in increased Mode I initiation toughness; a b) superior quality specimen contains no voids near the precrack or within the sample (2 vf.% EPON 862/W).

Sample validation is done using μCT, where examples can be seen in Figure 6-2. Samples where the crack tip intersects a void, Figure 6-2a, at the point of initiation were excluded from the data as crack tip blunting by the void causes increased initiation toughness values, as shown in Chapter 5 where notch radius affects $K_{Ic,i}$.

6.2 A-PNC Results and Discussion

Baseline epoxy and A-PNC fracture testing results are discussed, starting with A-CNT morphology and other features identified in the A-PNC specimens.

6.2.1 Effect of A-CNT Morphology on Crack Propagation

Preliminary CT specimens were manufactured using $\sim$ 5 mm tall A-CNT forests. Forests used for this were as-grown and undensified, thus specimens with low void content were achieved. While A-PNC specimens failed in a brittle manner with no increase in the Mode I initiation critical stress intensity factor, $K_{Ic,i}$ (related to the Mode I strain energy release rate at initiation, $G_{Ic,i}$, through Equation 2.4), over their baseline counterparts, the A-CNTs do affect crack propagation. In baseline specimens, the crack propagates straight across the specimen (perpendicular to the back face). In A-PNC specimens, the crack propagates towards the bottom of the forest as can be seen in Figure 6-3. This is observed in all A-PNC specimens and is due to the spatially-varying nature of the A-CNT forest where the PNC region created towards the roots of the A-CNT forest likely has a sufficiently lower resistance to crack propagation, relative to that of the A-PNC mid-region where cracks initiates, due to lower CNT number density.

The mechanism for this is likely due to a combination of increased effective modulus towards the top of the A-CNT forest and/or different interfacial interaction between the polymer and the CNTs over the height of the forest due to spatial gradations such as the turbostatic graphitic layer that is more pronounced at the top of the forest. It is unclear as to whether the cracks deflect transversely up the A-CNTs for a distance before fracturing through the matrix in a step-wise manner, or whether it deflects while moving through the matrix before intersection a CNT. Additionally, this phenomenon of crack deflection to the bottom of the forest A-PNC region was observed in every compact tension specimen manufactured with $\sim$ 5 mm tall A-CNT forest regardless of orientation within the test fixture, thereby eliminating suspicion of test artifacts.

A combination of this phenomenon, as well as the difficulty in $\sim$ 5 mm tall A-CNT

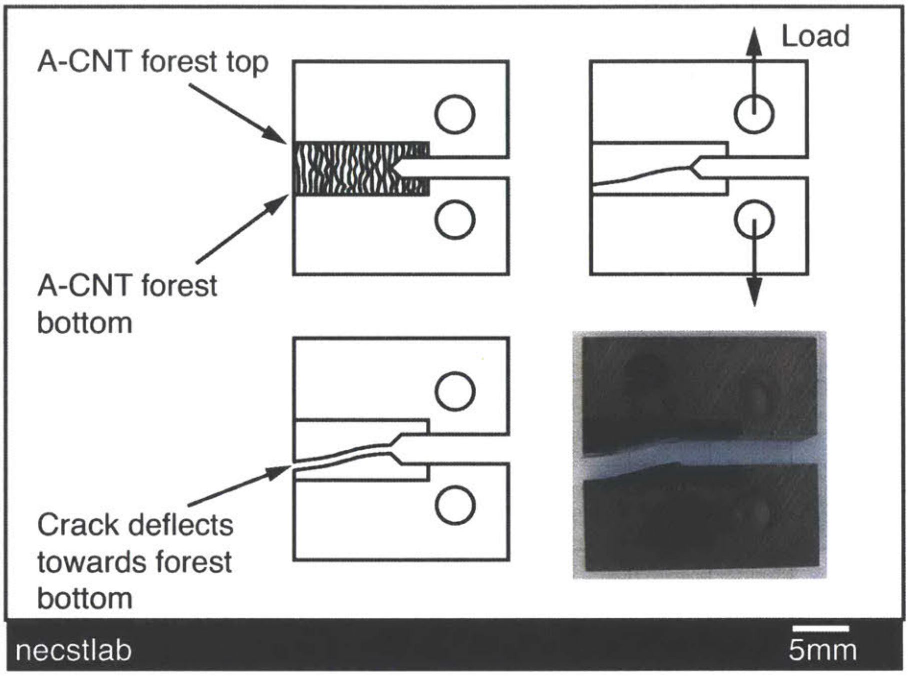

Figure 6-3: Illustration of crack deflection towards the bottom of the forest in 1 vf.% RTM6 A-PNCs manufactured from ~ 5 mm tall A-CNT forests. This is attributed to the gradient morphology previously discussed in Chapter 4.

forest densification led to a selection of the alternate 2 mm A-CNT forest as the primary morphology for further study. Additionally, given the reduction in ~ 2 mm tall A-CNT forest aerial dimensions during densification, SENB specimens are further utilized due to the reduced ligament length, offering the ability to manufacture variable and high volume fraction specimens.

6.2.2 Preliminary RTM6 Single Edge Notch Beam (SENB) Specimens

Preliminary RTM6 A-PNC specimens formed the early work in this thesis, and test results are shown in Figure 6-4. High void content and crack sharpening issues prompted manufacturing technique refinement and investigations using EPON 862/W. However, from μCT, the 1 vf.% specimens are void free and thus, the increase in $K_{Ic,i}$ is likely attributable to the presence of A-CNTs.

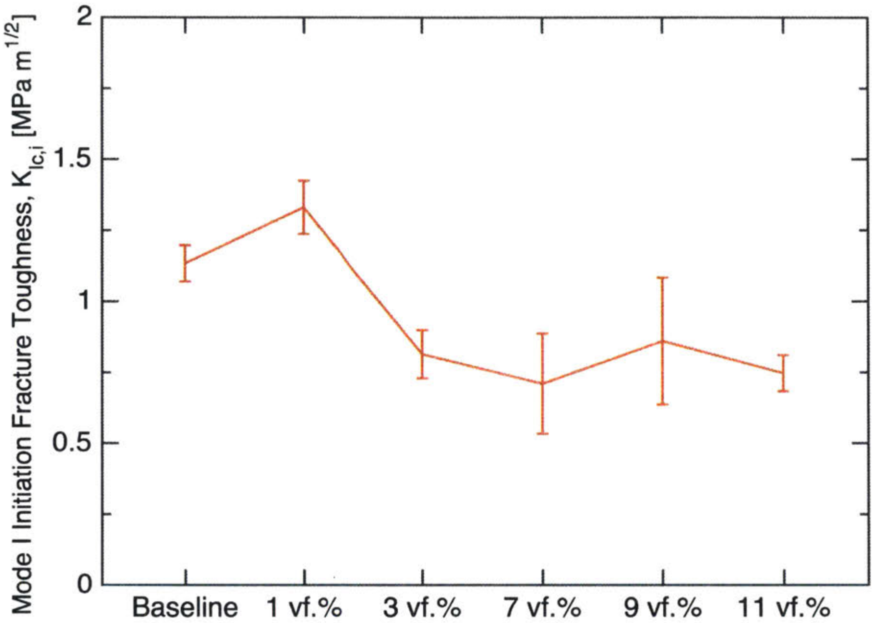

Figure 6-4: Preliminary $K_{Ic,i}$ results for RTM6 show an increase for 1 vf.% over baseline specimens with a decrease for higher volume fractions of A-CNTs.

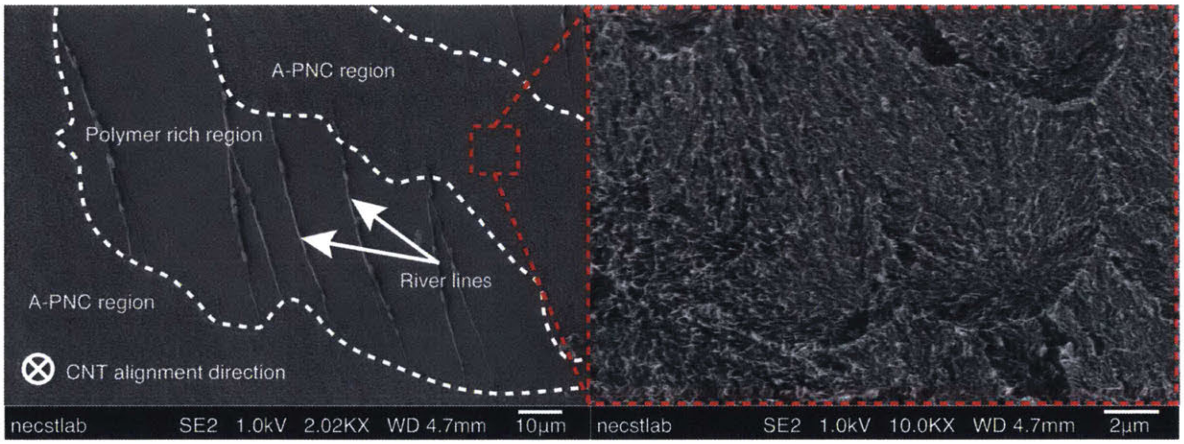

Figure 6-5: Fracture surface of a 1 vf.% RTM6 SENB specimen reveals a) local densification of the A-CNT forest due to capillary forces resulting in an inhomogeneous A-PNC. The b) A-PNC region of the fracture surface shows CNT pullout and parabolic fracture contours indicative of marginal toughening.

Fractography of the 1 vf.% RTM6 A-PNC specimen, seen in Figure 6-5 reveals the previously mentioned capillary densification of the A-CNTs. During wetting, the capillary action that enables epoxy to wick into the forest, causes local densification into bands of A-PNC and pure polymer. Based on the ratio of resin rich regions to A-PNC regions, the local volume fraction is ~ 2 vf.%. The pure epoxy region behaves like baseline specimens with a smooth surface while the A-PNC region is rougher with parabolic type contours, as shown in Figure 6-5b. It is suggested that these parabolic features are the locus created due to the intersection of the moving planar crack front and radially growing craze or secondary crack fronts[181–184]. Its shape is dependent on the ratio of crack velocity to craze or secondary crack velocity[181]; the parabolic shape suggests slower crack propagation through the A-PNC region of the specimen. Thus, toughening is present, but at insufficient levels to cause crack arrest after initiation. Also note that river lines[185] are seen between local A-PNC patches indicating that additional energy is expended when transitioning between local microstructurally disparate zones. Furthermore, Figure 6-5b shows CNTs that were pulled out of the surface during crack propagation, and the pullout length is measured to be ~ 1 μm. For these specimens, crack arrest in some higher vf.% samples occurs due to the presence of voids. For the 1 vf.% sample, however, no crack arrest occurs and due to rapid, unstable nature of the crack propagation, R_{PNC}-curves cannot be produced.

6.2.3 Butt-jointed EPON 862/W SENB Specimens

Given the challenges in creating high volume fraction densified A-CNT forests due to the stiffness gradient present in the as-grown forest, even at ~ 2 mm, butt-jointed forests were utilized as a method to counteract the tendency of individual forests to bend during uniaxial densification by creating stiffness symmetry about the joint, as discussed in Section 4.3.

$K_{Ic,i}$ results from the butt-jointed SENB specimens are presented in Figure 6-6 and shows that the butt-jointed A-CNT forest has no statistically significant effect on the initiation toughness of the baseline EPON 862/W, even for volume fractions up to 8%. This result is expected based on the nature of the butt-joint (as imaged in Section 4.3) i.e., the CNTs do not interpenetrate but rather an interface exists between the two forests, where a crack is likely to propagate at the interface between forests rather than through the forests. Fractography of representative surfaces reveals some infrequent evidence of pulled-out CNTs with lengths of ~ 1 μm, irrespective of the A-CNT volume fraction. The orientation of the CNTs at this interface is not known.

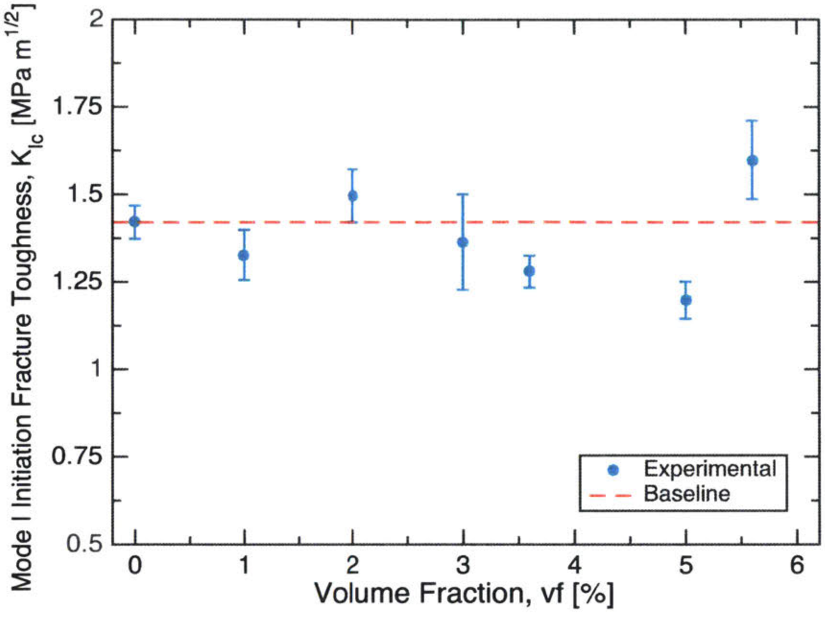

Figure 6-6: $K_{Ic,i}$ results for EPON 862/W butt-jointed samples showing no statistical significance over baseline.

6.2.4 Single Forest EPON 862/W SENB Specimens

The alternate method for A-CNT densification, as discussed in Section 4.3 is the application of a compressive load to the top of the A-CNT forest during densification to prevent out-of-plane forest buckling. The effect of this vertical constraint is a $\sim$ 100 μm compressed zone at the roots of the A-CNT forest. The effect of this zone on polymer infiltration by capillarity is unknown. Additionally, given the tendency of the A-CNT forest to expand from the densified form during polymer curing, uniaxial densification beyond 5 vf.% either results in samples that expand (and sometimes buckle) within the silicone mold, irrespective of the restraining mesh sheets. For this reason, uniaxial densification is limited to $\leq$ 5 vf.% (however 10 vf.% uniaxial A-CNT densification is achievable, but A-PNC final volume fraction is reduced due to expansion).

$K_{Ic,i}$ initiation fracture toughness testing results for the single forest EPON 862/W are shown in Figure 6-7, with 10-20 samples being used for each data point, depending on specimen quality as assessed by μCT (standard error used to indicate the uncertainty of the mean). Crack arrest is observed by DIC in some samples, and a representative image is shown in Figure 6-8. Additionally, this is supported by the load-displacement curve for the specimen, see Figure 6-9a, where the load does not drop to zero after initiation as is seen in the baseline specimens (Figure 6-9b) but increases again until the next load drop etc. However, post fracture analysis using μCT indicates crack intersection with voids as the cause of the crack arrest. Thus, all good quality specimens fracture in a brittle manner, similar to the representative curve shown in Figure 6-9b.

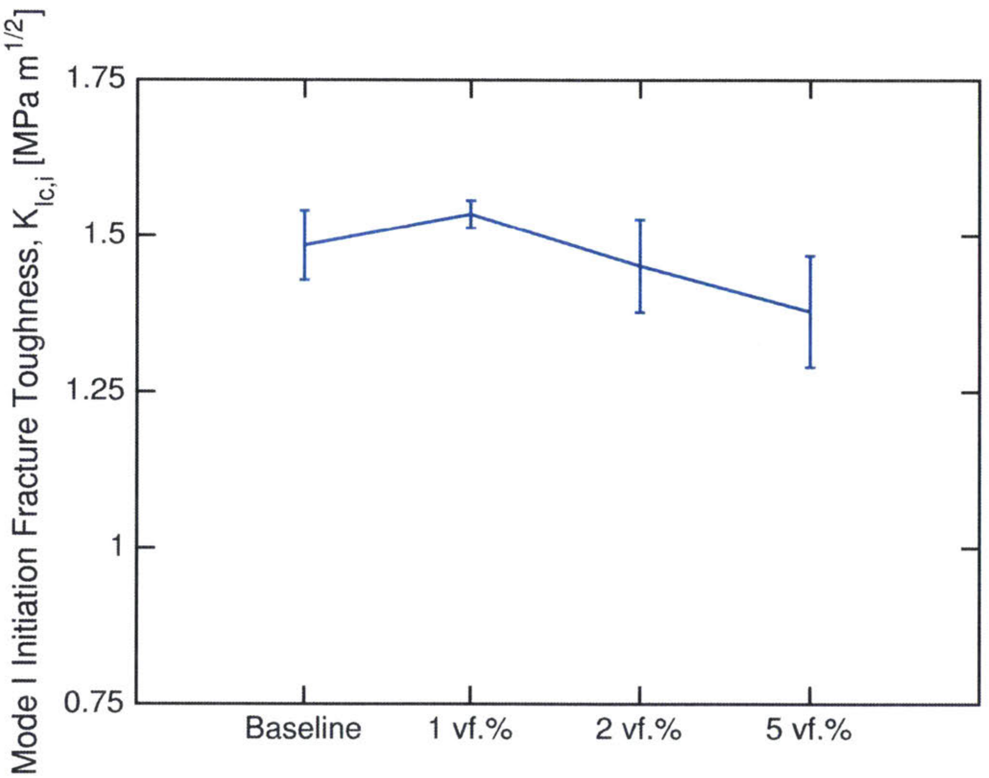

Figure 6-7: EPON 862/W single forest A-PNCs with volume fractions of 1, 2 and 5 vf.% are tested and resulting $K_{Ic,i}$ is compared to baseline. There is no statistical significance in the data indicating that A-CNTs offer any change in $K_{Ic,i}$ initiation toughness over baseline specimens.

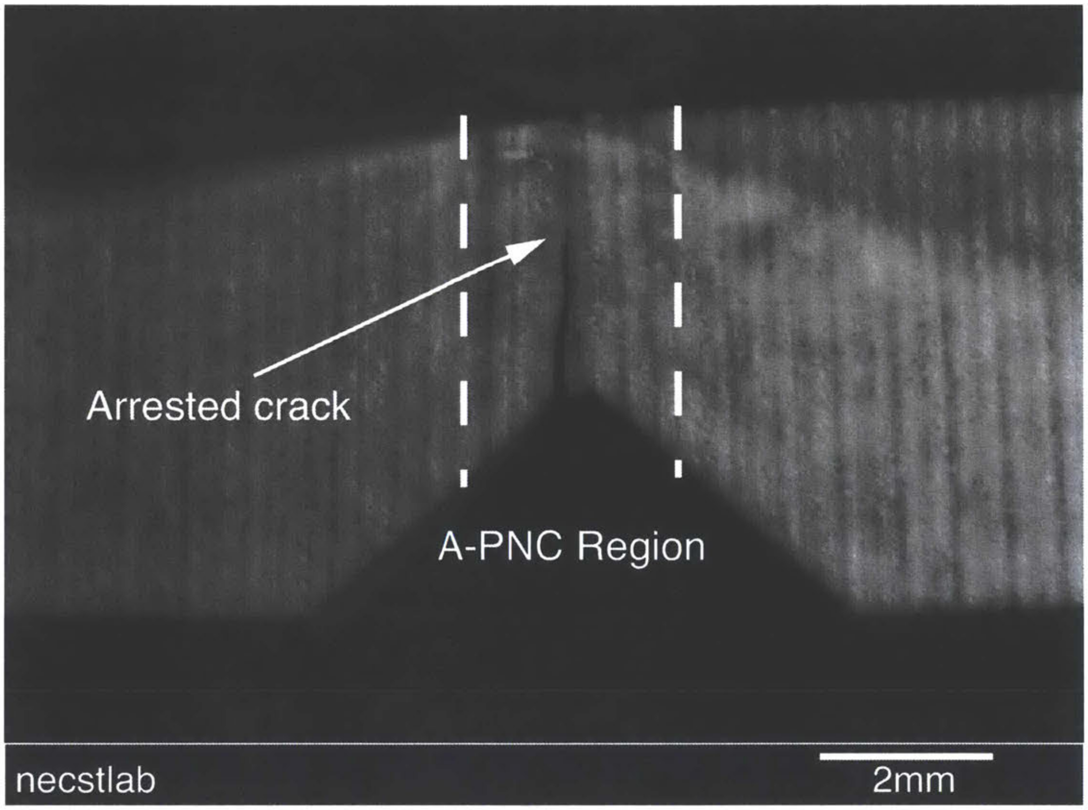

Figure 6-8: DIC image capturing crack arrest during $K_{Ic,i}$ SENB three point bend testing of a 5 vf.% EPON 862/W A-PNC. This occurrence is due to crack intersection with voids during propagation.

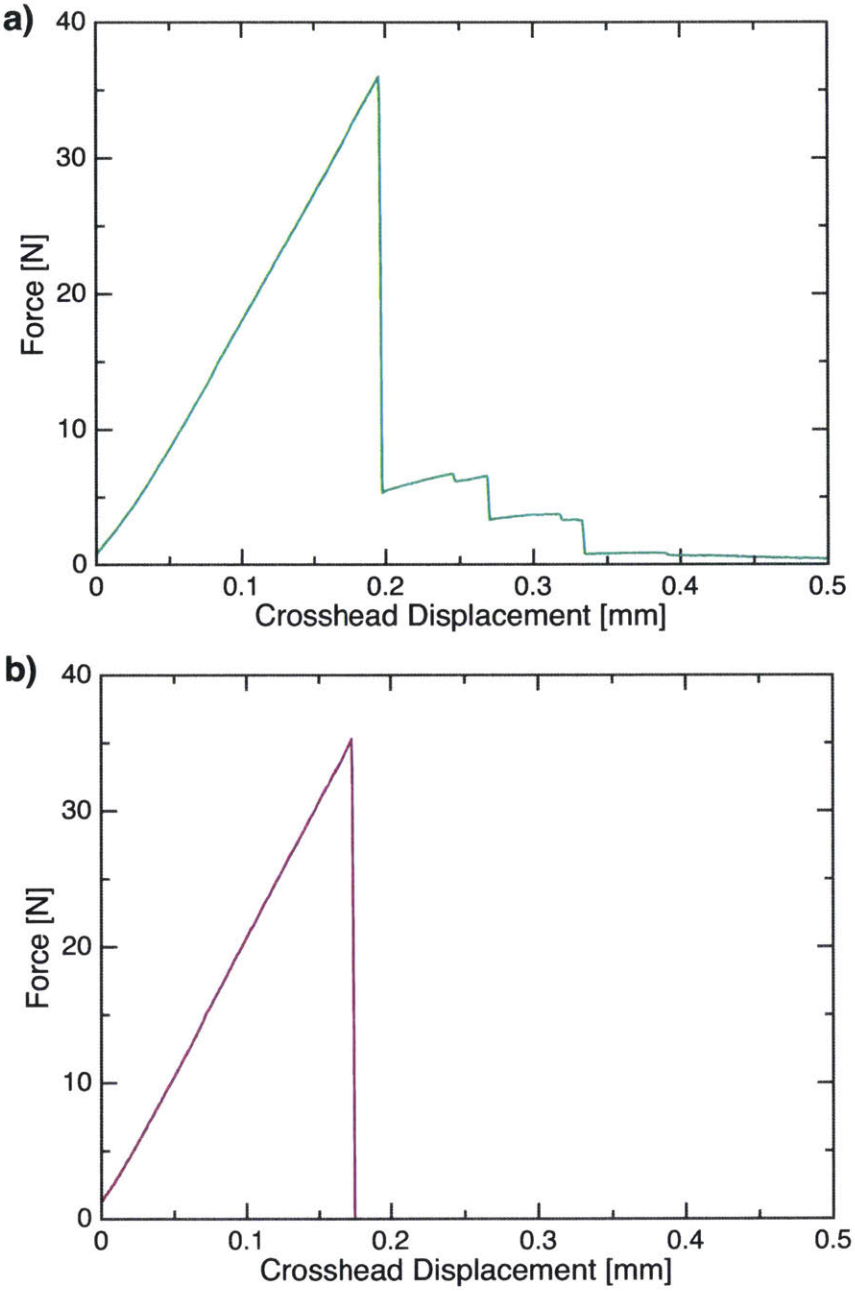

Figure 6-9: Representative load-displacement curves of an EPON 862/W 5 vf.% A-PNC: a) containing voids where crack arrest is observed, with various load drops following initiation as seen beyond 0.2 mm displacement, while b) brittle fracture (without crack arrest) in a void-free 5 vf.% A-PNC has a sudden drop to zero following crack initiation.

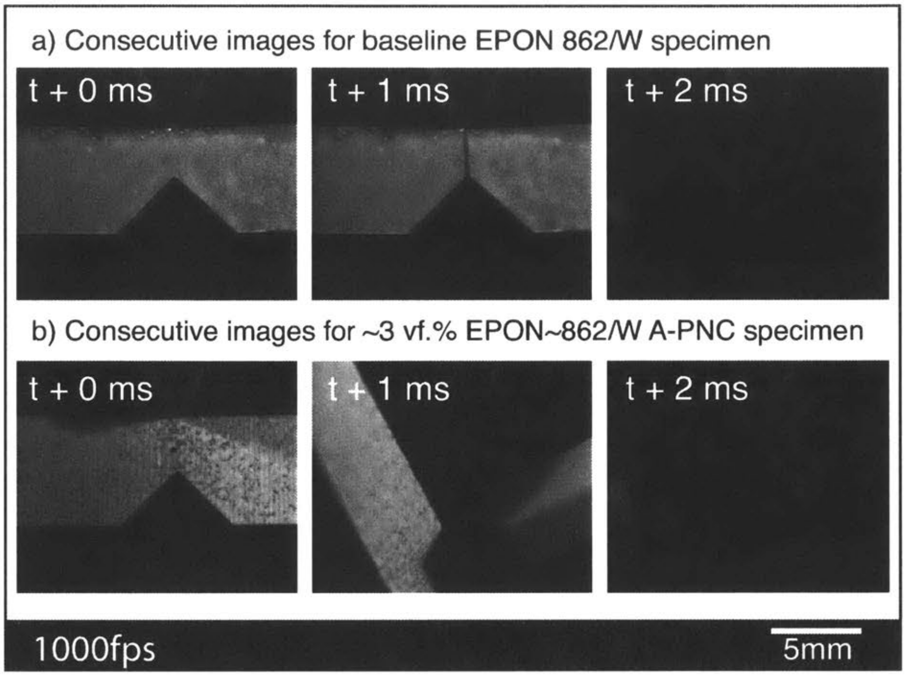

Figure 6-10: Sequential DIC images showing brittle fracture in representative a) baseline and b) void free 5 vf.% EPON 862/W A-PNC specimens. Imaging is performed at 1000 frames per second with total duration of crack propagation through the sample being < 1 ms.

In brittle-type unstable fracture, crack growth is so rapid that it is impossible to control the applied moment to observe it[186]. Representative sequential images for baseline and 3 vf.% A-PNC specimens are shown in Figure 6-10. Despite, DIC capturing images at 1 ms, cracks cannot be captured propagating through the brittle specimens. Steady state R_{PNC}-curves are thus not achievable.

A-CNT Pullout Observations

Figure 6-11 shows SEM images of the separated crack surfaces of various volume fractions of A-CNTs ranging from 1-5 vf.%. CNTs clearly project out of the fracture surface, demonstrating CNT pull-out and showing the toughening mechanism of crack bridging. Pull-out holes cannot be discerned on the fracture surface from A-CNTs remaining on the mating surface, likely due to resolution and imaging techniques. Additionally, it is unclear as to whether these CNTs have broken and pulled out from the polymer, or the outer wall "sheath" of the multi-wall CNT (MWNT). Sword-in-sheath pull-out with the outer CNT layer(s) remaining adhered to the matrix, may occur but cannot be resolved by SEM. Future TEM studies of the CNT/epoxy interface and the fracture path should resolve this issue.

The A-CNTs are grown to $\sim$ 2 mm in length with a relatively short $\sim$ 1 μm exposed pullout length. This could be caused by several factors: firstly, high interfacial shear strength between the A-CNT and the epoxy matrix which reduces pull-out length. It must be noted that high interfacial strength is beneficial to the tensile properties of the PNC because breaking the A-CNTs takes advantage of their high tensile strength rather than the weaker polymer-CNT interface bond. Secondly, a low CNT strength can lead to fracture of the CNT near the crack plane. A high prevalence of defects will result in small fiber slip lengths at lower applied stresses. Thirdly, a combination of (1) and (2) would be high interfacial shear causing the load to be carried, primarily, by weak CNTs, which are broken during crack opening at a defect site present in the A-CNT.

Additionally, when observing SEMs of fracture surfaces, the number of A-CNTs pulled out are significantly less than the volume fraction. Average counts of pulled out A-CNTs show that only 1-8% of A-CNTs present in the A-PNCs are engaged in fracture[180]. Thus, for an A-PNC specimen with an A-CNT loading of 5 vf%, the value used to determine volume fraction v_f in fiber pull-out and debonding calculations, G_p and G_d, respectively, is 0.005 when using a conservative CNT engagement percentage of 10%. For calculation of the pull-out toughness contribution, G_p, frictional pull-out stress, τ_f is assumed to be similar to that of carbon fiber[180] at $\sim$ 10 MPa[187]. And, for debonding toughness contribution, G_d, the interfacial toughness, G_{int}, is assumed to be 0.2 Jm^{-2}[188]. From TEM images in Chapter 4, the A-CNT radius, r, is $\sim$ 5 nm. From this, the toughness contributions from pull-out and debonding are $\sim$ 3.3 Jm^{-2} and $\sim$ 0.2 Jm^{-2}, respectively, trivial relative to the epoxy intrinsic toughness of 700 Jm^{-2} for EPON 862/W for example.

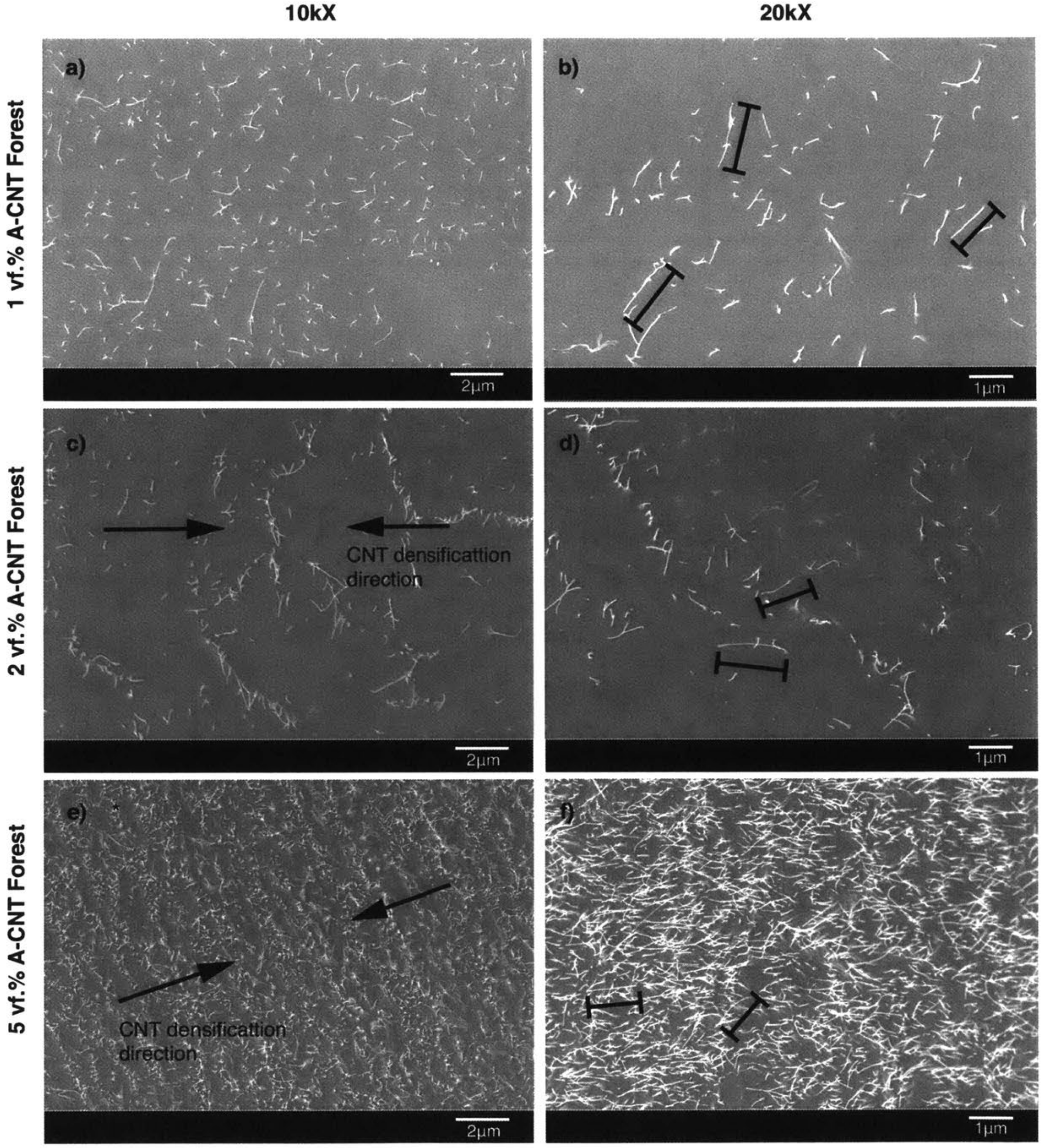

Figure 6-11: Fractography of fractured EPON 862/W A-PNC specimens with 1, 2 and 5 vf.% A-CNT loading showing volume fraction independent CNT pull-out lengths of < 1 μm. Additionally note that densification increases the number count of CNTs pulled out per unit area, and the densification direction can be seen to affect the A-CNT arrangement.

For RTM6 baseline specimens with an elastic modulus of ~ 3 GPa[100,163], a Poisson ratio of 0.4[100,189], and $K_{Ic,i}$ of ~ 1 MPa m$^{1/2}$, the strain energy release rate at initiation, $G_{Ic,i}$, is found to be 300 Jm^{-2} when using Equation 2.4. Similarly for EPON 862/W with with an elastic modulus of ~ 2.5 GPa[190,191], a Poisson ratio of 0.4[189], and $K_{Ic,i}$ of ~ 1.5 MPa m$^{1/2}$, $G_{Ic,i}$ is found to be 700 Jm^{-2}. For a brittle material, the initiation strain energy release rate is equal to the steady state strain energy release rate as discussed in Chapter 2, and can be plotted as a horizontal line, R_{epoxy} in Figure 6-12 (EPON 862/W value is used).

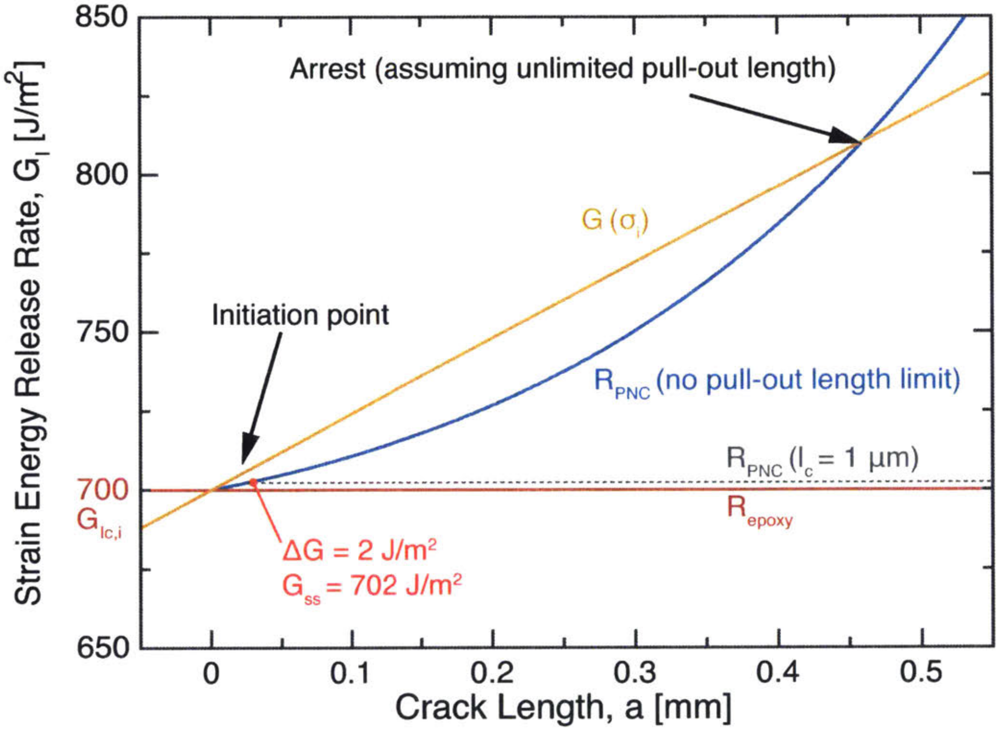

Figure 6-12: Conceptual graphical explanation for lack of crack arrest in A-PNC specimens (collaborative[180]).

To accurately discuss the lack of crack arrest, the total G_p and G_d values presented above cannot be used, but rather the change, ΔG_{CNT}, is required to predict the additional toughening offered by the A-CNTs, and to create an R_{PNC}-curve that develops from initiation to a steady state value. If A-CNTs did not break and the pull-out length is allowed to continue indefinitely with crack propagation, the R_{PNC}-curve (blue in Figure 6-12) will continue to grow and intersect the $G(\sigma_1)$-curve (green in Figure 6-12) due to the applied initiation stress.

At this intersection point, neglecting dynamic crack growth effects, crack arrest would occur at $\sim$ 0.5 mm from the initiation point, corresponding to a pull-out length of $\sim$ 7.5 μm; a value 7.5 × larger than achieved in the specimens herein. A steady state curve for R_{PNC} will only be reached if a limiting pull-out length due to fiber breakage is included.

For this work with a limited CNT pull-out length of $\sim$ 1 μm, the ΔG_{CNT} is calculated to be $\sim$ 2 Jm^{-2} once steady state is reached, providing a G_{ss} for the A-PNC of $\sim$ 702 Jm^{-2}, with a limited R_{PNC}-curve (as shown by the grey dashed line) that does not intersect $G(\sigma_1)$, hence no arrest is observed. Note that this ΔG_{CNT} is less than the above supplied $G_p + G_d$, as not all the CNTs have pulled out or debonded in the crack wake. Note that for these calculations, the instantaneous length, l_{inst} of an A-CNT pulling out as a function of crack length can be determined using $\phi = 1^\circ$ as approximated by DIC (at an instance where the unstable propagation coincided with image capture).

Apparent Transverse Cracking and Crack Deflection

Optical microscopy of some fracture surface revealed what appears to be step-wise crack deflection from the initiated crack plane towards the bounds of the CNT/polymer interface. However, upon closer inspection using μCT, the detail of Figure 6-13 shows that the crack intersects a void and deflects longitudinally through the void, demonstrating an apparent phenomenon of crack deflection. Although toughening by voids is not the desired outcome in this work, it must be noted that unique void structures are created by the A-CNTs during the infusion process. An interesting observation is that the void orientation influences whether the crack continues to propagate through the midplane or deflect to the interface. If the crack intersects a "convex void", as shown in Figure 6-13, the crack is gradually deflected outwards towards the interface. However, if the crack intersects a "concave void", it continues to travel through the midplane of the A-PNC forest Figure 6-14.

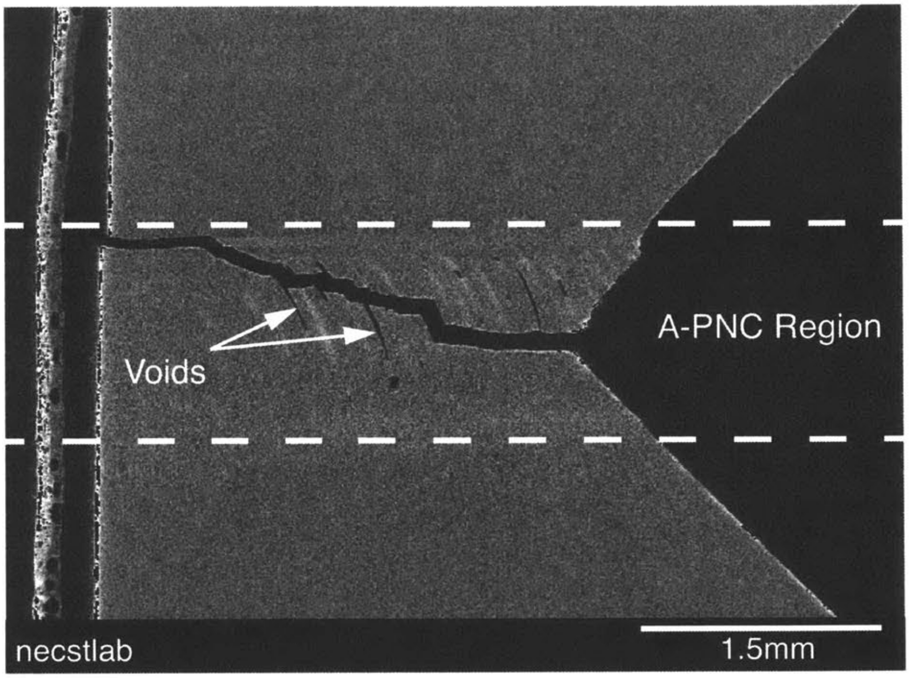

Figure 6-13: μCT shows that instances of crack jump to the interface results due to the presence of "convex voids" in the A-PNC region of a 5 vf.% EPON 862/W sample.

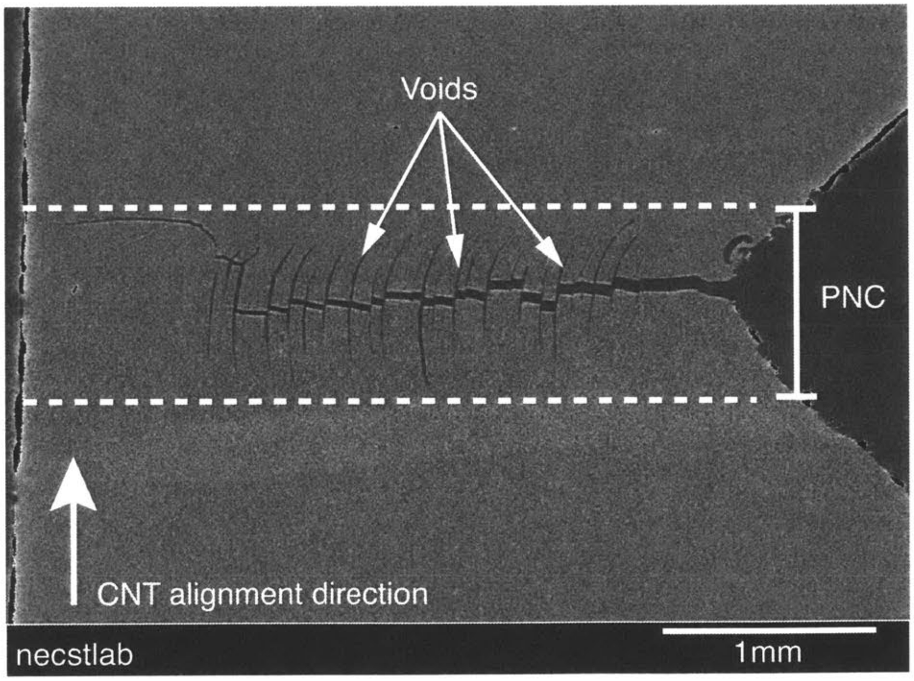

Figure 6-14: Crack path through an EPON 862/W $\sim$ 6 vf.% (A-CNT forest densified to 10 vf.%) sample containing "concave voids" arranged transverse to the crack plane.

6.3 Conclusions

The testing results herein demonstrate that CNT-reinforced polymer nanocomposites exhibit features associated with toughening behaviour, namely crack bridging as evidenced by fiber pull-out on the fracture surfaces. Results are available only for initiation toughness, which show that A-CNTs do not contribute to toughness at initiation, and any contribution likely falls within test error. Steady state R_{PNC} could not be produced due to the inability to arrest cracks (calculated toughening based on fracture surfaces indicates resistance is not expected) or track unstable crack growth. This is likely due to the following or a combination thereof:

- Test specimen geometry: while it is ideally modeled (based on the $\sim 1\ \mu$m pull-out lengths) that the toughening contribution from the A-CNTs reaches steady state very soon after crack initiation, it is possible that successful development of DCB specimens or further work using compact tension specimens could produce arrest events that allow R-curves to be established.
- A-CNT contribution to toughening, as predicted by a high-level model, is minimal and the R_{PNC} is likely to fall below $G_(\sigma_i)$. Thus, the steady state result is an unstable crack which cannot be tracked due to the limited DIC sampling rate of 1 ms. Firstly, future work should employ the use of a high speed camera and, secondly, a mechanical tester with more resolution and sensitivity to load values should be utilized.
- Given the minimal contribution of the A-CNTs to crack growth, precrack refinement may assist in reducing the slope of the $G_(\sigma)$ at initiation.
- Based on the pull-out lengths of maximum $\sim 1\ \mu$m, insufficient toughening is provided by the A-CNTs to halt or slow crack propagation. This is likely due to high interfacial bonding as well as low strength of defective A-CNTs. The lack of nano-scale surface perfection in the as-grown CNTs due to carbon impurities is likely a strong contributor to the high interfacial strength. For increased toughening, the interface must debond at a lower stress than at which the fiber breaks, while simultaneously producing friction during sliding.
- It is likely that residual stress could exist at the crack tip due to introduction of the

razor precrack. Future work should include optical microscopy of thin pure polymer precracked specimens with polarized light to asses the crack tip and any residual stress distribution around the crack tip from birefringence patterns. If residual stress is introduced due to precracking, butterfly-shaped patterns showing plastic deformation or fringe patterns showing residual stress, will be seen surrounding the crack tip[175]. It may be possible to bring about stress relaxation by allowing the A-PNC to anneal in an oven. Additionally, the crack tip will likely close to a smaller radius during the anneal, which is a desirable outcome given the need for a precrack more similar to a natural crack.

Given this, future work should focus on either engineering the carbon nanotube structure (such as increasing strength through defect site reduction, perhaps by thermal anneal) or tailoring the interface between the CNT and the polymer to increase or control composite toughness. Coating micron-scale fibers with a conformal layer of polymer sizing is a standard practice to alter the bonding between micro-fibers and the matrix, including in aerospace grade composite materials. In A-PNCs, the presence of "nano-sizing" on the A-CNTs may create a defined and tailorable intermediate layer with a modulus and perhaps a coefficient of thermal expansion somewhere between the bulk matrix and the A-CNT. This eases the stress concentration that builds up at the boundary associated with large mismatches of modulus and thermal properties, likely improving nanocomposite toughness.

Additionally, it is well-known that residual stresses influence deformation and cracking in laminated composites. Residual matrix stress induces matrix cracking within the ply, and in crossply systems transverse cracking occurs in the interlaminar region. Residual stress arises due to a mismatch in the coefficient of thermal expansion (CTE) between the different media in the composite. When considering the PNCs, it should be noted that there is potential for residual stresses to be present due to the mismatch of CTEs between the CNTs and the epoxy matrix. The CTE for CNTs has been reported in literature to be an order of magnitude smaller than polymers[192–194]. While there are differences in CTE based on chirality, and orthotropy, where slightly positive or slightly negative values are seen, for comparison to polymers, a CTE for CNTs of $-1.5 \times 10^{-6} K^{-1}$ at room temperature is noted.

Epoxy has a room temperature CTE of $\sim 60 \times 10^{-6} K^{-1}$. As previously mentioned, during the PNC manufacture process, the A-CNTs are infused with uncured liquid epoxy. During the cure process at 149°C, the A-CNTs will contract and the polymer expands. At the end of the cure (assuming polymer chain orientation is unaffected by the presence of the A-CNTs), both the polymer and the A-CNTs are thermally strained but mechanically unstrained. On post-cure cooling, the polymer tends to contract while the CNTs tend to expand. Assuming ideal interfacial bonding, self-equilibrating residual stresses will result due to the mechanical strains that develop between the material phases. The residual primarily longitudinal tension in the matrix could increase crack-opening while the residual compression in the CNTs could decrease crack opening. It is hypothesized that residual longitudinal tension would reduce the ability of the A-CNTs to bridge the crack. Furthermore, there is residual shear stress at the fiber/matrix interface that is coupled to interfacial sliding which is in turn coupled to the strength and toughness of the A-PNC. The presence of residual stresses complicates the determination of the PNC toughness contributions from the CNTs due to crack-bridging and pull-out.

Chapter 7

Mechanical and Thermal Properties of Aligned Carbon Nanotube Polymer Nanocomposites

To further understand how A-CNTs affect the A-PNC when compared to bulk, additional thermal and mechanical characterizations are performed. Nanoindentation can be utilized to gather both quasi-static data such as indentation modulus[195,196], as well as dynamic data such as storage and loss moduli, and $\tan(\delta)$. Dynamic nanoindentation (nanoDMA) can be used to determine whether the MWNTs used herein increase damping of the PNC through sliding at the A-CNT/matrix interface, as might be indicated by $\tan(\delta)$.

The nature of this work is preliminary, and future work is required to expand the data and establish whether trends and observations are merely inherent variation or accurate representations of the A-PNC materials in general. Additionally, unless otherwise noted standard error is used to compare means (center point).

7.1 Test Methods and Sample Preparation

Nanoindentation only requires samples on the micro- to milli-meter scale. Thus, $\sim$ 1 mm tall A-CNT forests grown on a 10 mm × 10 mm wafer are utilized as their increased morphological uniformity over the forest height maximizes compressibility to ~ 30 vf.%. Following the biaxial densification method presented in Chapter 4, the A-CNT forests are biaxially densified to produce A-PNCs containing 1, 5, 10, 20 and 30 vf.% A-CNTs. Both RTM6 and EPON 862/W are used for this work, and A-PNCs are manufactured following the procedure outlined in Chapter 5. The resulting A-PNCs are divided into three sample sizes and types for 1) quasi-static and dynamic nanoindentation testing, 2) DSC and 3) TGA analyses.

For the quasi-static nanoindentation and nanoDMA tests, a mirror-like cryomicrotomed surface is required to reduce measurement error that may stem from surface roughness. Because the stress measurements determined by indentation are based on the contact area of the tip, indenter contact depth and tip geometry, it is known that if the indenter tip indents a peak or valley, highly variable measurements are obtained[197]. Additionally, due to the expected non-isotropic response created by the A-CNTs, A-PNC test samples are cryomicrotomed such that nanoindentation and nanoDMA can be performed both parallel and perpendicular to the A-CNTs, as depicted in Figure 7-1. Polishing is not performed as fine control over A-CNT orientation cannot be achieved, and local heating caused by polishing may alter material properties at the surface where testing is performed.

Quasi-static nanoindentation and nanoDMA is performed using a Hysitron TI 950 Tribo Indenter (located at ARL's Aberdeen Proving Ground in the Vehicle Technology Directorate) with a diamond Berkovich tip (three-sided pyramid) having a 150 nm tip radius and 142.35° pyramidal angle. It is necessary to establish an indentation depth such that minor surface imperfections do not cause data variation, and thus a 1 μm indentation depth is targeted (note A-CNT spacing in a 1 vf.% 1 mm tall forest is ~ 80 nm). This depth is achieved with a force of 1800 μN. For nanoDMA, the amplitude for frequency oscillation is 5 nm and is achieved with a 50 μN dynamic load amplitude, performed at maximum indentation depth.

TGA can provide information about the mass content and thermal stability of the A-PNC specimens of various volume fractions, and analyses are performed, at MIT's Institute for Soldier Nanotechnology, with a Discovery TGA TGA1-0075 that is controlled by a DSC/TGA DCC1-00177 data station. Approximately 5 mg of the A-PNC sample is heated in an open platinum pan in excess air, and a TGA sweep is performed from room temperature to 900°C

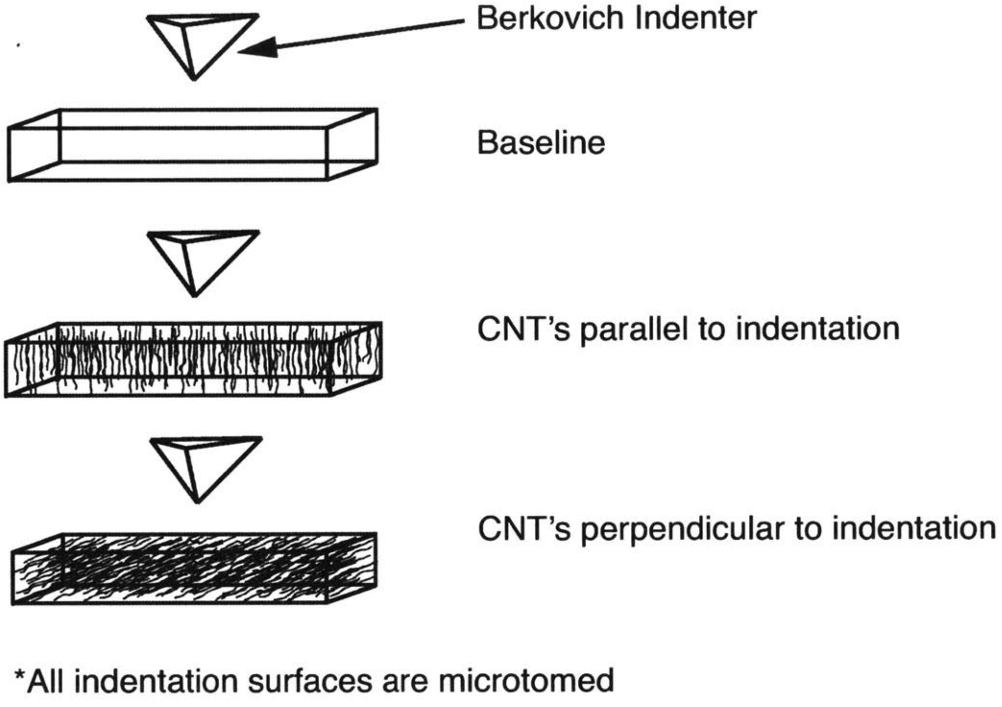

Figure 7-1: Illustration showing orientations of the A-PNC samples for both quasi-static nanoindentation and nanoDMA testing. Note that indentation is performed using a Berkovich tip.

at a rate of 10°C/min.

Additionally, DSC can be used to assess the thermal behavior of the synthesized polymer nanocomposites, typically showing features such as T_g in the case of thermoset polymers, and other primary transition features such as melting/crystallization in thermoplastics. DSC is performed, at the Institute for Soldier Nanotechnology, using a Discovery DSC RCS1-3277 with a DSC1-0107 cooling system, where a $2-5$ g A-PNC section is hermetically sealed with an aluminum pan and lid, and subjected to a heat-cool-heat cycle (ramp rate 5°C) with a -90°C to 200°C range, depending on polymer thermal stability as determined by TGA.

7.2 Quasi-static Nanoindentation

Quasi-static nanoindentation is performed using a loading function consisting of a force ramp from 0 μN to 1800 μN over a period of 5 sec, followed by a 1800 μN hold for 5 sec, and finally unloading from 1800 μN to 0 μN over 5 sec. This load function is specifically designed to load the specimen quasi-statically, then during the hold it allows for relaxation of the material around the indenter tip such that full contact is achieved, and this is followed by quasi-static unloading from which accurate linear elastic moduli can be obtained[196,198,199].

The nanoindenter provides a reduced modulus of elasticity, E_r, that is found using methods described by Oliver and Pharr[199], and calculated by:

$$E_r = \frac{S}{2\beta}\sqrt{\frac{\pi}{A(h_c)}} \tag{7.1}$$

Where β is a constant and depends on the geometry of the indenter ($\beta = 1.034$ for Berkovich), A is the tip contact area which is a function of h_c , the indentation contact depth (calibrated using sapphire), and S is the measured unloading tangent stiffness found[198] using the change in force dP and the change in depth dh :

$$S = \frac{dP}{dh} \tag{7.2}$$

The Young's modulus for the sample material, E_s, can typically be calculated based on a relationship between E_r and the Young's modulus and Poisson ratio of the indenter (E_{ind}, ν_{ind}) and the test specimen (E_s, ν_s) through[197,199]:

$$\frac{1}{E_r} = \frac{2\beta\sqrt{A(h_c)}}{S\sqrt{\pi}} = \frac{(1-\nu_{ind}^2)}{E_{ind}} + \frac{(1-\nu_s^2)}{E_s} \tag{7.3}$$

However, this relationship may only be utilized for the baseline specimens as the derivation of Equation 7.3 implicitly assumes material isotropy. Additionally, for comparison of baseline samples to manufacturer specifications, Gair[197] notes that given the indenter tip is diamond ($E_{ind} = 1100$ GPa, $\nu_{ind} = 0.07$) and that epoxies have a Poisson ratio of $\nu_s = 0.4$[100], Equation 7.3 can be simplified to:

$$E_s \approx E_r\ (1-\nu_s^2) = 0.75\ E_r \tag{7.4}$$

The above expressions are applicable to purely elastic behavior during unloading. For materials that undergo viscous deformation, it is necessary to account for these effects by correcting the outputted reduced modulus, E_r (from the Hysitron TI 950 Tribo Indenter), to a more accurate indentation modulus, (E_I), and is termed anelastic correction. When considering Equation 7.1, a deviation from mechanics stems from the measurement of S and a correction for this is in the form[197,200]:

$$\frac{1}{S} = \frac{1}{S_a} + \frac{\dot{h}}{|\dot{P}|} \tag{7.5}$$

Where $\dot{h}$ just prior to the end of the hold and $\dot{P}$ at the beginning of unloading are used to find the more accurate S as a function of the measured stiffness S_a. The updated S can then be returned into Equation 7.1 to find the more accurate indentation modulus, E_I[197]. Even in fully cured, thermoset epoxies, some viscoelasticity is present, and can be corrected for using data post-processing. If no anelastic effects are detected, data will remain unmodified as $\dot{h}$ will be 0 in the ideally elastic case (see Gair[197] for Python script). Thus, all quasi-static nanoindentation results are reported as the indentation modulus E_I for comparative purposes.

Due to inherent directionality introduced when using the A-CNTs, testing is performed both parallel and perpendicular to the nanotube orientations, and near the middle of the specimen to avoid edge effects. Samples are $\sim$ 1 mm thick thus eliminating the likelihood of substrate interferance (a general rule is that indentation depth must be $<$ 10 % of the sample thickness). Additionally, local variations due to A-CNT bundling or capillary densification are averaged by collecting 4 × 4 grids with 5 μm center-to-center spacing between each point (16 data points) at three different locations on the cryomicrotomed surface (48 points per specimen).

Representative EPON 862/W A-PNC load-displacement curves are shown in Figure 7-2 for the perpendicular orientation. E_r is determined by finding the tangent of the unload curve immediately following the hold phase because this region most accurately represents linear elastic behavior[201]. It is noted that with increasing A-CNT content, the slope of the unload segment increases, i.e., E_r increases, and the amount of inelastic deformation at hold decreases[197], as seen by the decreasing change in depth during the hold segment. Representative curves of the 5 vf.% EPON 862/W A-PNC sample for both the parallel and perpendicular orientations are represented in Figure 7-3 to highlight how the micromechanical response differs when A-CNTs are loaded in compression (parallel) versus bending (perpendicular). Note that E_I is determined from E_r by correcting for anelastic effects[197].

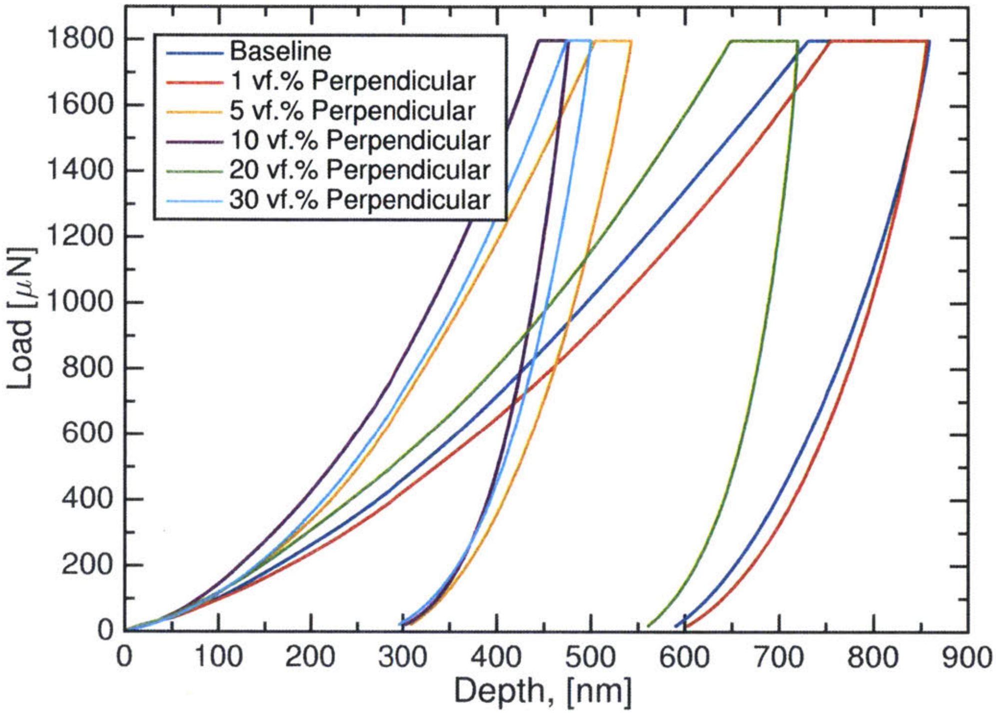

Figure 7-2: Representative quasi-static nanoindentation force-displacement curves for A-PNCs of various volume fractions made from EPON 862/W in the perpendicular direction, showing the load path of load-hold-unload. E_r is determined as the tangent to the unload curve at the beginning of the segment, from which E_I is determined through anelastic correction. Note that the 20 vf.% does not fall in the anticipated location, this phenomenon is discussed in text.

Using the collected quasi-static nanoindentation data for EPON 862/W and RTM6, average E_I is plotted as a function of volume fraction in Figure 7-4 and Figure 7-5, respectively. Figure 7-4 shows that the addition of A-CNTs in EPON 862/W A-PNCs profoundly increases stiffness when examined with the baseline samples. For the 1 vf.%, a $\sim$ 50% increase is observed in both the parallel and perpendicular directions. Beyond 1 vf.%, the results of the two orientations diverge and a statistically significant improvement is observed for the parallel orientation when compared to the perpendicular orientation. At 30 vf.%, the parallel configuration offers a $\sim$ 270% increase over baseline with an E_I of $\sim$ 10 GPa, while the perpendicular specimen shows a $\sim$ 140% improvement. Similar to EPON 862/W,

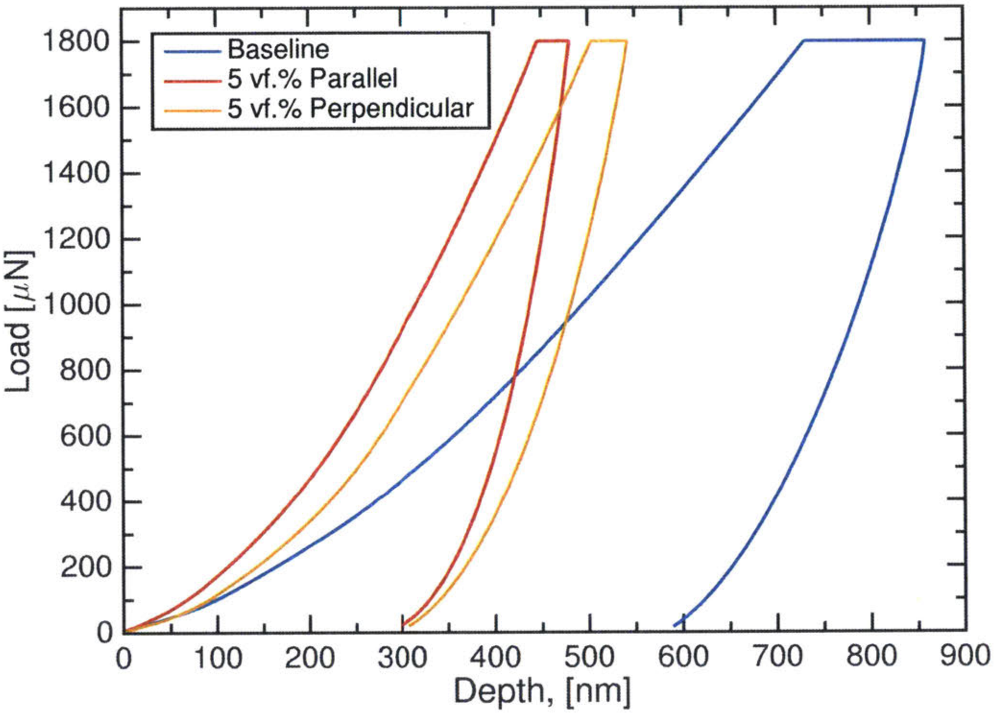

Figure 7-3: Representative quasi-static nanoindentation force-displacement curves for 5 vf.% EPON 862/W A-PNCs orientated both parallel and perpendicular to the axis of indentation, showing the influence of A-CNT orientation on the indentation response.

RTM6 A-PNC specimens show that the parallel orientation is stiffer than the perpendicular orientation, however, the statistical significance can be disputed. Additionally, the E_I improvement in the RTM6 is not as markedly as that of the EPON 862/W, likely due to the larger RTM6 matrix stiffness masking the contribution from the added A-CNTs. Note that 30 vf.% RTM6 A-PNC specimens have been excluded due to suspected data collection error, however, a similar trend to EPON 862/W is likely.

It is clear from Figure 7-4 and Figure 7-5 that a linear rule-of-mixtures improvement cannot be responsible for the non-linear trend. In both the EPON 862/W and RTM6 A-PNC systems, E_I reaches a local maximum at 10 vf.% and 5 vf.%, respectively, followed by a local minimum at 20 vf.%, beyond which E_I is observed to increase again. More data is required to establish whether this trend is consistently observed, and RTM6 30 vf.% samples must be re-manufactured. With this in mind, the 20 vf.% local minimum is also observed by Gair[197] in poly(urethane-urea) A-PNC specimens with the same volume fraction increments, and it is hypothesized[197] that the initial increase from baseline to the local maximum can be modelled as a rule-of-mixtures improvement where increasing A-CNT content increases E_I. However, beyond the local maximum, the spacing between the A-CNTs decreases to a critical point where large chain formation (or cross-linking) is likely inhibited due to reduced mobility, which gives rise to a less crosslinked and therefore more compliant matrix. A decreased E_I will result as the matrix contributes to load carrying to a lesser extent. Additionally, it is suggested[197] that beyond 20 vf.%, a cross-over is reached where the A-CNT volume fraction is sufficiently high such that the A-CNTs carry increasing loads with increasing volume fraction (more tightly packed), irrespective of reduced matrix load carrying properties.

Nanoindentation on densified A-CNT forests alone, performed by Cebeci et. al[159], show an exponential increase in E_I, with a 20 vf.% A-CNT forest having an E_I of $\sim$ 982 ± 108 MPa, a $\sim$ 600 × enhancement over baseline having an E_I of $\sim$ 1.7 ± 0.2 MPa; the mid-range 10 vf.% A-CNT forest has an E_I of $\sim$ 150 ± 11 MPa. From this, it is described that the non-linear trend with volume fraction is due to A-CNT spacing[159,202]. When considering the hypothesis for describing the local minima and maxima in storage modulus, the A-CNT nanoindentation may support this theory. At 10 vf.% A-CNT loading in an A-PNC, modulus improvement may result from a "("better-than-both) interaction between the polymer and the A-CNTs, as the modulus of the A-CNT forest alone is 30× smaller than the matrix. At the point where suspected confinement affects matrix performance, the modulus contribution of A-CNTs is 1 GPa at the minimum (free-standing forest), and it is likely that matrix still greatly contributes to the effective modulus, despite the reduction is matrix properties. Extrapolating the E_I curve presented by Cebeci et. al in Figure 7-6 will lead to a substantial increase in A-CNT forest E_I contribution, negating the effects of the deteriorating matrix

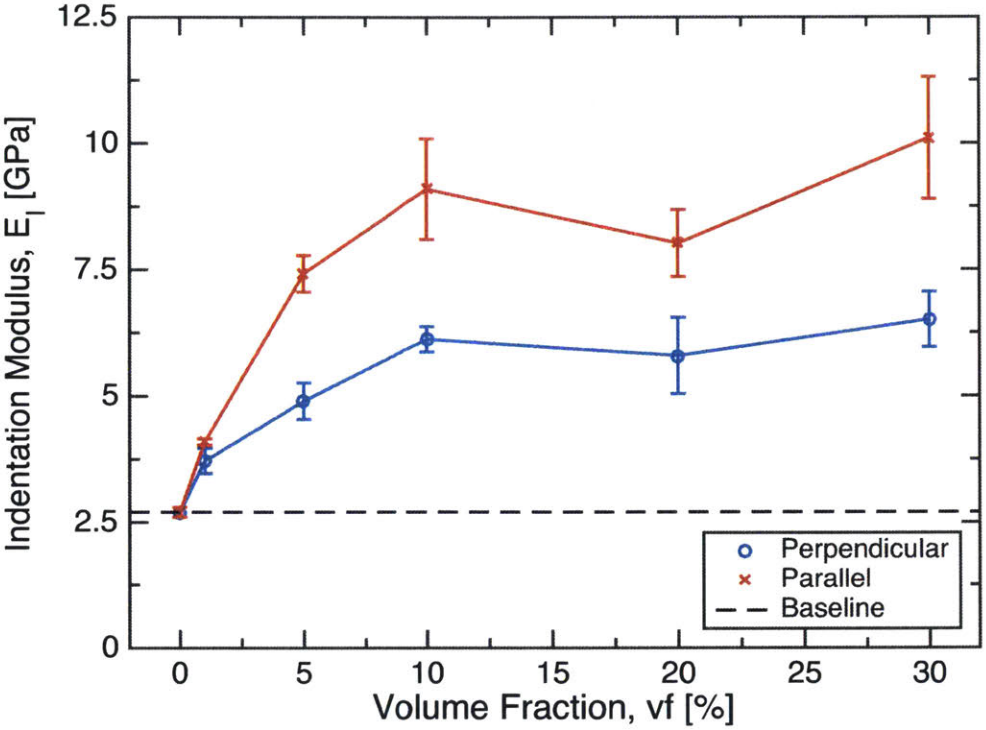

Figure 7-4: Indentation modulus, E_I, as a function of volume fraction for EPON 862/W A-PNC specimens. The specimen loaded parallel to the indenter shows a statistically significant increase over the perpendicular specimens, which are stiffer than the baseline pure polymer.

load carrying capabilities due to chain length limitations.

Handlin et. al[100], using similar RTM6 A-PNCs up to 18 vf.%, performs tensile testing to establish modulus and also observes that the parallel orientation has an increased stiffness over the perpendicular orientation. Handlin et. al suggest a volume fraction independent Poisson ratio of 0.4 and using $E_s = 0.84E_I$, the tensile test data[100,189] can be scaled up for comparison of tensile testing and quasi-static nanoindentation for the RTM6 A-PNC systems, Figure 7-7. Handlin et. al show that tensile modulus increases with increasing A-CNT volume fraction, whereas the quasi-static nanoindentation presents a local maximum followed by a local minimum. Mechanistically, the unique A-CNT morphology can very well lead to the disparity in results as different phases will dominate depending on the load application. Consider perpendicular loading, for example, in compression (indentation): A-CNTs are supported by successive layers of A-CNTs, while the polymer matrix acts as a binder. In tension, however, the load is almost solely carried by the matrix. Nevertheless,

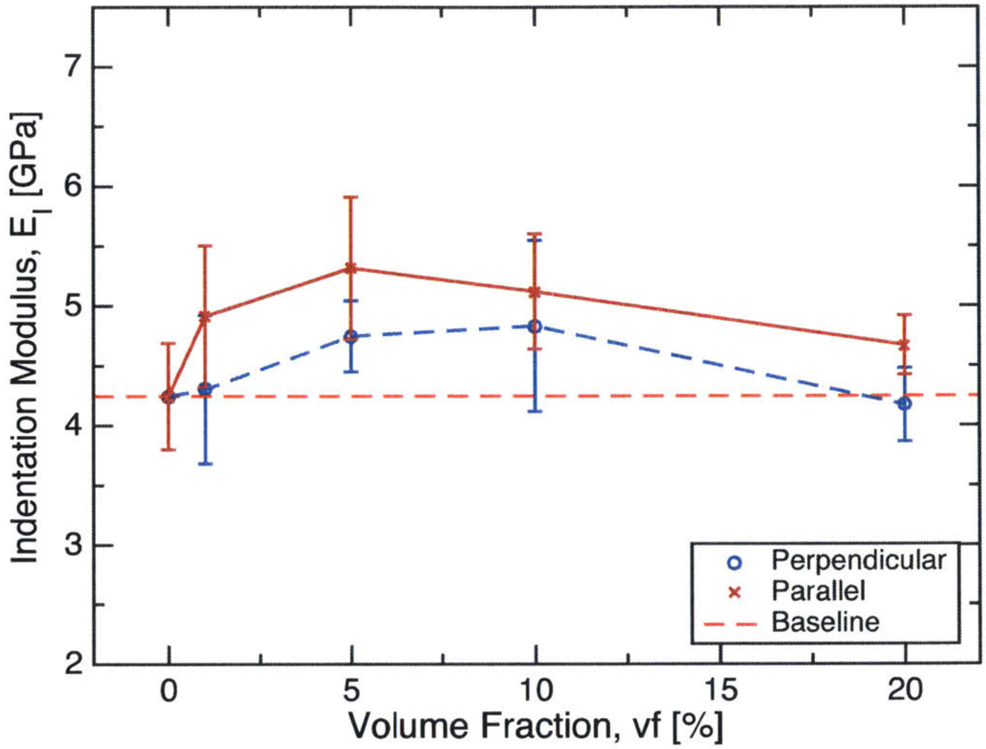

Figure 7-5: Indentation modulus, E_I, as a function of volume fraction for RTM6 A-PNC specimens. Similar to EPON 862/W, the parallel configuration is improved over the perpendicular configuration.

trends in non-isotropy support those of quasi-static nanoindentation, and order of magnitude modulus comparison is valuable. Provided that future quasi-static nanoindentation duplicate tests follow the same trend, detailed modeling is suggested to understand the disparity between the tensile and nanoindentation load cases.

The baseline indentation moduli can also be compared to manufacturer supplied data. The manufacturer[163] provides a tensile Young's modulus of 2.9 GPa for the RTM6 epoxy system, and this is further confirmed by tensile tests performed by Handlin et al.[100]. E_I for the RTM6 baseline specimen is determined to be $\sim$ 4 GPa, and using Equation 7.4 (note that E_I is used in place of E_r thus $E_s = 0.84E_I$), the calculated modulus of the sample, E_s, is determined to be $\sim$ 3.3 GPa. Regarding EPON 862/W, Zhou et. al[190] offer a tensile Young's modulus of 2.46 GPa, similar to that determined by Kim et al.[191] of 2.72 GPa. The E_I for this EPON 862/W specimen is $\sim$ 2.7 GPa, providing a slightly lower than reported[190,191]

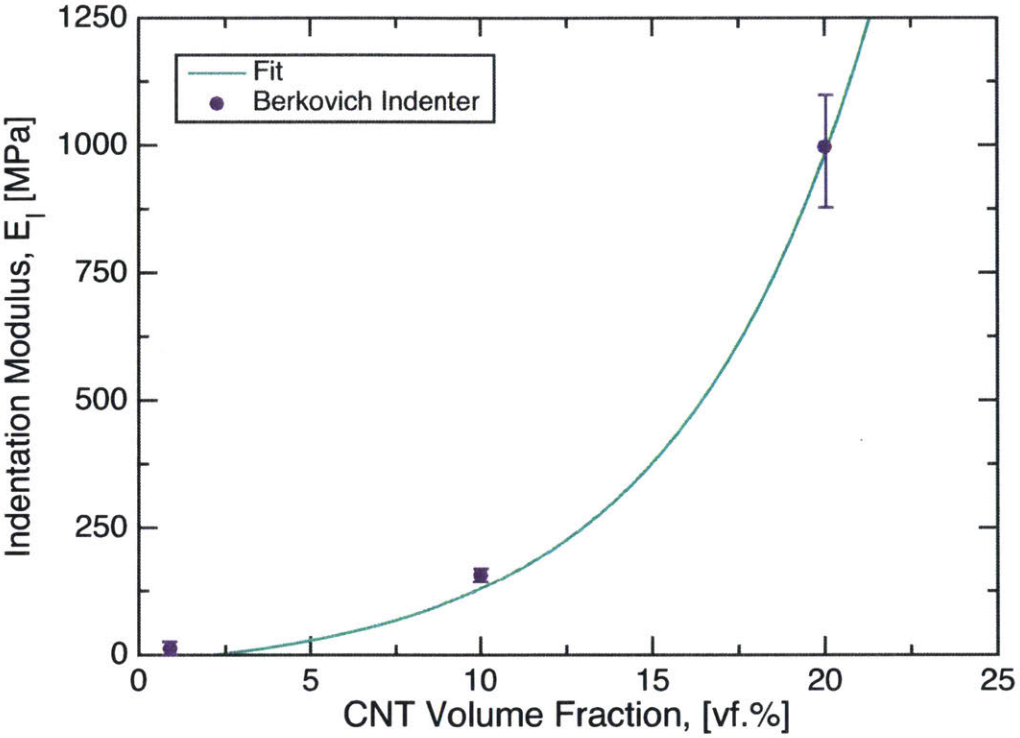

Figure 7-6: Indentation modulus of A-CNT forests increase exponentially with increasing densification (adapted from original[159]).

E_s of ~ 2.3 GPa. As previously mentioned, the data presented herein is preliminary and a single specimen may not be a statistically representative of a fully populated test matrix.

7.3 Dynamic Nanoindentation

Performing dynamic analyses on A-PNCs is of significant interest to establish whether the A-CNTs offer any significant changes to dynamic mechanical properties such as storage (E') and loss (E'') moduli, and tan(δ). In viscoelastic materials E' describes the elastic contribution to material response while E'' describes the viscous contribution[203]. These are defined as:

$$E' = \frac{\sigma_o}{\varepsilon_o} \cos(\delta) \tag{7.6}$$

$$E'' = \frac{\sigma_o}{\varepsilon_o} \sin(\delta) \tag{7.7}$$

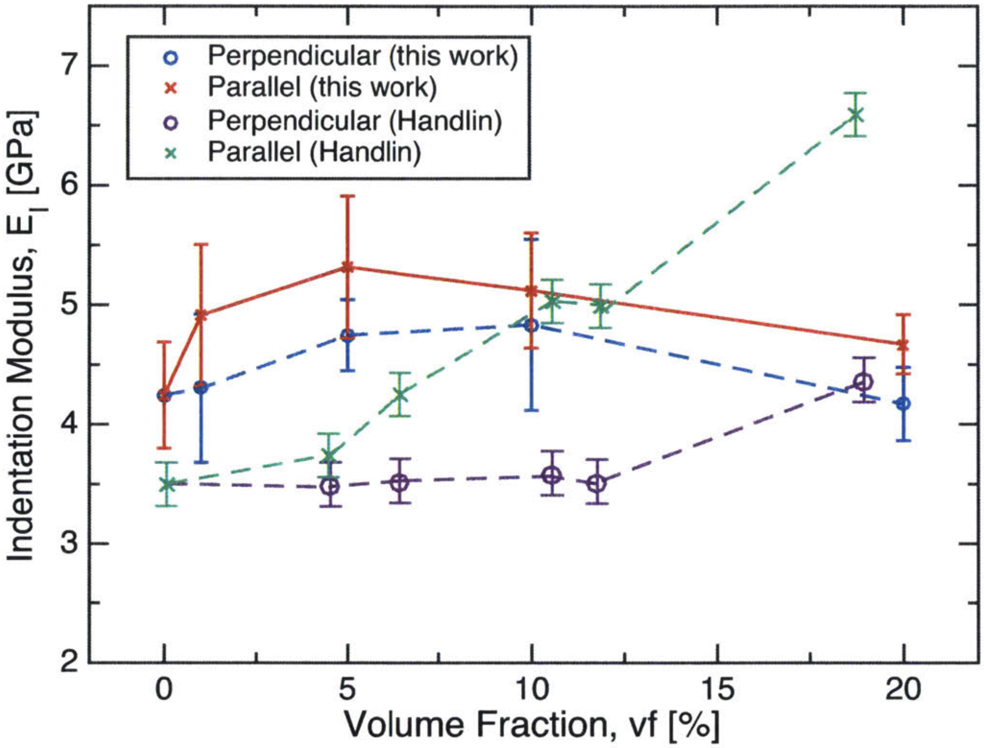

Figure 7-7: Tensile modulus data presented by Handlin[100], compared to indentation modulus, E_I, as a function of volume fraction for RTM6 A-PNC specimens can be performed.

Where σ_o is the dynamic stress, ε_o is the dynamic strain and δ is the phase lag between σ_o and ε_o. From this:

$$\tan(\delta) = \frac{E''}{E'} \tag{7.8}$$

The $\tan(\delta)$ quantifies the way in which a material absorbs and disperses energy. It expresses the out-of-phase time relationship between a dynamic force and the resultant force that is transmitted to the supporting body. Thus, $\tan(\delta)$ quantifies the effectiveness of a material's damping capabilities. The higher the $\tan(\delta)$, the greater the damping coefficient. Dynamic mechanical analysis (DMA) is typically utilized to gather these properties, however, based on the A-PNC dimensional limitations, full scale DMA would be restricted to low volume fraction specimens. NanoDMA, on the other-hand, requires samples with dimensions on the order of hundreds of microns. A challenge with nanoDMA is that a ~ 1 μm area is tested (note that A-CNT spacing is 80 nm at 1 vf.%) at a given time which can result in highly variable data, especially at low volume fraction samples where capillary densification causes resin rich regions between A-PNC pillars as seen in Chapter 6. A resin rich region will have a lower Young's modulus than that of the A-PNC pillar, as shown by quasi-static nanoindentation, and it is likely that the dynamic properties will vary accordingly. This can, however, be mitigated by collecting data over various regions of the cryomicrotomed surface. In this work, 3 × 3 grids with 5 μm center-to-center spacing between each point (9 data points) are collected at three different locations (27 points per specimen). Testing is done using a step-wise frequency sweep from 1 Hz to 200 Hz with a 10 Hz increments, and at each increment, 200 cycles are performed[197]. As previously mentioned cycling is performed with a dynamic amplitude of 5 nm created by an oscillating 50 μN load.

EPON 862/W

Storage modulus for EPON 862/W with various volume fractions is presented as a function of frequency in Figure 7-8. For both the parallel (Figure 7-8a) and perpendicular (Figure 7-8b) orientations, it is seen that the addition of A-CNTs increases the storage modulus. This result is anticipated as the A-CNTs increase stiffness in A-PNCs, as shown from quasi-static nanoindentation presented in Figure 7-4. Because storage modulus is frequency independent, the data can more easily be seen in Figure 7-9 where average storage modulus is presented as a function of volume fraction. With the exception of the 10 vf.% perpendicular test, the storage modulus data follows a similar trend to that shown by quasi-static nanoindentation tests. Note that there is a statistically insignificant difference between the 1 vf.% and baseline, and it is thought that the waviness and inter-CNT spacing exhibited by the 1 vf.% A-CNT forest results in a coil type compression as opposed to a more columnar type compression that is expected from the less wavy, more densely packed densified forests, limiting the the effectiveness of 1 vf.% A-CNT loading on stiffness.

While loss modulus is presented in Figure 7-10, the damping capabilities are more easily explained using tan(δ) as presented in Figure 7-11. With the exception of 1 vf.%, Figure 7-11a and b, show that increasing A-CNT volume fractions reduces tan(δ). Thus, as a general statement, less damping is offered with the addition of $>$ 1 vf.% A-CNTs. tan(δ) decreases with the addition of the reinforcement because the relaxation amplitude of polymer chain segments are locally restricted due to the presence of the > 1 vf.% A-CNTs. With regards to the increased $\tan(\delta)$ value of the 1 vf.% A-PNC specimen, more specifically in the parallel orientation: if the assumption that waviness and inter-CNT spacing offers a more coil type compression rather than a column type compression, increased damping capabilities are likely. With the reduction of waviness and interstitial spacing, the column type loading of the A-CNTs will restrict the viscoelastic behavior due to the decreasing load carried by the matrix with increasing volume fraction. Two exceptions to this rule appear to exist: 10 vf.% in the parallel orientation and 20 vf.% in the perpendicular orientation. As described for nanoindentation where a local minimum occurs in E_I at $\sim$ 20 vf.%, A-CNT spacing in this range (densification variation is additionally probable) is possibly preventing long chain formation and restricts complete cross-linking. With a decrease in cross linking, damping capability would be expected to increase (beyond that seen for the 5-10 vf.% range) for the load share taken by the matrix. Again, by further increasing the A-CNT volume fraction to $\sim$ 30 vf.%, the A-CNT interstitial spacing decreases to a point where majority of the load is carried by the A-CNTs, irrespective of the decreased load carrying capabilities of the matrix. Additionally, for all cases, $\tan(\delta)$ and loss modulus decrease with increasing frequency indicating a high rate stiffening response is present where the loss modulus decreases relative to the storage modulus.

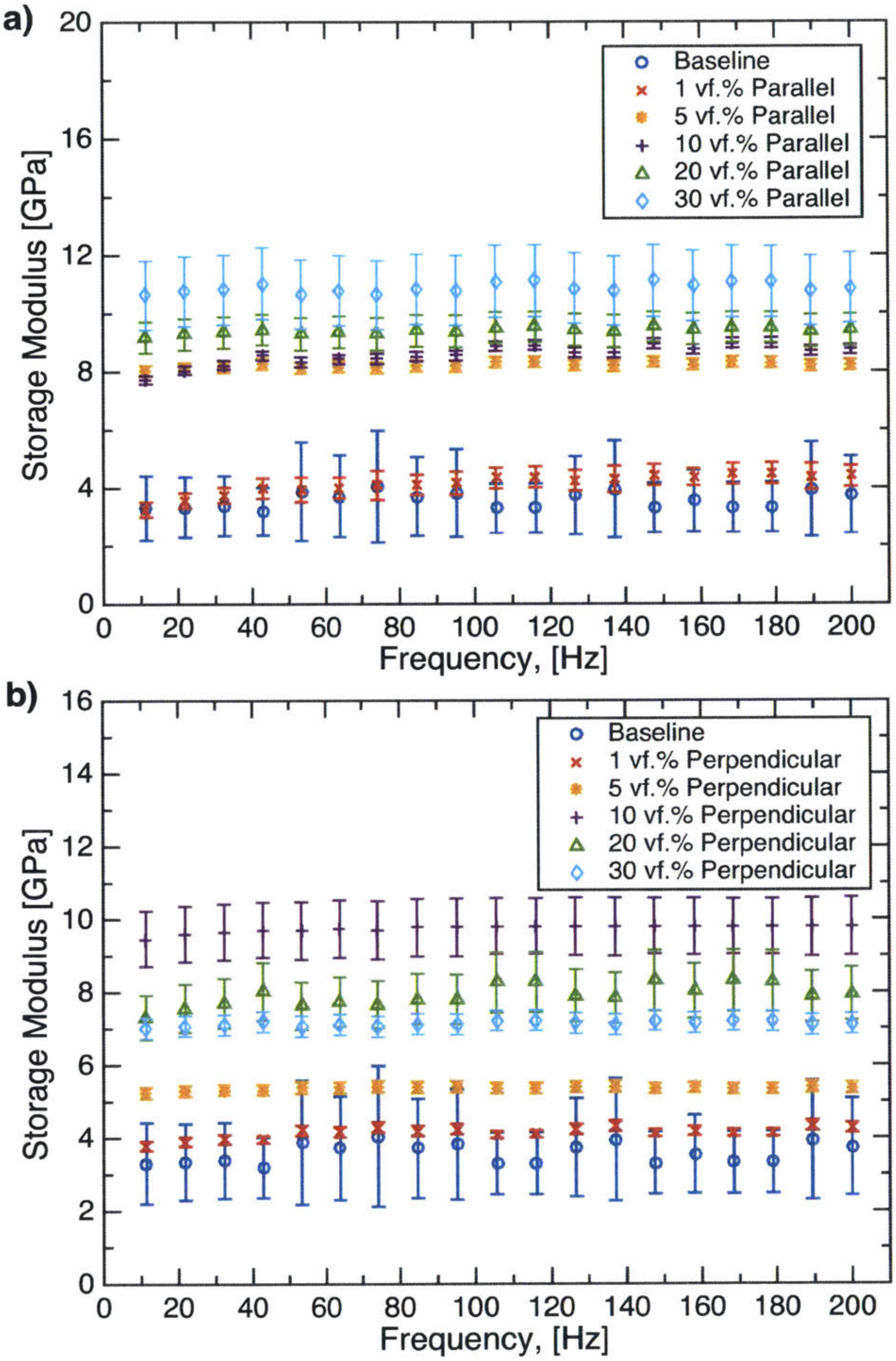

Figure 7-8: A statistically significant increase over EPON 862/W baseline specimens is achieved with the addition of A-CNTs in both the a) parallel and b) perpendicular orientations. Note that storage modulus appears to be insensitive to frequency.

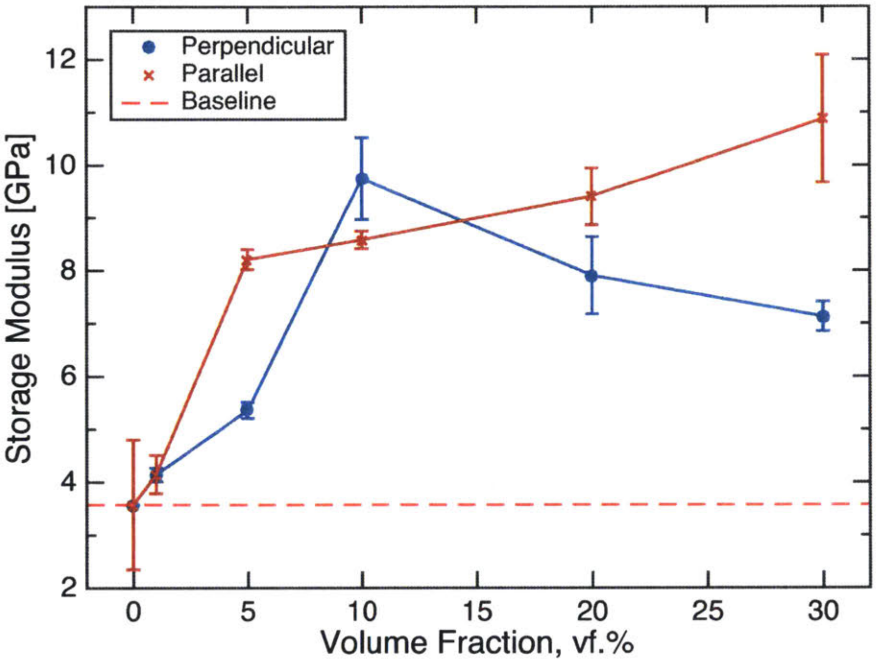

Figure 7-9: Due to the rate insensitivity of storage modulus as shown in Figure 7-8, average storage modulus as a function of volume fraction can be shown, elucidating the contributions offered by the various volume fraction A-CNTs to the EPON 862/W A-PNCs.

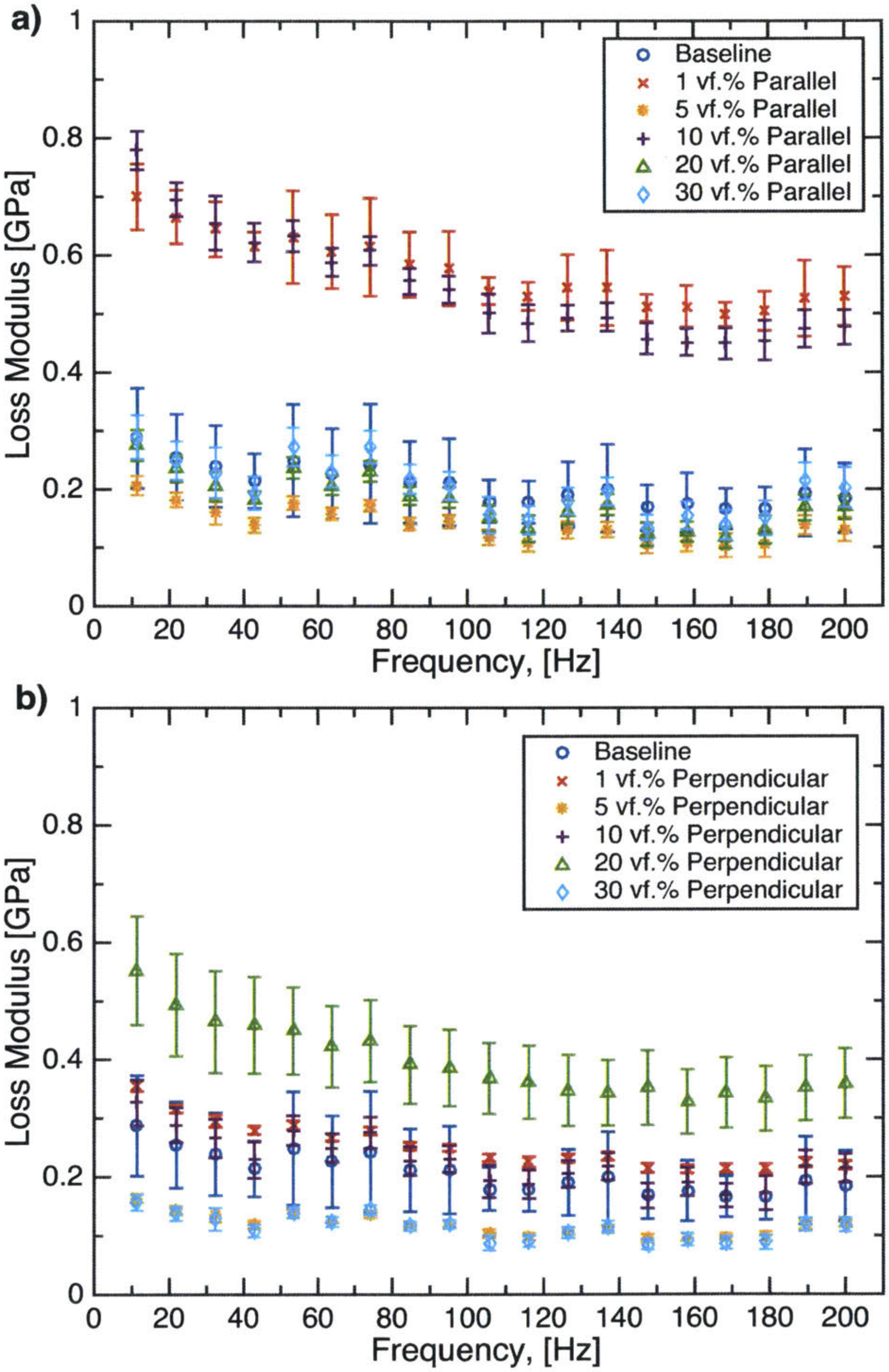

Figure 7-10: EPON 862/W A-PNC loss modulus as a function of frequency.

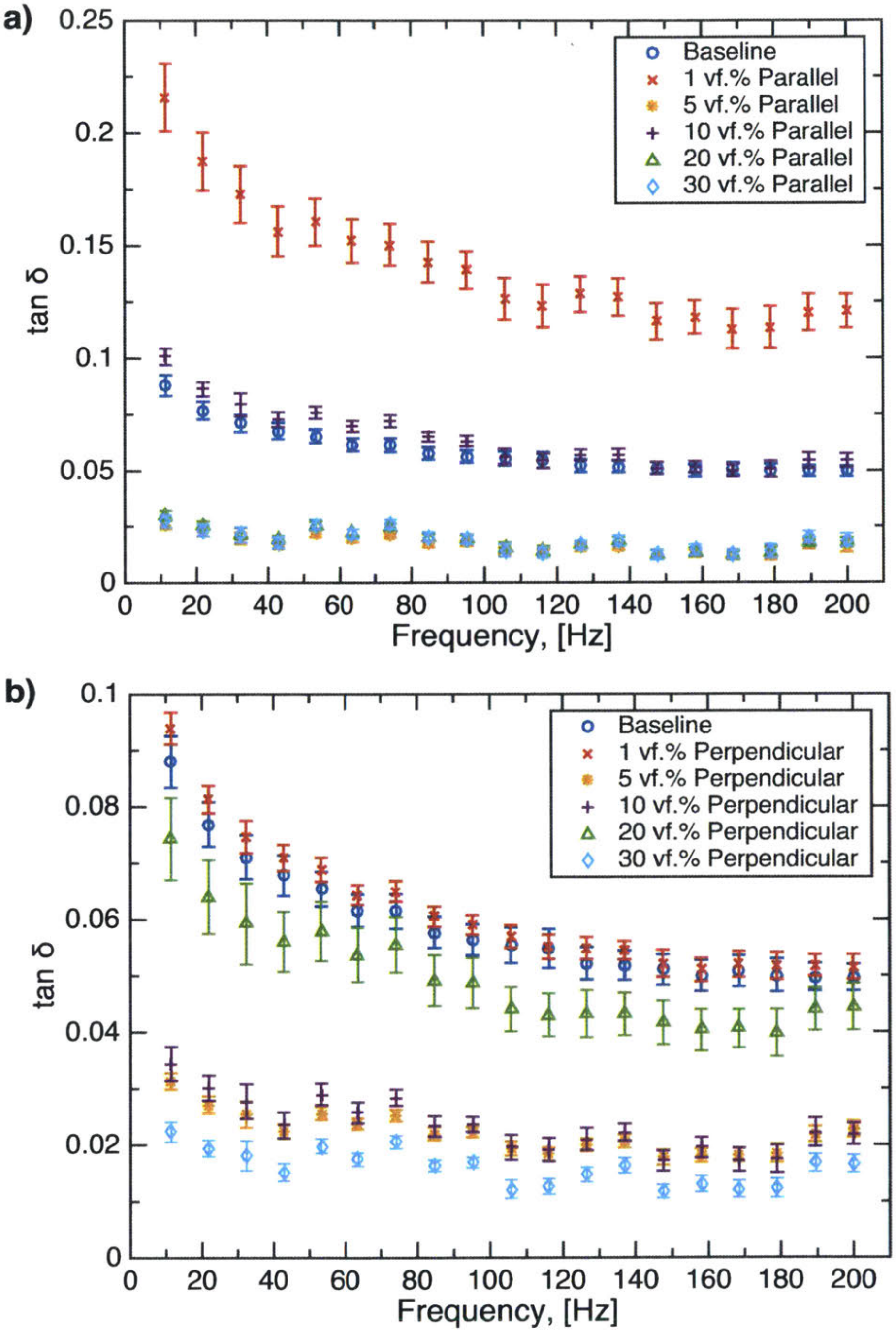

Figure 7-11: tan(δ) for EPON 862/W A-PNC specimens shows that, with the exception of 1 vf.% A-CNTs, damping capability is decreased with the addition of A-CNTs. Additionally rate stiffening behaviour can be seen by the decreasing tan(δ) with increasing frequency.

RTM6

Storage modulus results for RTM6 A-PNCs are shown in Figure 7-12. Similar to the EPON 862/W specimens, storage modulus is rate independent in the tested range and the effects of increased A-CNT volume fraction can more easily be seen in Figure 7-13 where the same trend for quasi-static nanoindentation is observed as in the nanoDMA data (see Figure 7-5). Note that the data points for the 1 vf.% perpendicular orientation at 32.4, 105.7, 116.2, and 168.6 Hz have been removed owing to the large variations observed in Figure 7-12, as these are not representative of typical storage modulus values. Loss modulus and tan(δ) are shown in Figure 7-14 and Figure 7-15, respectively. From these plots, RTM6 appears to be frequency insensitive permitting the production of Figure 7-16a and Figure 7-16b where A-CNT contribution is more clearly elucidated. Again, the large variation points observed for the 1 vf.% perpendicular orientation at 32.4, 105.7, 116.2, and 168.6 Hz have been removed from the loss modulus average, this is unnecessary for tan(δ) as the observation scales for both storage and loss modulus. When considering the RTM6 A-PNC average loss modulus as a function of volume fraction, the same trend is observed as for the storage modulus in both orientations, where the A-CNTs offer a $\sim$ 40% and $\sim$ 6% increase, respectively, over the baseline specimen. There is no statistically significant difference in tan(δ) over baseline for either loading orientation, and this suggests that the effects of the A-CNTs scale both the storage and loss moduli equally.

Attention must be drawn to the large variation seen in the 1 vf.% perpendicular orientation in the storage and loss moduli, more clearly highlighted in Figure 7-17. This peculiar observation was initially thought to be caused by an error in data collection. However, careful observation of the 32.4, 105.7, 116.2, and 168.6 Hz frequencies (especially prominent in Figure 7-15) for all specimens appear to have statistically significant peaks at these frequency locations. More samples must be tested to confirm this observation, however, given the appearance of these peaks for all specimens, it is speculated that this is a matrix specific resonance response that is being amplified with the addition of 1 vf.% A-CNTs when tested in the perpendicular orientation. The occurrence of peaks at both 105.7 and 116.2 Hz could be explained as peak straddling, as shown in Figure 7-18 (reproduced[204]).

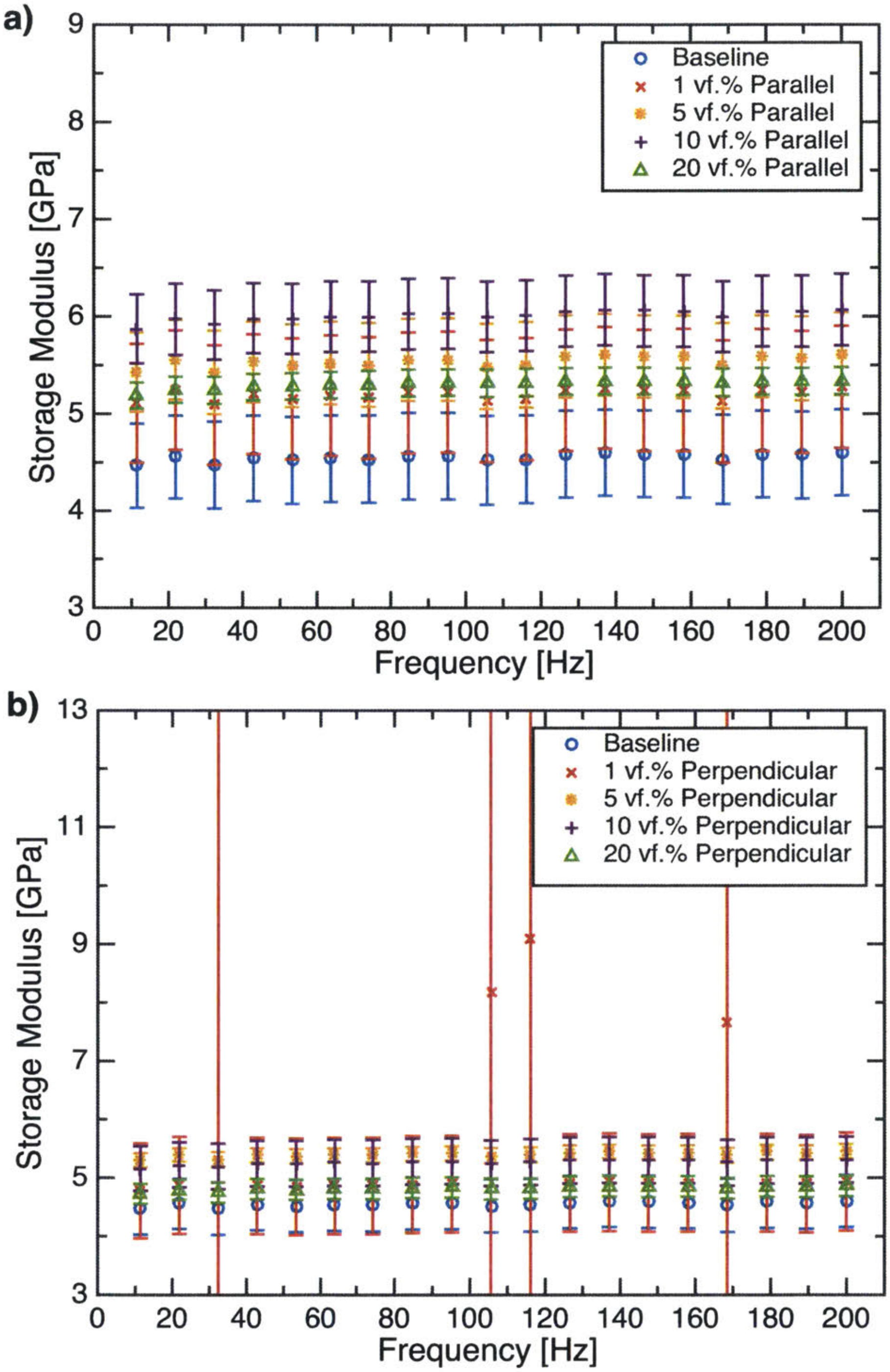

Figure 7-12: Storage modulus of a) parallel and b) perpendicular RTM6 A-PNC specimens of various volume fractions showing across-the-board improvement over baseline with the addition of A-CNTs.

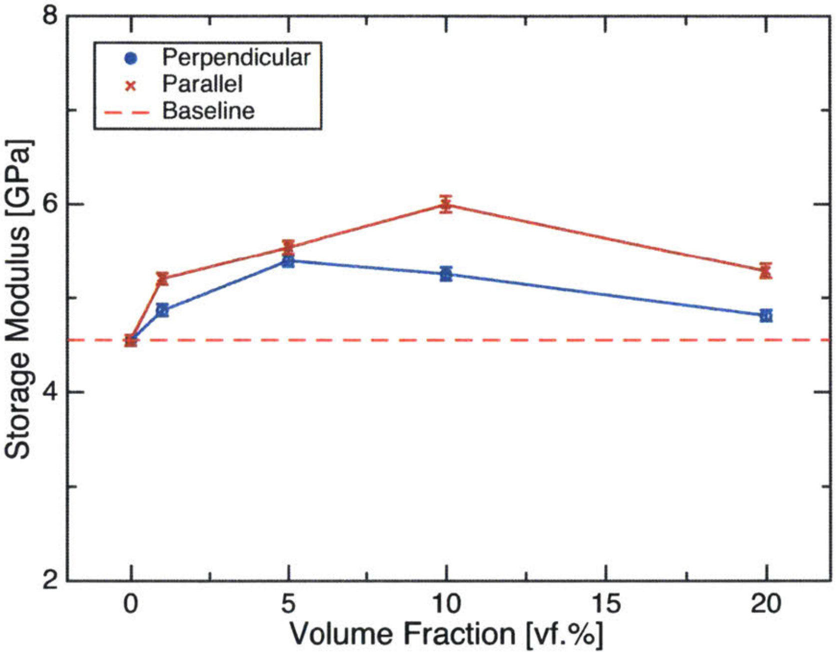

Figure 7-13: Comparison of average storage moduli for the parallel and perpendicular orientations of RTM6 A-PNCs as a function of volume fraction where the parallel orientation is seen to offers increased improvements over the perpendicular orientation. Additionally a local minimum occurs at $\sim$ 20 vf.% which is likely due to polymer confinement preventing cross-linking.

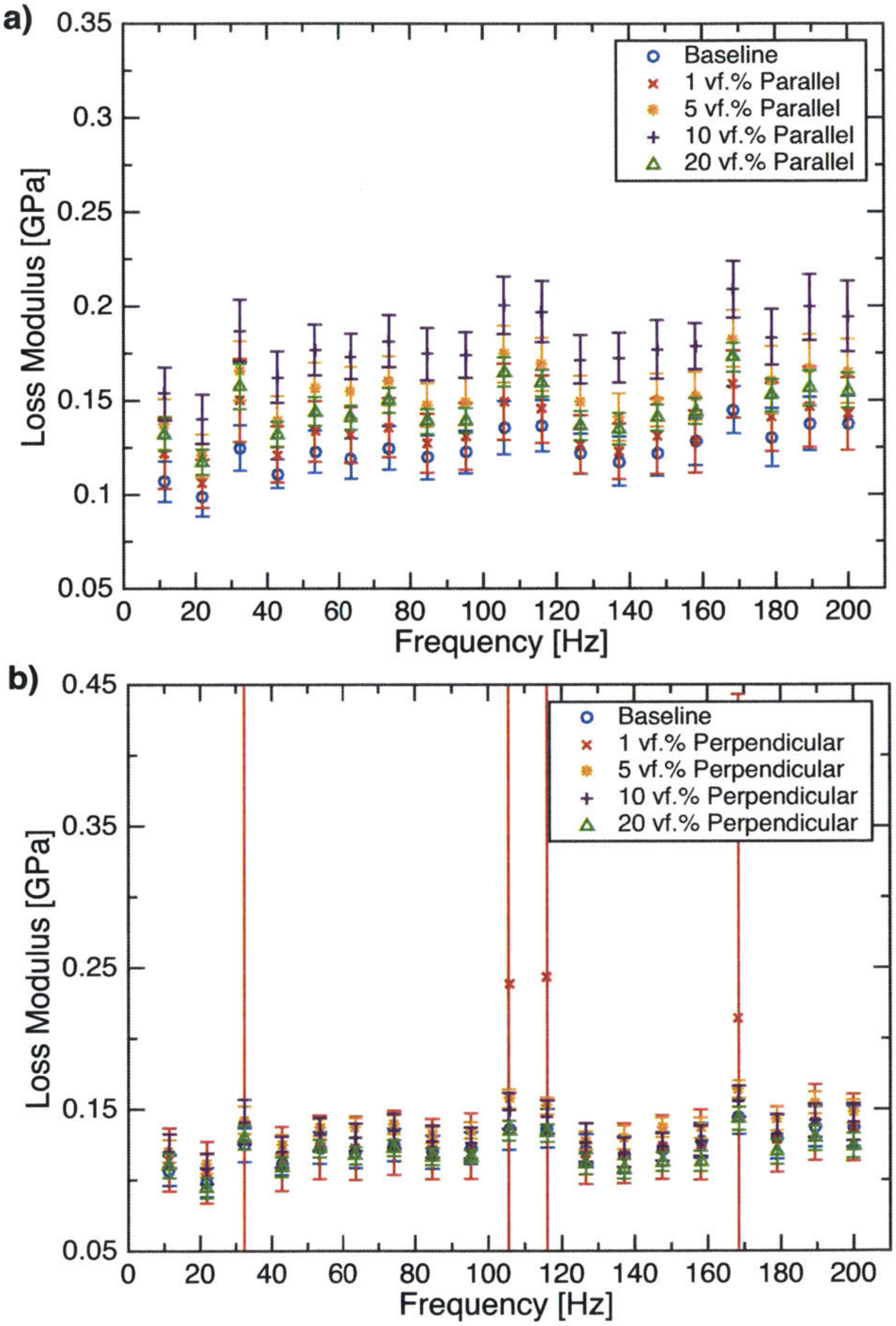

Figure 7-14: Loss modulus appears frequency independent in both the a) parallel and b) perpendicular orientations for RTM6 A-PNCs of various volume fractions. It can be seen that A-CNTs offer marginal loss modulus improvements over baseline in all A-PNCs.

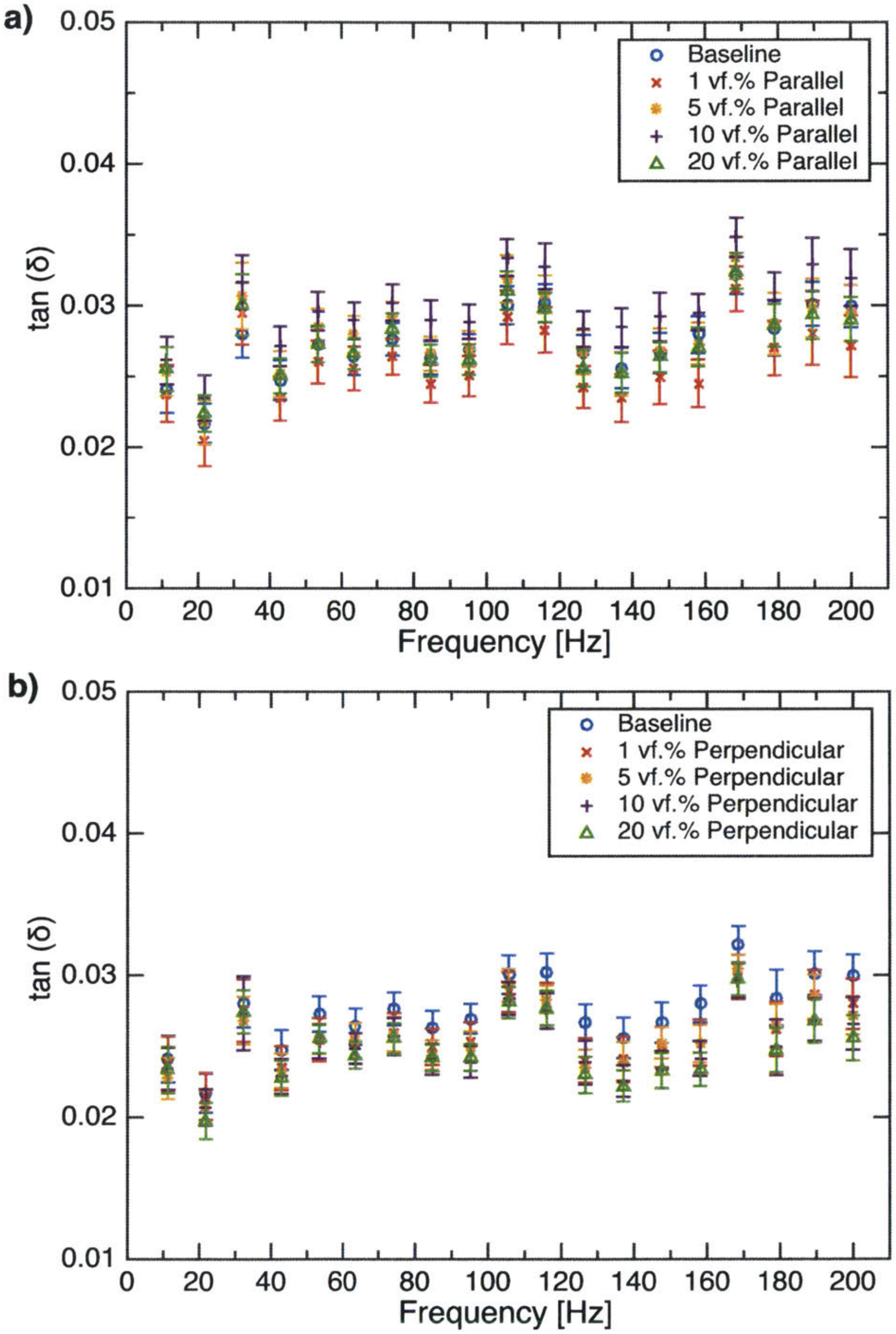

Figure 7-15: $\tan(\delta)$ for RTM6 A-PNC specimens of various volume fraction in the a) parallel and b) perpendicular orientation. It can be seen that $\tan(\delta)$ is frequency independent, within error.

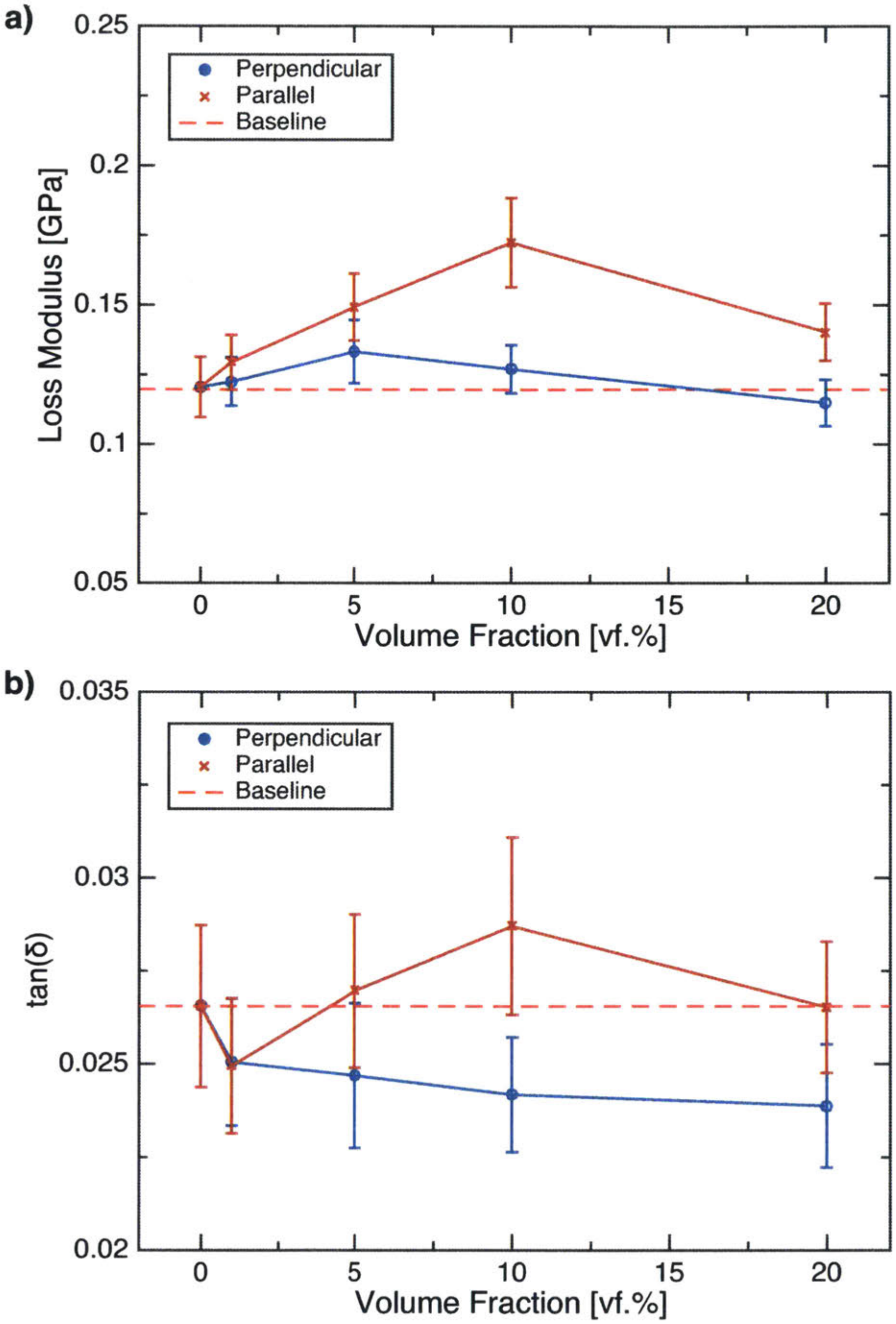

Figure 7-16: Frequency independent a) average loss modulus and b) average $\tan(\delta)$ more easily show the effect of A-CNT loading on the dynamic mechanical properties of RTM6 A-PNC specimens. Loss modulus is improved over baseline following a similar trend as storage modulus where the parallel orientation has more pronounced effects of the perpendicular orientation. There is no statistically significant difference in $\tan(\delta)$ when baseline is compared to A-PNCs, suggesting increases in loss modulus and storage modulus scale equally.

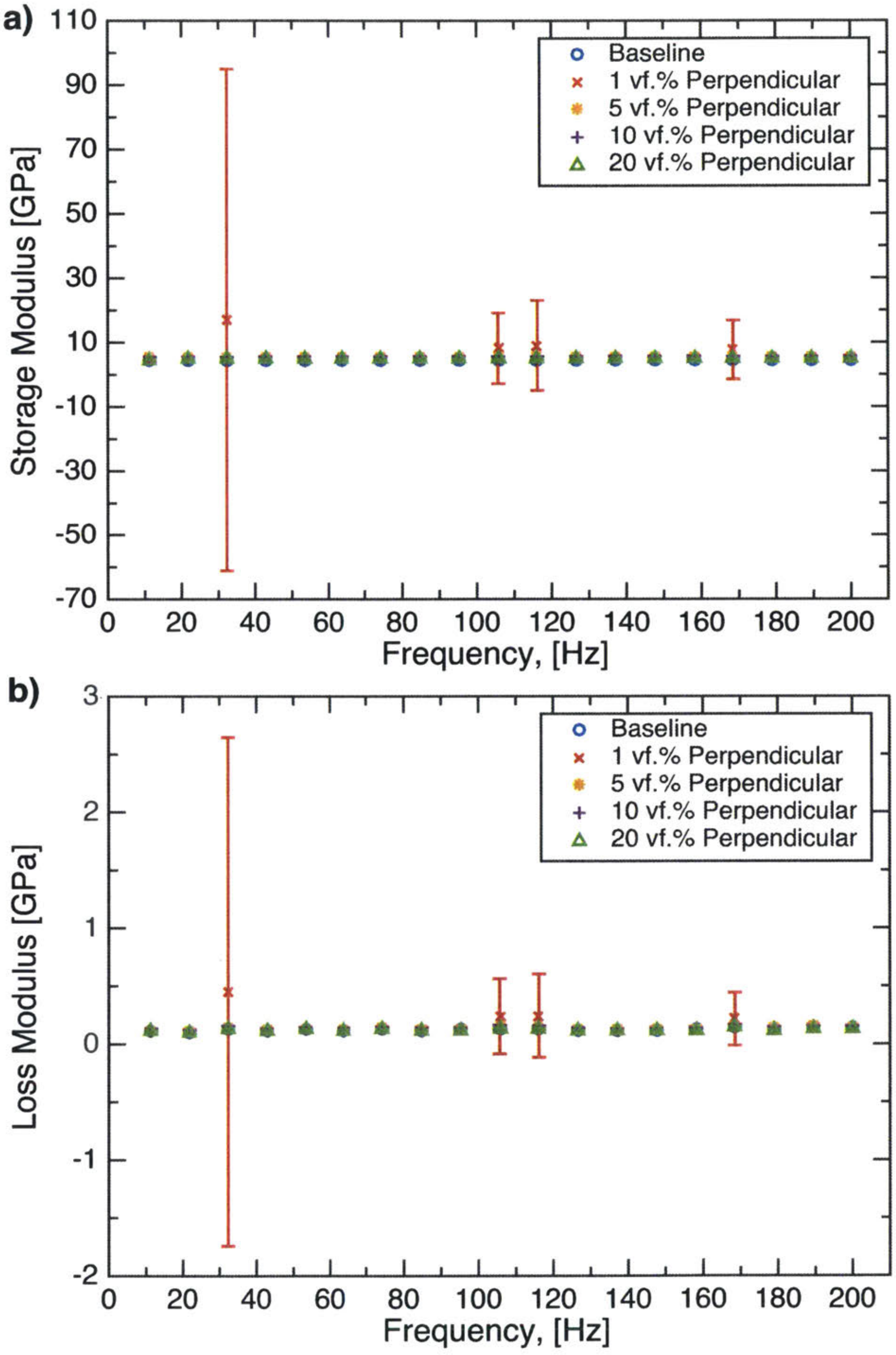

Figure 7-17: Full-scale a) storage and b) loss moduli for RTM6 A-PNCs of various volume fraction in the perpendicular orientation showing the large variation at 32.4, 105.7, 116.2, and 168.6 Hz for 1 vf.% A-CNT loading.

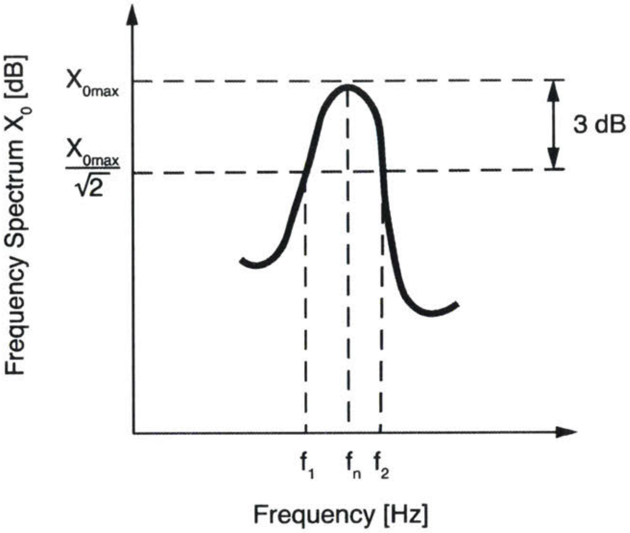

Figure 7-18: Illustration of a resonance peak, reproduced[204], presenting a possible explanation for the large variation observed at 105.7 Hz and 116.2 Hz in the 1 vf.% perpendicular RTM6 A-PNC.

RTM6 and EPON 862/W micromechanical testing shows that A-CNTs offer different effects to these two different epoxy systems. One commonality is that storage modulus is independent of frequency, and follows a similar profile as that seen in quasi-static nanoindentation testing where a local minimum occurs at ~ 20 vf.% A-CNT loading. It is thought that as interstitial space between the A-CNTs decrease, long chain formation is prevented causing increased compliance of the matrix, decreasing load carrying capabilities. Further increasing the A-CNT loading to ~ 30 vf.%, again increases indentation and storage moduli, attributed to the exponential increase in A-CNT forest modulus (as shown by Cebeci et. al[159]) compensating for the suspected decreased in the matrix stiffness. Performing thermal characterizations on the A-PNC samples may elucidate the origin of these findings.

7.4 Thermogravimetric Analysis

The thermal behavior of the synthesized polymer nanocomposites are shown in the TGA thermograms for EPON 862/W and RTM6 in Figure 7-19a and Figure 7-19b, respectively. The decomposition onset temperature of the A-PNCs are unaffected by the presence of

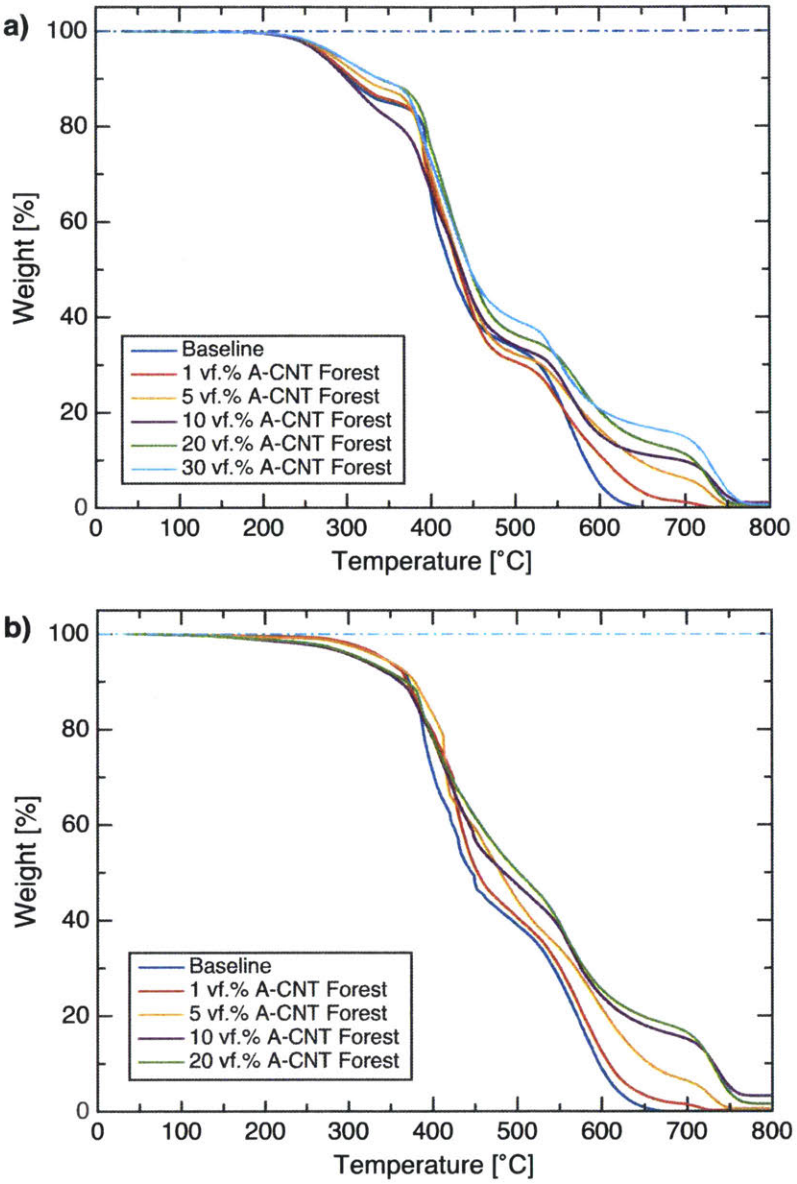

Figure 7-19: TGA thermograms for a) EPON 862/W and b) RTM6 A-PNCs of various volume fractions. For EPON 862/W, thermal degradation of the matrix begins at ~ 200°C, and for RTM6, this occurs at ~ 250°C. In both cases, the A-CNTs lose thermal stability from ~ 550°C, consistent with previously discussed TGA of the A-CNT forest alone.

the A-CNTs. In addition, all EPON 862/W nanocomposites are found to be stable up to ~ 200°C. And, for RTM6 the onset of thermal degradation begins at ~ 200°C, however it can be argued that significant mass loss only begins at ~ 250°C. In both polymer systems, the A-CNT degradation begins at ~ 550°C and ends at ~ 750°C, consistent with observations made for A-CNT forests in Chapter 4. From Figure 7-19a and Figure 7-19b, the A-CNT loading shows an expected trend with A-CNTs contributing more to the mass percentage of the specimen with increasing volume fraction, this is most noticeable between $\sim$ 650°C and $\sim$ 700°C.

A general comment must be made that the mass fraction of A-CNTs should scale with volume fraction, and more significant A-CNT mass contributions should be observed for the higher volume fraction A-PNCs, i.e., $\geq$ 10 vf.%. The less than expected volume fraction might be attributed to expansion of the A-CNT forest during infiltration and curing, and likely explains the E_I and storage modulus rule-of-mixtures disparity. However, A-CNT expansion may not be uniform within the A-PNC specimen as a result of possible non-uniform densification. Thus, because the A-PNCs were divided into three separate specimens, a conclusive link between the three tests is only speculative. Care must be taken in the manufacture of future A-PNC specimens to more accurately track final specimen dimension which may be used to infer final volume fraction.

7.5 Differential Scanning Calorimetry

As mentioned in Chapter 5, EPON 862/W has a fully cured T_g of $\sim$ 150°C[162] while RTM6 shows a fully cured T_g of $\sim$ 200°C[163]. Thus, DSC scans are performed such that the temperature ranges from -90°C to slightly before the onset of significant degradation as determined by TGA, so that this range includes the matrix T_g.

DSC thermograms are shown in Figure 7-20a and Figure 7-20b for EPON 862/W and RTM6 A-PNCs, respectively. The glass transition behavior of the pure epoxy and nanocomposites cannot be seen and future work in using thermal nanoDMA is needed to determine whether A-CNTs affect T_g behavior.

The behavior exhibited by both polymers is similar with two main features: a low temperature peak (enclosed by the black dashed line) that develops with mid-range A-CNT loading and the higher temperature escarpment that flattens with increasing A-CNT loading. The low temperature peak that occurs between -40°C and -60°C in EPON 862/W, and -45°C

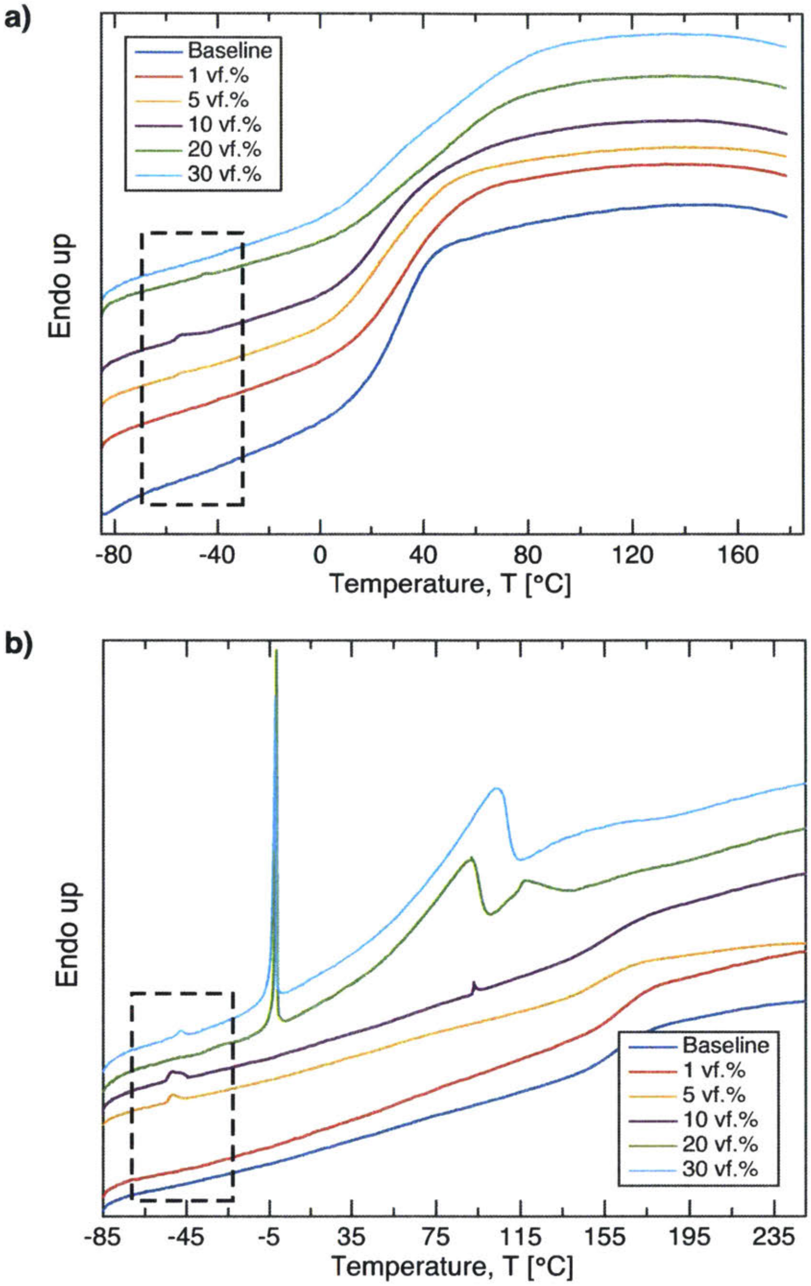

Figure 7-20: Second pass DSC thermograms for a) EPON 862/W and b) RTM6 A-PNCs show the development of a beta transition peak at low temperature (enclosed by the dashed line) for 5-20 vf.% A-CNT loading. Additionally a flattening of the high temperature transition occurs with increasing A-CNT volume fraction likely due to a decreasing chain molecular weight resulting from confinement effects.

and −65°C in RTM6 is likely a beta transition. A beta transition occurs as the temperature and free volume begin to increase, side chains begin to have enough space to move and the material develops some toughness. The beta peak increases with increasing volume fraction of A-CNTs, until a maximum at 10 vf%, after which the peak decreases again. Note that RTM6 DSC scans of the 20 vf.% and 30 vf.% A-PNC are suspected to be contaminated. This beta transition trend is consistent with the hypothesis that there is a point where inter-CNT spacing begins to prevent long chain formation or cross-linking, this will result in more unlinked side chains that will relax at this transition point. The transition that occurs at ~ 40°C in EPON 862/W, and ~ 170°C in RTM6, broadens with increasing A-CNT volume fraction, and is likely due to the increasing inhibition of long chain formation, leading to decreased molecular weight.

7.6 Conclusions

The conclusions drawn from the work presented are preliminary in nature and in order to make more substantive conclusions, data validation with repeat test specimen manufacture is necessary. However preliminary, interesting mechanical and thermal property responses are observed in both the RTM6 and EPON 862/W specimens. Both quasi-static and dynamic nanoindentation results, in both polymer systems, present a general trend (primarily in the parallel orientation) where the addition of A-CNTs offer indentation, storage and loss moduli increases over baseline to a local maximum at ~ 10 vf.% due to A-CNT/matrix "better-than-both" interactions. However, as A-CNT interstitial spacing decreases further to ~ 20 vf.%, long chain formation is likely inhibited resulting is excess unlinked side chains. This decrease in cross-linking increases compliance of the matrix, changing the trend observed up to ~ 10 vf.%. Beyond ~ 20 vf.% A-CNT loading in the A-PNCs, the exponentially increasing indentation modulus of a free standing A-CNT forest with increasing volume fraction, as shown by Cebeci et. al[159], likely compensates for the increased compliance of the less crosslinked matrix, and moduli increase again. These effects are supported by DSC where a development of beta transition peaks, associated with side chain relaxation, are seen with increasing volume fraction up to ~ 10 vf.%. This observation supports the hypothesis that small chains are formed with reduced cross-linking (reduced cross-linking leaves more side chains free to relax). Beyond $\sim$ 10 vf.% these beta transition peaks decrease again owing to increased confinement preventing mobility of the unlinked side chains. Additionally, the higher temperature transition (linked to molecular weight reduction), gets progressively flatter further supporting the idea that progressively smaller chains are forming due to confinement.

Chapter 8

Conclusions and Recommendations

RTM6 and EPON 862 A-PNC specimens of various A-CNT volume fractions have been fabricated and tested, both mechanically and thermally. During Mode I fracture toughness testing, these CNT-based nanocomposites show crack deflection, fiber bridging, and pullout, however these toughening mechanisms are insufficient to arrest a crack, and initiation toughness is unaffected by the presence of A-CNTs. While Mode I initiation fracture toughness is unaffected by the A-CNTs (within error), further mechanical testing was done and preliminary specimens show evidence that indentation, storage and loss moduli are increased with the addition of A-CNTs. During the development of specimen manufacturing methods for this work, numerous findings are documented that contribute to the body of knowledge used in the assessment of test data, and provide the foundation for future work.

8.1 Summary of Thesis Contributions

A-CNT Morphology and Growth Envelope

The dimensional limits of A-PNCs are determined by the dimensional limits of the A-CNT forest, as-grown or densified, and maximization of the A-CNT forest height and size, within the bounds of the CVD growth system, was key to specimen geometry planning. Parametric changes in growth conditions have been related to morphological changes in the A-CNT forests through the use of various complementary test techniques, and it is found that increasing growth time increases the A-CNT forest height only up to $\sim$ 5 mm, beyond which vertical growth is terminated[120] (the growth time at this transition is $\sim$ 50 mins). Owing to the base-growth conditions, an accumulation of non-CNT carbon impurities is deposited on the forest with a net thickness increase at the top crust being larger than at the roots. While the increased height is favorable for increased A-PNC dimensions, volume fraction tailoring, through mechanical densification, cannot be performed due to the the stiffness gradient that exists over the height. Thus, with the intention of A-CNT densification, forests $<$ 2 mm (growth time at $\sim$ 20 mins) are more appropriate. If cm-scale A-PNCs are required, uniaxial densification is necessary to preserve the A-CNT forest width, which is limited to 2 cm currently, and up to $\sim$ 14 vf.% can be achieved if the initial forest length of 14 cm is densified to 1 cm (assuming a 1 vf.% A-CNTs in the as-grown forest volume). Higher volume fraction A-CNT forests are more easily achieved using $\sim$ 1 mm tall A-CNT forests (growth time at $\sim$ 9 mins) as the above-mentioned stiffness gradient is negligible, allowing biaxial densification up to $\sim$ 30 vf.%.

When considering forests grown for longer than 50 mins (beyond the vertical growth termination point), it has been observed that an increasing amount of carbon impurities are deposited onto the A-CNTs, continuously building up circumferential graphitic layers conformally on the A-CNTs. For example, in a 3 hr growth (i.e., 130 mins beyond termination), the top of the A-CNT forest is almost completely bulked (as in chemical vapor infusion, CVI), leaving no inter-CNT space. Concurrent to the radius increases, a six-fold increase in force is required to remove an 80 min forest from the substrate when compared to the 50 min, likely caused by an accumulation of graphitizing carbon around the catalyst. Future work is required to study the true adhesion mechanism, and further work in actively cementing or releasing an already carbon-cemented A-CNT forest from the wafer, is recommended.

A-PNC Manufacture

Manufacturing of an A-PNC forest consists of two main steps following A-CNT densification, namely infiltration of polymer (herein EPON 862/W or RTM6 epoxies) into the A-CNT forest, and A-PNC curing. The RTM6 cure cycle is provided by the manufacturer[5,100,163] and deviation from this cure cycle is not observed in the literature. On the other-hand, numerous cure cycles are presented in the literature[162,164,166? –168] for EPON 862/W, and a suitable cure cycle for this work is selected by considering degree of cure (DoC) variation within a manufactured specimen using a 2^2 full factorial design with temperatures at 121°C and 177°C, and curing times at 4 hrs and 6 hrs, with center points at 149°C and 5 hrs. The cure cycle with the smallest coefficient of variance in DoC occurs at the upper time boundary of 6 hrs at a temperature of 149°C: this cure cycle is selected, bearing in mind that an A-PNC is typically cured twice when integrated into a larger, e.g., SENB fracture, test specimen.

Following establishment of the cure cycle, infiltration methods are developed to limit A-PNC void content by controlling the infusion parameters: temperature, time and vacuum pressure. A key tool in this process is the utilization of μCT to assess the A-PNC internal structure in a series of iterative infusion experiments. Diluting the epoxy with solvents yields specimens with large voids that are aligned in the densification direction, thus polymer infiltration was performed by decreasing polymer viscosity by temperature alone. Once cured using the selected cure cycle, the A-PNCs are integrated into larger specimens surrounded by polymer to allow full scale testing of the limited-dimension A-PNCs.

A critical aspect in specimen manufacture for Mode I fracture toughness testing is the creation of a sharp precrack. In brittle epoxies, however, destruction of the specimen is frequent when tapping a razor blade in an already machined notch, as suggested by ASTM D5045[84]. Thus a study was performed to assess the notch radius contribution to Mode I initiation toughness (using EPON 862/W specimens). A “natural crack” was only achieved in one specimen, and when compared with samples sharpened by sliding/sawing a razor blade in the machined notch, the $K_{Ic,i}$ was only $\sim$ 7% smaller. For this reason, sharpening by razor sliding/sawing was selected.

Mode I Fracture Toughness

A primary goal of this thesis was to study both Mode I initiation and steady state toughness, however only Mode I initiation toughness results were achieved. Valid EPON 862/W SENB test samples (without voids in the crack path) of 1, 2 and 5 vf.% A-CNT loading (2 mm tall forests) fracture in an unstable brittle manner that cannot be captured using DIC at a frame rate of 1 ms. However, fractography shows A-CNT pull-out of ~ 1 μm indicating that the toughening mechanisms of crack bridging, debonding and pull-out are present. Also shown is that $< 10\%$ of the total expected number of A-CNTs are actually engaged in pullout during the fracture process. High-level calculations of A-CNT (10% engagement of a 5 vf.% A-CNT forest) contribution to toughening show that in RTM6 and EPON 862/W, ΔG_{CNT} is $\sim 200\ \times$ and $\sim 350\ \times$ smaller than G_{epoxy}, respectively. This falls within test error, and is insufficient to arrest a crack. A-CNT pull-out lengths of ~ 7.5 μm would be required, in this test case, to arrest the crack. Preliminary RTM6 A-PNC SENB specimens show increased initiation toughness with the addition of 1 vf.% A-CNTs, beyond which results decrease, likely due to poor specimen quality.

While 2 mm tall A-CNT forests were used for the body of the Mode I toughness testing in the SENB configuration, preliminary CT specimens employed 1 vf.% 5 mm tall forests. During fracture, the crack deflects from the midplane of the specimen to the region of the bottom of the A-CNT forest, irrespective of test sample orientation in the mechanical tester. These samples highlight the effect that the gradient A-CNT forest morphology has on the crack behavior in an A-PNC, which may not be noticeable in A-PNCs employing shorter forests. The increased number density and outer radius (impurities included) at the top of the forest likely creates a stiffer A-PNC locally when compared to the lower density, low impurity region at the bottom of the forest, preferentially driving the crack to the bottom of the A-PNC.

Additional Mechanical and Thermal Properties

While A-CNTs do not significantly contribute to increasing Mode I fracture toughness when added to epoxies in this work, they do increase storage, loss and indentation moduli, as tested by quasi-static and dynamic nanoindentation. Increasing A-CNT volume fraction does not lead to a linear increase in tested moduli, but rather a local maximum is reached at $\sim$ 10 vf.%, followed by a local minimum at $\sim$ 20 vf.%, beyond which moduli increase again. It is suspected that at $\sim$ 10 vf.%, the degree of cross-linking of the polymer begins decreasing and smaller chains are formed as a result of local confinement. At $\sim$ 20 vf.%, the compliance of the matrix increases to a point where load is mainly carried by the A-CNTs, however there is a net decrease as the A-CNT contribution is insufficient at this volume fraction to compensate for the increased matrix compliance[197]. From nanoindentation studies of densified A-CNT forests by Cebeci et.al[159], it is shown that A-CNT indentation modulus increases exponentially with increasing volume fraction. This exponential increase in A-CNT indentation modulus is consistent with the increase in A-PNC moduli after $\sim$ 20 vf.%, where the A-CNTs carry more load, irrespective of the increasing compliance of the epoxy matrix. These hypotheses are supported by DSC, where a low temperature peak associated with side chain relaxation (beta transition), increases in intensity up to $\sim$ 10 vf.% and then decreases. If cross-linking decreases with increasing volume fraction, an increasing amount of side chains will remain unlinked and will increase the side chain relaxation response (increased beta transition peak). It is likely that at $\sim$ 10 vf.%, the interstitial space begins to decrease side chain mobility thus inhibiting relaxation when heated from $-90°$C; the peak will thus being to decrease with increasing volume fraction. Additionally, the flattening of the mid-temperature knee is linked to the molecular weight of the polymer chains, suggesting that chain size decreases with increasing A-CNT loading.

8.2 Recommendations for Future Work

When considering methods to increase the Mode I fracture toughness and cause crack arrest in A-PNCs, key parameters can be tailored, namely; increasing the A-CNT pull-out length, engaging an increased amount of A-CNTs, further reducing the crack notch contribution to initiation toughness, and decreasing residual stress at the crack tip (if present). In this area, recommendations include:

- Increasing the A-CNT pull-out length can likely be achieved through two main avenues: 1) increasing A-CNT strength by decreasing defect density or 2) tailoring the interface to increase the friction of pull-out. Deposition of a polymer "nanosizing" can potentially alter the interface between the A-CNT and the matrix by acting as a compliant interlayer, thereby increasing friction of pullout. Increasing the strength of the A-CNTs by reducing the presence of defects can likely be achieved by a high temperature thermal anneal. By decreasing the number of defects, near-surface fracture will likely be reduced and pull-out length will increase, as well as pullout vf.%.
- Precrack refinement may assist in reducing the slope of $G_(\sigma)$ at initiation. The method of refinement should not alter polymer properties through localized heating, and care must be taken not to plastically deform the crack tip. Optical microscopy using polarized light of pure epoxy specimens that have been crack sharpened may indicate whether this phenomenon is occurring. Thermal anneal of the crack tip may reduce the presence of residual stress, and the crack tip will likely decrease during this process, which is a desirable outcome given the need for a precrack more similar to the ideal natural crack.
- While increasing the A-CNT volume fraction is a possible option to increase pull-out and debonding contributions to toughness, better returns may be achieved by engaging more A-CNTs in the fiber bridging process. It is hypothesized that the low number of A-CNTs that pull out are a result of fiber breakage at the crack surface: interface tailoring by creating a more compliant interlayer or increased A-CNT strength might lead to more A-CNTs being engaged in pullout.

The future work required for the additional mechanical and thermal characterizations consists mainly of specimen repeats for validation of observed trends in TGA, DSC and static and dynamic nanoindentation. Provided that future quasi-static and dynamic nanoindentation tests duplicate this work's results, detailed modeling is suggested to understand the observed mechanistic trends. Also, small angle x-ray scattering (SAXS) would complement DSC data, to establish the causes of the beta transition peak evolution and the flattening of the mid-temp range transition. Attention must be paid to the post-cure dimensions of the resulting A-PNC specimens to better infer the final volume fraction. TGA or 3D TEM tomography could be used to verify approximations of post-cure volume fraction based on final specimen dimensions.

Furthermore, this work highlights that the addition of A-CNTs to create multiscale composites might involve more complex relationships between the micro and nanoscales as no improvements to initiation toughness of A-PNCs (a representative volume element of the reinforced hierarchical composite interface) are observed. The outcome aside, the study of A-PNCs alone is an exciting field, and the future work listed here outlines the next steps to in the development of A-PNCs for utilization in multifunctional applications. The development of manufacturing techniques and expanding the A-CNT growth envelope (with associated morphologies) will enable further research on engineering A-PNCs using a variety of polymeric systems, with many applications and avenues for exploration.

Bibliography

[1] Airbus. Airbus continues to play major role in composites revolution. *Airbus Press Centre*, 2009.

[2] B. Lu. The Boeing 787 Dreamliner: Designing an Aircraft for the Future. *Journal of Young Investigators*, 2010.

[3] T. Chady. Airbus versus Boeing - Composite Materials: The sky's the limit. *Le Mauricien*, 2013.

[4] Aviation Safety. Status of FAA's Actions to Oversee the Safety of Composite Airplanes. *Aviation Safety*, 2011.

[5] S. S. Wicks. *Manufacturing and Fracture of Hierarchical Composite Materials Enhanced with Aligned Carbon Nanotubes.* PhD thesis, Massachusetts Institute of Technology, 2014.

[6] L. Scelsi, M. Bonner, A. Hodzic, C. Soutis, C. Wilson, R. Scaife, and K. Ridgway. Potential Emissions Savings of Lightweight Composite Aircraft Components Evaluated through Life-cycle Assessment. *Express Polymer Letters*, 5(3):209–217, 2011.

[7] J. R. Duflou, Y. Deng, K. Van Acker, and W. Dewulf. Do Fiber-reinforced Polymer Composites Provide Environmentally Benign Alternatives? A Life-cycle Assessment-based study. *MRS Bulletin*, 37(4):374–382, 2012.

[8] K. Lu. The Future of Metals. *Science*, 328(5976):319–320, 2010.

[9] T. Dursun and C. Soutis. Recent Developments in Advanced Aircraft Aluminium Alloys. *Materials & Design (1980-2015)*, 56:862 - 871, 2014.

[10] C. Soutis. Fibre Reinforced Composites in Aircraft Construction. *Progress in Aerospace Sciences*, 41(2):143 - 151, 2005.

[11] J. N. Coleman, U. Khan, W. J. Blau, and Y. K. Gun'ko. Small but Strong: A Review of the Mechanical Properties of Carbon Nanotube–Polymer Composites. *Carbon*, 44(9):1624–1652, 2006.

[12] B. E. Kilbride, J.N. Coleman, J. Fraysse, P. Fournet, M. Cadek, A. Drury, S. Hutzler, S. Roth, and W. J. Blau. Experimental Observation of Scaling Laws for Alternating

Current and Direct Current Conductivity in Polymer-carbon Nanotube Composite Thin Films. *Journal of Applied Physics*, 92(7):4024–4030, 2002.

[13] B. Lee, Y. Baek, M. Lee, D. Jeong, H. Lee, J. Yoon, and J. Kim. A Carbon Nanotube Wall Membrane for Water Treatment. *Nature Communications*, 6, 2015.

[14] J. Aizenberg, J. C. Weaver, M. S. Thanawala, V. C. Sundar, D. E. Morse, and P. Fratzl. Skeleton of Euplectella sp.: Structural Hierarchy from the Nanoscale to the Macroscale. *Science*, 309(5732):275–278, 2005.

[15] P. Fratzl and R. Weinkamer. Nature's Hierarchical Materials. *Progress in Materials Science*, 52(8):1263 – 1334, 2007.

[16] U. G. K. Wegst, H. Bai, E. Saiz, A. P. Tomsia, and R. O. Ritchie. Bioinspired Structural Materials. *Nat Mater*, 14(1):23–36, 01 2015.

[17] F. Inam, D. W. Y. Wong, M. Kuwata, and T. Peijs. Multiscale Hybrid Micro-nanocomposites based on Carbon Nanotubes and Carbon Fibers. *J. Nanomaterials*, 2010:9:1–9:12, January 2010.

[18] H. Qian, G. Kalinka, K. L. A. Chan, S. G. Kazarian, E. S. Greenhalgh, A. Bismarck, and M. S. P. Shaffer. Mapping Local Microstructure and Mechanical Performance around Carbon Nanotube Grafted Silica Fibres: Methodologies for Hierarchical Composites. *Nanoscale*, 3:4759–4767, 2011.

[19] S. S. Wicks, R. Guzmán de Villoria, and B. L. Wardle. Interlaminar and Intralaminar Reinforcement of Composite Laminates with Aligned Carbon Nanotubes. *Composites Science and Technology*, 70(1):20 – 28, 2010.

[20] Q. Zhang, J. Liu, R. Sager, L. Dai, and J. Baur. Hierarchical Composites of Carbon Nanotubes on Carbon Fiber: Influence of Growth Condition on Fiber Tensile Properties. *Composites Science and Technology*, 69(5):594 – 601, 2009.

[21] E. Bekyarova, E. T. Thostenson, A. Yu, H. Kim, J. Gao, J. Tang, H. T. Hahn, T.W. Chou, M. E. Itkis, and R. C. Haddon. Multiscale Carbon Nanotube–Carbon Fiber Reinforcement for Advanced Epoxy Composites. *Langmuir*, 23(7):3970–3974, 2007.

[22] J. Blanco, R. G. García, E.J.and Guzmán de Villoria, and B. L. Wardle. Limiting Mechanisms of Mode I Interlaminar Toughening of Composites Reinforced with Aligned Carbon Nanotubes. *Journal of Composite Materials*, 43(8):825–841, 2009.

[23] R. B. Pipes and N. J. Pagano. *Interlaminar Stresses in Composite Laminates Under Uniform Axial Extension*, pages 234–245. Springer Netherlands, Dordrecht, 1994.

[24] I. Y. Stein. *Impact of Morphology and Confinement Effects on the Properties of Aligned Nanofiber Architectures.* PhD thesis, Massachusetts Institute of Technology, 2016.

[25] N. Yamamoto, R. Guzmán de Villoria, and B. L. Wardle. Electrical and Thermal Property Enhancement of Fiber-reinforced Polymer Laminate Composites through Controlled Implementation of Multi-walled Carbon Nanotubes. *Composites Science and Technology*, 72(16):2009 – 2015, 2012.

[26] V. P. Veedu, A. Cao, X. Li, K. Ma, C. Soldano, S. Kar, P. M. Ajayan, and M. N. Ghasemi-Nejhad. Multifunctional Composites using Reinforced Laminae with Carbon Nanotube Forests. *Nat Mater*, 5(6):457–462, 06 2006.

[27] I. Y. Stein, D. J. Lewis, and B. L. Wardle. Aligned Carbon Nanotube Array Stiffness from Stochastic Three-dimensional Morphology. *Nanoscale*, 7(46):19426–19431, 2015.

[28] J. P. Salvetat, J. M. Bonard, N. H. Thomson, A. J. Kulik, L. Forró, W. Benoit, and L. Zuppiroli. Mechanical Properties of Carbon Nanotubes. *Applied Physics A*, 69(3):255–260, 1999.

[29] J. P. Salvetat-Delmotte and A. Rubio. Mechanical Properties of Carbon Nanotubes: A Fiber Digest for Beginners. *Carbon*, 40(10):1729 – 1734, 2002. Carbon Nanotubes: The Present State.

[30] X. L. Xie, Y. W. Mai, and X. P. Zhou. Dispersion and Alignment of Carbon Nanotubes in Polymer Matrix: A review. *Materials Science and Engineering: R: Reports*, 49(4):89 – 112, 2005.

[31] Q. Wang, J. Dai, W. Li, Z. Wei, and J. Jiang. The Effects of CNT Alignment on Electrical Conductivity and Mechanical Properties of SWNT/Epoxy Nanocomposites. *Composites Science and Technology*, 68(7):1644–1648, 2008.

[32] E. J. Garcia, B. L. Wardle, and A. J. Hart. Joining Prepreg Composite Interfaces with Aligned Carbon Nanotubes. *Composites Part A: Applied Science and Manufacturing*, 39(6):1065 – 1070, 2008.

[33] V. P. Veedu, A. Cao, F. X. Li, K. Ma, C. Soldano, S. Kar, P. M. Ajayan, and M. N. Ghasemi-Nejhad. Multifunctional Composites using Reinforced Laminae with Carbon Nanotube Forests. *Nat Mater*, 5(6), 2006.

[34] A. Rotem and Z. Hashin. Failure Modes of Angle Ply Laminates. *Journal of Composite Materials*, 9(2):191–206, 1975.

[35] G. J. Dvorak and N. Laws. Analysis of Progressive Matrix Cracking In Composite Laminates II. First Ply Failure. *Journal of Composite Materials*, 21(4):309–329, 1987.

[36] P. Chang, A. P. Mouritz, and B. N. Cox. Properties and Failure Mechanisms of Z-pinned Laminates in Monotonic and Cyclic Tension. *Composites Part A: Applied Science and Manufacturing*, 37(10):1501–1513, 2006.

[37] S. T. Buschhorn, S. S. Kessler, N. Lachmann, J. Gavin, G. Thomas, and B. L. Wardle. Electrothermal Icing Protection of Aerosurfaces Using Conductive Polymer Nanocomposites. In *54th AIAA/ASME/ASCE/AHS/ASC Structures, Structural Dynamics, and Materials Conference*, page 1729, 2013.

[38] S. S. Wicks, R. Guzmán de Villoria, B. L. Wardle, S. S. Kessler, and C. T. Dunn. Carbon Nanotube (CNT) Enhancements for Aerosurface State Awareness. *Carbon*, 2011.

[39] R. F. Gibson. A Review of Recent Research on Mechanics of Multifunctional Composite Materials and Structures. *Composite Structures*, 92(12):2793 - 2810, 2010.

[40] D. R. Paul and L. M. Robeson. Polymer Nanotechnology: Nanocomposites. *Polymer*, 49(15):3187 - 3204, 2008.

[41] A. J. Crosby and J. Lee. Polymer Nanocomposites: The "Nano" Effect on Mechanical Properties. *Polymer Reviews*, 47(2):217–229, 2007.

[42] S. Iijima. Helical Microtubules of Graphitic Carbon. *Nature*, 354(6348):56, Nov 07 1991.

[43] E. W. Wong, P. E. Sheehan, and C. M. Lieber. Nanobeam Mechanics: Elasticity, Strength, and Toughness of Nanorods and Nanotubes. *Science*, 277(5334):1971–1975, 1997.

[44] J. P. Lu. Elastic Properties of Single and Multilayered Nanotubes. *Journal of physics and chemistry of solids*, 58(11):1649–1652, 1997.

[45] J. Salvetat, G. A. D. Briggs, J. Bonard, R. R. Bacsa, A. J. Kulik, T. Stöckli, N. A. Burnham, and L. Forró. Elastic and Shear Moduli of Single-walled Carbon Nanotube Ropes. *Physical review letters*, 82(5):944, 1999.

[46] M. Yu, O. Lourie, M. J. Dyer, K. Moloni, T. F. Kelly, and R. S. Ruoff. Strength and Breaking Mechanism of Multiwalled Carbon Nanotubes under Tensile Load. *Science*, 287(5453):637–640, 2000.

[47] R. E. Smalley, M. S. Dresselhaus, G. Dresselhaus, and P. Avouris. *Carbon Nanotubes: Synthesis, Structure, Properties, and Applications*, volume 80. Springer Science & Business Media, 2003.

[48] A. V. Krasheninnikov, K. Nordlund, M. Sirviö, E. Salonen, and J. Keinonen. Formation of Ion-irradiation-induced atomic-scale Defects on Walls of Carbon Nanotubes. *Physical Review B*, 63(24):245405, 2001.

[49] L. Yang, I. Greenfeld, and H. D. Wagner. Toughness of Carbon Nanotubes Conforms to Classic Fracture Mechanics. *Science advances*, 2(2):e1500969, 2016.

[50] E. T. Thostenson, Z. Ren, and T. Chou. Advances in the Science and Technology of Carbon Nanotubes and their Composites: A Review. *Composites Science and Technology*, 61(13):1899 - 1912, 2001.

[51] A. H. Barber, R. Andrews, L. S. Schadler, and H. D. Wagner. On the Tensile Strength Distribution of Multiwalled Carbon Nanotubes. *Applied Physics Letters*, 87(20):203106, 2005.

[52] M. Yu, O. Lourie, M. J. Dyer, K. Moloni, T. F. Kelly, and R. S. Ruoff. Strength and Breaking Mechanism of Multiwalled Carbon Nanotubes Under Tensile Load. *Science*, 287(5453):637–640, 2000.

[53] R. J. Young, I. A. Kinloch, L. Gong, and K. S. Novoselov. The Mechanics of Graphene Nanocomposites: A Review. *Composites Science and Technology*, 72(12):1459–1476, 2012.

[54] M. F. L. De Volder, S. H. Tawfick, R. H. Baughman, and A. J. Hart. Carbon Nanotubes: Present and Future Commercial Applications. *Science*, 339(6119):535–539, 2013.

[55] N. Yamamoto, A. J. Hart, E. J. Garcia, S. S. Wicks, H. M. Duong, A. H. Slocum, and B. L. Wardle. High-yield Growth and Morphology Control of Aligned Carbon Nanotubes on Ceramic Fibers for Multifunctional Enhancement of Structural Composites. *Carbon*, 47(3):551–560, 2009.

[56] C. M. Manjunatha, A. C. Taylor, A. J. Kinloch, and S. Sprenger. The Effect of Rubber Micro-particles and Silica Nano-particles on the Tensile Fatigue Behaviour of a Glass-fibre Epoxy Composite. *Journal of Materials Science*, 44(1):342–345, 2009.

[57] R. Li, E. F. Antunes, A. H. Liotta, C. Parschau, M. Payne, and B. L. Wardle. Woven Hierarchical Aerospace Composite Laminates with Aligned Carbon Nanotube Bulk Reinforcement. *57th AIAA/ASCE/AHS/ASC Structures, Structural Dynamics, and Materials Conference*, 2016.

[58] E. J. Garcia, B. L. Wardle, and A. J. Hart. Long Carbon Nanotubes Grown on the Surface of Fibers for Hybrid Composites. *AIAA Journal*, 46(6), 2008.

[59] E. J. Garcia, B. L. Wardle, A. J. Hart, and N. Yamamoto. Fabrication and Multifunctional Properties of a Hybrid Laminate with Aligned Carbon Nanotubes Grown In-situ. *Composites Science and Technology*, 68(9):2034 – 2041, 2008.

[60] S. S. Wicks, W. Wang, M. R. Williams, and B. L. Wardle. Multi-scale Interlaminar Fracture Mechanisms in Woven Composite Laminates Reinforced with Aligned Carbon Nanotubes. *Composites Science and Technology*, 100:128 – 135, 2014.

[61] E. T. Thostenson, W. Z. Li, D. Z. Wang, Z. F. Ren, and T. W. Chou. Carbon Nanotube/Carbon Fiber Hybrid Multiscale Composites. *Journal of Applied Physics*, 91(9):6034–6037, 2002.

[62] G. Pagani, M. J. Green, P. Poulin, and M. Pasquali. Competing Mechanisms and Scaling Laws for Carbon Nanotube Scission by Ultrasonication. *Proceedings of the National Academy of Sciences*, 109(29):11599-11604, 2012.

[63] J. Stegen. Mechanics of Carbon Nanotube Scission under Sonication. *The Journal of chemical physics*, 140(24):244908, 2014.

[64] C. A. Amadei, I. Y. Stein, G. J. Silverberg, B. L. Wardle, and C. D. Vecitis. Fabrication and Morphology Tuning of Graphene Oxide Nanoscrolls. *Nanoscale*, 8(12):6783–6791, 2016.

[65] Y. Geng, M. Y. Liu, J. Li, X. M. Shi, and J. K. Kim. Effects of Surfactant Treatment on Mechanical and Electrical Properties of CNT/Epoxy Nanocomposites. *Composites Part A: Applied Science and Manufacturing*, 39(12):1876 – 1883, 2008.

[66] J. C. Williams and E. A. Starke Jr. Progress in Structural Materials for Aerospace Systems. *Acta Materialia*, 51(19):5775 – 5799, 2003. The Golden Jubilee Issue. Selected topics in Materials Science and Engineering: Past, Present and Future.

[67] P. D. Mangalgiri. Composite Materials for Aerospace Applications. *Bulletin of Materials Science*, 22(3):657–664, 1999.

[68] B. McCarthy, J. N. Coleman, R. Czerw, A. B. Dalton, M. In Het Panhuis, A. Maiti, A. Drury, P. Bernier, J. B. Nagy, B. Lahr, et al. A Microscopic and Spectroscopic Study of Interactions between Carbon Nanotubes and a Conjugated Polymer. *The Journal of Physical Chemistry B*, 106(9):2210–2216, 2002.

[69] B. McCarthy, J. N. Coleman, S. A. Curran, A. B. Dalton, A. P. Davey, Z. Konya, A. Fonseca, J. B. Nagy, and W. J. Blau. Observation of Site Selective Binding in a Polymer Nanotube Composite. *Journal of Materials Science Letters*, 19(24):2239–2241, 2000.

[70] E. Assouline, A. Lustiger, A. H. Barber, C. A. Cooper, E. Klein, E. Wachtel, and H. D. Wagner. Nucleation Ability of Multiwall Carbon Nanotubes in Polypropylene Composites. *Journal of Polymer Science Part B: Polymer Physics*, 41(5):520–527, 2003.

[71] X. Xie, K. Aloys, X. Zhou, and F. Zeng. Ultra-High Molecular Mass Polyethylene/Carbon Nanotube Composites Crystallization and Melting Properties. *Journal of thermal analysis and calorimetry*, 74(1):317–323, 2003.

[72] A. H. Barber, S. R. Cohen, and H. D. Wagner. Measurement of Carbon Nanotube–Polymer Interfacial Strength. *Applied Physics Letters*, 82(23):4140–4142, 2003.

[73] P. Pötschke, T. D. Fornes, and D. R. Paul. Rheological Behavior of Multiwalled Carbon Nanotube/Polycarbonate Composites. *Polymer*, 43(11):3247–3255, 2002.

[74] J. N. Coleman, M. Cadek, R. Blake, V. Nicolosi, K. P. Ryan, C. Belton, A. Fonseca, J. B. Nagy, Y. K. Gun'ko, and W. J. Blau. High Performance Nanotube-Reinforced Plastics: Understanding the Mechanism of Strength Increase. *Advanced Functional Materials*, 14(8):791–798, 2004.

[75] H. Cebeci, R. Guzmán de Villoria, A. J. Hart, and B. L. Wardle. Multifunctional Properties of High Volume Fraction Aligned Carbon Nanotube Polymer Composites with Controlled Morphology. *Composites Science and Technology*, 69(15–16):2649 – 2656, 2009.

[76] E. E. Medeiros, A. M. da Silva Dias, and A. L. Christoforo. Numerical Simulation of Mechanical Fracture Testings. *International Journal of Materials Engineering*, 2(5):61–66, 2012.

[77] D. Hull and T. W. Clyne. *An Introduction to Composite Materials.* Cambridge university press, 1996.

[78] M. Janssen, J. Zuidema, and R.J.H. Wanhill. *Fracture Mechanics.* Delft University Press, 2002.

[79] ASTM International. ASTM D5528: Standard Test Method for Mode I Interlaminar Fracture Toughness of Unidirectional Fiber-Reinforced Polymer Matrix Composites. Standard, ASTM International, 2013.

[80] R. Sadeghian, S. Gangireddy, B. Minaie, and K. Hsiao. Manufacturing Carbon Nanofibers Toughened Polyester/Glass Fiber Composites using Vacuum Assisted Resin Transfer Molding for Enhancing the Mode-I Delamination Resistance. *Composites Part A: Applied Science and Manufacturing*, 37(10):1787 – 1795, 2006.

[81] P. Karapappas, A. Vavouliotis, P. Tsotra, V. Kostopoulos, and A. Paipetis. Enhanced Fracture Properties of Carbon Reinforced Composites by the Addition of Multi-Wall Carbon Nanotubes. *Journal of Composite Materials*, 43(9):977–985, 2009.

[82] A. Godara, L. Mezzo, F. Luizi, A. Warrier, S.V. Lomov, A.W. van Vuure, L. Gorbatikh, P. Moldenaers, and I. Verpoest. Influence of Carbon Nanotube Reinforcement on the Processing and the Mechanical behaviour of Carbon Fiber/Epoxy Composites. *Carbon*, 47(12):2914 – 2923, 2009.

[83] A. T. Seyhan, M. Tanoglu, and K. Schulte. Mode I and mode {II} Fracture Toughness of E-glass Non-crimp Fabric/Carbon Nanotube (CNT) Modified Polymer based Composites. *Engineering Fracture Mechanics*, 75(18):5151 – 5162, 2008.

[84] ASTM International. ASTM D5045: Standard Test Methods for Plane-Strain Fracture Toughness and Strain Energy Release Rate of Plastic Materials. Standard, ASTM International, 2014.

[85] F. H. Gojny, M.H.G. Wichmann, U. Köpke, B. Fiedler, and K. Schulte. Carbon Nanotube-Reinforced Epoxy-Composites: Enhanced Stiffness and Fracture Toughness at Low Nanotube Content. *Composites Science and Technology*, 64(15):2363 – 2371, 2004. Developments in carbon nanotube and nanofibre reinforced polymers.

[86] E. T. Thostenson and T. Chou. Processing-Structure-Multi-Functional Property Relationship in Carbon Nanotube/Epoxy Composites. *Carbon*, 44(14):3022 – 3029, 2006.

[87] Y. Zhou, F. Pervin, L. Lewis, and S. Jeelani. Fabrication and Characterization of Carbon/Epoxy Composites Mixed with Multi-walled Carbon Nanotubes. *Materials Science and Engineering: A*, 475(1–2):157 – 165, 2008. International Symposium on Inorganic Interfacial Engineering 2006.

[88] O. Gryshchuk, J. Karger-Kocsis, R. Thomann, Z. Konya, and I. Kiricsi. Multi-wall Carbon Nanotube Modified Vinylester and Vinylester–based Hybrid Resins. *Composites Part A: Applied Science and Manufacturing*, 37(9):1252–1259, 2006.

[89] M.R. Ayatollahi, S. Shadlou, and M. M. Shokrieh. Fracture Toughness of Epoxy/Multi-walled Carbon Nanotube Nano-composites under Bending and Shear Loading Conditions. *Materials & Design*, 32(4):2115 – 2124, 2011.

[90] L. Sun, G. L. Warren, J.Y. O'Reilly, W.N. Everett, W.N. Lee, D. Davis, D. Lagoudas, and H. J. Sue. Mechanical Properties of Surface-Functionalized SWCNT/Epoxy Composites. *Carbon*, 46(2):320 – 328, 2008.

[91] P. C. Ma, J. Kim, and B. Z. Tang. Effects of Silane Functionalization on the Properties of Carbon Nanotube/Epoxy Nanocomposites. *Composites Science and Technology*, 67(14):2965 – 2972, 2007. Polymer Nanocomposites - Modeling, Mechanical and Functional PropertiesPolymer Nanocomposites.

[92] N. Lachman and H. D. Wagner. Correlation between Interfacial Molecular Structure and Mechanics in CNT/Epoxy Nano-composites. *Composites Part A: Applied Science and Manufacturing*, 41(9):1093 – 1098, 2010. Fracture of Composites Conference: Interfacial interactions in composites and other applications.

[93] E. T. Thostenson and T. Chou. Aligned Multi-walled Carbon Nanotube-Reinforced Composites: Processing and Mechanical Characterization. *Journal of Physics D: Applied Physics*, 35(16):L77, 2002.

[94] L. Jin, C. Bower, and O. Zhou. Alignment of Carbon Nanotubes in a Polymer Matrix by Mechanical Stretching. *Applied Physics Letters*, 73(9):1197–1199, 1998.

[95] C. K. Najeeb, J. Chang, J. Lee, and J. Kim. Fabrication of Aligned Ultra-thin Transparent Conductive Films of Single-walled Carbon Nanotubes by a Compression/Sliding Method. *Scripta Materialia*, 64(2):126 – 129, 2011.

[96] Q. Cheng, J. Wang, K. Jiang, Q. Li, and S. Fan. Fabrication and Properties of Aligned Multi-walled Carbon Nanotube-Reinforced Epoxy Composites. *Journal of Materials Research*, 23(11):2975–2983, 2008.

[97] T. Ogasawara, S. Moon, Y. Inoue, and Y. Shimamura. Mechanical Properties of Aligned Multi-walled Carbon Nanotube/Epoxy Composites Processed using a Hotmelt Prepreg Method. *Composites Science and Technology*, 71(16):1826 – 1833, 2011.

[98] E.J. García, A.J. Hart, B.L. Wardle, and A.H. Slocum. Fabrication and Nanocompression Testing of Aligned Carbon-Nanotube–Polymer Nanocomposites. *Advanced Materials*, 19(16):2151–2156, 2007.

[99] J. Lee, I. Y. Stein, M. E. Devoe, D. J. Lewis, N. Lachman, S. S. Kessler, S. T. Buschhorn, and B. L. Wardle. Impact of Carbon Nanotube Length on Electron Transport in Aligned Carbon Nanotube Networks. *Applied Physics Letters*, 106(5):053110, 2015.

[100] D. Handlin, I. Y. Stein, R. Guzmán de Villoria, H. Cebeci, E. M. Parsons, S. Socrate, S. Scotti, and B. L. Wardle. Three-dimensional Elastic Constitutive Relations of Aligned Carbon Nanotube Architectures. *Journal of Applied Physics*, 114(22):224310, 2013.

[101] B. L. Wardle, D. S. Saito, E. J. García, A. J. Hart, R. Guzmán de Villoria, and E. A. Verploegen. Fabrication and Characterization of Ultrahigh-Volume- Fraction Aligned Carbon Nanotube–Polymer Composites. *Advanced Materials*, 20(14):2707–2714, 2008.

[102] S. Wu, R. B. Ladani, J. Zhang, A. J. Kinloch, Z. Zhao, J. Ma, X. Zhang, A. P. Mouritz, K. Ghorbani, and C. H. Wang. Epoxy Nanocomposites Containing Magnetite-Carbon Nanofibers Aligned Using a Weak Magnetic Field. *Polymer*, 68:25 – 34, 2015.

[103] R. B. Ladani, S. Wu, A. J. Kinloch, K. Ghorbani, J. Zhang, A. P. Mouritz, and C. H. Wang. Improving the Toughness and Electrical Conductivity of Epoxy Nanocomposites by Using Aligned Carbon Nanofibres. *Composites Science and Technology*, 117:146 – 158, 2015.

[104] Z Xia, L Riester, W.A Curtin, H Li, B.W Sheldon, J Liang, B Chang, and J.M Xu. Direct Observation of Toughening Mechanisms in Carbon Nanotube Ceramic Matrix Composites. *Acta Materialia*, 52(4):931 – 944, 2004.

[105] R. Andrews and M. C. Weisenberger. Carbon Nanotube Polymer Composites. *Current Opinion in Solid State and Materials Science*, 8(1):31 – 37, 2004.

[106] X. Zhou, E. Shin, K. W. Wang, and C. E. Bakis. Interfacial Damping Characteristics of Carbon Nanotube-Based Composites. *Composites Science and Technology*, 64(15 SPEC. ISS.):2425–2437, 2004. cited By 198.

[107] N. A. Koratkar, J. Suhr, A. Joshi, R. S. Kane, L. S. Schadler, P. M. Ajayan, and S. Bartolucci. Characterizing Energy Dissipation in Single-walled Carbon Nanotube Polycarbonate Composites. *Applied Physics Letters*, 87(6):063102, 2005.

[108] Jeffrey R Potts, Daniel R Dreyer, Christopher W Bielawski, and Rodney S Ruoff. Graphene-based polymer nanocomposites. *Polymer*, 52(1):5–25, 2011.

[109] T. Ramanathan, A. A. Abdala, S. Stankovich, D. A. Dikin, M. Herrera-Alonso, R. D. Piner, D. H. Adamson, H. C. Schniepp, X. R. R. S. Chen, R. S. Ruoff, et al. Functionalized Graphene Sheets for Polymer Nanocomposites. *Nature nanotechnology*, 3(6):327–331, 2008.

[110] Ray H. Baughman, Anvar A. Zakhidov, and Walt A. de Heer. Carbon Nanotubes - the Route Toward Applications. *Science*, 297(5582):787–792, 2002.

[111] D. Jacobs. Constitutive Model of Aligned Carbon Nanotube/Nafion Nanocomposite Ionic Electroactive Polymer Actuators. Master's thesis, Massachusetts Institute of Technology, 2016.

[112] J. Lee, I. Y. Stein, S. S. Kessler, and B. L. Wardle. Aligned Carbon Nanotube Film Enables Thermally Induced State Transformations in Layered Polymeric Materials. *ACS applied materials & interfaces*, 7(16):8900–8905, 2015.

[113] H. K. Mutha, Y. Lu, I. Y. Stein, H. J. Cho, M. E. Suss, T. Laoui, C. V. Thompson, B. L. Wardle, and E. N. Wang. Porosimetry and Packing Morphology of Vertically Aligned Carbon Nanotube Arrays via Impedance Spectroscopy. *Nanotechnology*, 28(5):05LT01, 2016.

[114] A. J. Hart and A. H. Slocum. Rapid Growth and Flow-mediated Nucleation of millimeter-scale Aligned Carbon Nanotube Structures from a Thin-film Catalyst. *The Journal of Physical Chemistry B*, 110(16):8250–8257, 2006.

[115] F. Banhart. Irradiation Effects in Carbon Nanostructures. *Reports on progress in physics*, 62(8):1181, 1999.

[116] A. V. Krasheninnikov and F. Banhart. Engineering of Nanostructured Carbon Materials with Electron or Ion Beams. *Nature materials*, 6(10):723–733, 2007.

[117] D. J. Lewis. Interlaminar Reinforcement of Carbon Fiber Composites from Unidirectional Prepreg Utilizing Aligned Carbon Nanotubes. Master's thesis, Massachusetts Institute of Technology, 2016.

[118] M. Bedewy, E. R. Meshot, H. Guo, E. A. Verploegen, W. Lu, and A. J. Hart. Collective Mechanism for the Evolution and Self-Termination of Vertically Aligned Carbon Nanotube Growth. *The Journal of Physical Chemistry C*, 113(48):20576–20582, 2009.

[119] E. R. Meshot and A. J. Hart. Abrupt Self-termination of Vertically Aligned Carbon Nanotube Growth. *Applied Physics Letters*, 92(11), 2008.

[120] M. Bedewy. Data-driven Understanding of Collective Carbon Nanotube Growth by In-situ Characterization and Nanoscale Metrology. *Journal of Materials Research*, 32(1):153–165, 2017.

[121] M. Bedewy, E. R. Meshot, M. J. Reinker, and A. J. Hart. Population Growth Dynamics of Carbon Nanotubes. *ACS Nano*, 5(11):8974–8989, 2011. PMID: 22023221.

[122] J. Han, R. A. Graff, B. Welch, C. P. Marsh, R. Franks, and M. S. Strano. A Mechanochemical Model of Growth Termination in Vertical Carbon Nanotube Forests. *ACS Nano*, 2(1):53–60, 2008. PMID: 19206547.

[123] X. Wang, Y. Feng, H. E. Unalan, G. Zhong, P. Li, H. Yu, A. I. Akinwande, and W. I. Milne. The Mechanism of the Sudden Termination of Carbon Nanotube Supergrowth. *Carbon*, 49(1):214 – 221, 2011.

[124] P. B. Amama, C. L. Pint, L. McJilton, S. M. Kim, E. A. Stach, P. T. Murray, R. H. Hauge, and B. Maruyama. Role of Water in Super Growth of Single-Walled Carbon Nanotube Carpets. *Nano Letters*, 9(1):44–49, 2009. PMID: 19046079.

[125] S. M. Kim, C. L. Pint, P. B. Amama, D. N. Zakharov, R. H. Hauge, B. Maruyama, and E. A. Stach. Evolution in Catalyst Morphology Leads to Carbon Nanotube Growth Termination. *The Journal of Physical Chemistry Letters*, 1(6):918–922, 2010.

[126] E. Shawat, V. Mor, L. Oakes, Y. Fleger, C. L. Pint, and G. D. Nessim. What is Below the Support Layer Affects Carbon Nanotube Growth: An Iron Catalyst Reservoir Yields Taller Nanotube Carpets. *Nanoscale*, 6(3):1545–1551, 2014.

[127] R. Yemini, A. Itzhak, Y. Gofer, T. Sharabani, M. Drela, and G. D. Nessim. Nickel Overlayers Modify Precursor Gases To Pattern Forests of Carbon Nanotubes. *The Journal of Physical Chemistry C*, 2017.

[128] J. Li, M. Bedewy, A. O. White, E. S. Polsen, S. Tawfick, and A. J. Hart. Highly Consistent Atmospheric Pressure Synthesis of Carbon Nanotube Forests by Mitigation of Moisture Transients. *The Journal of Physical Chemistry C*, 120(20):11277–11287, 2016.

[129] A. A. Puretzky, G. Eres, C. M. Rouleau, I. N. Ivanov, and D. B. Geohegan. Real-time Imaging of Vertically Aligned Carbon Nanotube Array Growth Kinetics. *Nanotechnology*, 19(5):055605, 2008.

[130] M. Stadermann, S. P. Sherlock, J. In, F. Fornasiero, H. G. Park, A. B. Artyukhin, Y. Wang, J. J. De Yoreo, C. P. Grigoropoulos, O. Bakajin, A. A. Chernov, and A. Noy. Mechanism and Kinetics of Growth Termination in Controlled Chemical Vapor Deposition Growth of Multiwall Carbon Nanotube Arrays. *Nano Letters*, 9(2):738–744, 2009. PMID: 19146455.

[131] S. Yasuda, T. Hiraoka, D. N. Futaba, T. Yamada, M. Yumura, and K. Hata. Existence and Kinetics of Graphitic Carbonaceous Impurities in Carbon Nanotube Forests to Assess the Absolute Purity. *Nano Letters*, 9(2):769–773, 2009. PMID: 19199754.

[132] M. E. Itkis, D. E. Perea, S. Niyogi, S. M. Rickard, M. A. Hamon, H. Hu, B. Zhao, and R. C. Haddon. Purity Evaluation of As-Prepared Single-Walled Carbon Nanotube Soot by Use of Solution-Phase Near-IR Spectroscopy. *Nano Letters*, 3(3):309–314, 2003.

[133] L. Bokobza and J. Zhang. Raman Spectroscopic Characterization of Multi-Wall Carbon Nanotubes and of Composites. *Express Polym. Lett*, 6(7):601–608, 2012.

[134] A. V. Krasheninnikov and K. Nordlund. Ion and Electron Irradiation-induced Effects in Nanostructured Materials. *Journal of applied physics*, 107(7):3, 2010.

[135] A. Jorio, M. A. Pimenta, A. G. S. Filho, R. Saito, G. Dresselhaus, and M. S. Dresselhaus. Characterizing Carbon Nanotube Samples with Resonance Raman Scattering. *New Journal of Physics*, 5(1):139, 2003.

[136] M. S. Dresselhaus, A. Jorio, M. Hofmann, G. Dresselhaus, and R. Saito. Perspectives on Carbon Nanotubes and Graphene Raman Spectroscopy. *Nano Letters*, 10(3):751–758, 2010. PMID: 20085345.

[137] S. Osswald, M. Havel, and Y. Gogotsi. Monitoring oxidation of Multi-walled Carbon Nanotubes by Raman Spectroscopy. *Journal of Raman Spectroscopy*, 38(6):728–736, 2007.

[138] A. C. Ferrari and D. M. Basko. Raman Spectroscopy as a Versatile Tool for Studying the Properties of Graphene. *Nature nanotechnology*, 8(4):235–246, 2013.

[139] I. Y. Stein, A. J. Constable, N. Morales-Medina, C. V. Sackier, M. E. Devoe, H. M. Vincent, and B. L. Wardle. Structure-mechanical Property Relations of Non-graphitizing Pyrolytic Carbon Synthesized at Low Temperatures. *Carbon*, 117:411–420, 2017.

[140] M. S. Dresselhaus, G. Dresselhaus, and P. C. Eklund. *Science of Fullerenes and Carbon Nanotubes: Their Properties and Applications.* Academic press, 1996.

[141] L. S. K. Pang, J. D. Saxby, and S. P. Chatfield. Thermogravimetric Analysis of Carbon Nanotubes and Nanoparticles. *Journal of Physical Chemistry; (United States)*, 97:27, Jul 1993.

[142] X. H. Chen, C.S Chen, Q. Chen, F.Q Cheng, G. Zhang, and Z.Z Chen. Non-destructive Purification of Multi-walled Carbon Nanotubes Produced by Catalyzed {CVD}. *Materials Letters*, 57(3):734 – 738, 2002.

[143] I. Y. Stein and B. L. Wardle. Packing Morphology of Wavy Nanofiber Arrays. *Physical Chemistry Chemical Physics*, 18(2):694–699, 2016.

[144] I. Y. Stein, N. Lachman, M. E. Devoe, and B. L. Wardle. Exohedral Physisorption of Ambient Moisture Scales Non-monotonically with Fiber Proximity in Aligned Carbon Nanotube Arrays. *ACS nano*, 8(5):4591–4599, 2014.

[145] A. L. Yost, S. Shahsavari, G. M. Bradwell, R. Polak, F. Fachin, R. E. Cohen, G. H. McKinley, M. Toner, M. F. Rubner, and B. L. Wardle. Layer-by-layer functionalized nanotube arrays: A versatile microfluidic platform for biodetection. *Microsystems & Nanoengineering*, 1, 2015.

[146] H. Su, C. Chen, Y. Chen, D. Yao, H. Chen, Y. Chang, and T. Yew. Improving the Adhesion of Carbon Nanotubes to a Substrate Using Microwave Treatment . *Carbon*, 48(3):805 – 812, 2010.

[147] Z. Chen, Q. Zhang, P. Lan, B. Zhu, T. Yu, G. Cao, and D. den Engelsen. Ultrahigh-current Field Emission from Sandwich-grown Well-aligned Uniform Multi-walled Carbon Nanotube Arrays with High Adherence Strength. *Nanotechnology*, 18(26):265702, 2007.

[148] H. Nishijima, S. Kamo, S. Akita, Y. Nakayama, K. I. Hohmura, S. H. Yoshimura, and K. Takeyasu. Carbon-nanotube Tips for Scanning Probe Microscopy: Preparation by a Controlled Process and Observation of Deoxyribonucleic Acid. *Applied Physics Letters*, 74(26):4061–4063, 1999.

[149] A. Cao, V. P. Veedu, X. Li, Z. Yao, M. N. Ghasemi-Nejhad, and P. M. Ajayan. Multifunctional Brushes made from Carbon Nanotubes. *Nat Mater*, 4(7):540–545, 07 2005.

[150] S. Talapatra, S. Kar, S. K. Pal, R. Vajtai, L. Ci, P. Victor, M. M. Shaijumon, S. Kaur, O. Nalamasu, and P. M. Ajayan. Direct Growth of Aligned Carbon Nanotubes on Bulk Metals. *Nat Nano*, 1(2):112–116, 11 2006.

[151] Y. Zhang, E. Suhir, Y. Xu, and C. Gu. Bonding Strength of a Carbon Nanofiber Array to its Substrate. *Journal of Materials Research*, 21(11):2922–2926, 11 2006.

[152] I. Lahiri, D. Lahiri, S. Jin, A. Agarwal, and W. Choi. Carbon Nanotubes: How Strong Is Their Bond with the Substrate? *ACS Nano*, 5(2):780–787, 2011.

[153] ASTM International. ASTM B905: Standard Test Methods for Assessing the Adhesion of Metallic and Inorganic Coatings by the Mechanized Tape Test. Standard, ASTM International, 2016.

[154] ASTM International. ASTM D3359: Standard Test Methods for Measuring Adhesion by Tape Test. Standard, ASTM International, 2009.

[155] C. Y. Wang, T. H. Chen, S. C. Chang, S. Y. Cheng, and T. S. Chin. Strong Carbon-Nanotube Polymer Bonding by Microwave Irradiation. *Advanced Functional Materials*, 17(12):1979–1983, 2007.

[156] ASTM International. ASTM D5179: Standard Test Method for Measuring Adhesion of Organic Coatings to Plastic Substrates by Direct Tensile Testing. Standard, ASTM International, 2008.

[157] M. F. L. De Volder, S. J. Park, S. H. Tawfick, D. O. Vidaud, and A. J. Hart. Fabrication and Electrical Integration of Robust Carbon Nanotube Micropillars by Self-directed Elastocapillary Densification. *Journal of Micromechanics and Microengineering*, 21(4):045033, 2011.

[158] T. Wang, S. Chen, D. Jiang, Y. Fu, K. Jeppson, L. Ye, and J. Liu. Through-Silicon Vias Filled With Densified and Transferred Carbon Nanotube Forests. *IEEE Electron Device Letters*, 33(3):420–422, March 2012.

[159] H. Cebeci, I. Y. Stein, and B. L. Wardle. Effect of Nanofiber Proximity on the Mechanical Behavior of High Volume Fraction Aligned Carbon Nanotube Arrays. *Applied Physics Letters*, 104(2):023117, 2014.

[160] I. Y. Stein and B. L. Wardle. Coordination Number Model to Quantify Packing Morphology of Aligned Nanowire Arrays. *Physical Chemistry Chemical Physics*, 15(11):4033–4040, 2013.

[161] Hexion. Epon resin 862 technical data sheet.

[162] D. J. O'Brien, N. R. Sottos, and S. R. White. Cure-dependent Viscoelastic Poisson's Ratio of Epoxy. *Experimental Mechanics*, 47(2):237–249, 2007.

[163] Hexel. HexFlow RTM6-2 Product Data. *Online*, 2017.

[164] M. Theodore, M. Hosur, J. Thomas, and S. Jeelani. Influence of Functionalization on Properties of MWCNT–Epoxy Nanocomposites. *Materials Science and Engineering: A*, 528(3):1192–1200, 1 2011.

[165] M. Theodore, M. Hosur, J. Thomas, and S. Jeelani. Processing and Characterization of EPON 862 Reinforced with Functionalized MWCNTs. In *ICCM 16 Proceedings*, Kyoto Japan, 2007.

[166] F. Komuves, A. Kelkar, R. Mohan, and V. Kelkar. Prediction of Mechanical Properties of EPON 862 (DGEBF) - W (DETDA) using MD Simulations. In *51st AIAA/ASME/ASCE/AHS/ASC Structures, Structural Dynamics and Materials Conference*, Orlando, Florida, 2010.

[167] C. Chen and D. Curliss. Processing and Morphological Development of Montmorillonite Epoxy Nanocomposites. *Nanotechnology*, 14(6):643, 2003.

[168] J. S. Park, H. S. Kim, and H. H. Thomas. Healing Behavior of a Matrix Crack on a Carbon Fiber/Mendomer Composite. *Composites Science and Technology*, 69(7–8):1082–1087, 6 2009.

[169] S. C. Zunjarrao and R. P. Singh. Characterization of the Fracture Behavior of Epoxy Reinforced with Nanometer and Micrometer Sized Aluminum Particles. *Composites Science and Technology*, 66(13):2296–2305, 10 2006.

[170] R. Guo and E. Sachs. Modeling, Optimization and Control of Spatial Uniformity in Manufacturing Processes. *IEEE Transactions on Semiconductor Manufacturing*, 6(1):41–57, 1993.

[171] E. J. García, A. J. Hart, B. L. Wardle, and A. H. Slocum. Fabrication of Composite Microstructures by Capillarity-driven Wetting of Aligned Carbon Nanotubes with Polymers. *Nanotechnology*, 18(16):165602, 2007.

[172] N. Chakrapani, B. Wei, A. Carrillo, P. M. Ajayan, and R. S. Kane. Capillarity-driven Assembly of Two-dimensional Cellular Carbon Nanotube Foams. *Proceedings of the National Academy of Sciences*, 101(12):4009–4012, 2004.

[173] M. De Volder, S. H. Tawfick, S. J. Park, D. Copic, Z. Zhao, W. Lu, and A. J. Hart. Diverse 3D Microarchitectures made by Capillary Forming of Carbon Nanotubes. *Advanced Materials*, 22(39):4384–4389, 2010.

[174] S. H. Tawfick, M. De Volder, and A. J. Hart. Structurally Programmed Capillary Folding of Carbon Nanotube Assemblies. *Langmuir*, 27(10):6389–6394, 2011.

[175] K. Xiao, L. Ye, and Y. S. Kwok. Effects of Pre-cracking Methods on Fracture Behaviour of an Araldite-F Epoxy and its Rubber-modified Systems. *Journal of materials science*, 33(11):2831–2836, 1998.

[176] T. Nishida, Y. Hanaki, and G. Pezzotti. Effect of Notch-Root Radius on the Fracture Toughness of a Fine-Grained Alumina. *Journal of the American Ceramic Society*, 77(2):606–608, 1994.

[177] P. J. Schilling, B. R. Karedla, A. K. Tatiparthi, M. A. Verges, and P. D. Herrington. X-ray Computed Microtomography of Internal Damage in Fiber Reinforced Polymer Matrix Composites. *Composites Science and Technology*, 65(14):2071 – 2078, 2005.

[178] E. Masad, V. K. Jandhyala, N. Dasgupta, N. Somadevan, and N. Shashidhar. Characterization of Air Void Distribution in Asphalt Mixes using X-ray Computed Tomography. *Journal of Materials in Civil Engineering*, 14(2):122–129, Issue: object: doi:10.1061/jmcee7.2002.14.issue-2, revision: rev:1479371342616-9636:doi:10.1061/jmcee7.2002.14.issue-2, .

[179] M. Zamanian, M. Mortezaei, B. Salehnia, and J. E. Jam. Fracture Toughness of Epoxy Polymer Modified with Nanosilica Particles: Particle Size Effect. *Engineering Fracture Mechanics*, 97:193 – 206, 2013.

[180] Gao, Y. Mode I Fracture Toughness of Aligned Carbon Nanotube-Epoxy Nanocomposites with Various Nanotube Modifications. Master's thesis, Imperial College London, 2017.

[181] L. Wenbo and Y. Tingqing. Computer Simulation of Conic-shaped Patterns on Fracture Surfaces of Polymers. *Journal of applied polymer science*, 89(6):1722–1725, 2003.

[182] H. Henry and M. Adda-Bedia. Fractographic Aspects of Crack Branching Instability Using a Phase-field Model. *Physical Review E*, 88(6):060401, 2013.

[183] E. K. C. Lee, A. Rudin, and A. Plumtree. The Interpretation and Use of Fracture-surface morphology: A Special Case for Polystyrene. *Journal of materials science*, 30(8):2091–2096, 1995.

[184] D. M. Kulawansa, S. C. Langford, and J. T. Dickinson. Scanning Tunneling Microscope Observations of Polymer Fracture Surfaces. *Journal of materials research*, 7(05):1292–1302, 1992.

[185] D. Hull. *Fractography: observing, measuring and interpreting fracture surface topography.* Cambridge University Press, 1999.

[186] I. Narisawa, T. Murayama, and H. Ogawa. Internal Fracture of Notched Epoxy Resins. *Polymer*, 23(2):291 – 294, 1982.

[187] M. R. Piggott and D. Andison. The Carbon Fibre-Epoxy Interface. *Journal of reinforced plastics and composites*, 6(3):290–302, 1987.

[188] Y. Ganesan, C. Peng, Y. Lu, P. E. Loya, P. Moloney, E. Barrera, B. I. Yakobson, J. M. Tour, R. Ballarini, and J. Lou. Interface Toughness of Carbon nanotube reinforced epoxy composites. *ACS applied materials & interfaces*, 3(2):129–134, 2011.

[189] J. D. H. Hughes. The Carbon Fibre/Epoxy Interface: A Review. *Composites Science and Technology*, 41(1):13–45, 1991.

[190] Y. Zhou, F. Pervin, L. Lewis, and S. Jeelani. Experimental Study on the Thermal and Mechanical Properties of Multi-walled Carbon Nanotube-reinforced Epoxy. *Materials Science and Engineering: A*, 452:657–664, 2007.

[191] M. Kim, Y. Park, O. I. Okoli, and C. Zhang. Processing, Characterization, and Modeling of Carbon Nanotube-reinforced Multiscale Composites. *Composites Science and Technology*, 69(3):335–342, 2009.

[192] K. C. Hwang. Thermal Expansion of Single Wall Carbon Nanotubes. *Urbana*, 51:61801, 2004.

[193] Y. Maniwa, R. Fujiwara, H. Kira, H. Tou, H. Kataura, S. Suzuki, Y. Achiba, E. Nishibori, M. Takata, M. Sakata, et al. Thermal Expansion of Single-Walled Carbon Nanotube (SWNT) Bundles: X-ray Diffraction Studies. *Physical Review B*, 64(24):241402, 2001.

[194] F. Y. Wu and H. M. Cheng. Structure and Thermal Expansion of Multi-Walled Carbon Nanotubes Before and After High Temperature Treatment. *Journal of Physics D: Applied Physics*, 38(24):4302, 2005.

[195] D. P. Cole, H. A. Bruck, and A. L. Roytburd. Nanoindentation Studies of Graded Shape Memory Alloy Thin Films Processed Using Diffusion Modification. *Journal of Applied Physics*, 103(6):064315, 2008.

[196] Z. Xia, L. Riester, B. W. Sheldon, W. A. Curtin, J. Liang, A. Yin, and J. M. Xu. Mechanical Properties of Highly Ordered Nanoporous Anodic Alumina Membranes. *Rev. Adv. Mater. Sci*, 6(2):131–139, 2004.

[197] J. L. Gair Jr. *Nanotube-Matrix Interplay and Tunability in Ultrahigh Volume-Fraction Aligned Carbon Nanotube Poly(Urethane-Urea) Nanocomposites.* PhD thesis, University of Maryland, 2017.

[198] D. P. Cole and K. E. Strawhecker. An Improved Instrumented Indentation Technique for Tingle Microfibers. *Journal of Materials Research*, 29(09):1104–1112, 2014.

[199] W. C. Oliver and G. M. Pharr. An Improved Technique for Determining Hardness and Elastic Modulus Using Load and Displacement Sensing Indentation Experiments. *Journal of materials research*, 7(06):1564–1583, 1992.

[200] G. Feng and A. H. W. Ngan. Effects of Creep and Thermal Drift on Modulus Measurement Using Depth-sensing Indentation. *Journal of Materials Research*, 17(03):660–668, 2002.

[201] A. C. Fischer-Cripps. Analysis of Nanoindentation Test Data. In *Nanoindentation*, pages 39–75. Springer, 2011.

[202] L. Wang, C. Ortiz, and M. C. Boyce. Mechanics of Indentation into Micro-and Nanoscale Forests of Tubes, Rods, or Pillars. *Journal of Engineering Materials and Technology*, 133(1):011014, 2011.

[203] S. R. Cohen and E. Kalfon-Cohen. Dynamic Nanoindentation by Instrumented Nanoindentation and Force Microscopy: A Comparative Review. *Beilstein journal of nanotechnology*, 4(1):815–833, 2013.

[204] H. Kishi, M. Kuwata, S. Matsuda, T. Asami, and A. Murakami. Damping Properties of Thermoplastic-Elastomer Interleaved Carbon Fiber-Reinforced Epoxy Composites. *Composites Science and Technology*, 64(16):2517–2523, 2004.